Microseismology Research Group

THE UNIVERSITY of LIVERPOOL

Integrated Microseismic Monitoring and Numerical Modelling for the Determination of Fracture Architecture around Longwall Coal Mines for Geomechanical Validation.

Sub-Contract to ECSC Research Agreement No: 7229-AF/013

Application of Geophysical and Geodetic Techniques to the Determination of Structure and Monitoring of the Surface

Report for Period 1 December 1997 to 31 December 1998

Phase 1 Feasibility Proposal:

Retrospective analysis of combined geomechanical data and microseismic monitoring

P. Styles, A. Bryan-Jones, S. Toon and Z. Flynn

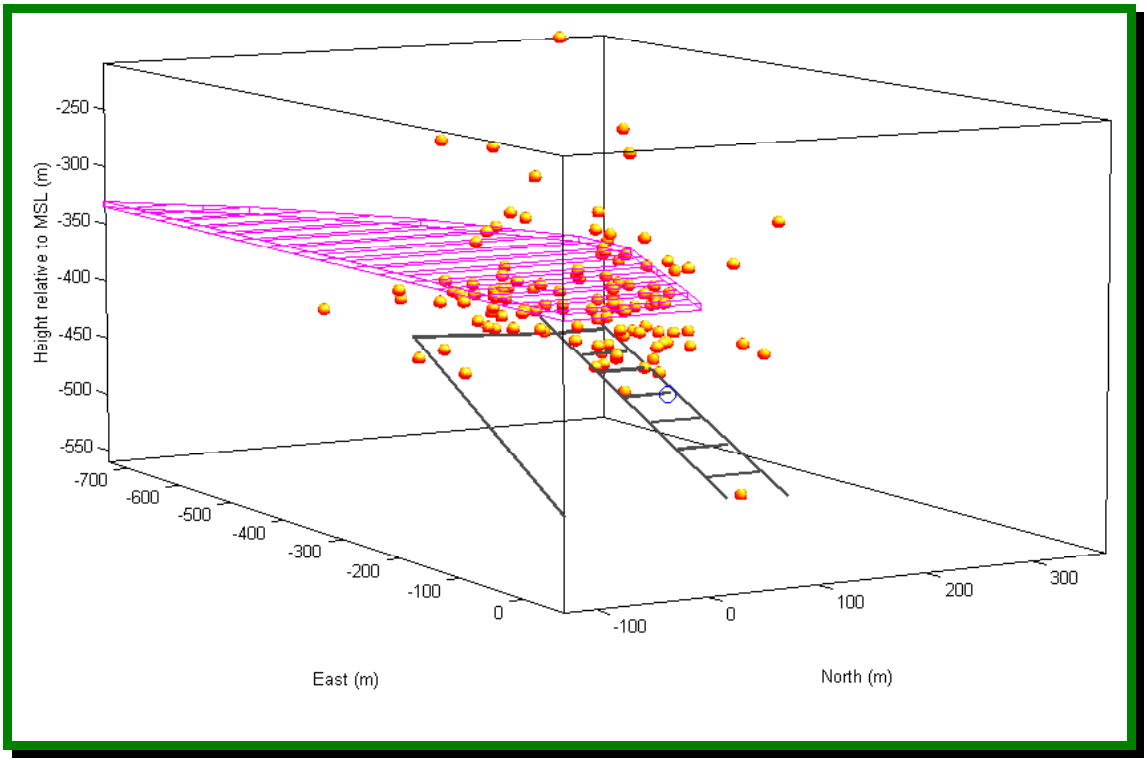

Microseismology Research Group

Integrated Microseismic Monitoring and Numerical Modelling for the Determination of Fracture Architecture Around Longwall Coal Mines for Geomechanical Validation.

Sub-Contract to ECSC Research Agreement No: 7229-AF/013
Application of Geophysical and Geodetic Techniques to the Determination of Structure and Monitoring of the Surface

Report for Period 1 December 1997 to 31 December 1998
Phase 1 Feasibility Proposal :

Retrospective analysis of combined geomechanical data and microseismic monitoring

P. Styles, A. Bryan-Jones, S.Toon and Z. Flynn

Microseismology Research Group
Department of Earth Sciences
University of Liverpool
Liverpool L69 3BX

Objectives

Knowledge of the extent and location of fracture development and the nature of the fracture process is critical to understanding the geomechanical behaviour of the rock-mass around zones of excavation, *eg Waste Repositories, Underground and Opencast Mines and Tunnels*. This project aims to integrate numerical modelling of rock behaviour with direct validation of fracture architecture from microseismic monitoring to permit dynamic numerical modelling and display using 3D Scientific Visualisation and Virtual Reality. Geomechanical modelling is an integral part of the design stage of construction of a mine or repository and microseismic monitoring has been carried out at a few sites (e.g. Asfordby Mine, UK, Gordonstone Mine, Australia). Despite this the two techniques have traditionally remained distinct. The first phase of this project is to examine the feasibility of using microseismic data for the validation of numerical models and the characterisation of rock-mass behaviour around long-wall coal faces.

CONTENTS

OBJECTIVES 1

CONTENTS 3

1 INTRODUCTION 7

1.1 Introduction 7

1.2 Longwall Mines 8

1.2.1 Traditional model of a longwall mine 8

1.2.2 Quantifying the behaviour of the rock-mass 10

1.3 Numerical Methods 11

1.4 Input Parameters For Numerical Modelling 12

1.4.1 Practical problems in determining parameters 12

1.4.2 Scaling parameters 12

1.5 Previous Modelling 13

1.5.1 Caving mechanisms 13

1.5.2 Subsidence modelling 14

1.6 Information which can be derived from Microseismic Monitoring of Relevance to Geomechanical Behaviour of Mines 16

1.7 General overview of microseismic monitoring in mining and other applications 19

1.7.1 Microseismic monitoring in Poland 19

1.7.2 Microseismic monitoring in Canada and USA 20

1.7.3 Microseismic monitoring in South Africa 21

1.7.4 Microseismic monitoring of collieries in other countries 22

1.8 Development of mining induced seismicity studies in the UK 23

1.8.1 UK coal mining induced seismicity 23

1.8.2 Mining induced seismicity in the Staffordshire and Nottinghamshire coalfields 24

1.8.3 Microseismic monitoring of Bilston Glen Colliery, Midlothian Coalfield, Scotland 26

1.8.4 Surface microseismic monitoring in the North Nottinghamshire coalfield 26

1.8.5 Borehole microseismology studies 27

1.9 GORDONSTONE COLLIERY 29
1.9.1 Background 29
1.9.2 Instrumentation 30
1.9.3 Analysis and Interpretation 30

2 GEOLOGICAL AND TECHNICAL BACKGROUND FOR ASFORDBY STUDY 37

2.1 Introduction 37

2.2 Geological setting of Asfordby Colliery 38
2.2.1 Structure and faulting 38
2.2.2 Geological succession 39

2.3 Relevant geomechanical models 41
2.3.1 Physical model of Asfordby stratigraphy 41
2.3.2 Golder Associates model of Asfordby stratigraphy 42
2.3.3 SCT model of general Coal Measure stratigraphy 43

2.4 Recording equipment 45
2.4.1 Receivers 45
2.4.2 Data recording equipment 48

2.6 Event frequency 49

3 MICROSEISMIC EVENT LOCATIONS 53

3.1 Introduction 53

3.2 Back azimuth propagation: Seismic event location using polarisation analysis 54
3.2.1 Method description 54
3.2.2 Accuracy of location method 55
3.2.3 Velocity model 63

3.3 Locations of microseismic events recorded during first phase of monitoring 68
3.3.2 Fishponds dataset 68
3.3.1 Cants Thorn 1 upper sonde dataset 70

3.4 Locations of microseismic events recorded during second phase of monitoring 82
3.4.1 Hole 1 dataset 82
3.4.2 Hole 2 dataset 94

3.5 Conclusions....94

4 SPATIAL CLUSTERING OF MICROSEISMIC EVENTS....97

4.1 Introduction....97

4.2 A method to determine significant structures....98
4.2.1 Concept....98
4.2.2 Method....99

4.4 Application of the collapsing method to the Phase-One dataset....103
4.4.1 Original locations....103
4.4.2 Collapsed locations....104

4.5 Application of the collapsing method to the Phase-Two hole 1 dataset....108
4.5.1 Original locations....108
4.5.2 Collapsed locations....109
4.5.3 Effects of different error values....115

4.6 Conclusions....117

5 MICROSEISMIC EVENT SOURCE MECHANISMS....119

5.1 Introduction....119

5.2 An amplitude ratio inversion method using a single three-component seismogram....122
5.2.1 Transforming data to a new co-ordinate system....122
5.2.2 Splitting seismic data into principal components....125
5.2.3 Grid search to find possible mechanisms....126
5.2.4 Transforming possible mechanisms to original co-ordinate system....128
5.2.5 Incorporating a layered velocity model....130
5.2.6 Discussion of assumptions....133

5.3 Synthetic tests....134
5.3.1 Random locations and random double-couple mechanisms....134
5.3.2 The effects of noisy data....136
5.3.3 The effects of event mislocation errors....138
5.3.4 Random locations and source mechanisms of a certain known type....139
5.3.5 Clustered locations with similar source mechanisms....141
5.3.6 Discussion of results of synthetic tests....142

5.4 Determining P-axis and T-axis orientations rather than double-couple mechanisms 143
5.4.1 Synthetic test 143
5.4.2 Discussion 146

5.5 Conclusions.....147

6 INFERRED STRESS ORIENTATIONS AND SOURCE MECHANISMS FOR ASFORDBY DATA 149

6.1 Introduction.....149

6.2 P-axis and T-axis orientations for Asfordby data 151
6.2.1 Comparing P-axis and T-axis orientations calculated for the same event recorded at two sondes 151
6.2.2 P-axis and T-axis orientations calculated for events recorded during Phase-One.....156
6.2.3 P-axis and T-axis orientations calculated for events recorded during Phase-Two 163

6.3 Double-couple mechanisms for Asfordby data.....169
6.3.1 Comparing double-couple mechanisms calculated for the same event recorded at two sondes.....169
6.3.2 Double-couple mechanisms calculated for events recorded during Phase-One 172
6.3.3 Double-couple mechanisms calculated for events recorded during Phase-Two 178

6.4 Conclusions.....185

7 CONCLUSIONS.....187

7.1 Introduction.....187

7.2 New and improved analysis techniques.....187

7.3 A typical response of the rock mass to mining activity as shown by the analysis of induced seismicity.....188

7.4 An atypical response of the rock mass to mining activity as shown by the analysis of induced seismicity.....189

7.5 Implications of this work and suggestions for future work.....190

REFERENCES.....193

1 INTRODUCTION

1.1 Introduction

Excavation of a volume of rock effects the stress field in the rock mass around that volume. The change in stress will cause strain to build up and fractures will form. The formation of these fractures generates seismic waves that travel through the rock mass. It is these seismic events that are termed mining-induced seismicity. Induced seismicity is the result of a man-made change in the stress field, whether it is from mining, exploitation of hydrocarbon reserves, large-scale surface quarrying, filling of reservoirs or large underground explosions. Mining-induced seismicity was once thought of as an undesirable side effect of mining, which in some cases it is as large induced earthquakes can cause huge amounts of damage to an excavation. However, it has been realised for almost 40 years now that studying the induced seismicity can be used as a tool to remotely interrogate the rock mass surrounding the excavation. This can have implications for the safety and productivity of a mine, but also allows the process of rock fracture to be studied between the laboratory and macroscopic scale. A typical mining induced seismicity study, where a volume of rock is excavated and the remaining rock mass deforms, can be thought of as an experiment that allows the geomechanical response of rock to a change in stress to be studied. Thus the study of mining induced seismicity provides an intermediate step between laboratory experiments, where fractures are typically microscopic and factors such as grain size can influence results, and the study of crustal scale earthquakes.

1.2 Longwall Mines

1.2.1 Traditional model of a longwall mine

Figure 1.1 Plan (top) and sectional (bottom) sketches of a typical longwall mine face.

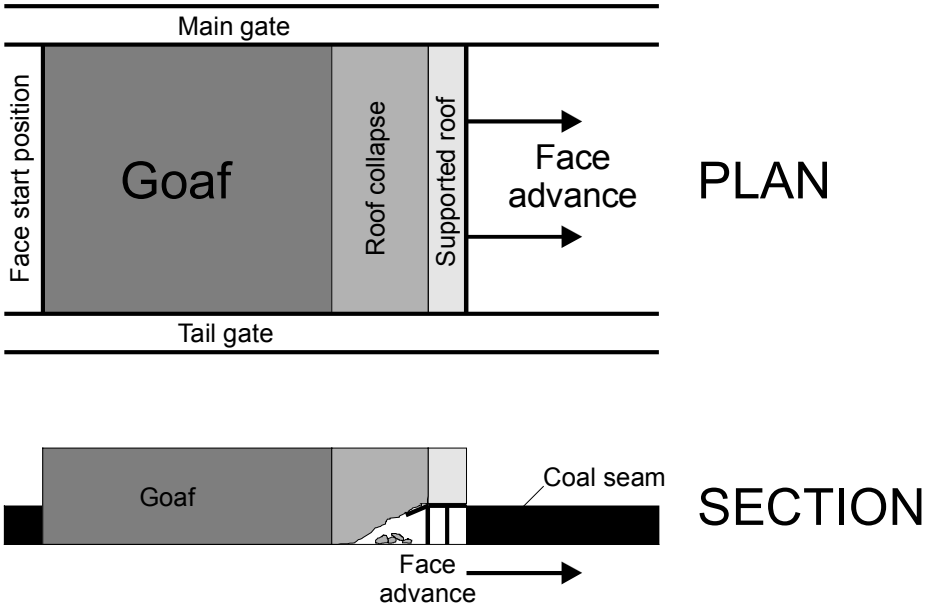

Figure 1.1 shows a sketch of a typical longwall face. To develop a longwall face, first the two gate roads are tunnelled. The face start position is cut to connect the two gate roads. The coal seam between the two gate roads is called a panel. The face then advances by cutting "shears" between the two gate roads i.e. the shearer starts at the S end of the face and moves N cutting a certain amount of coal until it reaches the other end of the face. The shearer then advances and cuts coal moving back along the face. The roof immediately behind the face is supported by hydraulic chocks, which move forward as the face advances. As the roof supports move forward, the roof collapses. The roof material bulks out as it collapses (i.e. it increases in volume) to fill the void left by the extraction of the coal seam. The collapsed roof material is called goaf. In some cases, the roof does not collapse in a continuous controlled manner, but collapses in large solid blocks. These can overload roof supports and cause severe problems at the face. This sort of roof collapse is called a weighting.

There is no one accepted model for the behaviour of strata around longwall faces. Considerable variation exists in both the approaches taken to and the assumptions underlying models described by different researchers. These differences often relate to specific details of the mine being studied. A general model explained by *McNally et al*, [1996] is described below.

Figure 1.2 Subsidence zones above a longwall panel. Diagram not to scale.

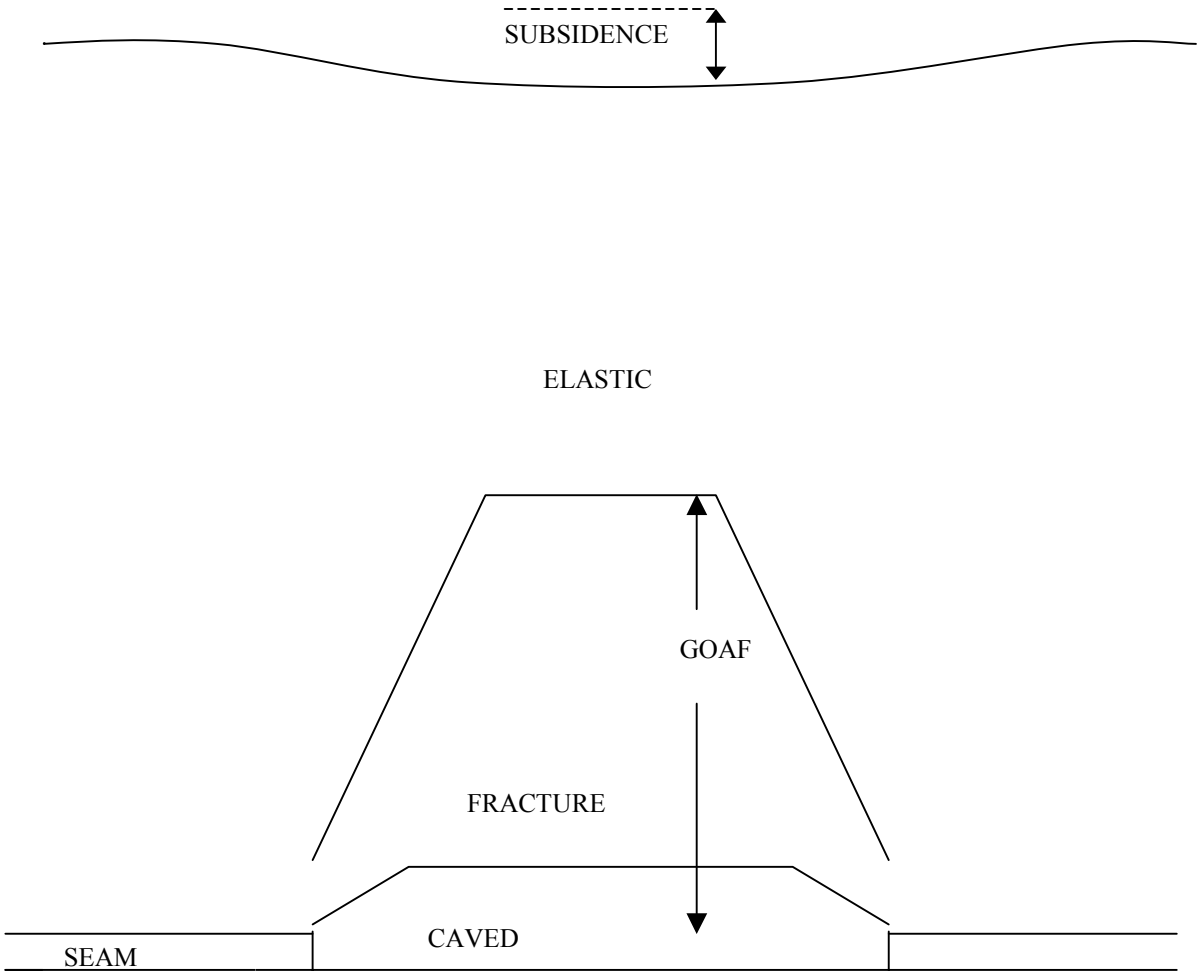

Prior to excavation, rock units will have an in situ horizontally and vertically balanced stress state in the ground. As an opening is created, the stresses in the surrounding rocks change, and an arch-shaped zone of tensional stress is created above the cavity. This causes the immediate roof layers to fracture and fall out as the mined width

increases, producing an area known as the *caved zone,* which is filled with a rubble of roof rock. This is a loose-packed zone, which is thought to bulk up to 120-130% of its in situ volume, producing a caved zone thickness of approximately 2-5 times the seam thickness.

Above the caved zone, is the *fracture zone*, where the rock-mass is still in situ, but is extensively fractured and destressed by shearing along bedding, joint extension and tensional breakage through previously intact rock. The fracture zone is taken as being about 10-20 times the seam thickness. However, in reality, a strong bed is usually encountered below this height which can bridge across the goaf pile as it narrows upwards, terminating the propagation of the fracture zone.

The upper roof strata above this zone is largely unfractured, but sags down elastically and is called the *Elastic Zone*. Over the panel centre, these beds are laterally compressed, while over ribs they are in tension. The amount of deformation is inversely proportional to the rock-mass modulus. The typical downward movement in the elastic zone is approximately 0.2% of its thickness.

1.2.2 Quantifying the behaviour of the rock-mass

Various approaches have been taken in the attempt to analyse the caving mechanism, including numerical models, empirical models, physical modelling and various forms of field measurement techniques. Most studies link the extent of fracturing to the seam extraction thickness. Currently the extent of the goaf is considered to be 50 times the seam thickness for a 200 m wide longwall panel, increasing linearly with increasing panel width [*Toon and Styles*, 1993].

The majority of studies in the past have suggested that there is tensile vertical fracturing ahead of the face [e.g. *Peng & Chiang*, 1984]. However, this has been contradicted by both Time Domain Refractometry which suggests that shear failure occurs ahead of the face, and by Microseismology [e.g. *Ishida et al*, 1993] which also describes a compressive shear fracture pattern in advance of the face. There is no

general consensus as to depth of fracturing in floor; other than it is significantly less than for the roof.

The factors affecting the behaviour of an individual mine are very complex, ranging from the interaction between seam thickness, depth, the magnitude and direction of the in-situ stresses, panel width, to the geomechanical properties of strata. The geology of the area will strongly influence the response of the ground to excavation, the most important factor is the gross lithology: the proportion of massive beds present [*Seedsman & Stewart*, 1996]. The geological structure of the strata, such as joints, bedding and planes of pre-existing weakness/strength will also influence the failure of the rock-mass [*Potgieter and Roering*, 1984]. Surface topography has been shown to have a significant effect on the response of the rock-mass to the excavation [*Holla*, 1997].

It is not surprising, therefore that models produced from different mines can describe very different behaviours, with widely ranging parameters. The eventual aim of this project however, is to use physical data on the geomechanical behaviour of the rock-mass (microseismic events) which can be located in time and space within the development of the mine, and to use these specific details to produce a model of the mine and for model validation. This method will therefore be widely applicable to a range of different mining scenarios.

1.3 Numerical Methods

Numerical modelling of rock behaviour around long-wall coal faces can be carried out using a variety of methodologies. These include Finite-Element modelling, Distinct-Element Modelling and most recently using the Particle-Flow Code developed by ITASCA. In most cases the modelling is carried out before the face begins and before any data are available which can reveal how the rock is behaving in-situ.

1.4 Input Parameters For Numerical Modelling

1.4.1 Practical problems in determining parameters

The geomechanical properties of the rock-mass are determined by laboratory tests on samples taken from the area. However, these tests do not take in to account the nature of the rock-mass on a large scale. Discontinuities such as joints will be present in the rock-mass. These are generally weaker than the surrounding rock, and will produce regions of preferential failure at lower stresses, thereby reducing the overall strength of the rock. It is therefore important to know the structure of the rock-mass on a large scale, so that any inhomogeneities, such as zones of inherent weakness or strength may be taken into account when assigning geomechanical properties to the rock.

There are sampling limitations in assessing a rock-mass which must be taken into account. Laboratory tests require specimens within a certain range of sizes. Consider a compression test to determine the Uniaxial Compressive Strength: if the sample is too big, then the equipment will not be able to bring the specimen to failure, but there is a practical limit on the minimum size of a sample. A specimen for a compression test should have a length within the range 0.02-0.2 m.

Test-samples are usually taken from drill core, but the drilling process induces torsional fractures along bedding planes, which breaks up the core. Intact samples of the required length are rare, and the stronger lithologies, such as sandstone which are less broken up will tend to be over-represented in a laboratory test [*McNally*, 1996]. Another problem comes from the condition of the drill core, which may have been allowed to dry out in storage for weeks before testing is carried out. This will change the strength of the rocks: a sandstone will become stronger on drying, whereas a mudstone will weaken.

1.4.2 Scaling parameters

The scaling of laboratory parameters to field values is an uncertain science; it is generally carried out using an empirical scaling factor. There are many methods of reduction techniques, for example the Rock Mass Classification system [*Bienawski*,

1978], which characterises the rock-mass using the Rock Mass Rating (RMR) and from this value calculates the in situ Young's Modulus. Reduction Factors [e.g. *Nicholson and Bienawski*, 1990] use the RMR to find a factor by which to reduce the laboratory-determined value of Young's Modulus to the actual value for the rock-mass.

The Hoek-Brown Failure Criterion allows for both the intact-rock response, and the influence of discontinuities within the rock-mass:

$$\sigma_1 = \sigma_3 \sqrt{m\sigma_c\sigma_3 + s\sigma_3^{\,2}}$$

where σ_1 and σ_3 are the maximum and minimum principal stresses respectively, σ_c is the Compressive Strength, and *m* and *s* are constants which depend on the properties of the rock [*Mohammad et al*, 1997a]. Despite this seemingly sophisticated method, the constants *m* and *s* are given values based on very broad criteria such as *"Thick-bedded sandstone"* (s = 0.5).

The in situ geomechanical properties of the rock-mass around most mines are not known. They are based on some empirical reduction of laboratory-derived parameters, which generally takes the form of an educated guess. This is an important point to remember when considering a model of a mine, and may account for some of the disparities seen between a model and the actual mine.

A method which can remotely determine the in-situ properties of the rock-mass and which can detect the nature and characteristics of strata failure would be and invaluable tool for validation of geomechanical models and for identification and classification of the response of the mine during operations.

1.5 Previous Modelling

1.5.1 Caving mechanisms

Some of the most comprehensive numerical modelling has been carried out by *Gale & Nemcik* of SCT (Wollongong, Australia) [1998] to understand ground caving

mechanisms. The model was developed using FLAC (Fast Lagrangian Analysis of Continua). The model is two-dimensional, simulating a zone down the centre of the longwall face. One metre "shears" were sequentially excavated to represent the progressive mining mechanism. A strain softening model was used, along with a coupled fluid pressure and rock failure approach to account for fluid flow as well as rock failure. The models were based on several key sites such as Appin Colliery, New South Wales, Australia, North Goonyella Mine, Queensland, Australia and Gordonstone Colliery.

The modelling produced two very different styles of caving, depending on the rock strength and the stress field. Firstly for weak ground, rock failure occurred well ahead of the face. Roof failure occurred as frequent sub-vertical fracturing and sheared bedding planes. No large caving blocks were formed, and fracturing occurred on a small scale. The peak stress concentrations were located well in advance of the longwall face, while around the face the ground was destressed. The failure was non-periodic. This model describes the characteristics seen from the Gordonstone microseismic data.

In the second model, rock-mass with a moderate strength and no weak bedding planes was found to exhibit a very different form of failure. The increased strength of the rock-mass caused the roof rock to only fracture at widely-spaced intervals, producing large caving blocks. Failure occurred above or ahead of the face in a weak layer within the roof. A network of fractures formed in this zone and propagated downwards to meet the longwall face. This produced much more catastrophic caving, with characteristic face-guttering and rib-spall being observed. This description is reminiscent of the behaviour observed at Asfordby Mine by *Styles et al* [1996], showing that it is possible to model uncharacteristic caving situations if the proper input parameters are used.

1.5.2 Subsidence modelling

Nottingham University have recently carried out research into the prediction of surface subsidence associated with longwall mining by numerical modelling [*Lloyd et al* 1997,

Mohammad et al 1997a]. The modelling was carried out using FLAC to produce a two-dimensional model to simulate the behaviour of the caved zone. The model was initially constructed for the UK Coal Measures, and this method was then applied to coalfields internationally [*Reddish et al*, 1998].

The model consisted of a longwall panel of 200 m width and 2 m extraction thickness at depths ranging from 100-800 m. A strain softening model was used with the Mohr-Coulomb failure criterion. An elastic stress/strain relationship before failure and a plastic relationship after failure had occurred. Pre- and post-failure input parameters were determined from lab tests and scaled to give the values for the in situ rock-mass using a modified Rock Mass Classification Rating for Young's Modulus [*Lloyd et al*, 1997].

Failure was simulated by allowing the roof and floor to converge. It was found that the roof sagged by 92% of the extraction thickness, whereas floor heave was only 8%. Surface subsidence was symmetrical about a maximum in the centre of the longwall panel. The validation of the final model was through a combination of post-failure stress patterns redistributed around the longwall panels, and the displacement distribution at the surface, using the Surface Engineer's Handbook surface subsidence prediction method. Finally the same methods were applied to fourteen different coal fields from Australian, USA, South African and Indian coal measures, and it was found that the models quite closely described the subsidence behaviour detected [*Reddish et al*, 1998].

Techniques for validating these models from remote observations of the geomechanical behaviour within the rock-mass in addition to surface subsidence observations would be extremely valuable.

Integrated Microseismic Monitoring and Numerical Modelling for the Determination of Fracture Architecture Around Longwall Coal Mines for Geomechanical Validation.

1.6 Information which can be derived from Microseismic Monitoring of Relevance to Geomechanical Behaviour of Mines

Seismic waves generated by induced seismic events generally travel large distances, and can be remotely recorded as ground vibrations by receivers such as geophones or accelerometers. Theories and methods from the fields of naturally occurring seismology and laboratory acoustic emission can be applied to the analysis of the recorded seismic waves, or seismograms. Information about the source of the seismic waves, the seismic event, can be obtained by this analysis. This information has a large number of applications, for example, to give warning of catastrophic collapse of the excavation, to test geomechanical models of the rock mass, or to study fracture mechanics. The amount of information about the seismicity that can be obtained depends on a number of factors e.g. the number or location of receivers that record an individual seismic event, the quality of the data.

The simplest information to obtain is the frequency of occurrence of induced seismic events i.e. the number of events recorded in a certain time. In the case of coal mining, changes in the frequency of events are caused by changes in production rate [e.g. *Bishop et al*., 1993], but it has also been proposed that changes in frequency of events could act as precursors to rockbursts[1], outbursts[2], and other catastrophic failure [e.g. *McKavanagh and Enever*, 1980; *Styles*, 1993]. The frequency of induced seismic events can be determined using a very simple network of receivers, or even just a single receiver. The quality of data is not an issue, as long as real seismic events and noise can be distinguished.

[1] A rockburst is the disintegration of a volume of rock at the edge of an excavation caused by a seismic event. Rockbursts occur in hard rock and soft rock mines. A rockburst at a coal face is sometimes called a coalburst.

[2] An outburst is the disintegration of a volume of rock caused by the movement of gas within the rock. Outbursts typically occur in coal mines (methane and CO_2) and potash mines (carbon dioxide and methane).

To obtain more information, the seismic data needs to be of a sufficient quality that analysis of the seismic waveforms is possible. The next piece of information that can be obtained, and which must be obtained if further analysis is to be successful, is the location of the seismic event. There are a number of methods by which the location of a seismic event can be calculated. Which method is used depends primarily on the number of receivers that record an individual seismic event, but it is possible to calculate a meaningful location using a single three-component record of the ground motion. The location of induced seismicity can depend on a number of factors, for example the location of mining activity [e.g. *Redmayne et al.*, 1996], the geology of the surrounding rock mass [e.g. *Bishop et al.*, 1993], or the presence of pre-existing zones of weakness such as faults [e.g. *Kaneko et al.*, 1990].

The individual event locations specify where the induced seismicity is, but do not give any indication as to the "size" of the induced seismicity, for example whether it will be felt or cause damage at the surface. The size of a seismic event is described by the source parameters, which can be calculated by analysing the recorded seismic waves in the frequency domain. Two source parameters that are routinely calculated in studies of mining-induced seismicity are the seismic moment and the stress release. Seismic moment is the most reliable measure of the strength of a seismic event, while the stress release is a measure of the reduction in stress during the seismic event. There are many source parameters that can be calculated, describing the duration of the fracture, the strength of the rock that fractures, or the spatial extent of the fracture, for example. Information about source parameters allows the behaviour of the rock mass to be better understood than if only the location of seismicity is considered. For instance, it allows regions of high and low energy or stress release to be identified, and identifying such regions may be very important in the prediction of catastrophic failure. From the source parameters of individual events, parameters that give a quantitative description of the seismicity can be calculated. These monitor the stability of the rock mass, in particular identifying regions where rock is becoming stronger or weaker, and demonstrate the behaviour of the rock mass well. *Mendecki* [1993, 1997a] gives a detailed description of most source parameters that can be calculated.

Integrated Microseismic Monitoring and Numerical Modelling for the Determination of Fracture Architecture Around Longwall Coal Mines for Geomechanical Validation.

Seismic source parameters describe the "size" of the failure of the rock mass that generates the seismic waves. The physical movement of the rock mass during the failure is described by the source mechanism. Given sufficient records of the same seismic event it is possible to accurately determine the source mechanism. Naturally occurring earthquakes are nearly all shear failures on a fault plane, which is best represented by the double-couple source mechanism. Recent studies have demonstrated that although many mining-induced seismic events are shear failures [e.g. *Spottiswoode*, 1984; *Hatherley et al*., 1997], there are also events that have a significant non-shear component [e.g. *Wong and McGarr*, 1990; *Gibowicz*, 1993; *Feignier and Young*, 1993]. Also, the time dependence of the source mechanisms can be examined to further understand the causes of the events. Thus by studying the source mechanisms of seismic events, the processes of fracture dynamics that cause the failure can be studied in detail. The source mechanism of a seismic event is related to the orientation of the stress tensor, and calculated source mechanisms of mining-induced events allows the stress field in the rock mass to be determined.

The advances made in the field of mining-induced seismicity, in technology and in theory, mean that our understanding of how a rock mass reacts to excavation is improving all the time. This in turn allows more accurate geomechanical models of the rock mass surrounding an excavation to be made. The various pieces of information that can be obtained from analysis of recorded seismicity can all be used to compare theoretical rock mass behaviour with the observed behaviour. Any significant departure from the theoretical behaviour can then be identified, and a decision on mining activity made accordingly. This has implications for the safety and productivity of mines. In addition, analysis of induced seismicity allows a better understanding of rock physics and fracture dynamics to be obtained since the behaviour of a real rock mass to a change in stress can be studied in detail

Integrated Microseismic Monitoring and Numerical Modelling for the Determination of Fracture Architecture Around Longwall Coal Mines for Geomechanical Validation.

1.7 General overview of microseismic monitoring in mining and other applications

Studies of mining induced seismicity have been carried out in a number of different mining regions around the world. The mining applications split into coal mining and hard-rock mining (e.g. gold mines) applications. Two other areas where monitoring induced seismicity has proved useful are hydrofracturing associated with geothermal power experiments [e.g. *Baria et al*., 1989], and excavation and monitoring of underground nuclear waste storage facilities [e.g. *Feignier and Young*, 1993]. In this overview three important mining regions are emphasised: Poland, Canada and USA, and South Africa. Coal mine microseismic monitoring applications are briefly reviewed for countries not in these three regions. Mining applications of microseismic monitoring generally concentrate on causes of and possible pre-cursors to rockbursts as these are major problems in most mining regions. Rockburst hazard in the UK is not such a great problem, and the objectives of UK mining induced seismicity studies are rarely to investigate rockbursts. There are more comprehensive reviews in the literature that describe the evolution of all aspects of mining induced seismicity [e.g. *Hardy*, 1977; *Gibowicz and Kijko*, 1994].

1.7.1 Microseismic monitoring in Poland

Seismicity induced by underground coal mining has been studied for many years in Poland, for example in the Upper Silesia coal basin [e.g. *Gibowicz*, 1984] where mining has been carried out for decades. Several underground seismic networks have been operated by the mining industry in Upper Silesia since the mid-1960s, and several thousand mine tremors are recorded annually. A dozen or so of these reach a local magnitude greater than 3, and occasionally an excessively large tremor with a magnitude exceeding 4 can occur [*Gibowicz*, 1984].

One recent study that is of particular relevance is that of *Wiejacz and Ługowski* [1997]. They obtained source mechanisms for seismic events induced in three regions of the Wujek coal mine. The majority of event source mechanisms they found were of a double-couple type nature. This fact was considered to be due to the rock mass being

non-uniform in strength and structure, the extraction of coal proceeding in specified directions and the extraction continuously changing the stress field. They found that in regions far away from any pre-existing faults the orientation of the double-couple mechanisms reflected the orientation of the long edge of the panel being mined or the orientation of the longwall face. In regions near faults the orientation of the double-couple mechanisms reflected the orientation of the faults. Most of the double-couple mechanisms were normal faulting type with near-vertical nodal planes.

1.7.2 Microseismic monitoring in Canada and USA

Most microseismic monitoring in Canada is carried out in hard-rock mines and concentrates on the investigation of rockbursts. Seismic monitoring systems are installed in the four mining districts of Ontario (Red Lake, Elliot Lake, Sudbury and Kirkland Lake) that experience rockbursts. Mining induced seismicity has also been observed and studied in the potash mining district of Saskatchewan. In a further application of technology developed for monitoring mining induced seismicity, the Queens University Group have deployed their microseismic network at the Underground Research Laboratory (URL) in Canada, a potential nuclear waste repository. Microseismic events induced by excavation of granite were recorded by an optimally designed network for study of focal mechanisms. Moment tensor inversion was applied to the recorded data, and it was found that most of the source mechanisms had volumetric changes [*Feignier and Young*, 1993]. The URL data has been extensively studied to understand how hard-rock (granite) responds to excavation [e.g. *Martin and Young*, 1993; *Maxwell and Young*, 1997].

Seismicity induced by hard-rock and coal mining has been studied in USA. The US Bureau of Mines was the major research organisation involved in studies of mining induced seismicity, in particular studying rockbursts, methods of predicting their occurrence, and devising means of their control [e.g. *Leighton*, 1984]. Several microseismic monitoring programmes have been conducted over the last 20 years in the coal mines of the Eastern Wasatch Plateau, Utah [*Wong and McGarr*, 1990]. An unusual aspect of these monitoring programmes has been that most of the detected seismic events occur down to depths of 2-3km beneath the mine workings. The

mechanisms of some of the detected events have been studied in detail and they provide some evidence for non-double-couple events.

1.7.3 Microseismic monitoring in South Africa

The first studies of induced seismicity in the deep gold mines of South Africa were in the early 1960s [*Cook*, 1963]. Since then there has been a continuing and comprehensive development of microseismic techniques and instrumentation. Earlier work in South Africa concentrated on the development of instrumentation for the location of microseismic events. In recent years the emphasis has changed, and more studies are now under way investigating matters such as source parameters, mine design, rock mass modelling, and rockburst prediction and control. These studies have led to the development of real-time monitoring systems such as the Integrated Seismic System (ISS) [*Mendecki*, 1993]. A review of some of the recent advancements made in South Africa is given by *Mendecki* [1997b].

Minney et al. [1997] describe the results of seismic monitoring of a retreating longwall at the New Denmark Colliery in South Africa. The stratigraphy of the roof of the panel being mined shows some similarities to the roof stratigraphy of Asfordby in that there are strong sandstones and dolerites in the roof at both mines. In longwall mining roof failure may occur continuously or cyclically. Continuous failure is the preferred roof failure mechanism and is usually associated with weak roof material. Cyclical failure is associated with strong, massive beams of sandstone or dolerite in the roof of the panel being mined. Cyclical failure can cause excessive loading of the supporting chocks, which effects the safety and productivity of the mine. *Minney et al.* [1997] demonstrated that monitoring the induced seismicity at New Denmark Colliery clearly showed cyclical roof failure. The seismic events they recorded were concentrated above the centre of the panel. The event locations showed a degree of randomness when compared to the roof stratigraphy, but plotting the seismic Deborah number (which describes whether the rock mass is behaving in a viscous or elastic manner [*Mendecki*, p209, 1997a]) showed that there were relationships between roof stratigraphy and location of seismicity. At the New Denmark Colliery the seam is at a

depth of 160m below the surface, whereas at Asfordby the depth is 500-550m below the surface.

1.7.4 Microseismic monitoring of collieries in other countries

A recent study carried out by CSIRO at the Gordonstone Colliery in Queensland, Australia will be described in detail in section 1.9. CSIRO have since carried out other studies, e.g. at Appin Colliery and South Blackwater Colliery but the results of these studies are as yet unpublished. The first microseismic monitoring of collieries in Australia was by *McKavanagh & Enever* [1980] who recorded seismic activity prior to outbursts of coal and methane in West Cliff Colliery, New South Wales.
Two different techniques have been used in French collieries to monitor seismic activity. These have been described by *Revalor et al.* [1990]. The first used was seismo-acoustic monitoring in most collieries that experienced rockbursts. The objective of this method is to monitor seismic energy release rate at the face and identify dangerous areas. The second technique is the seismic monitoring of the mine with an array of geophones or seismometers. This method allows the location and source mechanisms of the seismicity to be studied, and it was found that it gave a better understanding of some rockburst phenomena.

Outbursts have been a major problem in Japan. *Sato et al.* [1989] describe the results of microseismic monitoring at Horonai Coal Mine, Hokkaido, where mining is conducted at depths of about 1100m. Using an array of surface and underground sensors, over 20,000 events have been recorded. They found that the location of activity was controlled by mine geometry and the presence of old workings. Double-couple source mechanisms were obtained for some events, and these showed normal faulting implying that the major principal stress at the coal face was vertical. *Kaneko et al.* [1990] describe a period of monitoring at the Miike Coal Mine, which is prone to coalbursts with no associated gas. They found that geological discontinuities such as faults played a major role in determining the stress field about the face. They concluded that monitoring microseismicity allows the stress field to be monitored, and possible precursors to coalbursts could be identified.

Integrated Microseismic Monitoring and Numerical Modelling for the Determination of Fracture Architecture Around Longwall Coal Mines for Geomechanical Validation.

Microseismic monitoring of coal mines has also been carried out in a number of other countries, for example the former Czechoslovakia, Germany, and China. A review of much of this work is given by *Gibowicz & Kijko* [1994].

1.8 Development of mining induced seismicity studies in the UK

This section describes the development of mining induced seismicity studies around the UK. The earliest studies used arrays of surface seismometers to record induced seismic events, whereas more recent studies have used arrays of three-component seismometers cemented into boreholes. Not all studies of coal mining induced seismicity in the UK are described here, but rather a selection of studies that demonstrate important stages in the development of technologies and data analysis with time. The studies described also show the importance and benefits of understanding mining induced seismicity observed around coal mines.

1.8.1 UK coal mining induced seismicity

There have been reports of microseismic activity (generally unfelt, but sometimes felt) in UK coal mining areas since at least the turn of the century. The association of the activity with the extraction of deep-mined coal by longwall methods has often been assumed, but rarely proven [*Davison*, 1905; *Davison*, 1919; *Dollar*, 1951; *Neilson et al.*, 1984]. The British Geological Survey report that about 25% of small to moderate earthquakes (less than M_L=3.0) recorded by the UK regional seismometer network occur in the coalfields [*Redmayne*, 1988]. A map of British earthquakes (Figure 1.3) clearly shows concentrations of seismic activity in the Clackmannanshire, Midlothian, Staffordshire, Nottinghamshire and South Wales coalfields.

Sequences of tremors associated with coal mining have been reported over the past 20 or so years and individual tremors within these sequences are often felt. In 1975, after a damaging earthquake in the Stoke-on-Trent area and several smaller tremors, the British Geological Survey deployed a network of seismometers [*Browitt*, 1979] to monitor the spatial and temporal pattern of the seismic activity. The activity was monitored over the next five years, and *Westbrook et al.* [1980] found that the seismic

event rate correlated with coal production in both space and time. They concluded that the earth tremors were caused by longwall coal mining at a depth of 1000 metres, and that previous mining played an important part in the size of the tremors. The most recent example of a sequence of tremors associated with coal mining was that in the Musselburgh area, near Edinburgh, during the period October 1996 to January 1997 [*Walker and Galloway*, 1997]. The pattern and location of the seismicity demonstrated that it was caused by mining at the Monktonhall colliery in the Midlothian coalfield. Around twenty-five events were felt by members of the public during this sequence, and the largest event magnitude was M_L=2.0.

1.8.2 Mining induced seismicity in the Staffordshire and Nottinghamshire coalfields

Westbrook et al. [1980] and *Kusznir et al.* [1980, 1984] carried out a considerable period of monitoring of seismicity induced by coal extraction in the North Staffordshire coalfield. Using standard global seismological Willmore seismometers deployed at the surface, events as large as magnitude 3.5 were recorded. *Kusznir et al.* [1984] identified two separate mechanisms responsible for generating the recorded seismicity. Smaller events (M_L<2.5) with an implosional source mechanism were thought to be generated by waste collapse. Larger events (M_L>2.5) with shear source mechanisms occurred in the pillars of old workings in adjacent seams. They were caused by the superposition of the pillar stress-field and the front abutment pressure of the advancing face, when the face passed above or below the pillar.

Investigations by *Isaacs & Follington* [1988] during mining of the H65 panel at Cotgrave colliery, Nottinghamshire, showed that high loading levels on the powered supports were caused by failure of the Deep Soft Seam and the roof immediately above the Deep Hard Seam being mined. These beds were unable to transmit support resistance to the bridging siltstones above resulting in the generation of brittle failures that propagated into the overlying strata. This caused the roof to collapse in large blocks, which caused the high loading levels on the supports. This type of roof collapse is called weighting, and would be expected to generate microseismic activity. The remaining events, which were generally larger, were shown to be associated with pillar failure in workings above and below the active seam.

Integrated Microseismic Monitoring and Numerical Modelling for the Determination of Fracture Architecture Around Longwall Coal Mines for Geomechanical Validation.

Figure 1.3 A map of British seismic events (M_L>1.5) recorded by the BGS seismic network during the period 1980-1989 (published by British Geological Survey, Edinburgh).

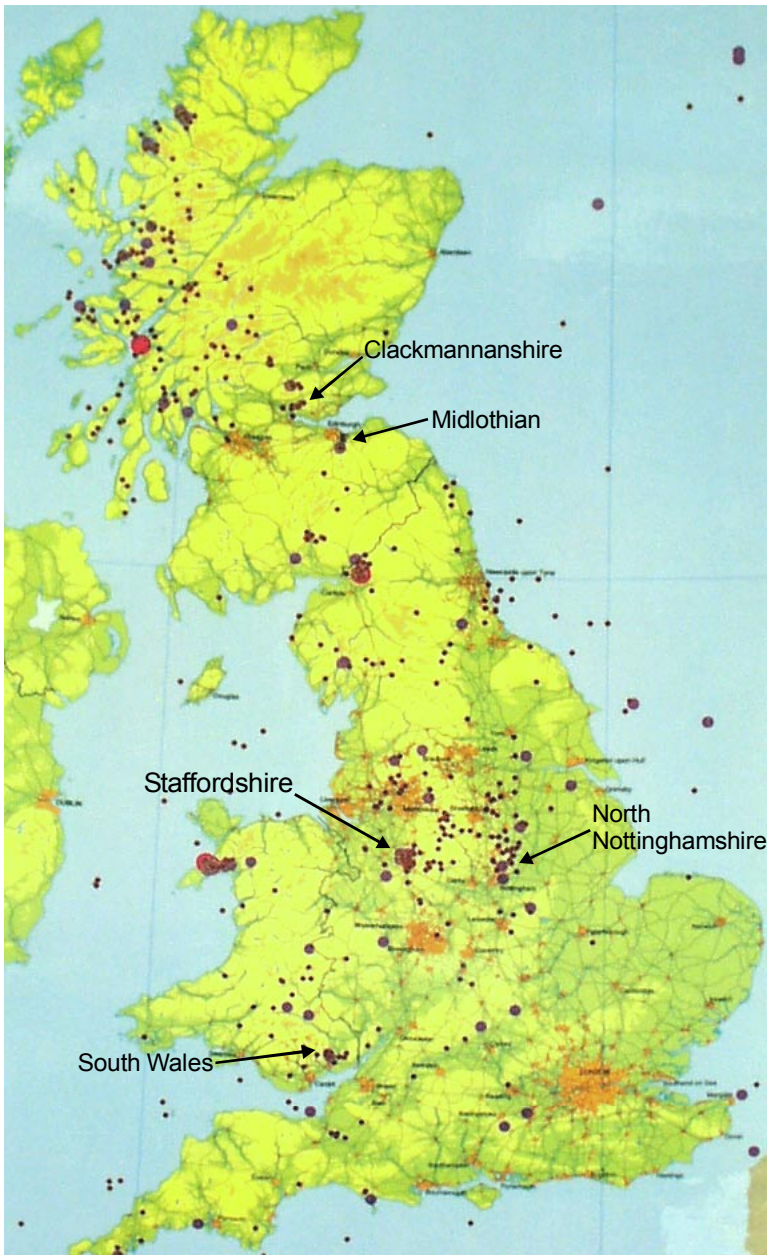

These studies showed that microseismic activity caused by the development of fractures associated with roof collapse could be monitored using surface seismic networks. The location of the seismic activity could only be determined with a limited precision, so the fracture development could not be studied in great detail.

Integrated Microseismic Monitoring and Numerical Modelling for the Determination of Fracture Architecture Around Longwall Coal Mines for Geomechanical Validation.

1.8.3 Microseismic monitoring of Bilston Glen Colliery, Midlothian Coalfield, Scotland

In November 1987, the British Geological Survey installed a seismometer network in and around Rosslyn Chapel in the Midlothian Coalfield [*Redmayne et al*., 1996]. Earthquakes had been causing damage in that area, in particular to the chapel itself. The network operated until January 1990 in which time 247 earthquakes were located. It was found that the locations of the earthquakes was closely associated, in both space and time, with mining activity, indicating that the earthquakes were mining induced. *Redmayne et al.* [1996] found a large proportion of the observed seismic activity occurred at the general depth of past mining in that area. They concluded that residual stresses from earlier workings were an important factor in generating seismicity, and could also be the reason for the large events being observed. A frequency-magnitude analysis showed that the maximum credible magnitude for the area was around M_L=3.0.

It was found that there was a higher level of ground motion and longer event duration for seismograms recorded at the chapel. This was attributed to amplification of the seismic signal by the soft sediments underlying the chapel, explaining the high intensities and damage caused at the chapel, and sites with similar foundations, by the effects of the induced earthquakes. In June 1989 production ceased at the Bilston Glen Colliery, and no seismicity was recorded by the network after 31st August, 1989.

1.8.4 Surface microseismic monitoring in the North Nottinghamshire coalfield

Over 130 separate earth tremors were recorded in the Thoresby area of Nottinghamshire, between July 1989 and August 1990. To determine whether the tremors were caused by mining activity, British Coal commissioned the University of Liverpool to deploy a network of surface seismometers in the area [*Bishop et al.*, 1993]. The workings of Thoresby colliery lie beneath Thoresby Park, and the surface rock in the area is the Sherwood Sandstone. Production began at Thoresby with extraction of the 2m thick Top Hard Seam in the middle Coal Measures, at a depth of about 650m. This seam was mined out by 1986, when extraction began of the Parkgate

Seam at a depth ranging from 700 to 820m. During the period of monitoring several panels started and finished their production lives.

The observed seismicity occurred in two parts of the stratigraphic section. Most of the seismic activity was between depths of 400m and 1000m in the Middle Coal Measures, with a peak in activity at the depth of the Parkgate workings. A large amount of activity occurred at much shallower depths, between ground level and 100m depth. This was in the Sherwood Sandstone. Some of these events formed linear swarms that were associated with large fissures seen at the surface in the village of Perlethorpe. Small cracks were also observed in the B6034 directly above the workings, and these too were presumably caused by the shallow activity in the Sherwood Sandstone.

It was concluded that the seismic events felt in the Thoresby Park area were caused by longwall mining in the surrounding collieries. The observed seismicity showed excellent correlation with mining production and occurred mainly at the depth of the workings. No seismicity was observed in the region of a particular panel before or after extraction. Once extraction had commenced, the seismic activity started from the same end of the longwall as production, and followed the face advance.

1.8.5 Borehole microseismology studies

The studies already described all used arrays of surface seismometers. An enormous increase in precision in the locations of events can be obtained by the deployment of a network of seismometers cemented into boreholes. As part of the Hot Dry Rock project operated by Cambourne School of Mines in Rosemanowes Quarry, Cornwall, hydrophones were deployed in shallow boreholes (200m). Seismic events caused by the hydraulic stimulation of granite were located with an accuracy of 20m [*Baria et al.*, 1989] down to depths of 2.5km.

Geophone packages, or sondes, are often cemented into boreholes during exploration of potential coal mines. They are used to prove continuity of the coal seam. A sonde is cemented into a borehole in the seam, and a shot is set off at seam level in a different

borehole. Seismic waves generated by the shot travel in the seam as guided waves i.e. they are totally internally reflected, hence there is little loss of amplitude as they propagate. This means they can travel great distances. If the guided waves are recorded by the sonde, then the seam is continuous between the sonde location and the shot location. After the continuity of the seam has been established, the sondes are not used again by the coal mine.

These sondes can be used to monitor seismicity induced by coal mining. The output of a six-component (two vertical, four horizontal) sonde in a borehole at seam level at Coventry Colliery, Warwickshire was recorded at the [*Toon & Styles*, 1993]. More than 2000 of high quality events were recorded in just two days of monitoring. Accurate locations could be obtained using three-component digital data a single sonde [*Toon*, 1990; *Toon et al.*, 1992; *Toon & Styles*, 1993]. The direction of polarisation of the P-wave particle motion was determined and was taken to be the source-receiver direction. The source-receiver distance could be calculated by examining the arrival times of the P-wave and S-wave assuming the velocity characteristics of the rock mass are known. Knowing the source-receiver direction and distance allows a hypocentral position to be established from a single sonde. It was found that most events were within 50m above or below the seam, with some activity extending to 300m above the seam (Figure 1.4). Seismic activity was observed along the length of the face, and the density of seismicity was approximately uniform along the length of the face. Maps of the stress release estimated for the events suggested that the area of highest stress release was in front of and behind the face at the centre of the panel [*Toon and Styles*, 1993].

Figure 1.4 Seismicity recorded during a 24-hour period at Coventry Colliery. The x-axis is perpendicular to the direction of face advance, the y-axis is in the direction of face advance. The sonde is located at the origin. The mined out panel is shown by the blue line, and each circle shows the location of an individual event [after *Toon & Styles*, 1993].

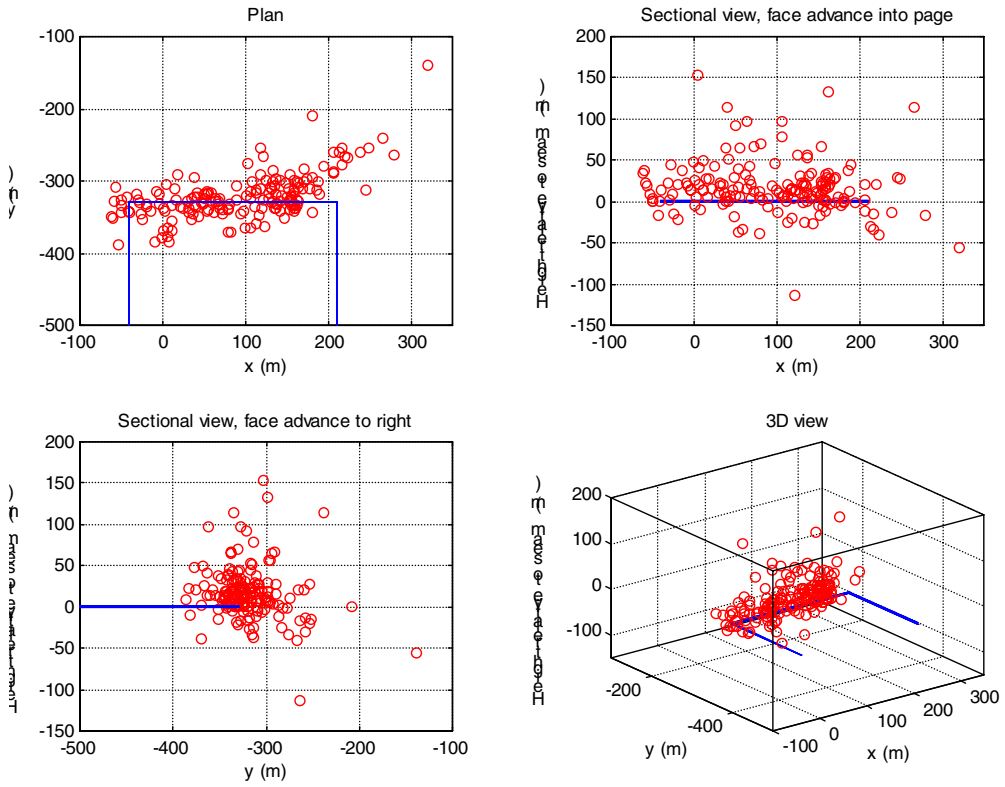

1.9 GORDONSTONE COLLIERY

1.9.1 Background

Gordonstone Mine is situated in the Bowen Basin, Queensland, Australia. Microseismic monitoring was carried out in this mine during September and October 1994 by CSIRO and Central Queensland University. Details of this work can be found in the report by Hatherley et al, 1995. The aim of this project was to record and analyse seismic events caused by longwall mining to determine whether the associated caving extended into overlying aquifers. Microseismic monitoring was carried out during the working of a long wall panel, Panel LW 103, with a face width of 250 m, and the data was then back-analysed.

Working was in the 3 m thick Permian German Creek Seam which lies at a depth of about 230m. This seam is overlain by 170 m of Permian cover and 60 m of Tertiary sediments and volcanics which act as aquifers. The dominant horizontal stress direction is NNE, parallel to the panel centreline and sub-parallel to the dominant coal cleat and roof strata joint directions.

1.9.2 Instrumentation

A brief summary of the instrumentation used in this study is given below. A three-dimensional array of detectors was distributed in three boreholes around the area of expected seismicity at longwall panel LW103. Seven triaxial geophone strings were deployed at 30 m intervals in each hole, together with some shallow holes to give a total of 27 triaxial stations. The borehole arrays were monitored using purpose-built hardware designed by CSIRO, and the data was then analysed on a Silicon Graphics workstation using the commercial software package XMTS supplied by ISSI.

1.9.3 Analysis and Interpretation

More than 1200 events were recorded during a 2-month period of which 629 events were of sufficient quality for further analysis. There was an average of approximately 50 events recorded per day. To determine the location of the events, information about the direction of travel of the waves was recorded. The velocities of the seismic waves observed were also needed. The P-wave velocity was determined to be 3.30 kms^{-1}. The accuracy of the locations was considered to be within 5-10 m.

The seismicity was found to be strongly correlated with periods of longwall production. Figures 1.5 and 1.6 show a plan view and vertical cross section of the location of the seismic events with respect to the working panel. Figures 1.7 and 1.8 show the same data but plotted in the frame of reference of the moving face. Comparison of these diagrams clearly shows that the location of seismicity is influenced by the stresses induced around the face position. These results agree well with the conventional models of excavations discussed above.

The events recorded mainly occurred within and above the panel LW 103 in an arcuate zone approximately 70 m wide, up to 70 m ahead of the face and extending back

behind it at the gateroads (figure 1.7). The strongest events were located in the roof and floor of the seam. The vertical extent of the seismic activity was about 120 m above the seam to a depth of approximately 30 m into the floor. The zone of activity extends upwards at an angle of approximately 50° to the horizontal. Laterally, the events tended to occur at the sides of the panel, in an envelope at an angle of about 15° from the vertical (figure 1.6)

The focal mechanisms were analysed for a number of events using a double couple solution to determine the fault-planes of the events, shown in Figure 1.9. The nodal planes are approximately parallel to the longwall face, and a compressive shear fracture pattern is indicated in the abutment ahead of the face, analogous to reverse faulting. The average dip of the fracture planes has been inferred to be 50° southwards.

The fracture pattern can be explained in terms of the downward bending force into the goaf, which fractures the strata ahead of the face, and the dominant compressive horizontal stress, which creates the reverse faulting mechanism. Piezometric data obtained from a borehole in the centre of the panel supports these findings. Subsidence monitoring conducted shows that minor subsidence commences at about 50 m ahead of face, with the majority of it occurring in a zone 175 m behind face. This interpretation is also supported by numerical modelling carried out on the mine to assess the mechanism of caving (Kelly et al, 1996).

Behind the face tensional cracking associated with the subsidence is expected along the previous compressive fractures and also perpendicular to the face. However, this is not seen in the microseismic data analysed. Approximately half of the events detected had impulsive P-waves and could be accurately located, but a large proportion of the remaining data had weak, emergent P-waves and could not be analysed. Within this group of unlocated events is inferred to be those events associated with tensional cracking and the actual subsidence. One possible explanation for this is that the strata at Gordonstone is very weak (UCS of the immediate roof and floor is approximately 5-15 MPa). Caving occurs immediately behind the face, but in stronger units where

bridging can occur, the shear and tensional cracking are both likely to produce more frequent and stronger seismic events.

Figure 1.5 Plan view of the location of the events in a geographical frame of reference [after *Hatherley et al*, 1995]

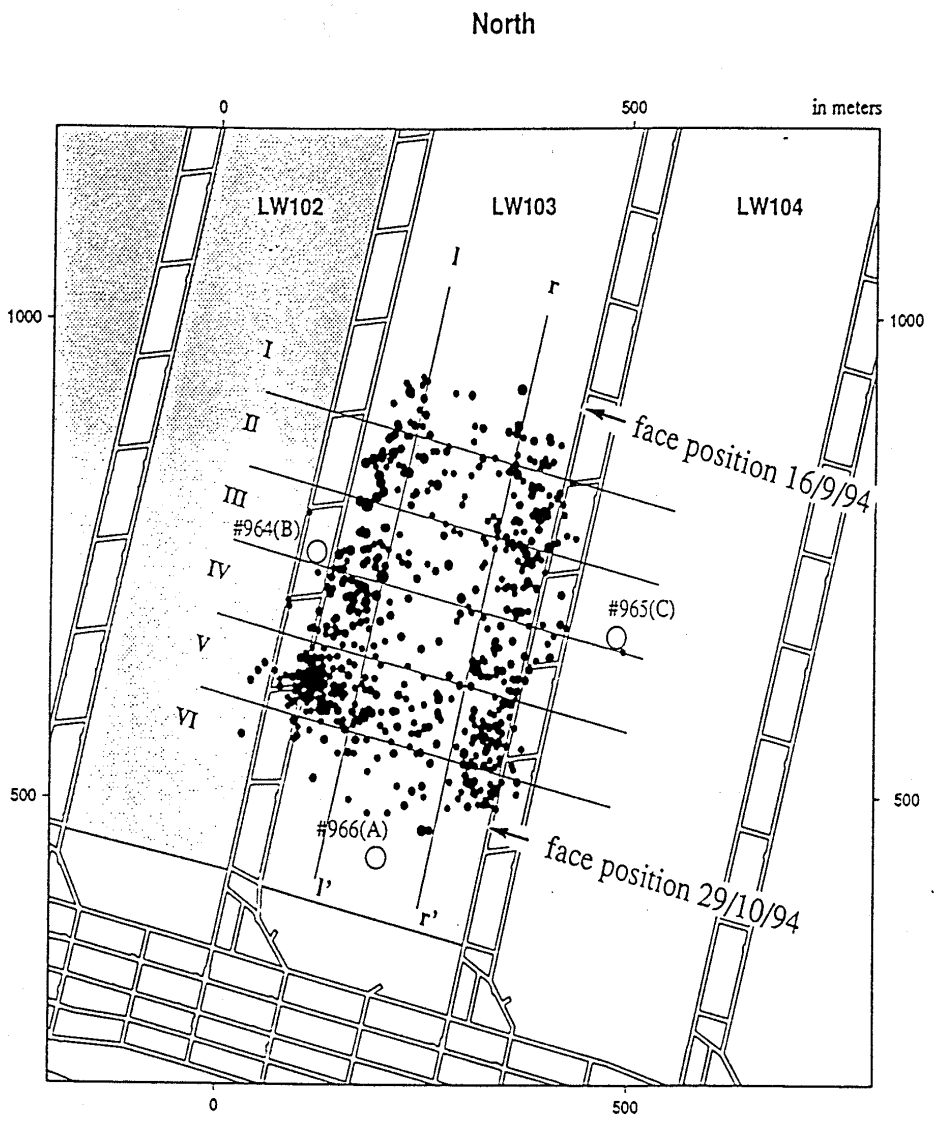

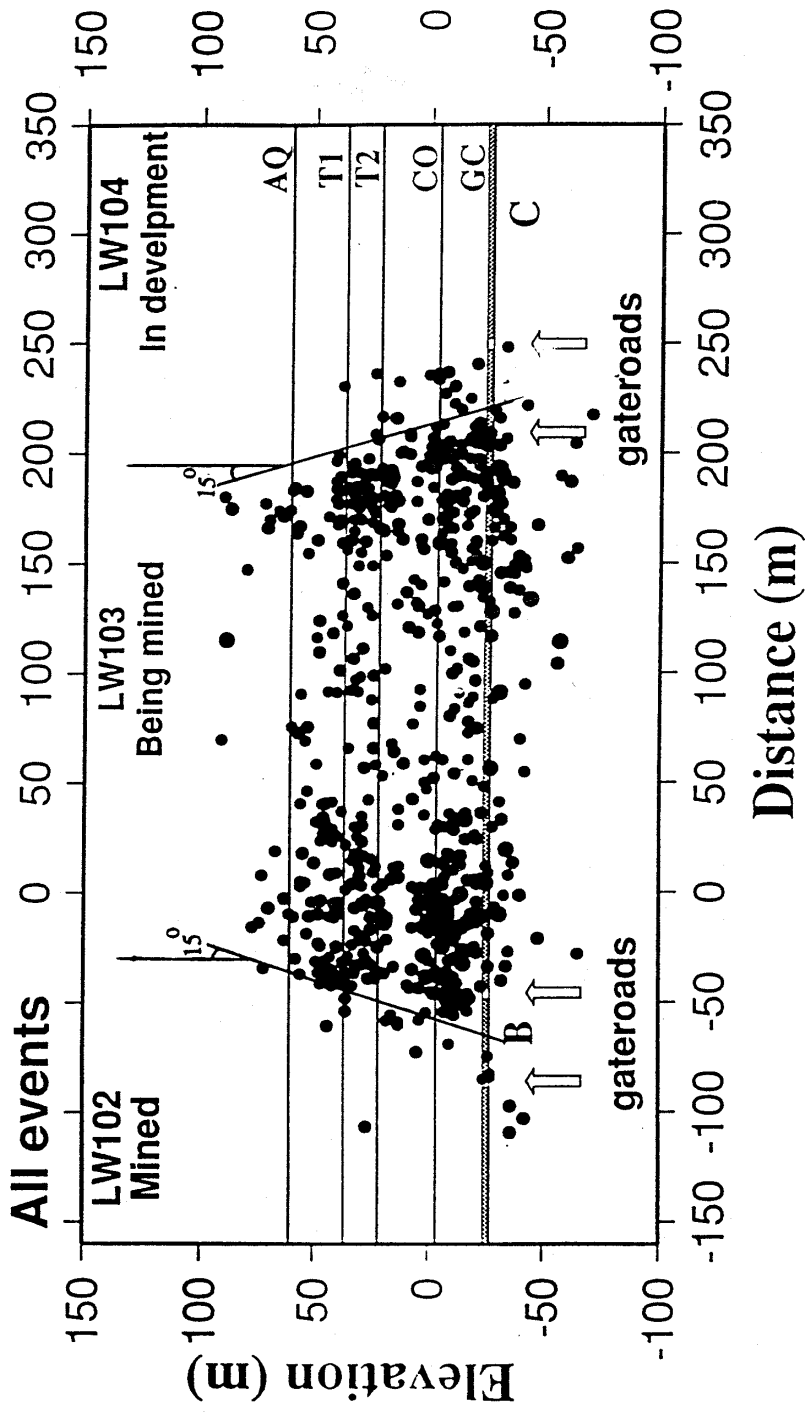

Figure 1.6 Cross section of events in a static frame of reference (after *Hatherley et al*, [1995])

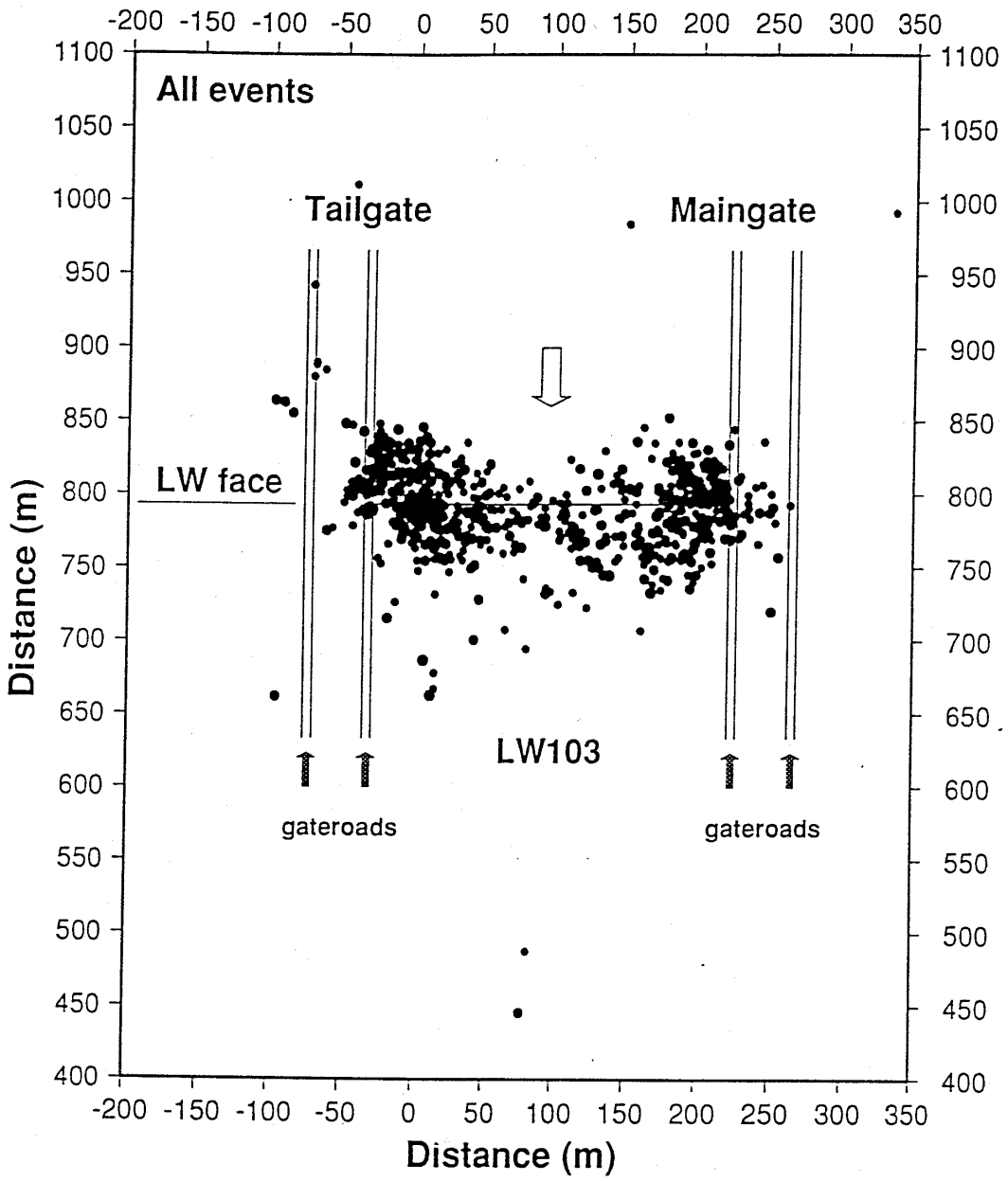

Figure 1.7 Plan view of the events normalised to a fixed longwall position. (After *Hatherley et al*, [1995])

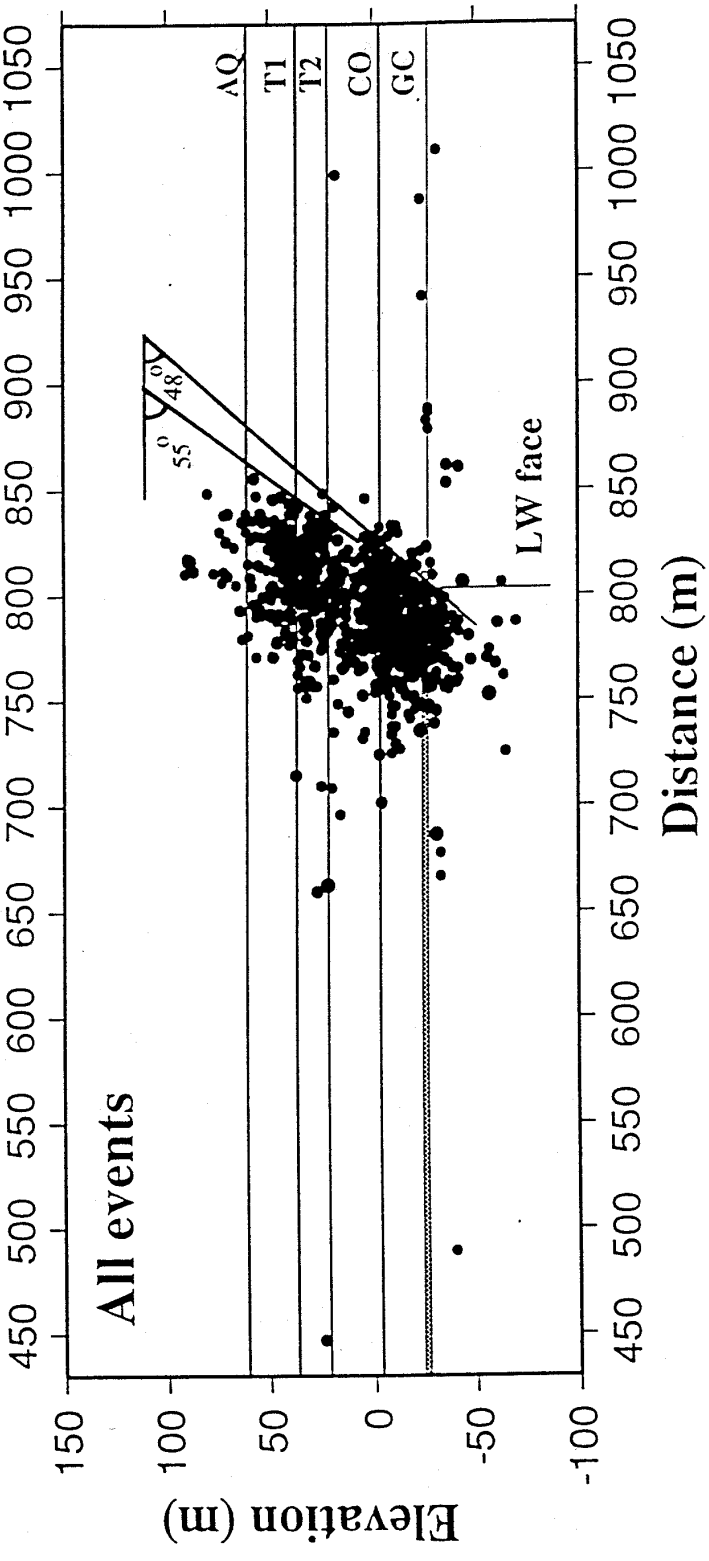

Figure 1.8 Vertical distribution of events within the frame of reference of the moving face. (After *Hatherley et al*, [1995])

Figure 1.9 Fault-plane solutions (on lower hemisphere) of 14 events in LW103. The shaded areas are under tension while the open areas are under compression. (After *Hatherley et al*, [1995])

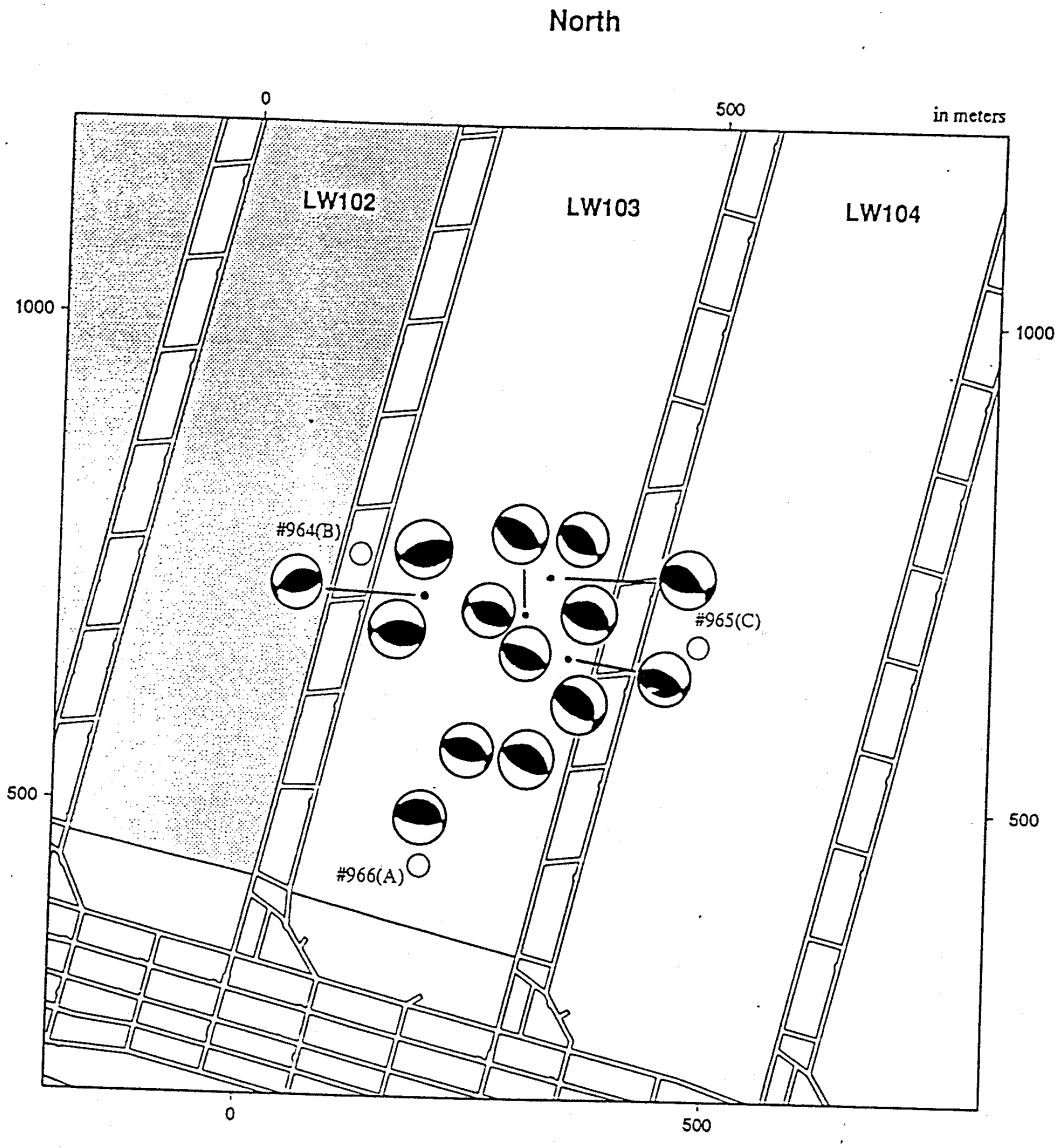

2 GEOLOGICAL AND TECHNICAL BACKGROUND FOR ASFORDBY STUDY

2.1 Introduction

Asfordby Colliery is located near the village of Asfordby in Leicestershire. The nearest major town is Melton Mowbray. Asfordby Colliery was developed initially by British Coal, and later by RJB Mining after privatisation of British Coal. The first panel mined was Panel 101 in the Deep Main Seam, and extraction commenced on 15th April 1995.

Panel 101 at Asfordby Colliery was chosen as the site of a microseismic monitoring experiment by the University of Liverpool and IMCL Ltd. (IMCL Research Contract 2069/3). This site was chosen for a number of reasons. Panel 101 was the first panel to be mined at a new mine where the nearest previous workings were about 20 miles away. This meant that any induced seismic activity was controlled entirely by the geomechanical response of the rock mass to the mining activity at Panel 101. Also, the presence of sills of variable thickness in the Coal Measures above the working seam and the close proximity (100 to 200 metres) to the Sherwood Sandstone aquifer were thought to potentially problematic. The principal objective of the investigation was to determine whether microseismic monitoring could detect and map fracturing associated with longwall extraction of coal. The interaction between induced microseismicity and geological structures was also investigated. Two phases of mining of Panel 101 were monitored. During the first phase, the face width was 240m and the total face advance before abandonment due to working conditions was 550m. The second phase that was monitored had a face width of 120m, and the face advance before abandonment was about 160m. Between these two phases, two panels were extracted successfully from another part of the mine with a face width of 60m but this face width was too narrow to be economically viable. Asfordby Colliery was abandoned in August 1997 after poor working conditions were experienced during the second phase of mining.

2.2 Geological setting of Asfordby Colliery

This geological description is based on *Whitworth et al.* [1994] and *Altounyan & Digby* [1996].

2.2.1 Structure and faulting

The Coal Measures at Asfordby mine form a southerly extension of the Carboniferous basin of South-East Nottinghamshire. The Coal Measures dip at a very shallow angle towards the North and North-East, into the basin. The dips increase to the South and the East where the Coal Measures onlap onto basement rocks. In the area of the Asfordby shafts the Coal Measures sit on extrusive volcanics of late Namurian or Westphalian age, comprising mainly of basalt lava flows. Over the rest of the Asfordby basin the Coal Measures are conformable on the Namurian Millstone Grit series.

Faults in the area of the Asfordby shafts generally strike East-West, approximately parallel to the southern edge of the basin. The faults are normal and have throws up to 100m, and most were active in post Triassic times. There is a secondary fault trend striking NW-SE which seismic surveys suggest was pre-Permian. A map of faulting in the Asfordby colliery area is shown as Figure 2.1. The location of Panel 101 is also shown. The site of Panel 101 was chosen to be relatively free of faults.

Figure 2.1 Map of faulting around Asfordby mine [after *Whitworth et al.*, 1994]. The location of Panel 101 is also shown.

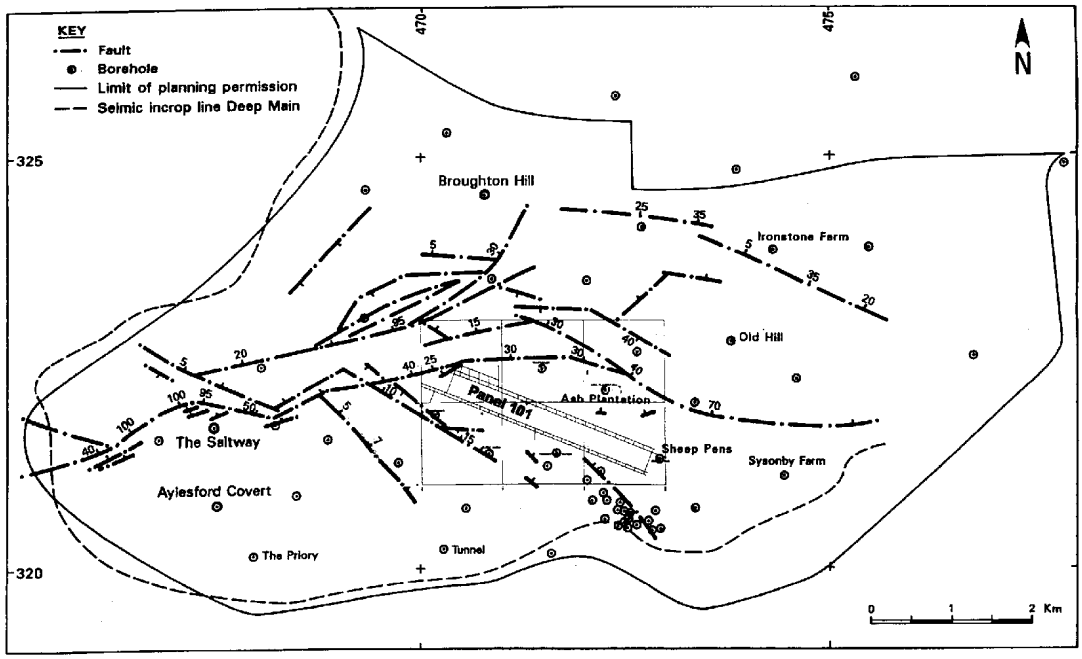

2.2.2 Geological succession

The general geological sequence in the Asfordby area is shown as Figure 2.2. The seam mined at Asfordby colliery is the Deep Main Seam, which lies approximately 500m below the ground surface. In the roof, approximately 100m above the seam, is the Sherwood Sandstone, which is a major aquifer in the area and is generally stronger than the mudstones and Coal Measures above and below it. The sonic derived UCS for the Cants Thorn 1 borehole suggests an average UCS of about 60Mpa (80Mpa peak) for the Sandstone, and an average UCS of 40Mpa for the mudstones and Coal Measures. The Sherwood Sandstone had a significant effect on the location of induced seismicity recorded by an earlier monitoring study at Thoresby Mine in Nottinghamshire [*Bishop et al.*, 1993], some distance from Asfordby. A large amount of seismicity occurred in the Sandstone, even though it was almost 800m above the seam being mined, which was associated with large fissures opening at the surface (see section 1.8.4 for a description of the Thoresby monitoring).

An unusual feature of the Coal Measures geology across parts of the Asfordby colliery area is the presence of a number of dolerite sills at different horizons. The individual

sills vary in thickness from zero to over 25m in places. The sills are believed to be generally strong. The sonic derived UCS log for the Cants Thorn 1 borehole suggests an average UCS of about 110MPa for the 2nd Waterloo Sill with peak strengths in excess of 170Mpa. The extent of the sills has been mapped using seismic and borehole data.

Figure 2.2 Generalised geological section at Asfordby mine [after *Whitworth et al.*, 1994].

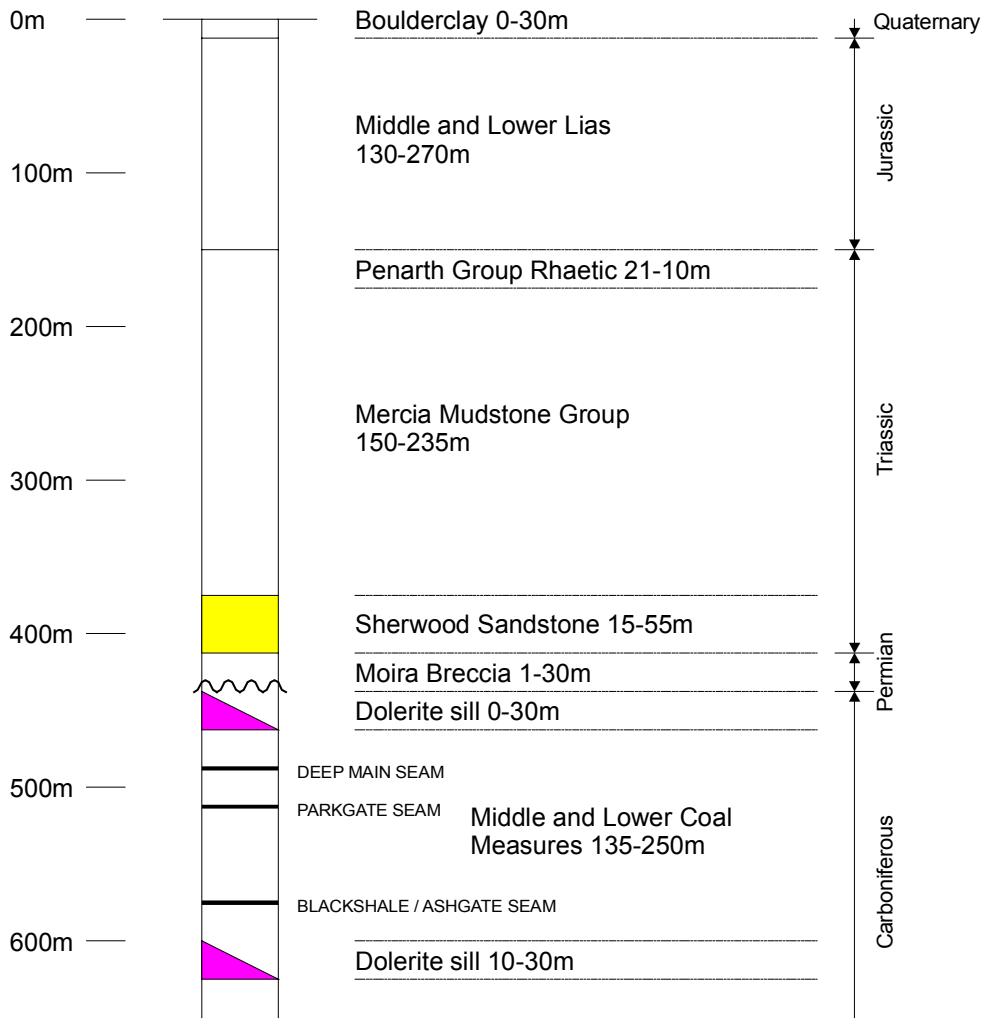

Altounyan & Digby [1996] summarise the geological conditions at Asfordby colliery as a "combination of moderately strong roof measures in the first 15m above the mined seam with moderate to strong massive beds close to an aquifer at 100-120m".

2.3 Relevant geomechanical models

There are three geomechanical models of the response of a rockmass to longwall excavation that are relevant to the Asfordby microseismic monitoring. The first is a physical model of the Asfordby stratigraphy [*Sun et al.*, 1992a, 1992b] by the Department of Mineral Resources Engineering, University of Nottingham. There are two numerical models, the model of the Asfordby stratigraphy by Golder Associates (UK) Ltd [*North and Jeffrey*, 1991] and the model of a general Coal Measure stratigraphy by Strata Control Technology (SCT) [*Gale and Nemcik*, 1998].

2.3.1 Physical model of Asfordby stratigraphy

Sun et al. [1992a, 1992b] describe the physical modelling results of subsurface fracture development associated with longwall mining operations. The physical modelling results were obtained by employing a large sand and plaster model loaded purely by gravity. The model was made to simulate the scaled in situ geological conditions at Asfordby Mine. The results of the modelling show fracture development and crack propagation as a longwall face advances. They demonstrate that the presence and position of a weak band, and the extraction thickness, have significant effects upon the overall fracture patterns above the excavation.

Sectional views of fracture patterns above an excavated panel are shown by *Sun et al.* [1992a, 1992b] for different extraction thicknesses. The sectional view of the 2.8m extraction thickness is reproduced here as Figure 2.3. Of note is a sub-vertical boundary to the fractured roof above the edges of the panel, which agrees with the microseismic observations of *Hatherley et al.* [1997] (see Figure 1.6). Sectional views of fracture patterns are also shown by *Sun et al.* [1992a] for different positions of a weak layer in the roof. The sectional view for the highest position of the weak layer is reproduced here as Figure 2.4. This shows an arch structure above the face, and a large unfractured block of roof that may collapse causing a weighting event at the face. The fracture patterns shown give an indication of the fracturing that might be caused by mining at Asfordby. Since fracturing is the cause of microseismic events, the patterns of seismicity observed at Asfordby can be compared to the fracture geometries from

the physical models to examine whether the physical models accurately demonstrate the response of the rock mass to longwall excavation.

Figure 2.3 The physically modelled fracture pattern for an extraction thickness of 2.8m [after *Sun et al.*, 1992b]. Fracturing is concentrated in two regions above the edges of the panel, with horizontal fractures spanning the face and joining these two regions

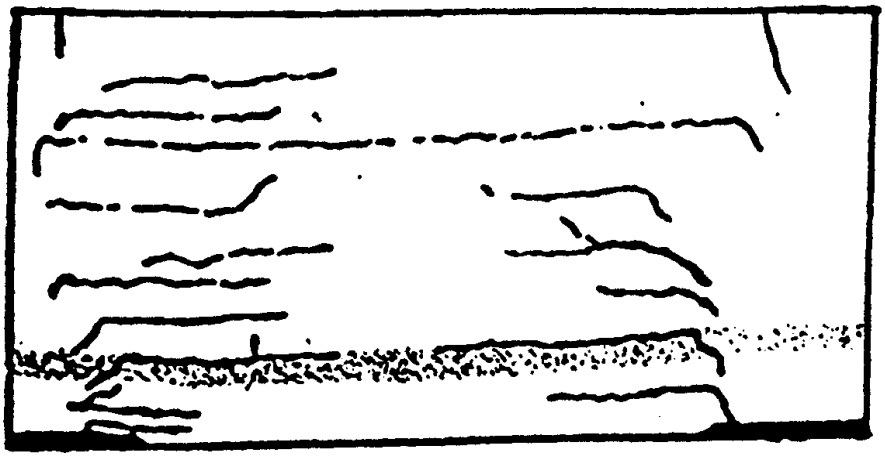

Figure 2.4 The physically modelled fracture pattern for the highest position of the weak (stippled) layer [after *Sun et al.*, 1992a].

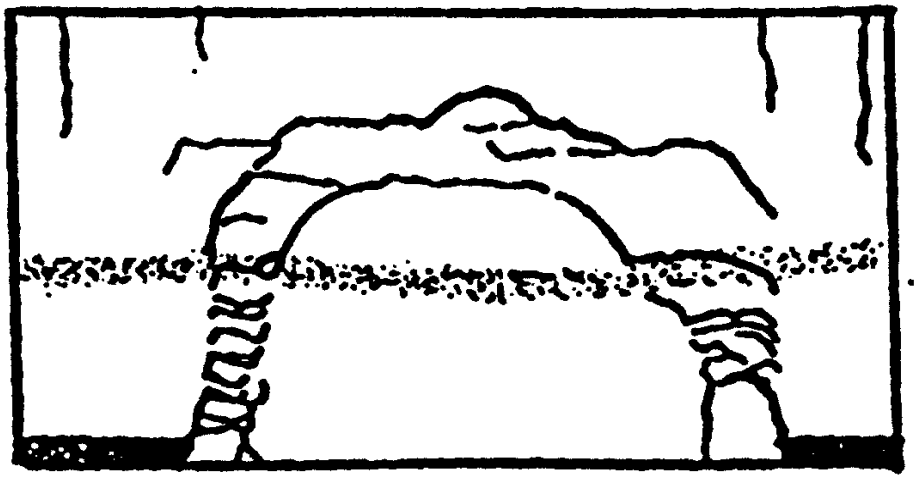

2.3.2 Golder Associates model of Asfordby stratigraphy

The Golder Associates numerical model of the Asfordby stratigraphy was developed as part of a project to investigate the potential for water inflow in the Asfordby area (ECSC Agreement 7220-AF/826). A finite element modelling method was developed

and tested against subsidence profiles of other collieries. The modelling evaluates the changes in "strain tensor", in particular the "tensile strain" and "compressive strain", around the excavation. It is unclear from the *North and Jeffrey* [1991] report what is meant by the "strain tensor", but presumably it is equivalent to the stress tensor, and the "tensile" and "compressive strains" have the orientations of maximum and minimum compressive stress respectively.

The main result of the numerical modelling is that the largest strains are above the edges of the extracted panel. Beyond the edge of the panel the "compressive strains" are approximately vertical. Above the centre of the panel the "tensile strains" are approximately vertical. The conclusions of the *North and Jeffrey* [1991] report are that the Asfordby workings are likely to have some occurrence of water on the faces, with the potential of weighting events. The location of Panel 101 was chosen to limit both of these effects, based on risk maps described in the *North and Jeffrey* [1991] report.

2.3.3 SCT model of general Coal Measure stratigraphy

The SCT model was developed in conjunction with CSIRO Division of Exploration and Mining in Brisbane, Australia. It was part of a CSIRO / SCT / ACARP (Australian Coal Association Research Program) project researching longwall caving mechanics. The results of microseismic monitoring by CSIRO at Appin Colliery and Gordonstone Mine [*Hatherley et al.*, 1997] have been used to validate and improve the geomechanical model.

Some of the objectives of the modelling were to predict rock fracture around longwall panels, understand caving mechanics in differing geologies, and assess longwall support requirements. The response to longwall mining of a 2-D longitudinal slice down the central zone of the panel is modelled by sequentially excavating 1m "shears" in the model. Advancing longwall supports provide support at the face. The stress redistribution, rock failure, and ground movement, were calculated using the finite difference code FLAC and rock failure and permeability routines developed by SCT. These routines were developed to realistically simulate actual behaviour of the strata.

Integrated Microseismic Monitoring and Numerical Modelling for the Determination of Fracture Architecture Around Longwall Coal Mines for Geomechanical Validation.

A more detailed description of the modelling approach is given by *Gale & Nemcik* [1998].

Two different roof geologies were modelled to demonstrate the variability in caving as a result of rock strength properties and stress field. One of these is a weak roof model with forward ground failure. In this caving style, no large caving blocks are formed, and the ground is heavily fractured in front of the face. The peak stress concentrations are located well ahead of the longwall face, and the ground is de-stressed in the vicinity of the face. The roof failure mechanism is characterised by the formation of frequent sub-vertical and sheared bedding planes that develop after each shear has been cut at the face. This style of roof failure has been verified by CSIRO microseismic monitoring [*Kelly et al*., 1996], and can be described as non-periodic on the large scale.

The second model exhibits a very different caving and fracture mechanism. This model has moderate strength roof strata, and the absence of weak bedding planes prevents frequent formations of fractures in the roof. Instead, major sub-vertical fractures develop at less frequent intervals forming large blocks of intact rock above the longwall face. The geometry of these blocks is defined by failure along a weak layer in the roof above or ahead of the face followed by a fracture network extending down to meet the longwall face. The intact blocks of roof collapse causing overloading of the roof supports. This style of roof failure has been verified from overburden movements measured by extensometers extending from the surface down to the coal seam in the centre of a longwall panel, and can be described as periodic.

The second of the two models presented by *Gale & Nemcik* [1998] is the more relevant to Asfordby given the moderately strong roof strata (see section 2.2.2). It is shown as figure 2.5.

Figure 2.5 View along the face of the fracture pattern predicted by a numerical model for strong roof conditions and periodic weightings [after *Gale & Nemcik*, 1998]. Face advance is to the left.

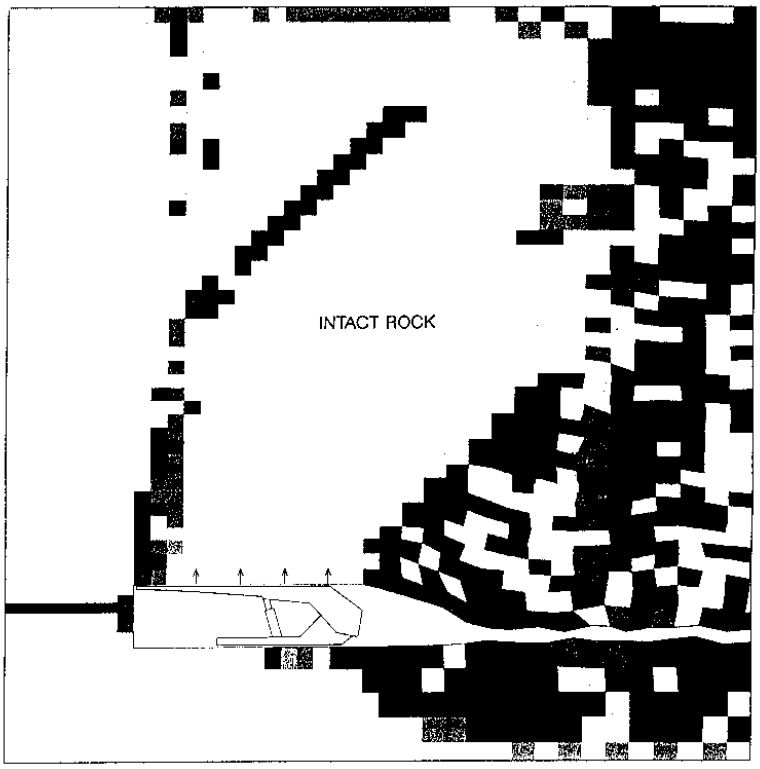

2.4 Recording equipment

2.4.1 Receivers

The first phase of mining was monitored using geophone groups (sondes) cemented into three surface boreholes. Two of these boreholes, Cants Thorn 1 and 2, were drilled specifically for the microseismic monitoring experiment. Four sondes were cemented into each of these two boreholes at a range of depths from seam level to 500m above the seam. The third borehole, Fishponds, was drilled during the exploration of the coalfield, and there was a sonde cemented at seam level in this borehole that had been used to test continuity of the Deep Main Seam by seismic transmittivity methods. The locations of these three boreholes relative to Panel 101 are shown as figure 2.6. The Fishponds sonde was used by the monitoring experiment because of its close proximity to the face starting position, although it was clear that it would soon be in the shadow of the goaf after extraction commenced.

Figure 2.6 The locations of the 5 boreholes used in the microseismic monitoring of the two phases of mining at Asfordby.

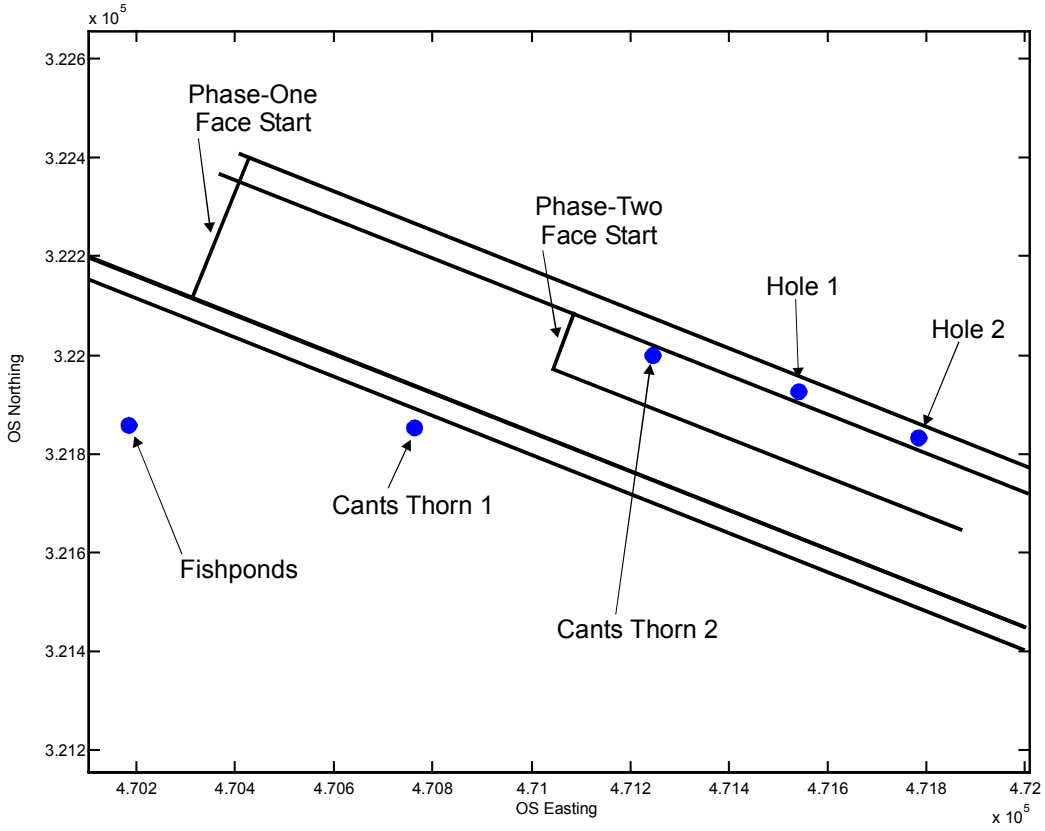

The second phase of mining was monitored using sondes cemented into two boreholes, Hole 1 and Hole 2, drilled into the roof of the main gate of Panel 101. One sonde was placed in each borehole. The location of these two holes relative to Panel 101 are also shown as figure 2.6. Hole 1 is the closer of the two holes to the face starting position for the second phase of mining.

Each sonde consists of 6 geophones installed in a brass barrel. The geophones are installed so there are two vertical geophones oriented in opposite directions along the long axis of the barrel, and four horizontal geophones oriented perpendicular to the long axis of the barrel. The arrangement of geophones in the sonde is illustrated in figure 2.7. If the sonde was placed in a vertical borehole, then the two geophones oriented along the long axis of the barrel will be oriented vertically, one positive upwards and one positive downwards. The four geophones oriented perpendicular to the long axis of the barrel would all be oriented in the horizontal plane. If the first of

the four geophones was oriented positive East, then the others would be oriented positive North-East, positive North and positive North-West. All the sondes used during the Asfordby experiment were installed in vertical boreholes. The azimuths of the 4 horizontal geophones in each sonde were determined using test shots (see section 3.2.2 in the next chapter).

Figure 2.7 The arrangement of the six geophones within a sonde. Each cylinder represents a geophone, the axis of the geophone is aligned along the axis of the cylinder. The white end of the cylinder is in the positive direction, the black end is in the negative direction. The blue wire frame represents the barrel of the sonde.

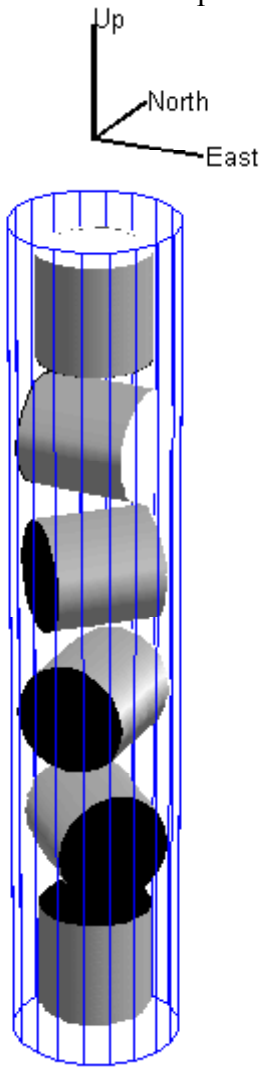

2.4.2 Data recording equipment

The signals from the geophones are transmitted to the surface by cable. The signals were monitored at the surface by a Vibrosound SP1 seismic monitor manufactured by Magus Electronic Ltd., Wheelock, Crewe, Cheshire. The Vibrosound SP1 has the ability to record 6 ground vibration channels and one sound-pressure channel with 24-bit digitisation, giving a bandwidth of greater than 118dB. Geophone sensitivities can be set, and there is a choice of sampling frequencies (250Hz, 500Hz or 1kHz). Signals from the geophones are monitored, and if the signal exceeds a pre-set threshold an event is recorded. The event data are stored on 20Mbyte Flash-EPROM cards. The total length of data per event can be up to 2499 samples, and the first recorded sample is taken a specified number samples before the trigger.

For the first phase of the Asfordby monitoring experiment, all events were recorded with a sampling frequency of 1kHz and an event length of 1500 samples. The pre-trigger length is 500 samples (i.e. each recorded event is 1.5 seconds long, and the trigger occurred at 0.5 seconds). This event length means that over 600 events can be written to one 20Mbyte card. A total of four Vibrosounds were used for the monitoring experiment, one monitoring the six geophones in the Fishponds borehole, two monitoring three tri-axial geophones from each sonde in the Cants Thorn 1 borehole, and one monitoring three tri-axial geophones from two of the sondes in the Cants Thorn 2 borehole. Each Vibrosound has an internal battery, but an external 12V power supply, re-charged by a solar panel, was also used. Flash cards and batteries only needed to be changed weekly during the period of monitoring.

For the second phase of monitoring, the same event length and sampling frequency were used. The Vibrosounds were installed in the mine after some modifications were made to make them operate under a letter of no objection from HMI. Two Vibrosounds were used, one monitoring the six geophones of the Hole 1 sonde, the other monitoring the six geophones of the Hole 2 sonde.

Each Vibrosound can act as either a or a slave as well as independently. During the Asfordby experiment the logistics of connecting Vibrosounds together meant that this

mode of operation was not possible. Full details of the instrumentation and the experiment can be found in *Styles et al*, [1996].

2.6 Event frequency

Changes in the frequency of occurrence of recorded events, i.e. how many events are recorded per day, have been used to show that observed seismicity is induced by mining activity [e.g. *Westbrook et al*., 1980] and have been proposed as potential precursors to outbursts and other catastrophic failure [e.g. *McKavanagh & Enever*, 1980; *Styles*, 1993]. The date and time of each event recorded during the microseismic monitoring of Asfordby are known, so it is easy to find if there are any changes in event frequency. During Phase-One of mining many difficulties were experienced at the face, such as poor roof conditions, water inflow, and weightings. If there is any correlation between the difficulties experienced and event frequency then the microseismicity could be associated with the processes causing the difficulties.

A histogram of the number of events recorded per day by all four Vibrosounds monitoring Phase-One of mining is shown as Figure 2.7. The time of principal mining events are also shown for comparison. There is considerable variation in event frequency during the period of monitoring. There is very little observed seismicity until the beginning of August 1995. The face advance at this time was about 300m, which is approximately when the face becomes square (i.e. face advance equals face width). The face width is 240m. Between 18th August 1995 and 7th September there was little observed seismicity. Poor roof conditions were experienced at the face during this period. Between 7th September and 17th September there is a massive increase in the amount of seismicity, with the number of events recorded per day approaching 40. Following this there is a decrease in seismicity followed by another increase around the 26th September. After a few days of this increased activity, the first weighting occurs. There is a decrease in seismic activity followed by an increase around the 10th October. After two days of the increased activity, a weighting and water inflow event occurred at the face. This led to a stop in mining activity until the restart on the 25th November. In this period there are some changes in event frequency.

After the restart there is an increase in event frequency followed quickly by a second water inflow. After this poor working conditions were experienced continually until the face was abandoned.

Figure 2.7 Histogram of number of events recorded per day by all sondes during Phase-One of monitoring. Dates are in the format MM/DD/YY. The times of principal mining events are also shown.

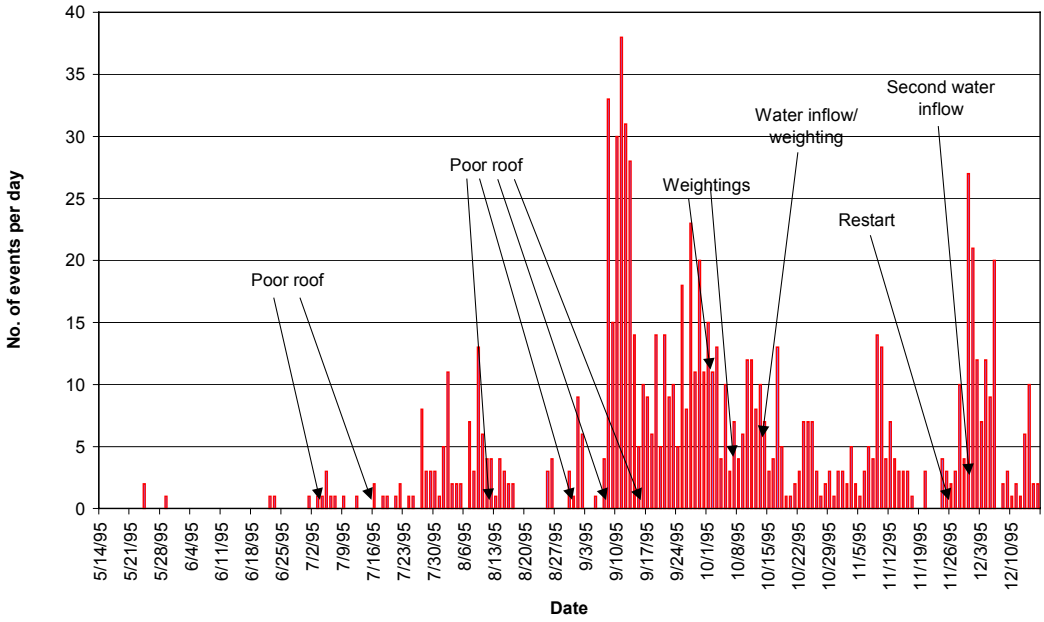

Figure 2.8 Histograms of number of events recorded per 7days at all sondes in one borehole during Phase-One of monitoring. The front (blue) columns are for the Cants Thorn 2 borehole, the middle (red) columns are for the Cants Thorn 1 borehole and the back (yellow) columns are for the Fishponds borehole.

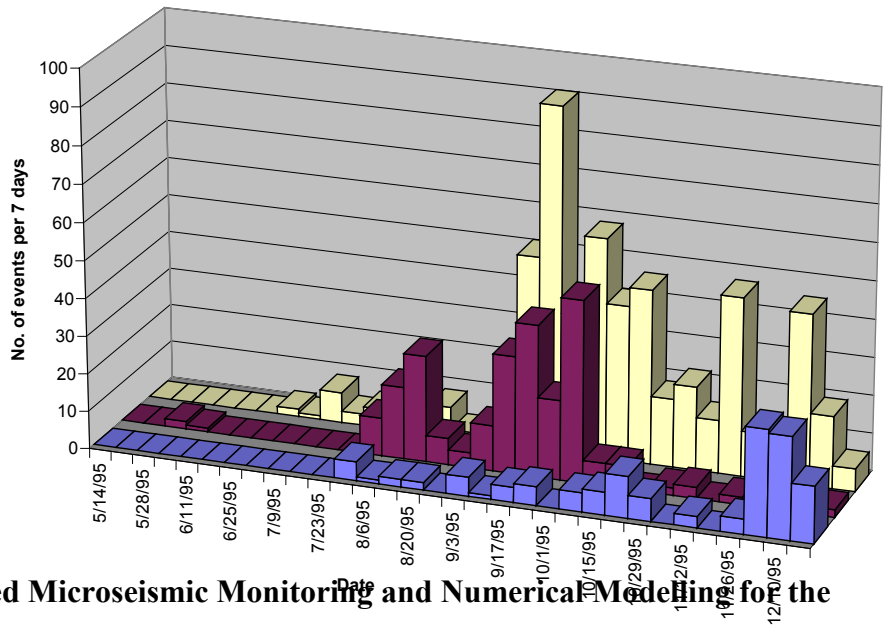

Figure 2.8 shows how the frequency of events recorded by sondes in different boreholes changed with time. These histograms are calculated with 7-day bins, so the values are number of events per seven days, because 1-day bins make this type of plot difficult to understand. The seismicity recorded at the different boreholes all show generally the same variations. The large increase in seismicity before both weightings is observed by sondes in the Cants Thorn 1 and Fishponds boreholes. The increase in seismicity after the restart is seen at the Cants Thorn 2 and Fishponds boreholes, and to a lesser extent by the Cants Thorn 1 borehole. The seismicity recorded at Cants Thorn 2 only increases after the restart, as the face gets closer to the borehole. The sonde in the Fishponds borehole records more events than the other sondes. This is because the sonde is in the seam and often triggers on higher amplitude guided waves that travel along the seam.

It appears that there is some correlation between the event frequency and some of the principal mining events. In particular, the two major weightings (1st October and 12th October) are preceded by an increase in seismic activity. The same is also true for the two water inflow events. Thus the processes causing these mining events are related in some way to the observed microseismicity, and studying the microseismicity should give a better understanding of the processes involved.

A histogram of the number of events recorded per day at the Hole 1 sonde during Phase-Two of monitoring is shown as Figure 2.9. There is considerable variation in the number of events recorded per day, with some periods of a few days showing no recorded activity. Unfortunately the dates of problems experienced at the face are not known, and without this information it is difficult to draw any firm conclusions about any association with observed seismicity. The frequency of occurrence of seismic events is only the first piece of important information that can be determined from the recorded seismic data.

Figure 2.9 Histogram of number of events recorded per day by Hole 1 sonde during Phase-Two of monitoring.

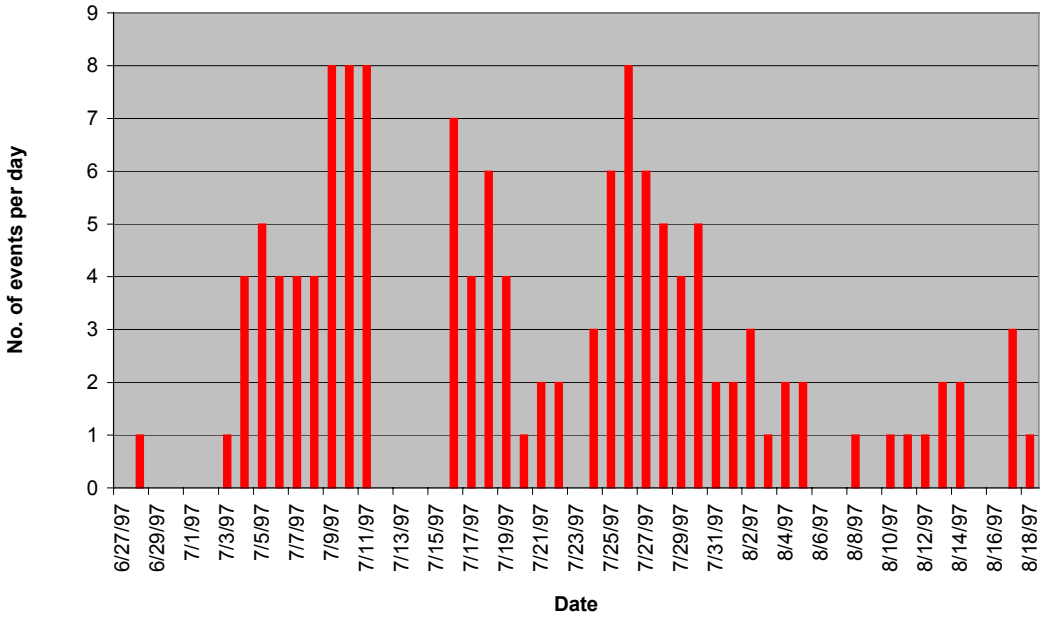

3 MICROSEISMIC EVENT LOCATIONS

3.1 Introduction

The aim of monitoring excavation-induced seismicity is to gain some insight into the effect that the excavation is having on the surrounding rock mass. To identify what region of the surrounding rock mass is being affected it is necessary to determine the locations of the recorded seismic events. There are a number of techniques that can be used to find the location of recorded seismic events. Which technique is used depends on a number of things e.g. the amount and quality of data available and accuracy of velocity model. Most location techniques use a number of records of the same event made in different locations. They find hypocentral parameters i.e. location and origin time, which best fit observed arrival times of certain seismic wave phases generated by that event. Some techniques find more than the hypocentre parameters for the event, for instance simultaneous location and velocity determination. These sophisticated techniques require a number of seismic records of each event. The Microseismology Research Group at the University of Liverpool has used some of these techniques before when monitoring longwall induced seismicity [e.g. *Styles et al.*, 1987a, 1987b, 1991]. A comparison of least-squares methods [e.g. *Lienert et al.*, 1986] with a microseismic event location method that used a simplex optimisation showed that the simplex method was more accurate [*Styles et al.*, 1987a]. This result was the same as obtained by *Riefenberg* [1989]. The studies previously carried out by the Microseismology Research Group that used a simplex optimisation method to locate microseismic events had networks of surface seismometers. The surface seismometers in these studies were linked so that microseismic events were always recorded on multiple receivers.

Nearly all of the seismic events recorded during the two phases of microseismic monitoring at Asfordby were recorded as a single three-component seismogram. This was because a different Vibrosound (see section 2.4.2) was monitoring each sonde, and the machines could not be linked together. A few events were recorded during the second phase on two sondes, both machines triggering independently. The small

amount of data available for each recorded event meant that the location of the event could not be calculated as the location which best fits observed arrival times. It is possible to calculate the location of a seismic event from a single three-component seismogram using the P-wave particle motion and the difference between P-wave and S-wave arrival times. Several previous studies by the Microseismology Research Group have used such a method [e.g. *Toon*, 1990; *Toon et al.*, 1992; *Toon and Styles*, 1993]. The method used in this study is a modification and improvement on those used by these earlier studies and is described in the following section.

3.2 Back azimuth propagation: Seismic event location using polarisation analysis

3.2.1 Method description

Polarisation analysis of vector fields has been a topic of research in a number of different physical systems e.g. ultra low-frequency magnetic fields [*Samson*, 1973], low-frequency seismology [*Montalbetti & Kanasewich*, 1970], and high-frequency seismology [*Bataille & Chiu*, 1991]. In the case of seismology, P-wave particle motion is linearly polarised along the direction of propagation of the wave. Thus polarisation analysis that determines the direction of P-wave particle motion also determines the direction of propagation of the P-wave. The direction of propagation will be the source-receiver direction if a constant velocity model is assumed. By finding the polarisation of the P-wave particle motion, a straight line can be defined in space on which the seismic event generating that P-wave must lie. For a more complex velocity model, a curve on which the seismic event must lie can be calculated from the P-wave polarisation.

A window of three-component seismic data, generally encompassing the first half-cycle of the P-wave, is taken. A singular value decomposition of the windowed data is used to calculate eigenvectors and eigenvalues. The eigenvector with the largest associated eigenvalue is taken as the direction of polarisation. Some polarisation analysis techniques remove any effects that noise in the data might have on the determined polarisation direction [e.g. *Vidale*, 1986]. Alternatively, a similar analysis can be carried out in the frequency domain in an attempt to limit the effect of noisy

data [*Park et al.*, 1987]. The data recorded during this study are of such good quality that the time domain analysis gives the same result as the frequency domain analysis. Thus the simpler time domain analysis that does not remove the effect of noise is used as it reduced computing time.

To find the distance to the source from the receiver, the delay time, Δt_{ps}, between P-wave arrivals and S-wave arrivals is used.

$$\Delta t_{ps} = t_s - t_p = \frac{d}{\beta} - \frac{d}{\alpha} \qquad \ldots(3.1)$$

In equation (3.1), t_p is the P-wave arrival time, t_s is the S-wave arrival time, α is the P-wave velocity, β is the S-wave velocity, and d is the source-receiver distance. Re-arranging equation (3.1) gives:

$$d = \frac{\Delta t_{ps} \alpha \beta}{\alpha - \beta} \qquad \ldots(3.2)$$

This simple equation is only true for a homogeneous velocity model, but it is very easy to extend it to a more complex velocity model by considering sections of constant velocity along the ray path.

The polarisation direction and P-S delay time allow us to calculate two possible event locations. Choosing between the two possible locations is normally very simple, based on proximity to mining operations i.e. the location closer to mining activity is more likely to be the correct location. In particular, it is often the case that one of the two possible locations is above ground level, and these can be ignored.

3.2.2 Accuracy of location method

In order to determine whether microseismic events can be used for geomechanical validation it is important to assess the likely accuracy with which they can be located.

There are three possible sources of error using the method described above, polarisation direction errors, picking errors, and velocity model errors. Velocity models are discussed in detail in the next section.

A possible method of estimating random polarisation direction errors is to determine the polarisation direction of different parts of the P-wave, and see how they differ. This analysis has been applied to all events of the datasets being examined. For each recorded event, the difference between determined azimuths and elevations for the first and second half cycles of the P-wave particle motion direction are found. These are taken as estimates of the error in azimuth and elevation of that event location.

Systematic polarisation direction errors caused by incorrect orientation of the geophones can be quantified by examining test shots. The geophone groups, or sondes, are installed in vertical boreholes, but only the vertical geophone can be assumed to have the correct orientation. Seismic records of test shots at a known location need to be examined to calculate the angle defining the matrix that transforms the three-component data from the sonde co-ordinate systems to a geographical co-ordinate system. These shot records are analysed to calculate the angle between the sonde and the geographic co-ordinates systems in the horizontal plane. This analysis is summarised in tables 3.1, 3.2, and 3.3 for the three sondes that have been used in this study.

Table 3.1 Orientation analysis of Cants Thorn 1 borehole upper sonde, used during the first phase of monitoring. Shots are fired at a range of depths in Cants Thorn 2 borehole. True orientation of shot from sonde is 16.9° anti-clockwise from East.

Shot no.	**Orientation**	**Correction**
1	-60.7°	77.6°
2	-59.2°	76.1°
3	-60.8°	77.7°
4	-60.3°	77.2°
5	-60.2°	77.1°
7	-59.8°	76.7°
8	-59.3°	76.2°
9	-59.8°	76.7°
Mean		76.9°
Standard deviation		0.6°

Table 3.2 Orientation analysis of Hole 1 sonde, used during the second phase of monitoring. Shots are fired from a variety of locations around the sonde. True orientations of shots are given as angles measured anti-clockwise from East.

Shot no.	Orientation	True orientation	Correction
1	70.79	167.86	-97.07
2	97.86	-167.9	-94.24
3	-134.74	-45	-89.74
4	-120.95	-28.74	-92.21
5	-107.87	-26.1	-81.77
6	-126.83	-25.03	-101.8
7	-115.19	-24.3	-90.89
9	-113.23	-17.53	-95.7
10	-112.42	-15.78	-96.64
11	-116.72	-14.23	-102.49
12	-114.67	-10.71	-103.96
13	-102.75	-3.73	-99.02
14	-83.43	30.4	-113.83
15	49.3	124.7	-75.4
16	56.17	144.76	-88.59
Mean			-94.9
Standard deviation			9.3

Table 3.3 Orientation analysis of Hole 2 sonde, used during the second phase of monitoring. Shots are fired from a variety of locations around the sonde. True orientations of shots are given as angles measured anti-clockwise from East.

Shot no.	Orientation	True orientation	Correction
3	-137.85	160.62	-118.47
4	37.79	160.64	-122.85
5	43.39	167.27	-123.88
6	70.44	-170.53	-119.03
7	-166.44	-46.08	-120.36
9	-136.01	-5.64	-130.37
10	-104.61	33.69	-138.3
11	9.89	125.94	-116.05
12	28.42	144.92	-116.5
13	32.4	149.6	-117.2
14	-151.17	152.47	-123.64
15	-146.75	153.69	-120.44
16	-143.41	154.54	-117.95
Mean			-121.9
Standard deviation			6.3

Table 3.1 suggests that the orientation of the Cants Thorn 1 upper sonde is known to better than one degree. This is perhaps an unrealistic accuracy, since all shots are at exactly the same azimuth from the sonde, and there is no way of determining any path

effects. The orientation analysis applied to the two sondes used during the second phase of monitoring, summarised in tables 3.2 and 3.3, probably gives a more realistic estimate of the sonde orientation error, about 10°. Of course this will be a systematic error in the locations of all events recorded at one sonde, and hence it is difficult to determine exactly what the error is. Sonde orientation errors explain why two locations determined for the same event recorded at two sondes may be further apart than estimated by the event specific error analysis.

The size of picking errors can differ from one event to another, as it is dependent on the quality of data. Errors in S-wave picks are likely to be larger than errors in P-wave picks because of interference between P-waves and S-waves and the lower frequency content of the S-waves. An estimate of the size of these errors is relatively simple upon examination of a number of seismograms. Ten events taken at random from the Cants Thorn 1 dataset recorded during the first phase of monitoring have been examined. For each event the range over which a P-wave or S-wave arrival pick could be made is estimated by making a number of picks of each arrival and measuring by how much they differ. The results of this analysis are given as table 3.4.

Table 3.4 Estimation of a typical picking error from analysis of ten events recorded during the first phase of monitoring.

Event	**P-wave range (ms)**	**S-wave range (ms)**	**Total picking error (ms)**
Au05_005	1	4	5
Au05_013	2	2	4
Au07_002	2	2	4
Au08_007	1	2	3
Au11_013	1	2	3
Au11_079	1	3	4
Au11_082	4	2	6
Au12_065	3	1	4
Au13_004	2	2	4
Au14_007	3	3	6
Average	**2**	**2**	**4**

The average picking error in P-S delay time is 4ms. Using a P-wave velocity of 3.2km/s, and an S-wave velocity of 1.78km/s, this picking error would lead to an error in source-receiver distance of 16m. This value is estimated as the source-receiver distance error for all events.

Given errors in the polar co-ordinates of the event location relative to the sonde location, the shape of the error volume within which the event must lie will be a truncated cone. The focus of the cone will be at the sonde if a homogeneous velocity model is assumed. It is possible to examine how well this method of estimating the location errors works by examining some of the events recorded during the second phase of monitoring at Asfordby. Forty-seven events were recorded at two sondes. After calculating two locations of the event using the two different records, and estimating the errors of each using the method described above, the two locations can be compared to see whether the error bounds overlap. A quantitative analysis comparing the two calculated locations of all the events that were recorded on two sondes is summarised in table 3.5. The displacement between the two locations is determined. Using the errors in azimuth, elevation and source-receiver distance estimated using the methods described above, the minimum displacement between possible event locations is calculated. If the error volumes overlap, this minimum displacement will be zero. If they do not overlap it will have some finite value.

The two estimated error volumes overlap for 47% of the events analysed. This would suggest that the errors estimated apply to a confidence level of 47%. If it is assumed that the actual errors, i.e. the difference between the calculated event location and the real event location, make up a normal distribution, then the estimated errors are approximately 0.63 times the standard deviation of the actual errors. Thus by multiplying the estimated errors by 1.59 (i.e. one over 0.63) an estimate can be made of the standard deviation of the location error for a given event. Table 3.6 shows the results of the analysis described above applied using estimated standard deviation errors. The two estimated error volumes relating to one standard deviation overlap for 74% of the events analysed. This gives a confidence level, i.e. 74%, which is close to the confidence level associated with one standard deviation in a normal distribution, i.e. 68%. Therefore the assumption that actual location errors are normally distributed, and that a reliable estimate can be made of the standard deviation of this distribution for each event, is justified. This means that errors in source-receiver distance are normally distributed with a standard deviation of 1.59 times 16m, or 25m.

Table 3.5 Comparison of differences in locations of events calculated from records at two separate sondes with error volumes calculated from estimated polar co-ordinate error bounds.

Event 1	Event 2	Location displacement (m)	Displacement between error volumes (m)
c2_03_001	d2_03_005	60	Overlapping
c2_03_002	d2_03_006	108	63
c2_03_003	d2_03_022	85	Overlapping
c2_03_004	d2_03_027	84	28
c2_03_005	d2_03_028	253	65
c2_03_006	d2_03_045	66	Overlapping
c2_03_007	d2_03_081	142	Overlapping
c2_03_008	d2_03_221	74	32
c2_04_001	d2_04_026	86	48
c2_04_002	d2_04_061	62	Overlapping
c2_04_003	d2_04_118	51	Overlapping
c2_06_005	d2_06_009	143	123
c2_06_142	d2_06_243	138	Overlapping
c2_06_189	d2_06_306	315	51
c2_06_246	d2_06_386	129	73
c2_06_303	d2_06_475	57	Overlapping
c2_07_013	d2_07_032	330	50
c2_07_014	d2_07_034	54	22
c2_07_016	d2_07_036	69	Overlapping
c2_07_022	d2_07_042	157	64
c1_06_005	d1_06_009	72	Overlapping
c1_06_142	d1_06_243	185	71
c1_06_189	d1_06_306	210	54
c1_06_246	d1_06_386	577	98
c1_06_303	d1_06_475	76	Overlapping
c1_07_013	d1_07_032	63	Overlapping
c1_07_014	d1_07_034	60	24
c1_07_016	d1_07_036	140	22
c1_07_022	d1_07_042	93	Overlapping
c2_06_005	d1_06_009	108	43
c2_06_142	d1_06_243	167	Overlapping
c2_06_189	d1_06_306	163	43
c2_06_246	d1_06_386	167	90
c2_06_303	d1_06_475	50	Overlapping
c2_07_013	d1_07_032	267	Overlapping
c2_07_014	d1_07_034	98	Overlapping
c2_07_016	d1_07_036	145	Overlapping
c2_07_022	d1_07_042	152	91
c1_06_005	d2_06_009	97	Overlapping
c1_06_142	d2_06_243	164	54
c1_06_189	d2_06_306	186	55
c1_06_246	d2_06_386	147	47
c1_06_303	d2_06_475	110	56
c1_07_013	d2_07_032	102	Overlapping
c1_07_014	d2_07_034	54	21
c1_07_016	d2_07_036	84	Overlapping
c1_07_022	d2_07_042	117	Overlapping

Table 3.6 Comparison of differences in locations of events calculated from records at two separate sondes with error volumes calculated from estimated 'one standard deviation' polar co-ordinate error bounds.

Event 1	Event 2	Location displacement (m)	Displacement between error volumes (m)
c2_03_001	d2_03_005	60	Overlapping
c2_03_002	d2_03_006	108	29
c2_03_003	d2_03_022	85	Overlapping
c2_03_004	d2_03_027	84	Overlapping
c2_03_005	d2_03_028	253	Overlapping
c2_03_006	d2_03_045	66	Overlapping
c2_03_007	d2_03_081	142	Overlapping
c2_03_008	d2_03_221	74	Overlapping
c2_04_001	d2_04_026	86	36
c2_04_002	d2_04_061	62	Overlapping
c2_04_003	d2_04_118	51	Overlapping
c2_06_005	d2_06_009	143	Overlapping
c2_06_142	d2_06_243	138	Overlapping
c2_06_189	d2_06_306	315	Overlapping
c2_06_246	d2_06_386	129	42
c2_06_303	d2_06_475	57	Overlapping
c2_07_013	d2_07_032	330	Overlapping
c2_07_014	d2_07_034	54	Overlapping
c2_07_016	d2_07_036	69	Overlapping
c2_07_022	d2_07_042	157	49
c1_06_005	d1_06_009	72	Overlapping
c1_06_142	d1_06_243	185	19
c1_06_189	d1_06_306	210	11
c1_06_246	d1_06_386	577	45
c1_06_303	d1_06_475	76	Overlapping
c1_07_013	d1_07_032	63	Overlapping
c1_07_014	d1_07_034	60	Overlapping
c1_07_016	d1_07_036	140	Overlapping
c1_07_022	d1_07_042	93	Overlapping
c2_06_005	d1_06_009	108	19
c2_06_142	d1_06_243	167	Overlapping
c2_06_189	d1_06_306	163	Overlapping
c2_06_246	d1_06_386	167	66
c2_06_303	d1_06_475	50	Overlapping
c2_07_013	d1_07_032	267	Overlapping
c2_07_014	d1_07_034	98	Overlapping
c2_07_016	d1_07_036	145	Overlapping
c2_07_022	d1_07_042	152	66
c1_06_005	d2_06_009	97	Overlapping
c1_06_142	d2_06_243	164	32
c1_06_189	d2_06_306	186	Overlapping
c1_06_246	d2_06_386	147	Overlapping
c1_06_303	d2_06_475	110	46
c1_07_013	d2_07_032	102	Overlapping
c1_07_014	d2_07_034	54	Overlapping
c1_07_016	d2_07_036	84	Overlapping
c1_07_022	d2_07_042	117	Overlapping

Figure 3.1 Cumulative frequency distributions of estimated azimuth and elevation errors for events recorded on at Cants Thorn 1 borehole upper sonde during the first phase of monitoring.

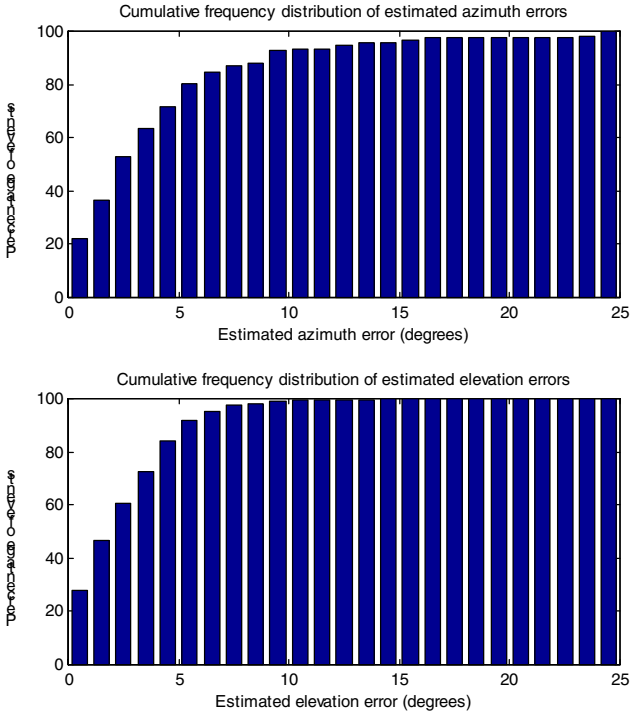

Figure 3.2 Cumulative frequency distributions of estimated azimuth and elevation errors for events recorded on at the Hole 1 sonde during the second phase of monitoring.

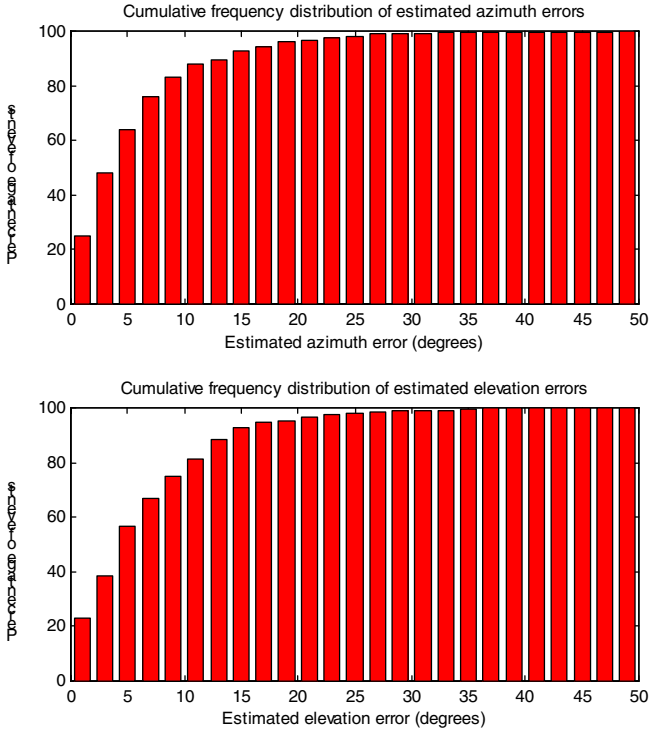

Cumulative frequency distributions of the estimated standard deviation of azimuth and elevation errors for each dataset are shown as figures 3.1 and 3.2. It should be noted that systematic errors in event location caused by the different orientations of the sondes within the boreholes have not been taken into account by this analysis. Thus it is likely for some of the pairs of locations the error bounds do not overlap because of this systematic error, and not because the event location errors are not large enough. This means that there may be a tendency to over-estimate error bounds for individual event locations.

Azimuth and elevation errors are both small, the means for each dataset are between 5° and 8°. It should be noted, however, that an incorrectly assumed velocity model is more likely to effect the elevation of the polarisation directions. The actual velocity model for a typical coal measure geology will approximate horizontal layers, and these have no effect on azimuth i.e. there are no lateral variations in velocity.

3.2.3 Velocity model

Using an incorrect velocity model is generally the largest source of error in any seismic event location technique. The simplest velocity model that can be assumed is a homogenous isotropic model. A better model for typical coal measure geology would be a 1-D laterally homogeneous layered velocity model.

There are two sources of velocity information available for this study; sonic logs of the Cants Thorn 1 and Cants Thorn 2 boreholes, and seismic data recorded at the sondes in Cants Thorn 1 for test shots at various depths in Cants Thorn 2. The velocity-depth profiles calculated from the sonic logs are shown as figure 3.3. The grey line is the sonic log velocity data. The velocity profiles from the Cants Thorn 1 and Cants Thorn 2 boreholes are very similar. This implies that any velocity model that is used can be assumed to be laterally homogeneous. The sonic log velocity profiles both show extremely low P-wave velocities at depths shallower than 50m relative to mean sea level (MSL), i.e. shallower than 100m below ground level. The P-wave velocity given by the sonic logs at these depths is typically 2.3km/s or lower. Low P-wave velocities in fact extend down to 200m below ground level. To test whether these low P-wave

velocities are real, a 2-D tomographic inversion is performed using the test shot seismic data.

Figure 3.3 Velocity-depth profiles for Asfordby from sonic logs (grey lines) and tomography (solid black lines). The velocity model assumed is shown as a dashed black line.

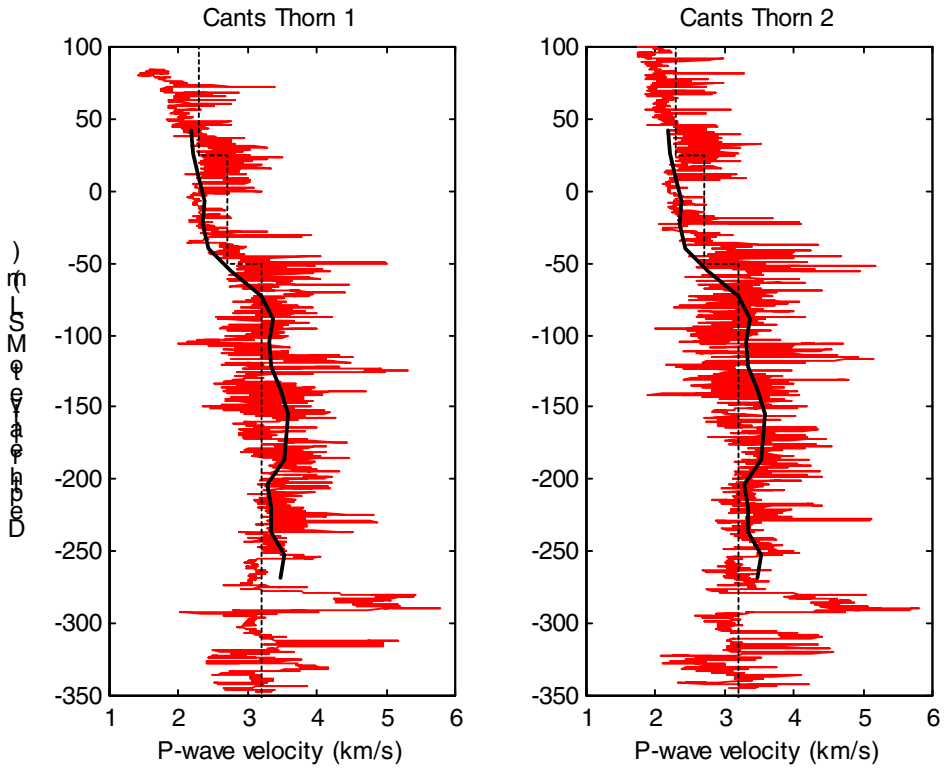

The test shot seismic data were recorded such that the trigger was the shot i.e. the zero time on the trace was the time of the shot, and hence the arrival time of the P-wave is the travel time. The locations of the shots and receivers are all known. A total of ten shots were fired and recorded at the four sondes in the Cants Thorn 1 borehole. Of the 40 seismic records, fifteen were found to be of insufficient quality to make a reliable pick of the P-wave arrival time. This means that the tomographic inversion is carried out using only 25 ray paths, but since the aim of applying the inversion is to confirm the sonic log data, 25 ray paths are felt to be sufficient. The data required for the tomographic inversion are the shot locations, the receiver locations, and the P-wave travel time for each shot-receiver pair. A simple tomographic inversion is applied i.e. no ray bending taken into account, and the method is described in appendix 3. The inversion is applied to a vertical plane intersecting the two boreholes. The plane is split

into a 20x20 grid, which gives an approximate cell size of 25m in length, 15m in depth. Altering the number of cells does not significantly change the results of the inversion. A velocity-depth profile is extracted from the region with the densest ray coverage and compared against the sonic log velocity-depth profiles.

Figure 3.4 Results of tomographic analysis applied to test shot data recorded in Cants Thorn 1; shots fired in Cants Thorn 2. Cants Thorn 1 is located at 0m, Cants Thorn 2 is located at 487m. The solid black lines show the shot-receiver raypaths, and the dashed black line shows the position of the velocity-depth profile shown in figure 3.3.

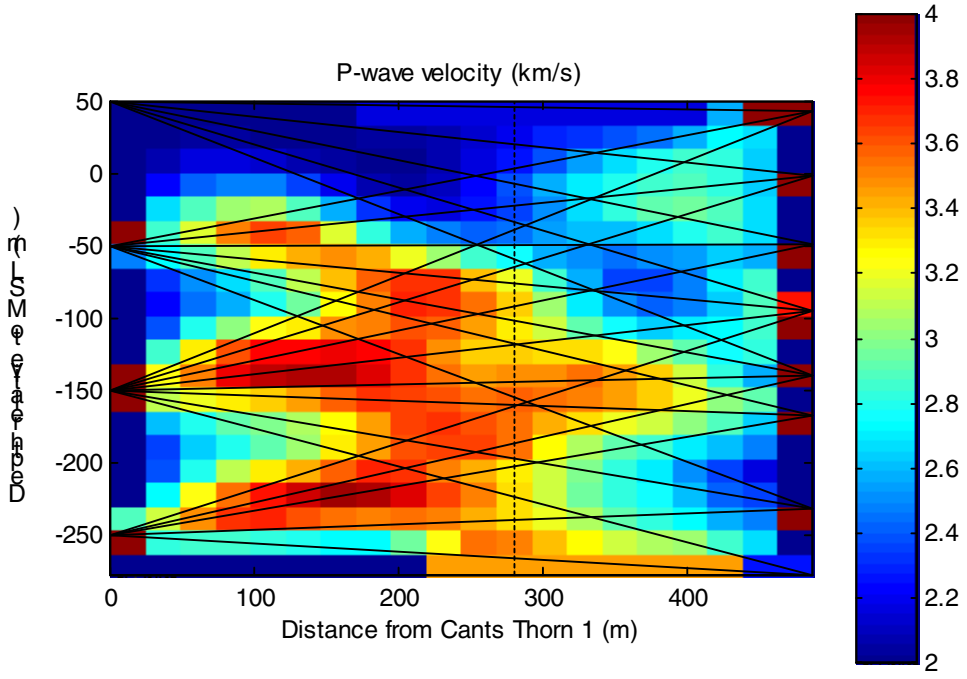

The results of the tomographic inversion are shown as figure 3.4. The initial P-wave velocity model is a homogeneous 3km/s velocity. The result obtained does not vary significantly for different initial velocity models. The final velocity model clearly shows the effects of the limited ray coverage. The densest ray coverage occurs between distances of 200m and 400m from Cants Thorn 1 towards Cants Thorn 2. In this region the velocity model obtained is approximately laterally homogeneous, although the resultant velocity model is at best only a very rough estimate, so no real conclusions can be drawn from it. The dashed vertical line on figure 3.4 shows the location of the velocity-depth profile taken from the final tomography velocity model in the region of densest ray coverage. The velocity-depth profile is shown on figure 3.3

as a solid black line. The velocity-depth profile from the tomography velocity model and the velocity-depth profile calculated from the sonic log data match very well. In particular, both velocity-depth profiles show the same low P-wave velocities above -50m relative to MSL.

Table 3.7 Details of the Asfordby seismic velocity model.

Height of base of layer (relative to MSL) (m)	P-wave velocity (km/s)	S-wave velocity (km/s)
25	2.3	1.28
-50	2.7	1.5
-	3.2	1.78

On figure 3.3 the velocity model assumed is shown as a dashed line. The details of this three-layer model are given in table 3.7. S-wave velocities were calculated assuming a P-wave to S-wave velocity ratio of 1.8 i.e. approximately that of a Poisson solid. The model assumed was felt to be the simplest possible velocity model that showed the same features as the sonic log data. The only large deviation of the sonic log velocity data from the assumed model is the high velocity region at -300m. This is the dolerite sill above the seam, and it is at the most 15m thick in the Panel 101 area. The P-waves recorded typically had a dominant frequency of 40-50Hz, which for a P-wave velocity of 3.2km/s makes the wavelength 80-64m. Thus the thickness of the dolerite sill is less than a quarter wavelength, and would not significantly affect the passage of seismic waves. In fact most of the seismic events recorded during the first phase of monitoring occur above this sill (see section 3.3.1), so the seismic waves for these events do not pass through it.

The assumed three-layer velocity model is homogeneous below -50m relative to MSL. Most of the seismic data recorded showed very simple P- and S-waveforms. An example of the quality of the data recorded is shown as figure 3.5. There appear to be very few reflected phases, and any there are have very little energy. This would suggest that there are no large changes in acoustic impedance in most of the region the seismic waves travel through. During the second phase of monitoring, all event locations are found to be well below -50m relative to MSL, so a homogeneous velocity model could be assumed for that phase of monitoring. There are a few events recorded

during the second phase of mining at more than one sonde. For a large proportion of these events, the two locations calculated by analysing data from each sonde independently are the same within estimated error bounds (see table 3.6). This suggests that the velocity model assumed in the region between these events and the sonde that recorded them is a good approximation to the actual velocity structure.

Figure 3.5 An example of the quality of data recorded during the periods of monitoring at Asfordby.

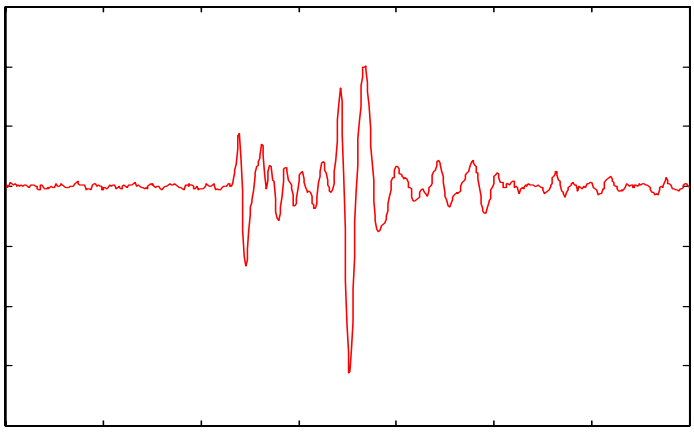

The back-azimuth propagation location method can be easily modified to use a 1D laterally homogeneous layered velocity model. The azimuth and elevation of the direction of propagation at the sonde are found in the same way i.e. by analysing the P-wave polarisation direction. The ray path is then followed back along the direction of propagation until it intersects a layer boundary. At the boundary the azimuth and elevation of the direction of propagation are calculated for the next layer. For a 1D layered velocity model the azimuth will remain constant, and the elevation in the next layer can be calculated using Snell's Law:

$$\frac{\sin\theta_1}{v_1} = \frac{\sin\theta_2}{v_2} \qquad \ldots(3.3)$$

In equation (3.3), θ_1 is the angle of incidence in the first layer, measured from the vertical i.e. 90° minus the elevation; θ_2 is the angle of incidence in the second layer; v_1 is the velocity in the first layer; v_2 is the velocity in the second layer. Thus a ray path

can be found along which the event location lies. The ray-path can be segmented into portions that travel through regions of constant velocity. The ray-path will be straight for these segments, and will only change direction at the interfaces between regions of different velocity. The positions of the intersection points between ray-path and interface are calculated and used to define the ray-path. A P-S delay time for each of the segments of ray-path can be calculated, and hence the P-S delay time at each of the intersection points can be calculated by summing those of the individual segments. The P-S delay times at each intersection point can be compared with the measured P-S delay time to find the two intersection points between which the event location must be. These intersection points will be the intersection point that has the closest P-S delay time that is less than the measured delay time and the intersection point that has the closest P-S delay time that is greater than the measured delay time. Interpolating between these two points using the measured P-S delay time to calculate the distance of the event from either of these points allows the event location to be found.

After the event location is found, a virtual sonde location can be calculated such that if the seismic waves propagated in the same direction of propagation as at the event location through a homogeneous velocity model and were recorded by the virtual sonde, the P-S delay time would be the same as that measured. This is done so that the geometry of the error volume can be easily defined. By assuming that the errors in azimuth and elevation of the propagation direction at the sonde are approximately the same as those at the event location, then the error volume will be a truncated cone with the focus at the virtual sonde location. Thus the azimuth and elevation errors in propagation direction measured at the sonde will be approximately the same as the azimuth and elevation errors of the polar co-ordinates of the event location relative to the virtual sonde location.

3.3 Locations of microseismic events recorded during first phase of monitoring

3.3.2 Fishponds dataset

Seismic data recorded at the sonde in the Fishponds borehole were of a poorer quality than that recorded at the other dedicated sondes. The sonde in the Fishponds borehole

is located in the seam, and seismic ray paths had generally travelled through regions of goaf and in the seam. The seismic transmission characteristics of the goaf and the interference of waves caused by in-seam ray-paths meant that recorded seismograms were of a very complex nature. The seismometer in the Fishponds borehole was not specifically for this study. It was initially used to determine transmission characteristics for seam continuity studies for the Asfordby take. In these studies, shots were fired at seam level in other boreholes, generating guided seismic waves in the seam. If the seismometer in the Fishponds borehole recorded these guided waves, then the seam was uninterrupted between the two boreholes. Thus the seismometer was placed to optimise recording of guided waves, which led to more complex seismic data being recorded than that recorded by receivers not in the seam.

Figure 3.16 shows a plan view of the calculated locations of microseismic events recorded at the Fishponds sonde during weeks 13 to 26. The depths of these events are difficult to determine because of the near-sonde effects of the seam i.e. the P-wave polarisation direction is determined for a P-wave phase that has been internally reflected within the seam. Thus only a plan view of the event locations is shown.

The events recorded at Fishponds are not uniformly spread and are concentrated along the tail gate, and form a large cluster. It is likely that events on the main gate side of the face have not been recorded because of the location of the sonde, especially since seismic waves would then be travelling almost entirely in the goaf. There are some events above the face, but again these will have ray paths through the goaf so probably a lower fraction of all the seismic events occurring in that area will be recorded than in the tail gate area.

Figure 3.16 Plan view of the locations of microseismic events recorded by the Fishponds sonde during week 13 to 26. The Fishponds sonde is located at seam level, at 0m East and 0m North. The Cants Thorn 1 upper sonde is shown as a circle for reference.

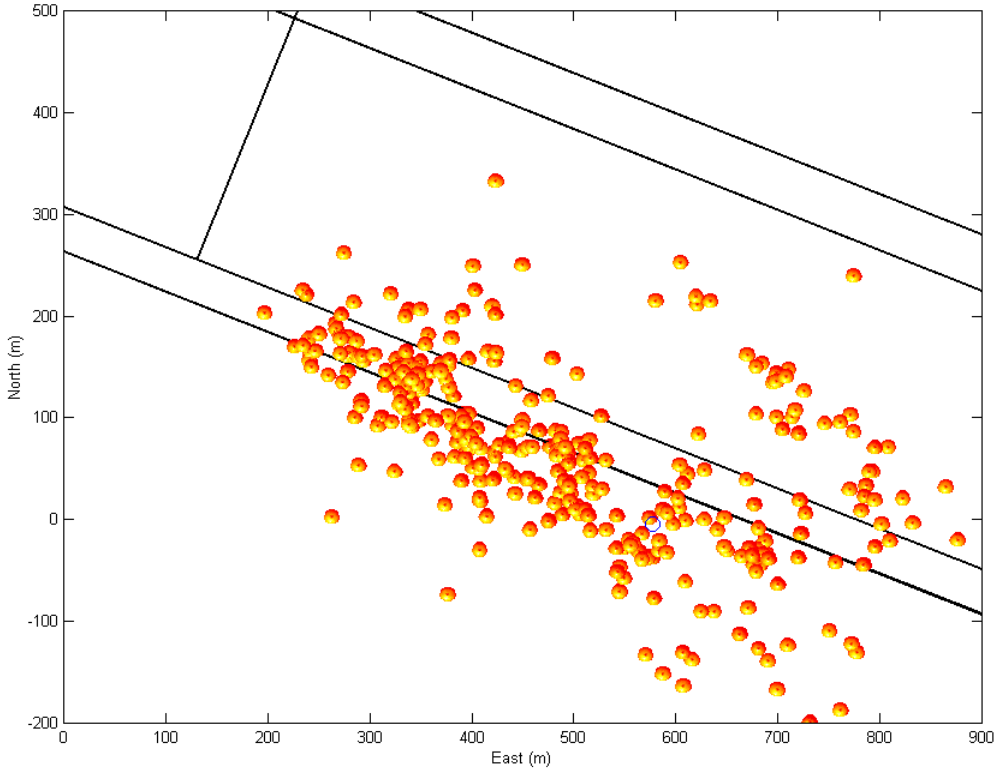

3.3.1 Cants Thorn 1 upper sonde dataset

There were a total of nine sondes used during the first phase of monitoring microseismic activity. Only those in the Cants Thorn 1 borehole had been correctly oriented using test shots. The sondes in the Cants Thorn 2 borehole were not oriented, and the sonde in the Fishponds borehole was oriented using a single event that was recorded on it and one of the Cants Thorn 1 sondes. Of the four sondes in the Cants Thorn 1 borehole, only the upper sonde recorded high quality data, due to increased 50Hz noise being induced on the longer cables to the lower sondes. In all, of the nine sondes only the Cants Thorn 1 upper sonde gave a dataset that could be analysed in detail to give results with an acceptable confidence.

The locations of all events recorded by the Cants Thorn 1 upper sonde are shown as figures 3.6 to 3.9. Figure 3.6 shows a plan view of the event locations. Each sphere represents an individual event. The circle shows the location of the Cants Thorn 1 upper sonde. The thick lines show the position of the main and tail gates, and the face starting position. The direction of face advance was approximately ESE. Figure 3.7 shows a sectional view looking along the direction of face advance i.e. looking ESE. The thick black line marks the seam being mined. Figure 3.8 shows a sectional view looking perpendicular to the direction of face advance i.e. looking NNE. Figure 3.9 shows a three-dimensional view of the event locations. The events cluster above the tail gate in a manner which was suggested by the locations derived from the Fishponds data but are much more tightly grouped.

The event location errors are not represented on figures 3.6 to 3.9. The estimated event location errors need to be considered when making an interpretation of the locations of recorded microseismic events. One way to do this is to plot an error volume for each event. An event location that has errors in polar co-ordinates will have an error volume in the shape of a truncated cone. The error volume can be plotted for polar co-ordinate errors of one standard deviation, and this will make the error volume a 68% confidence volume i.e. there is a 68% chance that the actual event location is within the volume plotted. Such plots for the Cants Thorn 1 upper sonde dataset are shown as figures 3.10 to 3.13. Error volumes are only plotted for events that have azimuth and elevation errors of less than 5°. Plotting error volumes for events with large azimuth and elevation errors makes the plots very difficult to understand as they obscure the most important information. In these plots it is the smallest volumes, relating to event locations with small errors, that are of the greatest importance. Figure 3.10 shows the same plan view as figure 3.6. Figures 3.11 and 3.12 show sectional views looking in the same directions as those shown as figures 3.7 and 3.8 respectively. Figure 3.13 shows the same three-dimensional view as figure 3.9.

Figure 3.6 Plan view of the locations of microseismic events recorded by Cants Thorn 1 upper sonde during the first phase of monitoring.

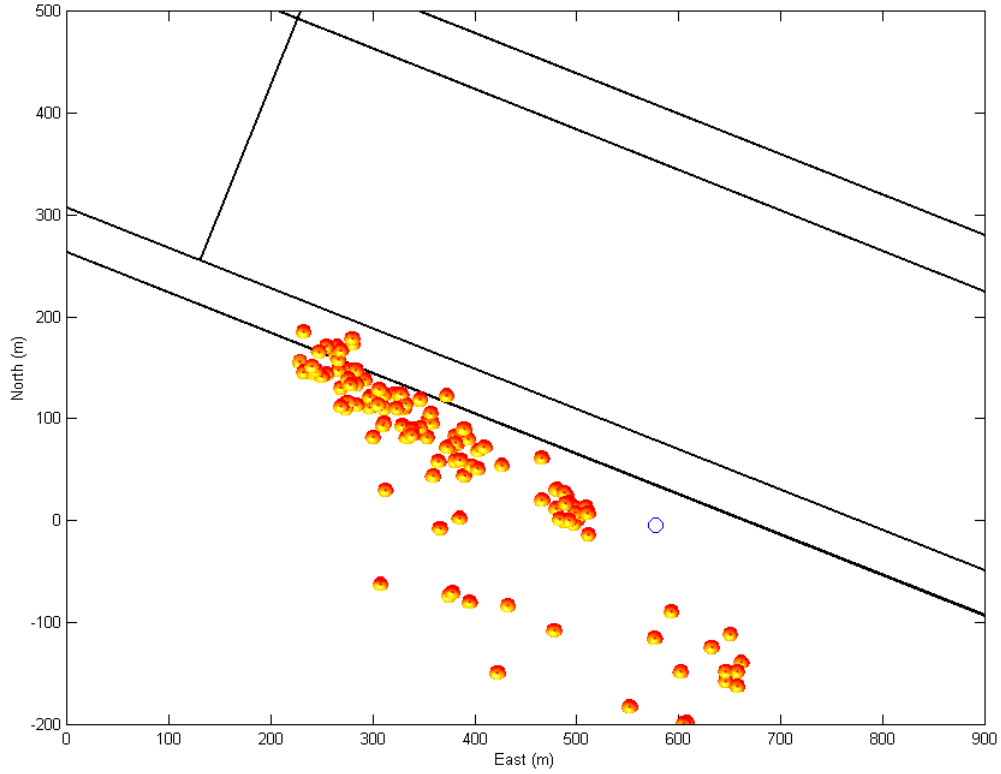

Figure 3.7 Sectional view of the locations of microseismic events recorded by Cants Thorn 1 upper sonde during the first phase of monitoring, looking perpendicular to the direction of face advance. Face advance is left to right on this plot.

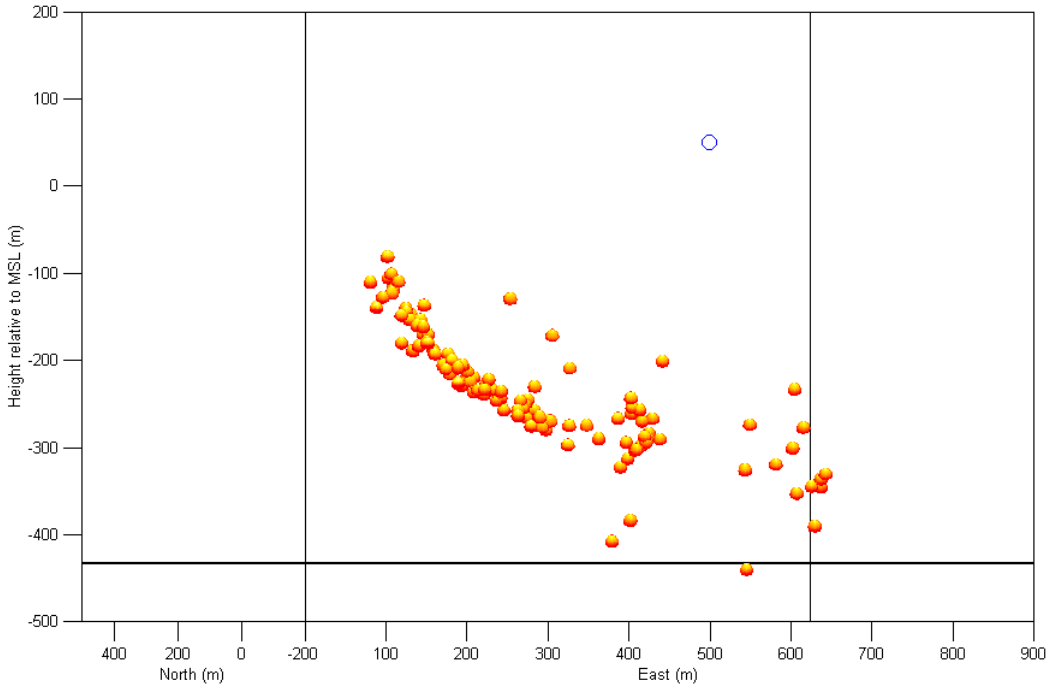

Figure 3.8 Sectional view of the locations of microseismic events recorded by Cants Thorn 1 upper sonde during the first phase of monitoring, looking in the direction of face advance. Face advance is into the page on this plot.

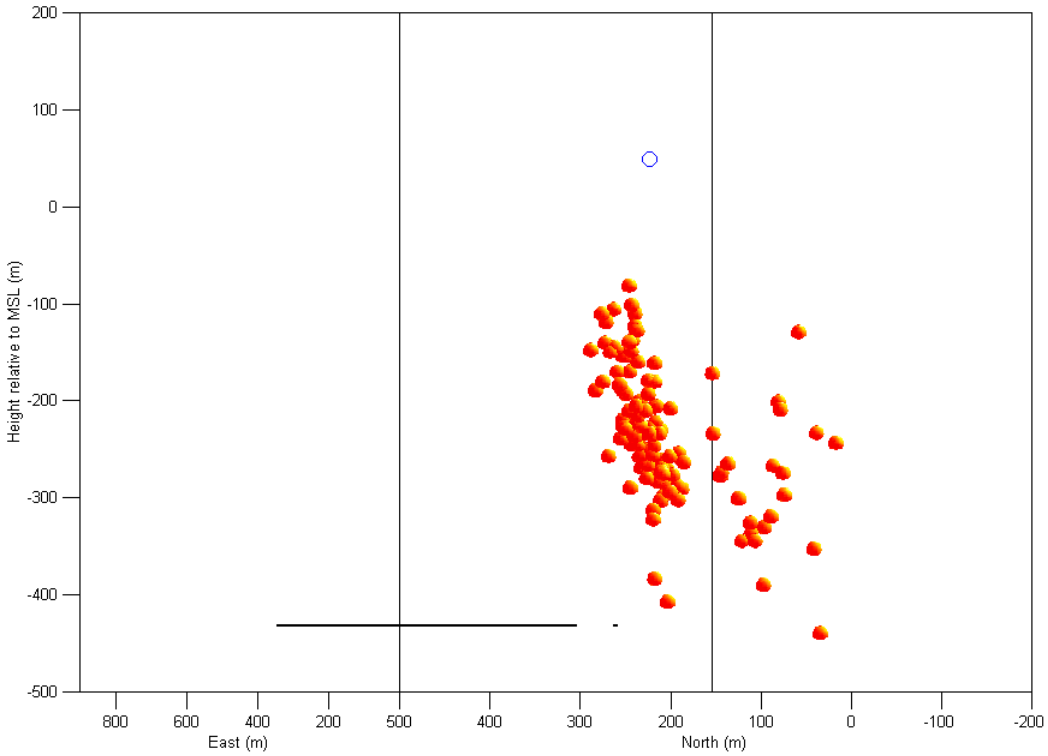

Figure 3.9 3-D view of the locations of microseismic events recorded by Cants Thorn 1 upper sonde during the first phase of monitoring.

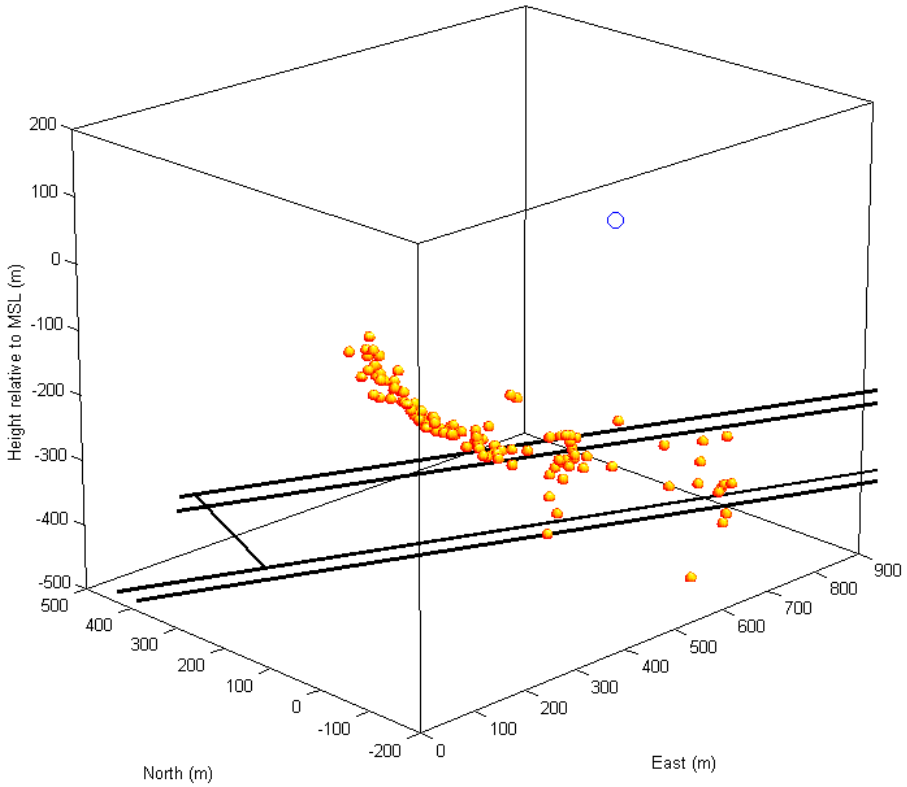

Figure 3.10 Plan view of the estimated one standard deviation location error volumes of microseismic events recorded by Cants Thorn 1 upper sonde during the first phase of monitoring. Error volumes are only shown for event locations with azimuth and elevation errors less than 5°.

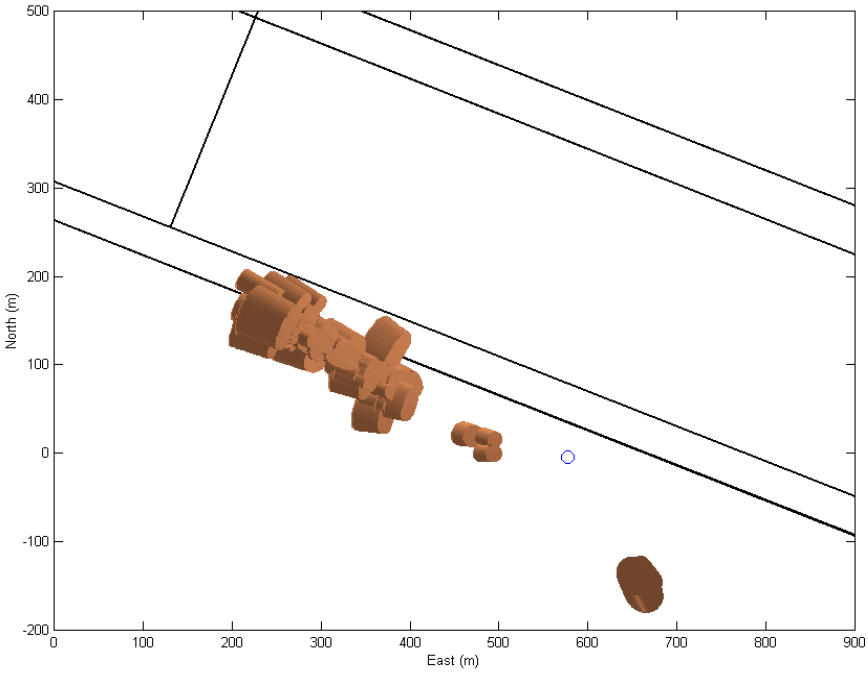

Figure 3.11 Sectional view of the estimated one standard deviation location error volumes of microseismic events recorded by Cants Thorn 1 upper sonde during the first phase of monitoring, looking perpendicular to the direction of face advance. Face advance is left to right on this plot. Error volumes are only shown for event locations with azimuth and elevation errors less than 5°.

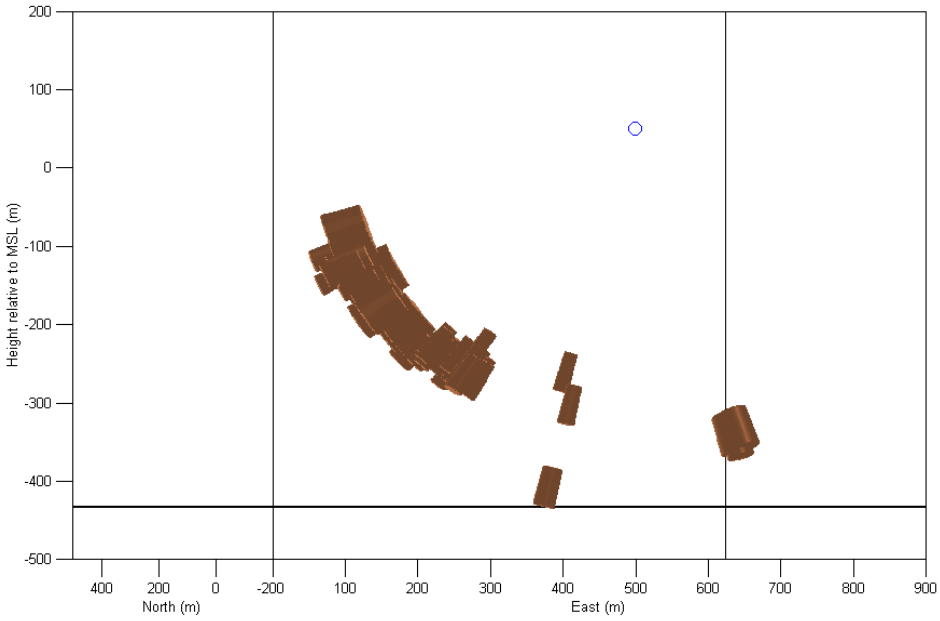

Figure 3.12 Sectional view of the estimated one standard deviation location error volumes of microseismic events recorded by Cants Thorn 1 upper sonde during the first phase of monitoring, looking in the direction of face advance. Face advance is into the page on this plot. Error volumes are only shown for event locations with azimuth and elevation errors less than 5°.

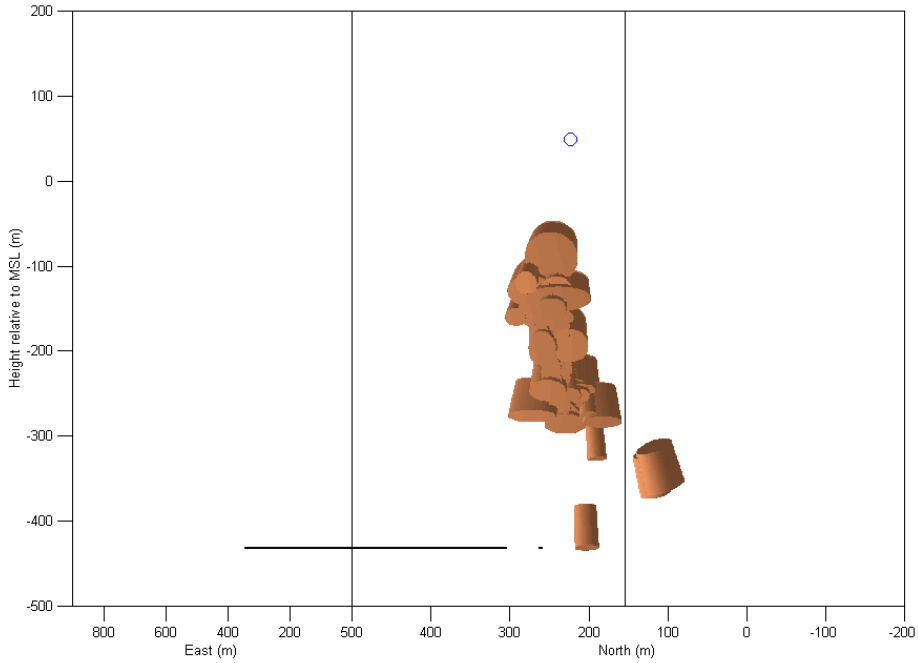

Figure 3.13 3-D view of the estimated one standard deviation location error volumes of microseismic events recorded by Cants Thorn 1 upper sonde during the first phase of monitoring. Error volumes are only shown for event locations with azimuth and elevation errors less than 5°.

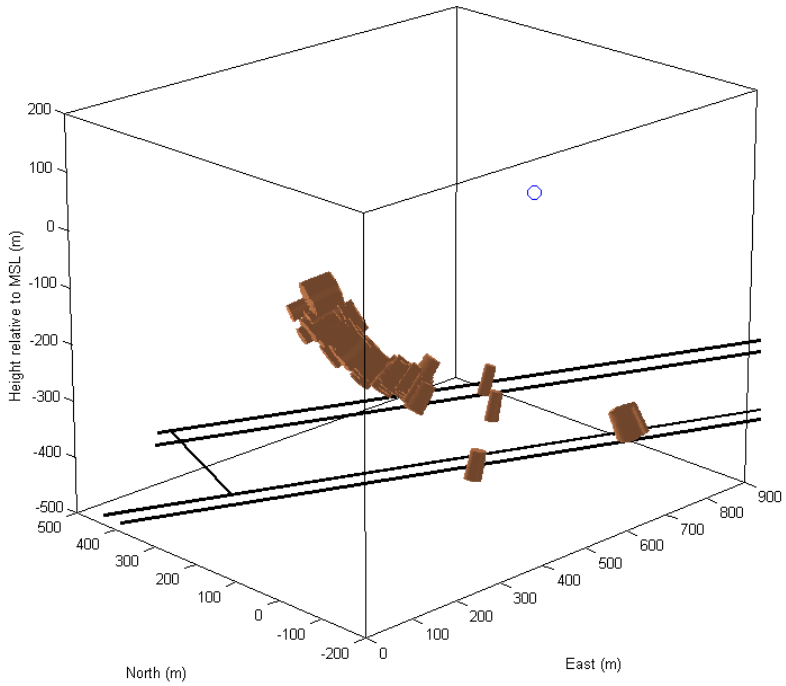

The most striking feature of the observed seismic activity is that it is totally different from the kind of activity observed during most studies of longwall coal mines [e.g. *Toon and Styles*, 1993; *Hatherley et al*, 1997], and the typical activity predicted by rock mechanical modelling [e.g. *Gale and Nemcik*, 1998]. Most seismic activity would be expected to occur in the region of the face, but this is definitely not the case here. In fact, there was no observed seismic activity above the panel being mined. The atypical nature of the observed seismic activity means that the rock mass surrounding the face is not behaving in the way predicted by rock mechanical models for continuous roof collapse, or studies of other mines. An appreciable difference between predicted and observed behaviour of the rock mass could adversely affect the safety of the mine since the mining strategy is planned with only the predicted behaviour being considered.

It is possible that the Cants Thorn 1 upper sonde cannot record seismic events that are located in the vicinity of the face. The seismic events that have been recorded are located predominantly to the South of the panel, the same side as the sonde. However, these events show a range of azimuths relative to the sonde that cover about 240°. This, and the fact that there is no known difference in geological conditions above the panel, makes it hard to see why events located above the panel would not be recorded by the Cants Thorn 1 upper sonde. One explanation could be that seismic events occurring above the panel have much smaller magnitudes than those recorded, and hence the seismic waves generated would have smaller amplitudes. This may be expected given the modelling results of *North and Jeffrey* [1991] (see section 2.3.2) who find that the strains above the edges of the panel are larger than above the centre of the panel. The smaller amplitude waves would mean a smaller signal to noise ratio, making it less likely that the event would be recorded. The problem with this explanation is that earthquake magnitudes follow a power law distribution, and there would be the occasional larger magnitude seismic event that should be recorded.

The seismic activity that was recorded is very different from what would be expected, regardless of whether or not some activity has not been recorded. The seismic event locations are concentrated in clusters, rather than being randomly distributed

throughout the rock mass. This implies that the seismic activity is occurring on discrete structures, and not throughout the rockmass. Most of the seismic events recorded are located in a very large cluster above the tail gate. This large cluster is between 100m and 300m above the seam, which means it begins in the Sherwood Sandstone aquifer and extends upwards. The cluster dips in the direction of mining at about 40° below the horizontal. At the lowest point there is a region of seismic activity that extends down from there almost to seam level. Thus there will be a fractured region extending from the aquifer down to seam level. This region will act as a pathway for water in the aquifer to travel down to the seam, and possibly lead to flooding of the mine.

The observed seismicity shown as figure 3.8 is very different to the fracture patterns obtained from physical models [*Sun et al*., 1992b], shown as figures 2.3 and 2.4. The edge of the model fractured zone above the panel has an approximately vertical orientation, and the same orientation is shown by the observed seismicity. However, there is no seismic evidence of the horizontal fractures above the panel that are shown in figure 2.3.

The pattern shown by the seismic events in figure 3.7 is very similar to the modelled fracture patterns for periodic weightings in moderate strength rock [*Gale and Nemcik*, figure 4, 1998], i.e. a fracture dipping in the direction of mining high above the face, and a vertical fracture connecting it to the face. A weighting is the sudden collapse of a large block of roof, which can have the effect of crushing the hydraulic rams that support the roof in the vicinity of the face making further extraction impossible until some remedial work can be carried out. Severe weightings can compromise the safety and economical viability of a mine. Periodic weightings were experienced at Asfordby, and were one of the problems that lead to the abandonment of the face. The correlation between the frequency of seismic events and problems experienced at the face has already been shown in section 2.6. It is possible by looking how the locations of seismic events change with time to make a further examination of this correlation. In particular, does the dipping fracture above the face form before the first weightings. If

this is the case, then it could be that the presence of the fracture was indicating that weighting problems would be experienced at some later time.

Figures 3.14 and 3.15 show how the locations of the seismic events changed from weeks 13 through to 26. These figures show a plan view and a three-dimensional view of the locations of events recorded during the respective time period. The amount of face advance during that time period is also shown by the dark rectangle. Very few (<10) seismic events were recorded before week 13. The face became square (i.e. total face advance equals face width) at around this time. The dipping fractured region above the tail gate develops from week 13 onwards. The ESE end of the fractured region, and therefore the lowest part, is being controlled by the face position. As the face advances, the seismicity moves down and to the ESE. The rate of seismic activity stays constant through weeks 13-15, and decreases during weeks 16-17. There is then a large increase in the rate of seismic activity during week 19. The seismic events recorded during week 19 locate along the dipping fractured region, and also form a new cluster at approximately 500m E and 0m N of the origin. This cluster is about 100m above the seam. During weeks 20 and 21 the rate of seismic activity decreased, and most of the recorded seismic events were concentrated in the lower cluster. In week 21, the first event is seen at seam level, directly below this second cluster. Also during week 21 a third cluster of events forms some 200m S of the face. In the weeks 22-26 there are more seismic events occurring between the second cluster and the seam. It was during week 23 that the first major weighting of the face occurred.

Figures 3.14 and 3.15 show that as the face advanced beyond the square position a linear fractured region formed high in the roof above the Sherwood Sandstone. This fractured region dips in the direction of face advance at 40° below the horizontal. As the face advanced, so the fractured region extended down dip. The fractured region extended to about 100m above the seam, the depth of the sandstone. A second fractured region then began to develop vertically down to the seam. Soon after this developed a major weighting event occurred at the face. During weeks 13 to 26 the seismic activity clearly shows the development of a fracture system that matches the

modelled fracture patterns for periodic weightings. Development of this fracture system coincided with the first weighting of the face.

The cluster of events above the tail gate is interpreted to be caused by a major new fracture propagating through the roof. This interpretation agrees with the rock mechanical model of *Gale and Nemcik* [1998] for strong roof conditions and periodic weightings of the face. Another possible interpretation is that there is a pre-existing fault plane where the cluster of seismicity is located, reactivated by the mining activity. The zone of reactivation may be controlled by the face position. This interpretation could equally well explain the observations made of the induced seismic activity, and if correct it would not necessarily support the model of *Gale and Nemcik* [1998]. It is possible that the main cluster of events is delineating the edge of the fracture zone predicted by the physical modelling [*Sun et al.*, 1992a, 1992b], but since there is no seismic evidence for the horizontal fractures above the panel, this interpretation is unlikely.

Figure 3.14 Seismic events recorded at Cants Thorn 1 upper sonde during weeks 13, 14, 15, and 16-17 (top plot week 13 events; bottom plot weeks 16-17 events).

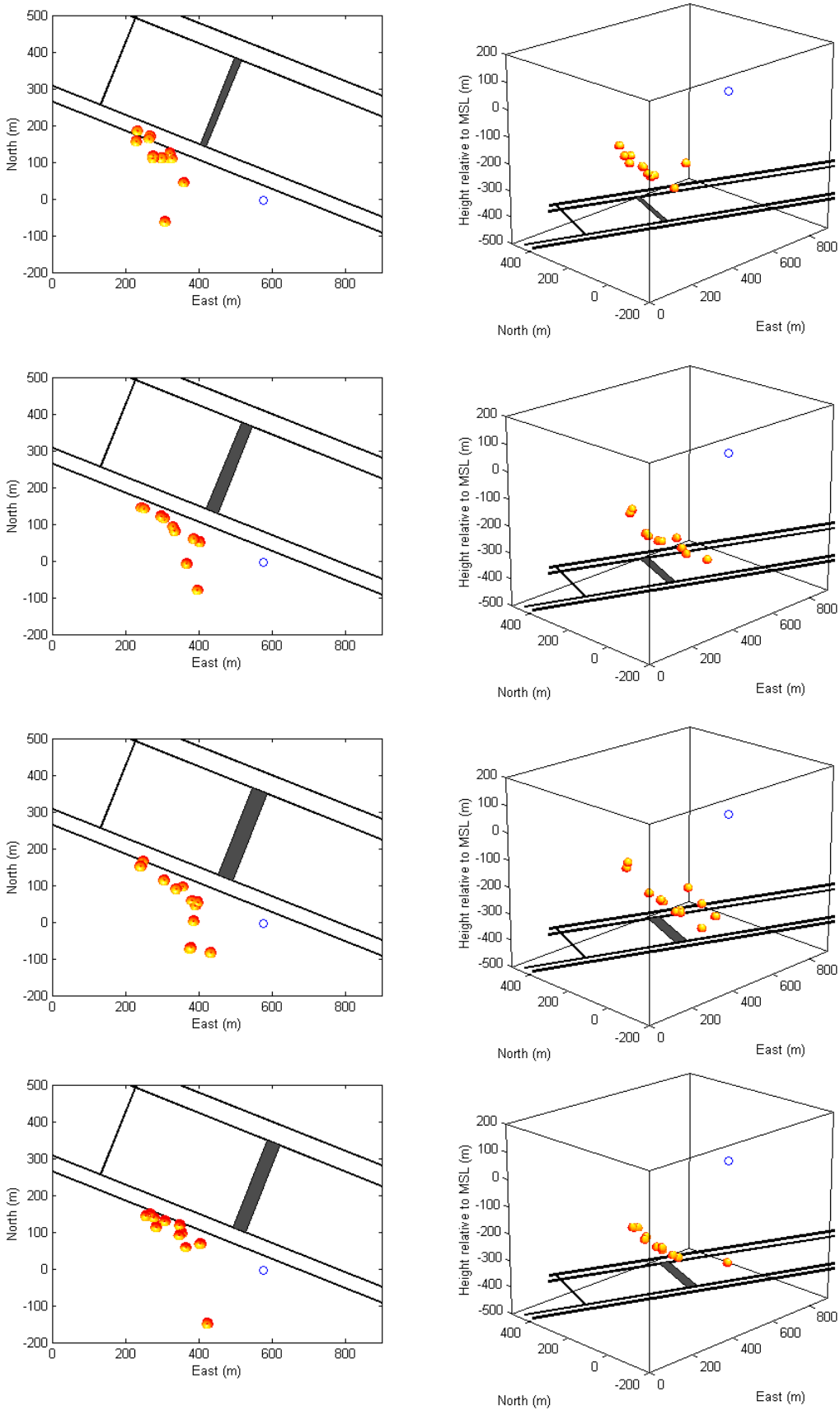

Figure 3.15 Seismic events recorded at Cants Thorn 1 upper sonde during weeks 19, 20, 21, and 22-26 (top plot week 19 events; bottom plot weeks 22-26 events).

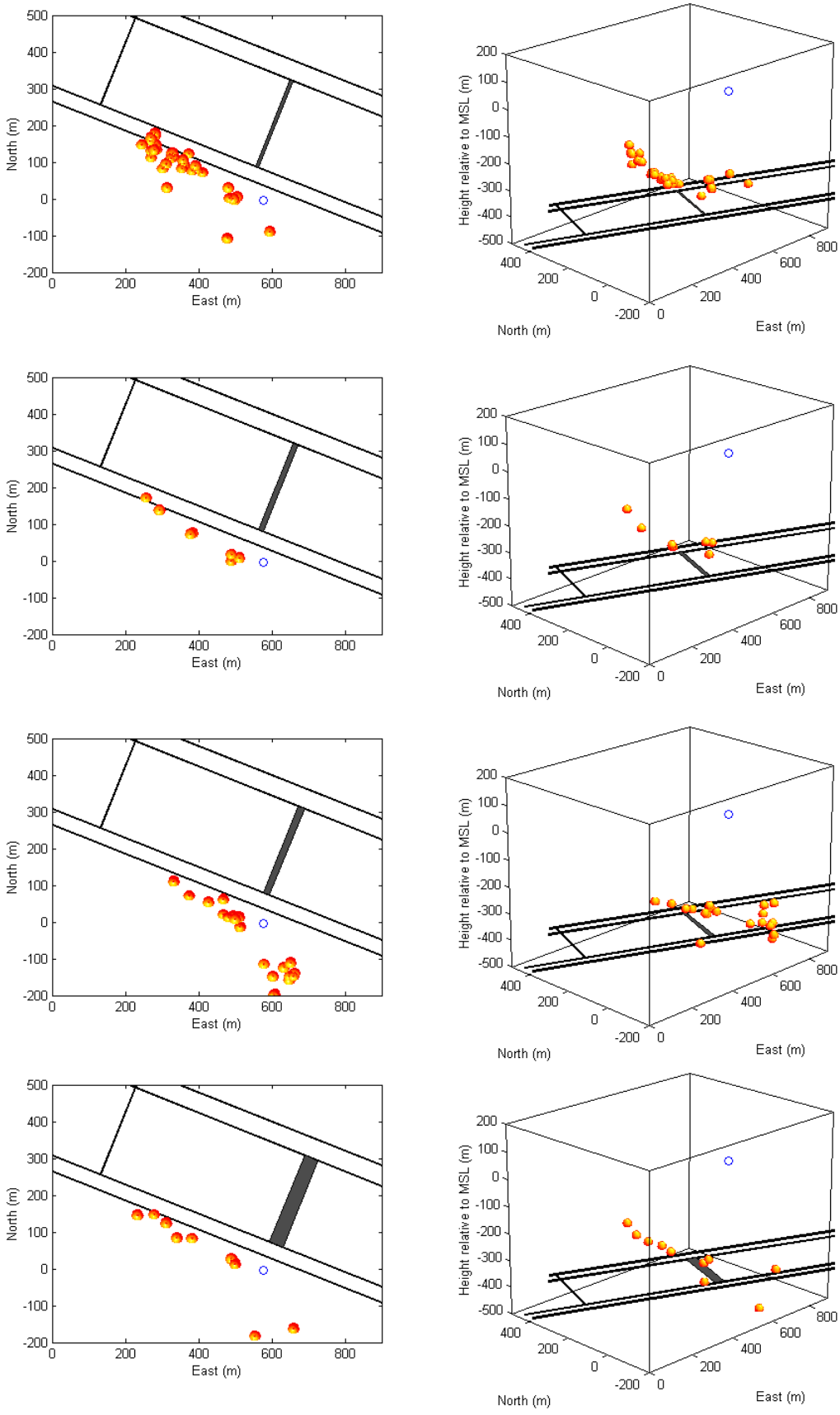

3.4 Locations of microseismic events recorded during second phase of monitoring

3.4.1 Hole 1 dataset

There were two sondes monitoring the second phase of mining, one in Hole 1, and one in Hole 2, both which were located in the cross cuts between the twin tail gates. Each sonde had two three-component sets of geophones being recorded. Hole 1 was closer to the face starting position, and therefore presumably closer to any seismic activity. The Hole 1 sonde recorded the greatest number of events, 141 in total. The data recorded are again of high quality, and locations have been calculated for 135 of the events.

The locations of all analysed events recorded by the Hole 1 sonde are shown as figures 3.17 to 3.20. Each figure shows two plots. The top plot in each figure shows the location of seismic events calculated by analysing one of the three-component seismograms. The bottom plot shows the location of seismic events calculated by analysing the second three-component seismogram. Figure 3.17 shows a plan view. Each sphere represents an individual event. The circle shows the location of the Hole 1 sonde. The thick lines show the position of the main and tail gates, and the face starting position. The direction of face advance was approximately ESE. The wire frame shows the position of a dolerite sill in the roof. Figure 3.18 shows a sectional view looking along the direction of face advance i.e. looking ESE. Figures 3.19 shows a sectional view looking perpendicular to the direction of face advance i.e. looking NNE. The thick black line marks the seam being mined. Figure 3.20 shows a three-dimensional view of the event locations.

Figure 3.17 Plan view of the locations of microseismic events recorded by the Hole 1 sonde during the second phase of monitoring. The top plot shows locations for data recorded on one of the three-component sets of geophones, the bottom plot shows locations for data recorded on the second set.

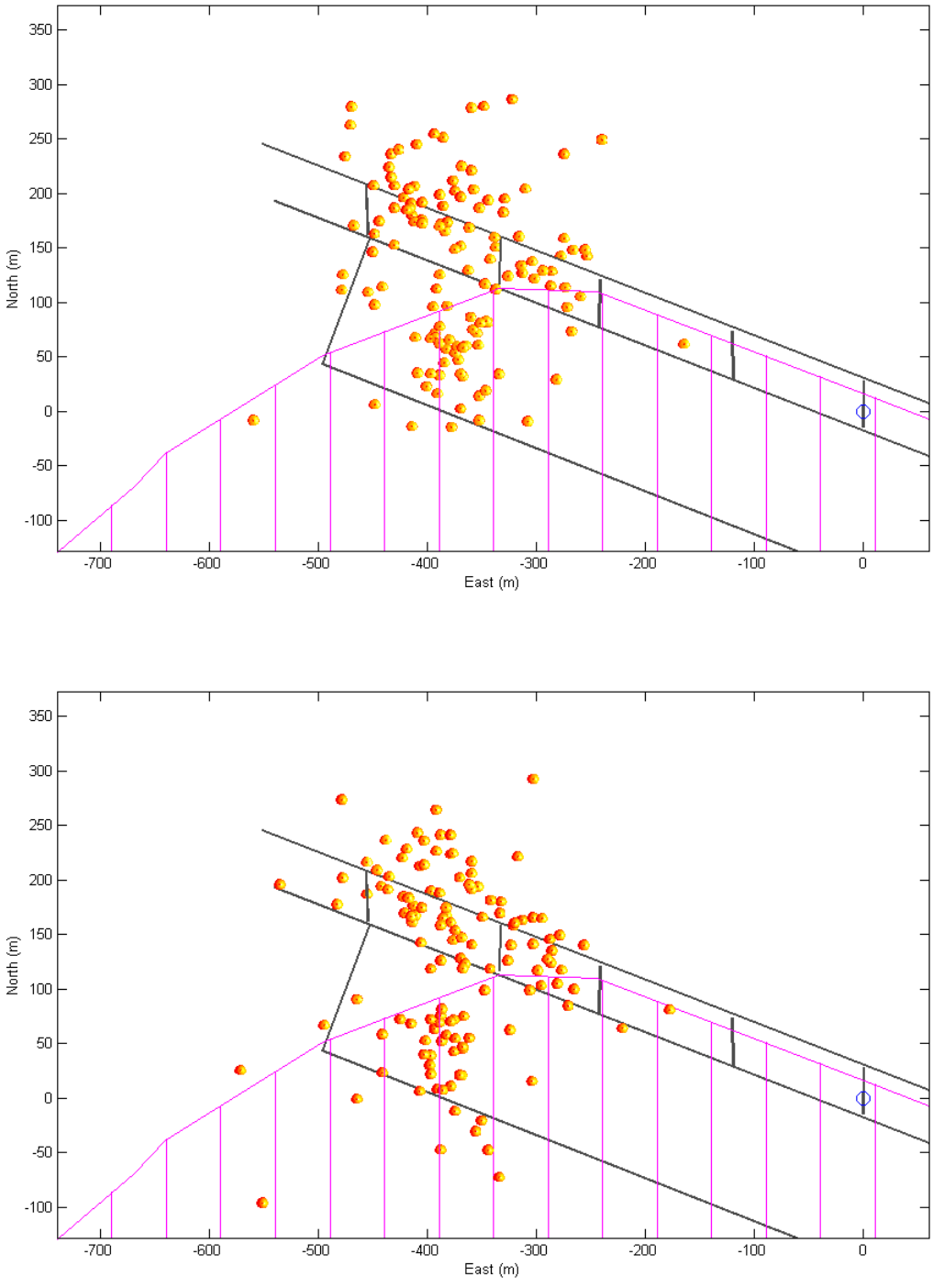

Figure 3.18 Sectional view of the locations of microseismic events recorded by the Hole 1 sonde during the second phase of monitoring, looking perpendicular to the direction of face advance. Face advance is left to right on these plots. The top plot shows locations for data recorded on one of the three-component sets of geophones, the bottom plot shows locations for data recorded on the second set.

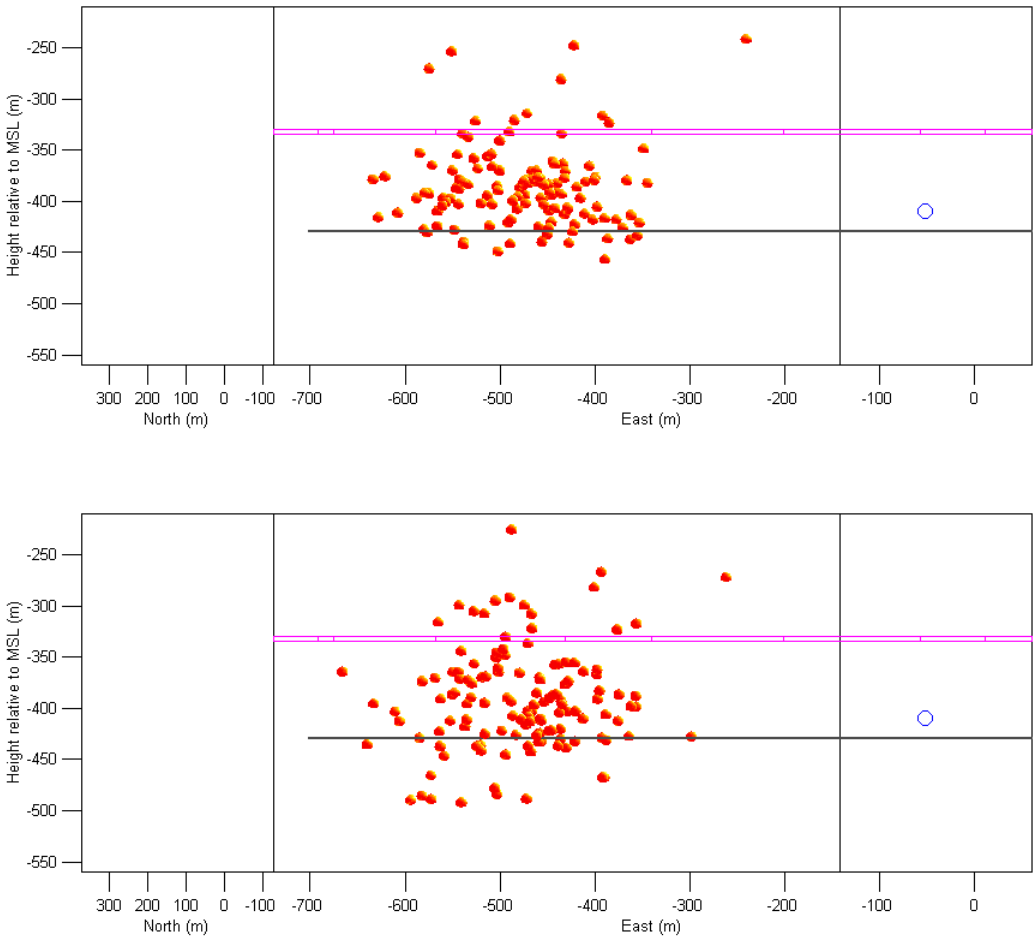

Figure 3.19 Sectional view of the locations of microseismic events recorded by the Hole 1 sonde during the second phase of monitoring, looking in the direction of face advance. Face advance is into the page on these plots. The top plot shows locations for data recorded on one of the three-component sets of geophones, the bottom plot shows locations for data recorded on the second set.

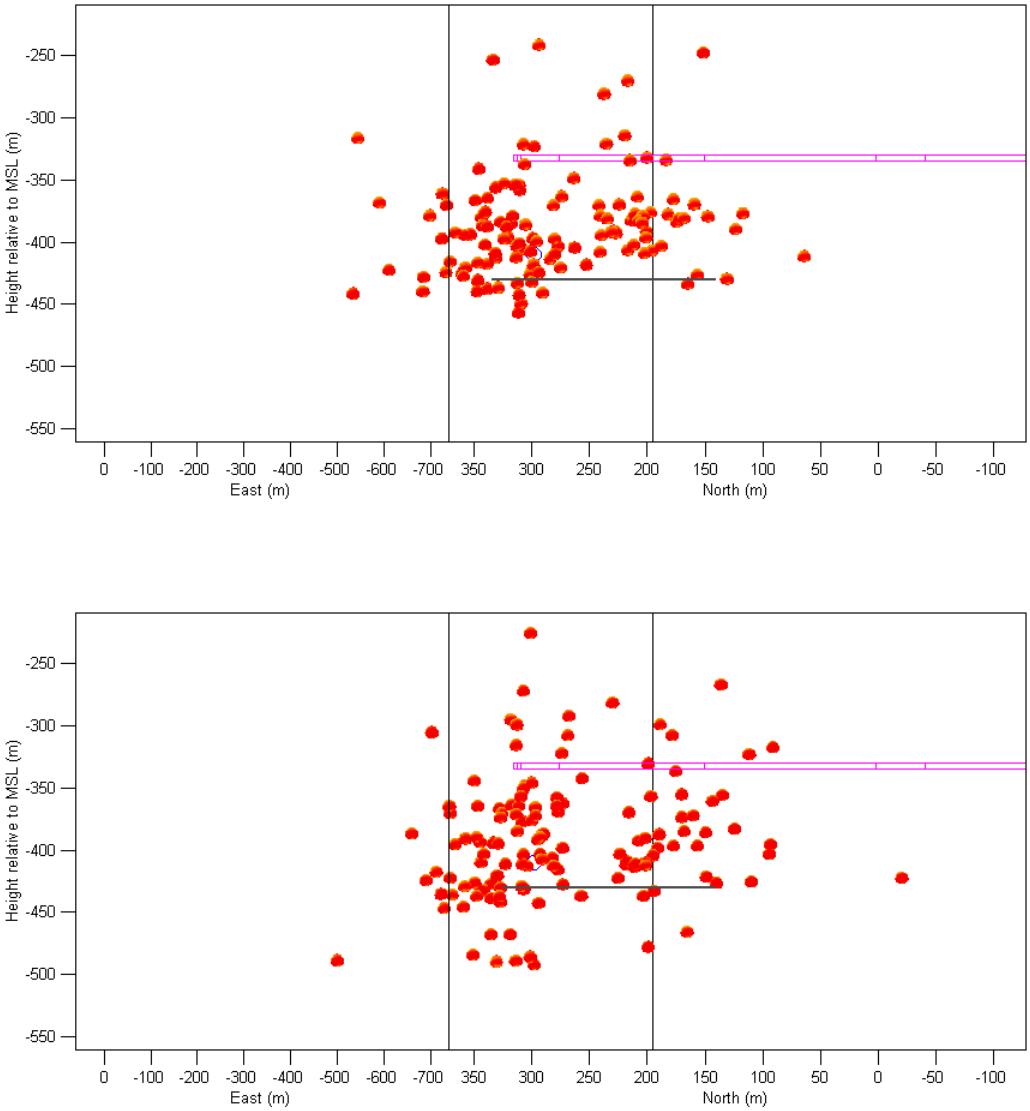

Figure 3.20 3-D view of the locations of microseismic events recorded by the Hole 1 sonde during the second phase of monitoring. The top plot shows locations for data recorded on one of the three-component sets of geophones, the bottom plot shows locations for data recorded on the second set.

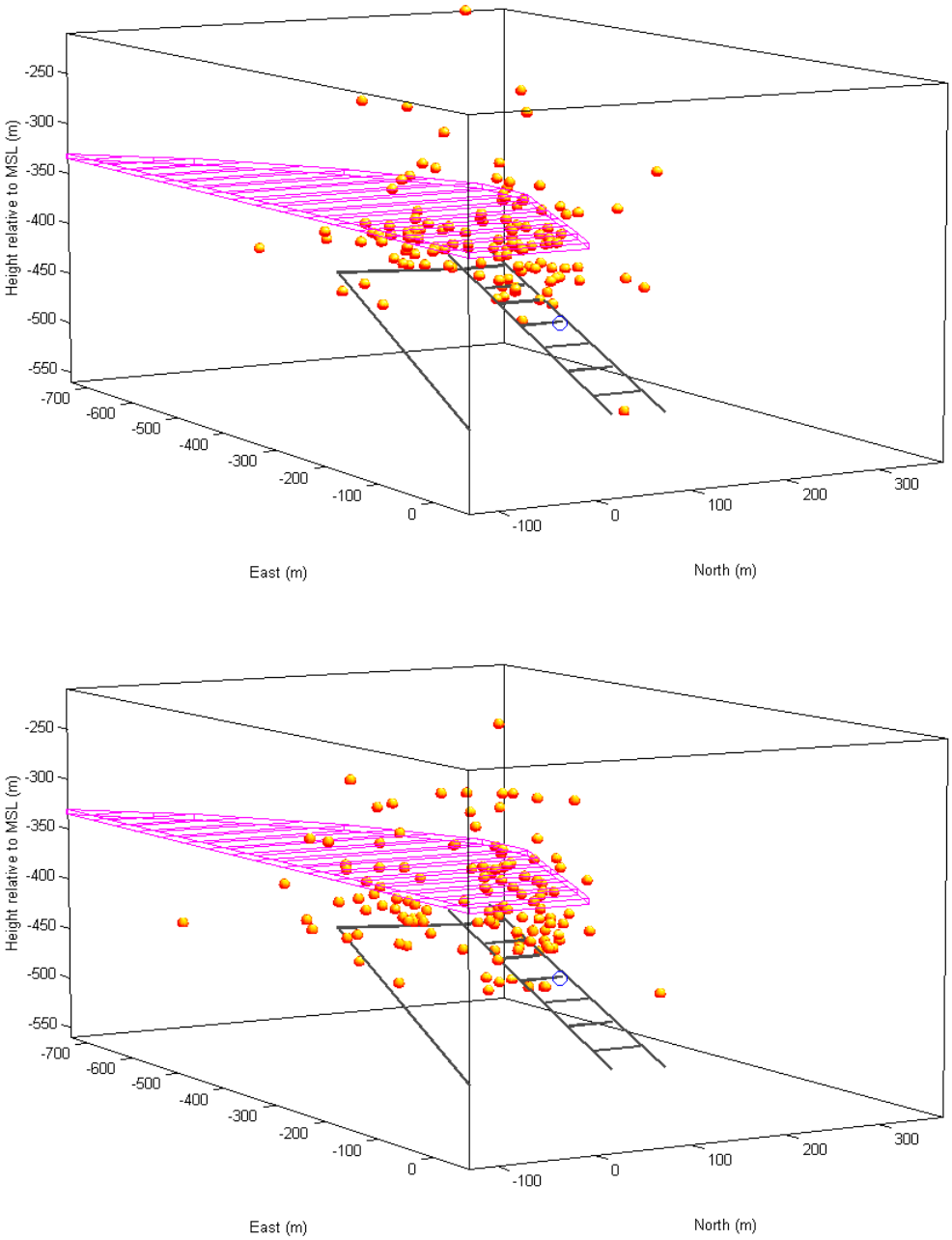

The event location errors are not represented on figures 3.17 to 3.20. As was discussed before, estimated event location errors need to be considered when making an interpretation of the event locations. Plots of the error volumes for one standard deviation errors in polar co-ordinates for the Hole 1 sonde dataset are shown as figures 3.21 to 3.24. These error volumes are therefore equivalent to a 68% confidence limit. Error volumes are only plotted for events that have azimuth and elevation errors of less than 5°. In these plots it is the smallest volumes, relating to event locations with small errors, that are of the greatest importance. Figure 3.21 shows the same plan view as figure 3.17. Figures 3.22 and 3.23 show sectional views looking in the same directions as those shown as figures 3.18 and 3.19 respectively. Figure 3.24 shows the same three-dimensional view as figure 3.20.

The seismic activity is very different from what was observed during the first phase of monitoring. As work began on the face, the seismic events recorded are located in the region of the main gate. The depths of these events ranges from about 30m below the seam to over 100m above the seam. This zone of seismicity does not extend below the sill. As the face approached the position where it became square, another cluster of seismic events began to occur. They are located below the sill, at a range of depths between seam level and about 60m above the seam. By examining the plots showing the estimated error volumes it can be seen that these seismic events form a distinct cluster separate from those occurring above the main gate. The cluster of events below the sill shows several different characteristics from the events above the main gate. The seismic waves generated by the events below the sill have a higher frequency than the waves generated by events above the main gate. Many of the events below the sill have a different P-wave first motion polarity from the other cluster. Both of these differences can be seen in figure 3.25 which shows one-component of the seismogram from an event in the cluster above the main gate, the low frequency event, and the same component from an event in the cluster under the sill, the high frequency event. Time series are shown on the left, and power spectra are shown on the right. The power spectra both have large peaks at 50Hz, which shows not all 50Hz noise has been removed. Both events also show large peaks at another frequency, and this is the dominant frequency of the seismic waves. The low frequency event shown in figure

3.25 has a dominant frequency of about 32Hz, and the high frequency event has a dominant frequency of about 80Hz. The amplitudes of the seismic waves are similar, although the low frequency event seismogram has slightly lower amplitude.

Figure 3.21 Plan view of the estimated one standard deviation location error volumes of microseismic events recorded by the Hole 1 sonde during the second phase of monitoring. The top plot shows locations for data recorded on one of the three-component sets of geophones, the bottom plot shows locations for data recorded on the second set.

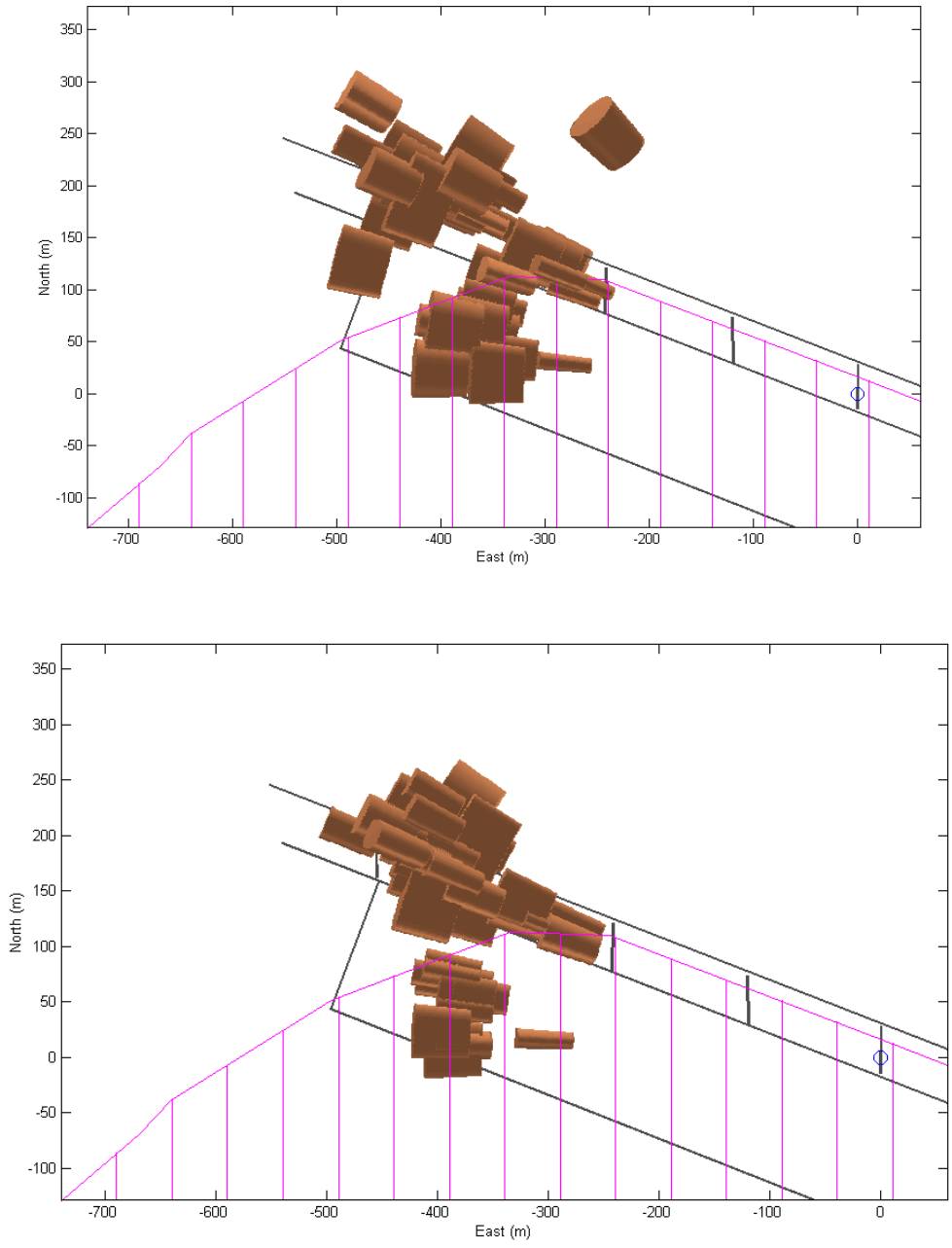

Figure 3.22 Sectional view of the estimated one standard deviation location error volumes of microseismic events recorded by the Hole 1 sonde during the second phase of monitoring, looking perpendicular to the direction of face advance. Face advance is left to right on these plots. The top plot shows locations for data recorded on one of the three-component sets of geophones, the bottom plot shows locations for data recorded on the second set.

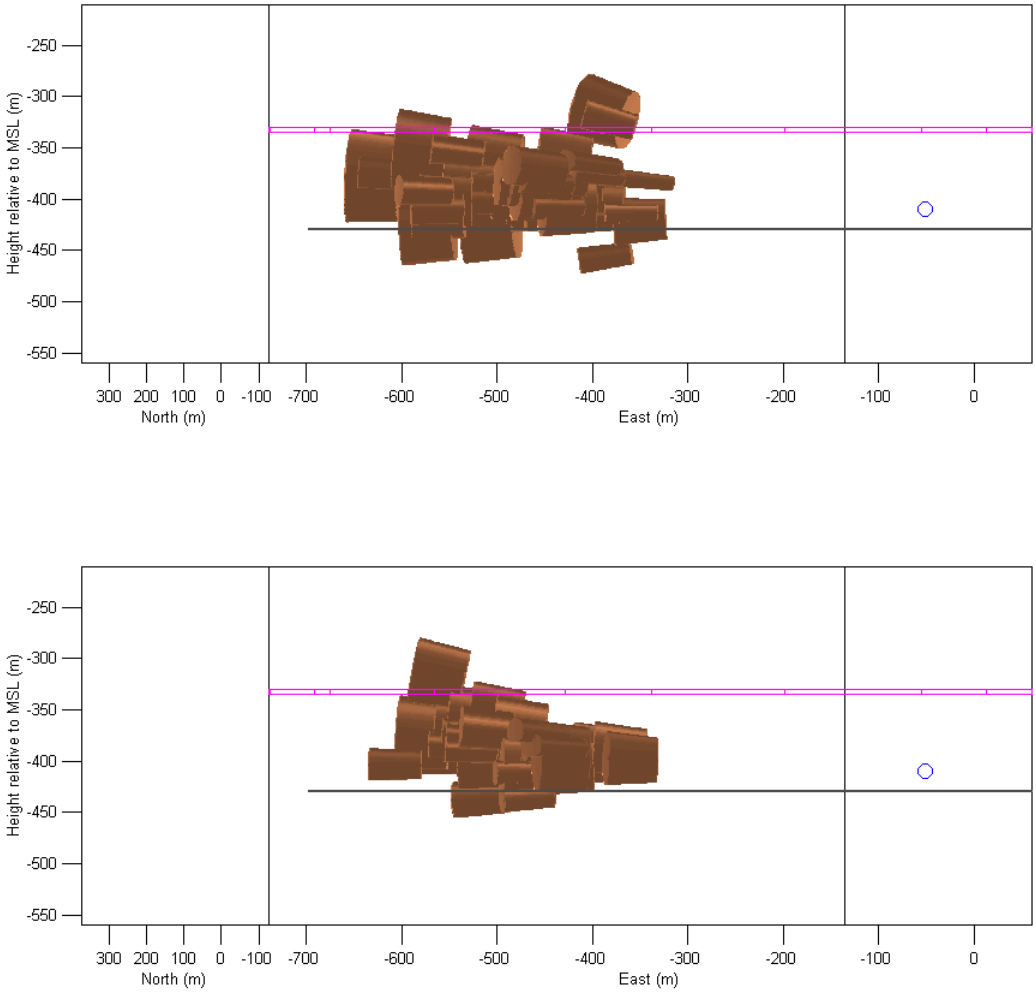

Figure 3.23 Sectional view of the estimated one standard deviation location error volumes of microseismic events recorded by the Hole 1 sonde during the second phase of monitoring, looking in the direction of face advance. Face advance is into the page on these plots. The top plot shows locations for data recorded on one of the three-component sets of geophones, the bottom plot shows locations for data recorded on the second set.

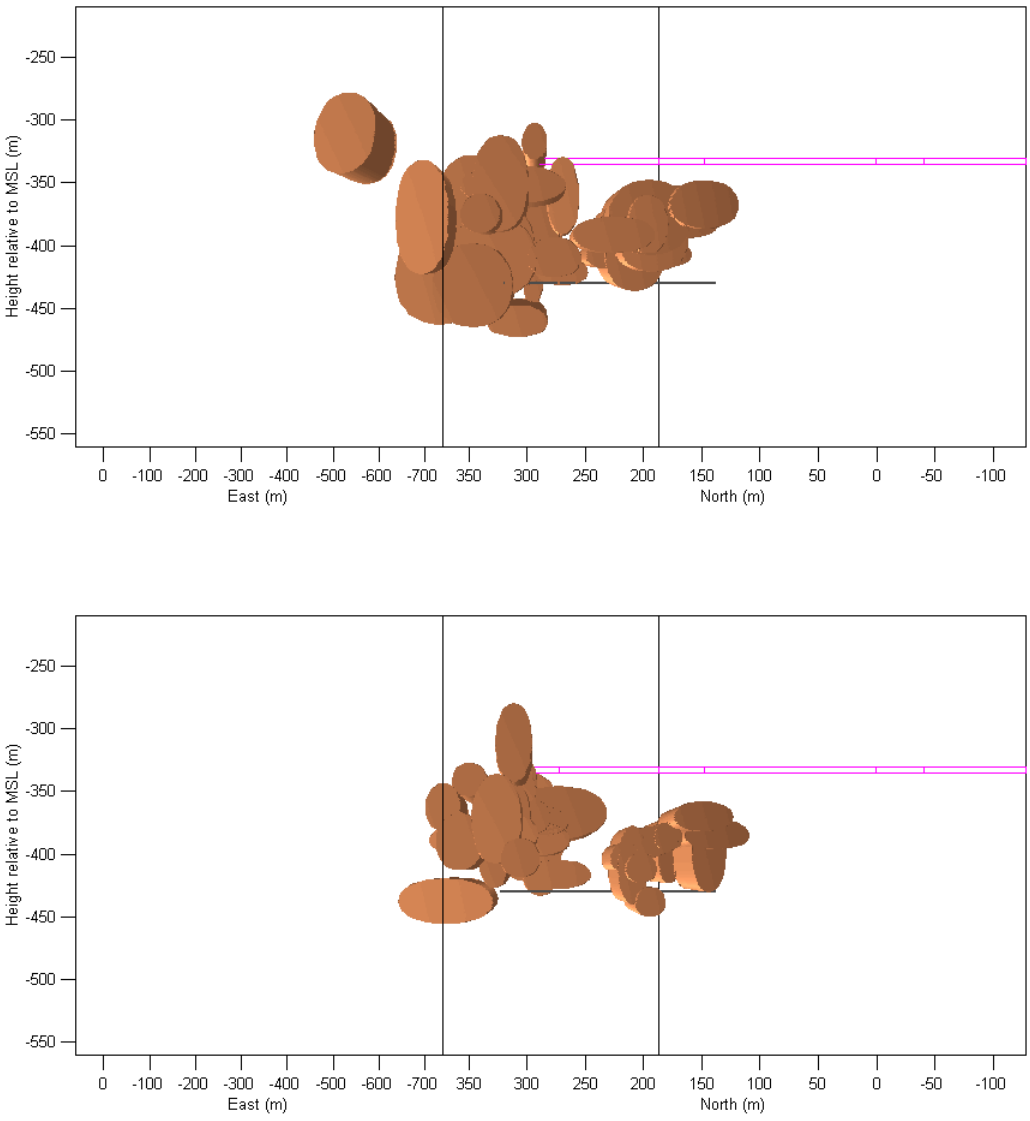

Figure 3.24 3-D view of the estimated one standard deviation location error volumes of microseismic events recorded by the Hole 1 sonde during the second phase of monitoring. The top plot shows locations for data recorded on one of the three-component sets of geophones, the bottom plot shows locations for data recorded on the second set.

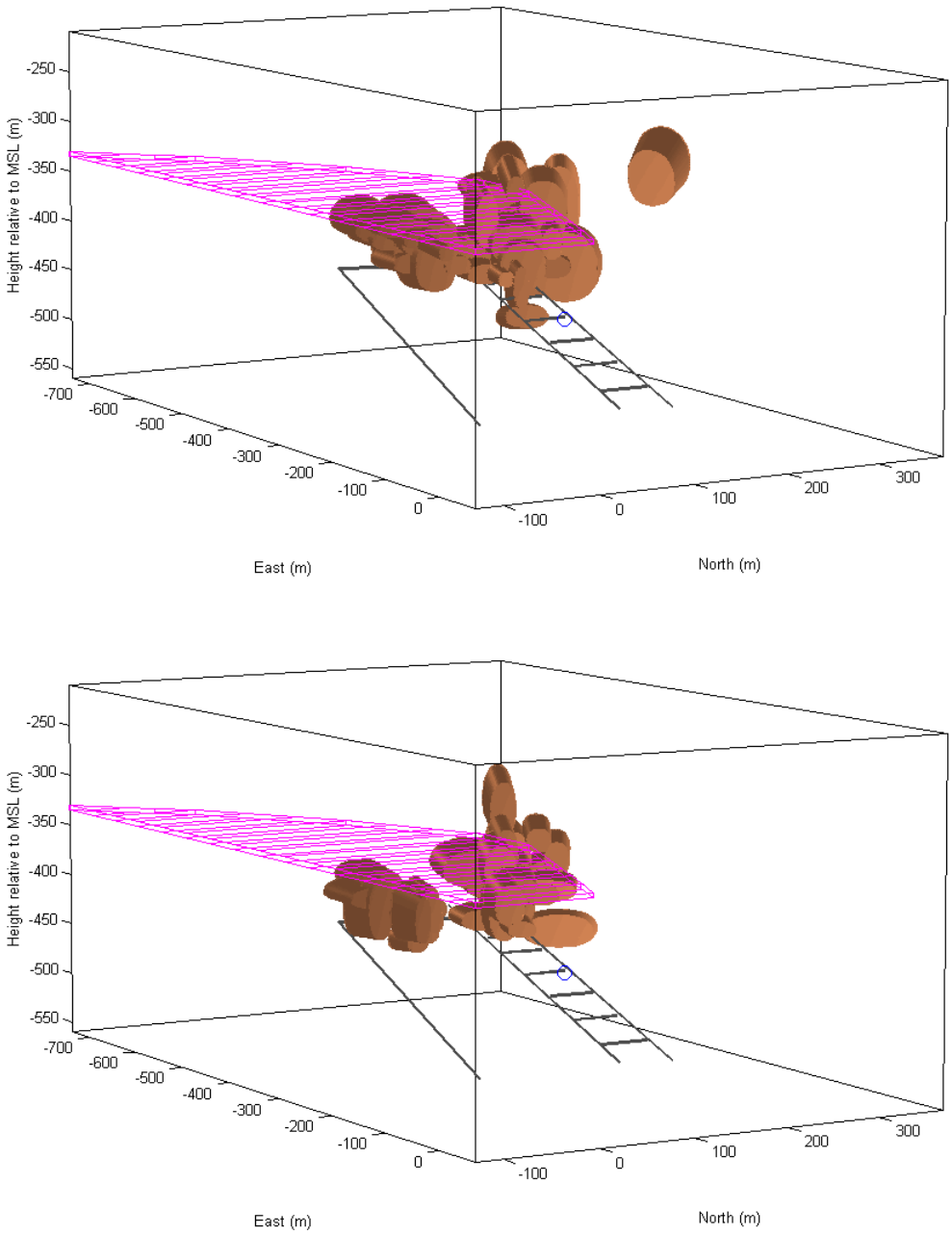

Figure 3.25 The different characteristics shown by the two clusters of events observed during the second phase of monitoring. The left hand plots show the time series, the right hand plots show power spectra. The top plots are for the low frequency event, the bottom plots are for the high frequency event.

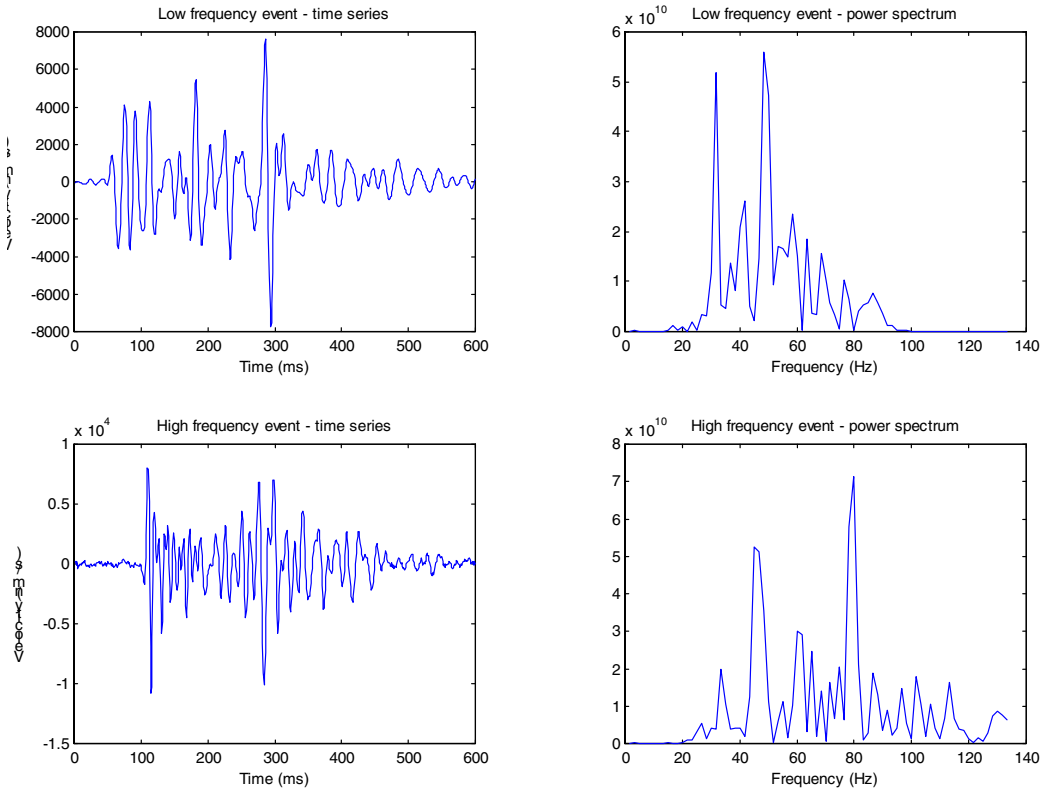

The location of seismic events is again not what might be expected given the results of similar studies. An increase in seismicity as the face becomes square is commonly observed. The events below the sill start to occur as the face approaches becoming square, and these show the most similarity to the results of other studies [e.g. *Hatherley et al.*, 1997]. Figure 3.19 shows that the observed seismicity has some of the characteristics of the physically modelled fracture patterns [*Sun et al.*, 1992a, 1992b]. Most seismic activity occurs above the main gate, with some activity occurring above the panel, which might be expected given the modelled fracture pattern shown as figures 2.3 and 2.4. The results of the first phase of monitoring showed large amounts of seismicity above the tail gate, but at greater heights above the seam. It is perhaps the case that the geological structure of this mine is such that most seismicity occurs above the edges of the working panel, and not towards the centre. Again this might be expected given the physically modelled fracture patterns shown as figures 2.3 and 2.4.

The strong sandstone in the roof could cause this as it holds up the roof then fractures and collapses in large blocks. This would explain the problems the mine experienced with periodic weightings of the face. The sill above the panel being worked in the second phase is closer to the seam than the sandstone. This may make the roof less susceptible to weightings. The sill does not span the entire face, which means supporting beams of dolerite cannot be left in place to hold up the roof. Supporting beams of a strong layer in the roof are a cause of weightings [*Minney et al.*, 1997]. It may be, then, that the presence of the sill above the face, but not spanning it, and below the sandstone means that the severe weightings experienced during Phase-One will not occur during Phase-Two. The seismicity above the panel observed during Phase-Two would imply that any blocks of intact roof rock that are forming do not extend far into the roof, at the most 40m above the seam. Thus the roof collapses in a more controlled manner, and the severe weighting events of Phase-One are not experienced during Phase-Two.

The observed seismic activity is more diffuse than that observed during the first phase of monitoring. The seismicity is still clustered into regions of dense seismic activity and regions of no seismic activity, but no distinct structures can be seen in the clouds of seismic events. The activity does not extend as far above the seam as that observed during the first phase. There are no seismic events observed at the height above the seam of the sandstone. The height into the roof that mining induced seismic activity extends is controlled by the width of the panel being mined [*Choi and McCain*, 1982; *Bieniawski*, 1987; *Peng and Chiang*, 1984; *Follington*, 1988]. The face width for the second phase is 120m, half that of the first phase, which is 240m. This explains why the seismicity does not extend as high into the roof, although it is possible that the sonde being located nearer to the seam level means it does not record events high in the roof.

Comparing the event locations calculated by analysing the two three-component sets of data recorded by the one sonde highlights the fact that interpretation needs to be made by considering the patterns of locations, and not individual events. The overall picture shown by the two plots in figures 3.17 to 3.20 is the same, although there are

many individual events that do not match up. A similar conclusion can be made after examining the plots of error volumes, although it must be remembered that event locations with large errors are not shown on these plots. An analysis similar to that summarised in table 3.5 shows that the error volumes calculated by analysing both three-component sets from one sonde overlap, as would be expected.

3.4.2 Hole 2 dataset

Fewer events were recorded by the Hole 2 sonde, only 29 in total. Fewer events were recorded because Hole 2 was farther away from the mining activity than Hole 1. Locations are calculated for all of these events. Twenty of the 29 events were recorded at Hole 1 also. The seismic data recorded at Hole 2 for these events is used along with the seismic data recorded at Hole 1 to test the accuracy of the event location method (see section 3.2.2). The results of this test show that the calculated locations of the events recorded at Hole 2 are the same within estimated error bounds as the calculated locations of the same events recorded at Hole 1. Thus the location of the seismic activity recorded at Hole 2 shows the same patterns as the activity recorded at Hole 1. These patterns are far better shown by the Hole 1 data because of the larger number of events, and they are described in detail above. The calculated locations of the events recorded at Hole 2 are not shown here for this reason.

3.5 Conclusions

The usefulness of the seismic event location technique described here has been demonstrated in previous studies e.g. *Toon and Styles* [1993]. The inclusion of error estimation has allowed more informed interpretations to be made, and patterns of seismicity due to geological structures and patterns due to location errors can be distinguished.

The locations of microseismic events recorded during Phase-One of monitoring show patterns that might be expected for strong roof conditions with periodic weightings of the face [*Gale and Nemcik*, 1998]. Fracturing of the aquifer is identified, and fluid pathways can be traced from the aquifer down to seam level, which explains the

flooding at the face. The location of seismic activity shows that the rock mass surrounding the mine is not behaving in the expected way, leading to the problems experienced and the eventual abandonment of the face and the mine at a cost of £400M.

The seismicity recorded during the second phase of monitoring shows different features to that of the first phase. This is due to the narrower face width, and the presence of a dolerite sill above the face. As the face moved below the sill, the patterns of seismicity observed are comparable to the patterns observed by other studies where roof collapse was continuous [e.g. *Toon and Styles*, 1993; *Hatherley et al.*, 1997]. Also, the location of seismic activity shows similarities to the fracture patterns predicted by physical models of the Asfordby stratigraphy [*Sun et al*., 1992a, 1992b]. The seismic activity implies that the roof is collapsing in a more expected fashion, and no weightings as serious as those experienced during Phase-One will be experienced. This is explained by the strong layer of the sill being below the sandstone thus inhibiting the formation of sandstone beams supporting large blocks of roof and causing weightings.

The locations of the recorded seismic events show the differences between the two phases of mining and explain why the mine experienced the problems it did. Comparison of the observed seismic activity with rock mechanical models and previous studies further explained the behaviour of the rock mass. The seismic activity in general shows strikingly different characteristics to what would be expected based on previous studies and rock mechanical models. One rock mechanical model that could adequately explain some of the observations made during Phase-One was that of *Gale and Nemcik* [1998] for strong roof conditions and periodic weightings of the face. This model also agrees with the conditions experienced at the face i.e. periodic weightings. However this model was not considered when the mining strategy for Asfordby was planned. Thus the possible problems that would be experienced were not known about until they occurred. The induced seismicity that is observed shows similarities to the situation modelled by *Gale and Nemcik* [1998] several weeks before the first weighting of the face. Near real-time processing of the seismic data may have

given enough warning of a possible weighting that the mining strategy could be altered so as to control the problem. The observations made during Phase-Two imply that the rock mass is behaving in the manner predicted by the physical modelling of *Sun et al.* [1992a, 1992b]. Although poor roof and face conditions were experienced during Phase-Two, they were not as serious as the conditions experienced during Phase-One (e.g. weightings, flooding), which is reflected by the seismic activity showing some patterns predicted by modelling and analogous studies.

Determining the location of mining induced seismicity is an invaluable tool that should be used to evaluate if the rock mass is behaving in the expected manner, and if not, to evaluate what changes in mining strategy can be made to control this unexpected behaviour. Near real-time processing of recorded seismic data could allow rock mechanical models to be constantly updated and improved. This would lead to predictions of the rock mass behaviour being more accurate, and hence the mine would become safer and more economical.

4 SPATIAL CLUSTERING OF MICROSEISMIC EVENTS

4.1 Introduction

A common problem in seismology is the interpretation of earthquake location data to determine any structures associated with seismic activity. Uncertainties in locations complicate this problem. Ideally uncertainties should be considered when any interpretation is being made. To allow this locations and uncertainties need to be displayed in an easily understandable way. Two ways in which this can be done is to plot error bars for each location, or to plot confidence volumes. These approaches tend to make diagrams overly complicated, which fails the criterion that diagrams are easily understandable.

Computational methods have been used to search for patterns in earthquake locations. One method is to find those locations that are in dense zones of seismicity, and assume that they are more likely to be associated with any structures. Alternatively, specific structures can be found that agree with the observed data. Examples of this are a search method that finds statistically significant planes of any orientation in a cloud of earthquake locations [*Fehler et al.*, 1987] and methods that use Principal Component Analysis [*Urbancic et al.*, 1993; *Spottiswoode and Milev*, 1998].

Jones and Stewart [1997] describe a method that uses the location uncertainties to simplify the earthquake cloud. The method is an iterative technique that moved earthquake hypocentres within bounds imposed by their location confidence ellipsoids in an attempt to find significant structures. The movement of hypocentres is compared with a theoretical distribution to determine when the iteration should cease. Synthetic testing illustrated that the method worked well, but had some limitations. Application of the method to a real data set showed that it greatly simplified the earthquake cloud, and very clear structures could be seen.

Prior to publication of the *Jones and Stewart* [1997] method, a similar analysis technique had been developed during the Asfordby study in an attempt to identify

structures around the coalface. One way in which the technique differed from that of *Jones and Stewart* [1997] was that event locations and estimated errors were expressed in polar co-ordinates. Initial results from application of this technique to synthetic and the real Asfordby data showed that it worked quite well. This technique was not iterative, and it used a simple minimisation to find the new location of an event based on the locations of all the events within its error bounds. The movement of event locations from their original positions was not compared to any theoretical distribution.

The method developed during the Asfordby study was improved by employing parts of the method of *Jones and Stewart* [1997]. Fundamentally it is very similar to the *Jones and Stewart* [1997] method except uncertainties in polar co-ordinates are used rather than Cartesian co-ordinates. Uncertainties in Cartesian co-ordinates do not apply to the event location data shown in the previous chapter because of the way the events have been located i.e. using the polarisation analysis technique. By defining uncertainties in polar co-ordinates, the uncertainty volume changes from an ellipsoid to a truncated cone. There are some other differences in the method, such as the introduction of a weighting factor when calculating the new event location, and the use of a different theoretical location movement distribution.

4.2 A method to determine significant structures

4.2.1 Concept

The concept behind this technique is very simple. Every event location has a spatial uncertainty volume, which is a three-dimensional probability density function. Consider the case of two events. If the uncertainty volumes only overlap for low probabilities then it is obvious that these events are spatially distinct and should be interpreted as such. If, however, the uncertainty volumes overlap for high probabilities the obvious interpretation is that these events are not spatially distinct, but occur on the same structure.

To extend this concept to more than two events, it is best to consider one event at a time. Any events that have uncertainty volumes that overlap with the uncertainty volume of the considered event for high probabilities can be assumed to occur on the same structure. The location of the considered event can then be moved within a specified uncertainty volume to a location that is more likely based on the locations of the other events. Repeating this for each event should lead to any significant structures in the data being highlighted as dense zones of seismicity. This process can be thought of as "collapsing" the event locations towards each other.

4.2.2 Method

The collapsing method must take account of the details of uncertainty volume estimation. The joint uncertainty distribution of the three spatial variables determines the geometry of the spatial uncertainty volume. It can be said with a certain confidence that the true location of an event lies within the joint spatial uncertainty volume for that confidence. For a large dataset the expectation would be that the number of true locations that lie within the uncertainty volumes at various levels of confidence would be consistent with the probability density function of the uncertainty volumes.

In the case of a linear problem, normally distributed uncertainty in the variables implies normally distributed uncertainties in the solutions. Therefore the data collapsing procedure should continue until the movement of locations from their original value matches some sort of normal distribution. *Jones and Stewart* [1997] state that the movement of locations from their original value should match a χ^2 distribution with three degrees of freedom. The method described here continues until the movement of locations from their original value matches a distribution of locations that have been perturbed from their original values by normally distributed errors in polar co-ordinates. The exact form of this control distribution is defined below. By searching for a certain distribution of event location movements, there is no constraint on the type of structure that might be defined by a cloud of locations. The movement of each location can be normalised in terms of the variable uncertainties to allow for locations of differing accuracy to be used together. *Jones and Stewart* [1997] showed

that their method was able to tolerate quite large variations in the estimates of variable uncertainties without significantly affecting their results.

An estimate of the uncertainty volume for each event location is required before the collapsing technique can be applied. In this study, events are located using a single three-component seismogram, utilising the P-wave polarisation and the P-S delay time. Therefore, the uncertainty volume is estimated as a truncated cone (see section 3.2.2). The errors in azimuth, elevation and displacement which are calculated as described in section 3.2.2 are representative of one standard deviation. An example of the shape of the uncertainty volume is shown as figure 4.1.

Figure 4.1 An example of the shape of uncertainty volume calculated from errors in polar co-ordinates i.e. azimuth, elevation, and source-receiver distance.

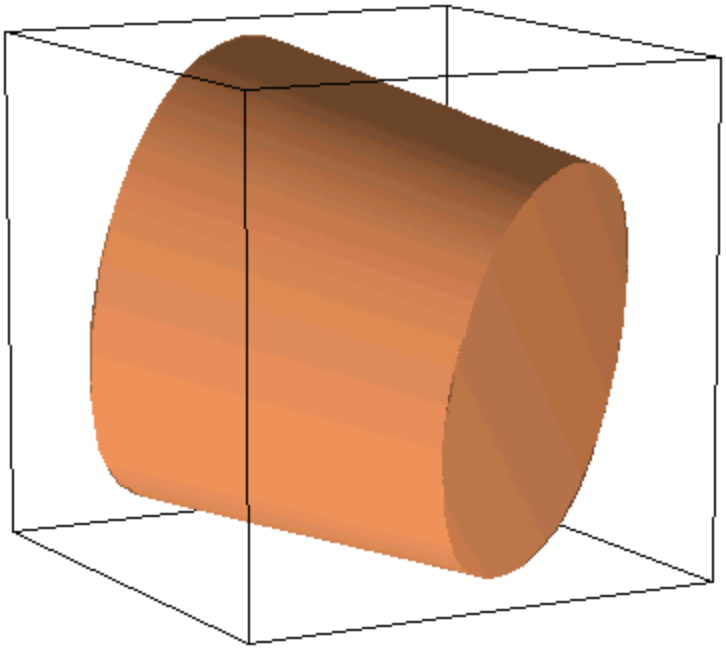

Once the geometry of the uncertainty volume is defined, the collapsing technique can be implemented. It is an iterative procedure that generates sets of collapsed locations until the movement of locations from their original position matches the control distribution.

To generate a set of collapsed locations, each location is considered in turn. The uncertainty volume for a certain confidence level is calculated for the location being considered. All other locations whose uncertainty volumes overlap the uncertainty volume of the event being considered are found. The centroid of these locations is calculated, using polar co-ordinates, after weighting has been applied to each location. The weighting is relative to the size of the estimated error for each location i.e. locations with small errors are given large weights and locations with large errors are given small weights. This means that the locations that are well determined will have more influence on the position of the centroid than those that are poorly determined. The location being considered is then moved towards the centroid. *Jones and Stewart* [1997] find that moving the location a fraction of the distance towards the centroid dampens oscillations in the data and reduces the number of iterations. The fraction they use is 0.61803, although the exact value does not seem to be critical. The value of 0.61803 is used as it mimics the golden section search in one dimension [*Press et al.*, 1986]. The new location is that event location for the next generation, and it is not considered in the current iteration. The geometry of the uncertainty volume remains unchanged throughout all iterations.

The next generation of event locations is generated for each iteration. The movement of each event location from its original location is calculated, and expressed as the sum over the three variables of the number of standard deviations of each variable. As previously stated this normalisation of the location movement means that locations with different uncertainties for each variable can be used. The distribution of location movement is expressed as a histogram of the normalised location movement using certain bins, and compared to the control distribution.

The control distribution is created using computer software such as MatLab that can generate random numbers from a specific distribution given certain parameters. To make the control distribution, firstly 10,000 event locations are created. All 10,000 event locations have exactly the same polar co-ordinates. The event locations are then perturbed from their original locations. For each event, one standard deviation error values for the azimuth, elevation and displacement are randomly generated. The error

values differ for each event, and they are stored in memory. The perturbation of each event from its original location is calculated by generating perturbations in azimuth, elevation and displacement. To calculate the azimuth perturbation for a given event location a random value is generated from a normal distribution that has a standard deviation equal to the azimuth error value for that event. Elevation and displacement perturbations are calculated in exactly the same way, and this is repeated for all 10,000 event locations. To move the perturbed locations back to their original position, each event location would have to be moved back by the calculated perturbations of its three co-ordinates. Thus the calculated perturbations are the same as the location movements described above. For each event location the perturbation of each co-ordinate is normalised by dividing by the one standard deviation error that was calculated for that co-ordinate of that event location. The normalised perturbations for the three co-ordinates can then be summed to calculate a normalised event location movement in exactly the same way as described above. The sum of normalised perturbations for all of the generated event locations are the control distribution. They define the distribution of event location movements for a perfect application of the collapsing method. The control distribution can then be expressed as a histogram using the same bins as are used when calculating the histogram for the distribution of event location movements found by the method. The control distribution histogram is normalised by dividing the values of the histogram by the number of event locations in the control distribution (10,000). Multiplying the normalised control distribution histogram by the number of actual event locations that the method moves gives a histogram against which the actual event location movement distribution histogram can be compared.

The normalised location movements are compared to the control distribution using two tests. To begin with, the Kolgomorov-Smirnov test [*Press et al*., 1986] is used. It compares the cumulative frequency of two distributions. Once there is an approximate match between the distributions, the chi-square test [*Press et al*., 1986] is used. This gives a measure of the probability that the distribution of normalised location movement could be drawn from the control distribution, and is the best test for two binned data sets. The chi-square test can only be used once there is an approximate

match between distributions, otherwise a local minimum of the misfit between distributions is generally found, and not the global minimum. The iteration is repeated until a minimum chi-square value is obtained. In the event of going past the minimum value, the process is taken back two generations and the fraction of the distance the location is moved towards the centroid is multiplied by 0.61803. The iteration then continues. The iteration is terminated when the fraction the location is moved has been reduced four times, or the decrease in misfit between distributions is less than 1%.

The collapsing method has only two variables. These are the numbers of standard deviations used as a cut off when constructing the uncertainty volume and the estimated standard deviation of the observable errors. The effect of changing the second of these variables is investigated in sections 4.4.3 and 4.5.3. One standard deviation, or a 68% confidence level, is used as a cut off for the method described here. *Jones and Stewart* [1997] use four standard deviations. The method described here is developed for use with mining induced seismic event locations, and the size of four standard deviation errors for such locations are so large as to hide any subtle structures controlling the locations of events.

Simple effects of the collapsing method can be easily visualised. Very isolated locations will be unaffected by the process, and remain in their original position. Two nearby locations will move towards their common centre. Locations on the edge of a large cluster will be drawn into that cluster.

4.4 Application of the collapsing method to the Phase-One dataset

4.4.1 Original locations

The calculated locations of 122 seismic events recorded by the Cants Thorn 1 upper sonde are shown as figure 3.6 to 3.9. There are several distinct clusters of events, and these are particularly well seen in figure 3.9. As previously discussed, the spatial clustering of seismic events can indicate geological structures having strong controls on the activity. Figures 3.10 to 3.13 show estimated error volumes for the locations. Distinct clusters can be clearly identified where the error volumes for a number of

events overlap with each other. Some interpretation can be made of the type of structure that the cluster of events is defining. For example, the large cluster 100m to 300m above the tail gate is probably defining a linear structure, although it is not possible to say whether the structure has zero volume or a finite volume.

Applying the collapsing method to the calculated locations should highlight any structures that are controlling the seismic activity. The seismic activity is very different from that which is expected around a longwall coalface [e.g. *Hatherley et al.*, 1997], and identifying any structures defined by the activity might help to explain why this is the case.

The event locations are calculated using a 1D layered velocity model (section 3.2.3). For each event a virtual sonde location is calculated such that given the calculated direction of propagation at the source and P-S delay time the event would be recorded at the virtual sonde for a homogeneous velocity model. The error volume for each event should then be calculated relative to the virtual sonde location for each event. Finding whether error volumes calculated in this way overlap is much more computer intensive than for error volumes calculated relative to the same sonde location for each event. Comparing plots of the error volumes calculated relative to the virtual sonde locations, and those calculated relative to the mean virtual sonde location show that there is little observable difference between them. Thus, error volumes calculated relative to the mean virtual sonde location are used when applying the collapsing method to cut down computing time.

4.4.2 Collapsed locations

The collapsing method is applied to the Cants Thorn 1 upper sonde dataset. The collapsing method terminates after 17 iterations. The distribution of movement of event locations is shown as figure 4.8. The value of the chi-square test for the distribution shown is 8.2, with 11 degrees of freedom, which gives a significance probability of 0.70. The significance probability is a number which describes the extent to which the data support the null hypothesis [*Daly et al*., 1995, p. 325]. In this case the null hypothesis is that the distribution of movement of event locations is the

same as the control distribution. The null hypothesis need only be rejected for very low values of the significance probability. A significance probability of 0.70 is high, and means the null hypothesis is supported. The high significance probability also supports the assumption that the errors in event location are normally distributed, and the values estimated for them give a measure of the standard deviation of the distribution.

Figure 4.8 The distribution of location movements compared to the control distribution after application of the collapsing method to the Cants Thorn 1 upper sonde dataset.

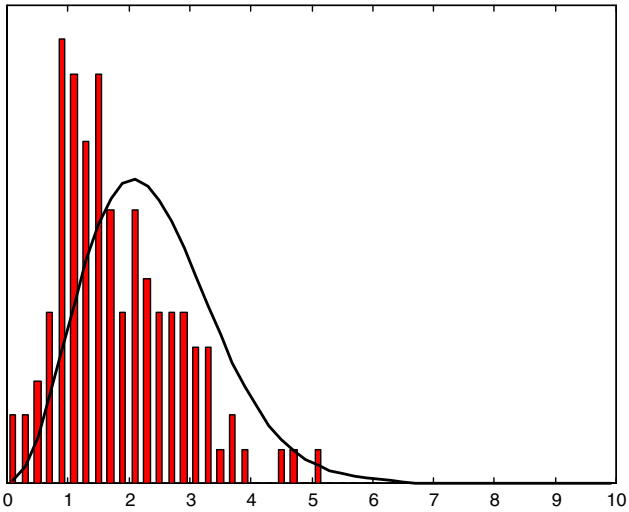

The collapsed locations are shown as figures 4.9 to 4.12. They show the same four views as figures 3.4 to 3.7 show of the original locations. Several possible structures can be clearly seen. The most important of these are the linear structure defined by the large number of events above the tail gate, and the beginning of a vertical structure running between it and the seam. These two structures do not appear to join up, however it was shown by synthetic tests that the collapsing method shortens linear structures. Thus it is likely that the two structures do join up. The structure above the tail gate dips at about 40° in the direction of mining. It runs from above the aquifer to the base of the aquifer. It has zero volume. The vertical structure begins at the base of the aquifer, and there is a small cluster of events at seam level directly below it. It is probable that these events are showing a vertical fracture from the aquifer to the seam, but the dimensions of the fracture are approximately the same as the errors, and hence

Figure 4.9 Plan view of the locations of microseismic events recorded by Cants Thorn 1 upper sonde after application of the collapsing method.

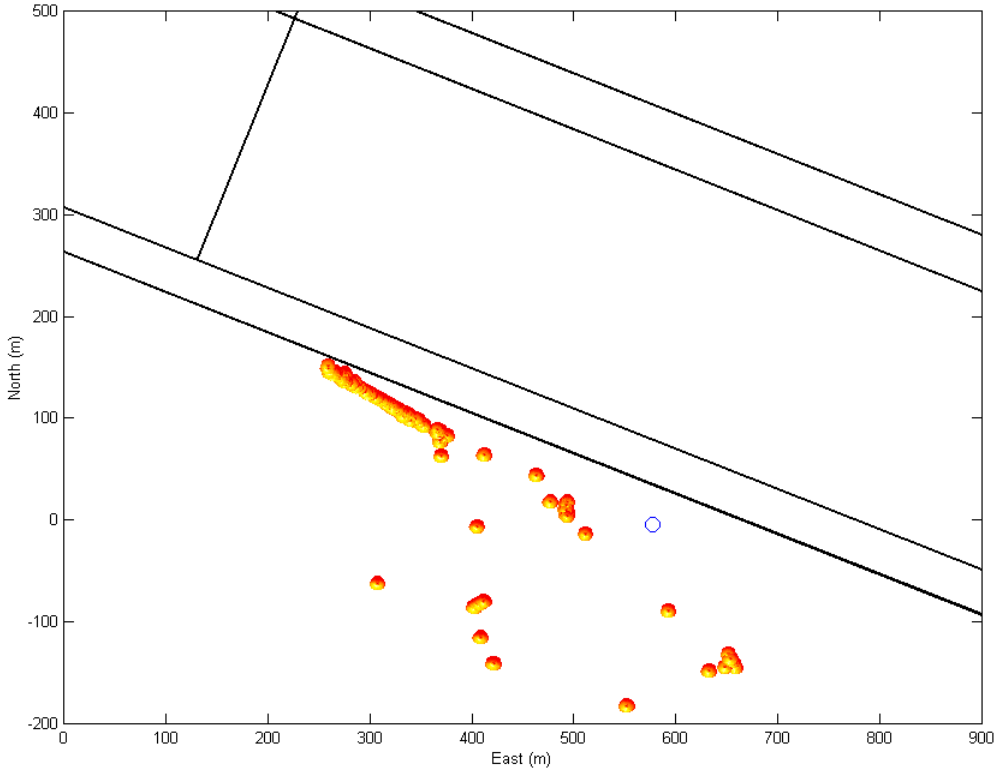

Figure 4.10 Sectional view of the locations of microseismic events recorded by Cants Thorn 1 upper sonde after application of the collapsing method, looking perpendicular to the direction of face advance. Face advance is left to right in this plot.

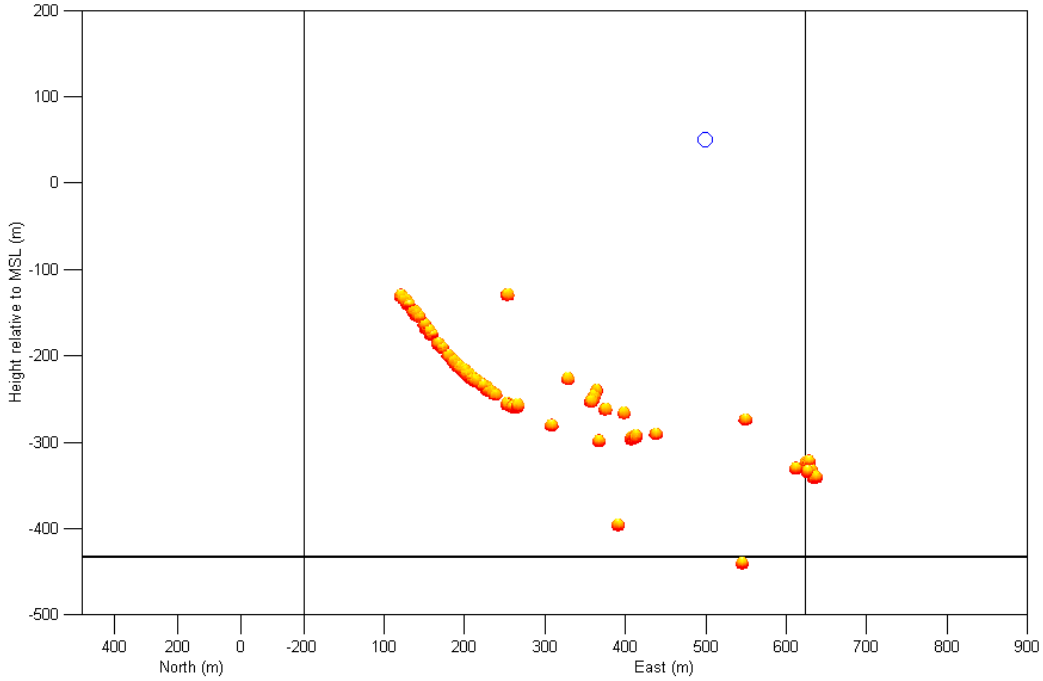

Figure 4.11 Sectional view of the locations of microseismic events recorded by Cants Thorn 1 upper sonde after application of the collapsing method, looking in the direction of face advance. Face advance is into the page in this plot.

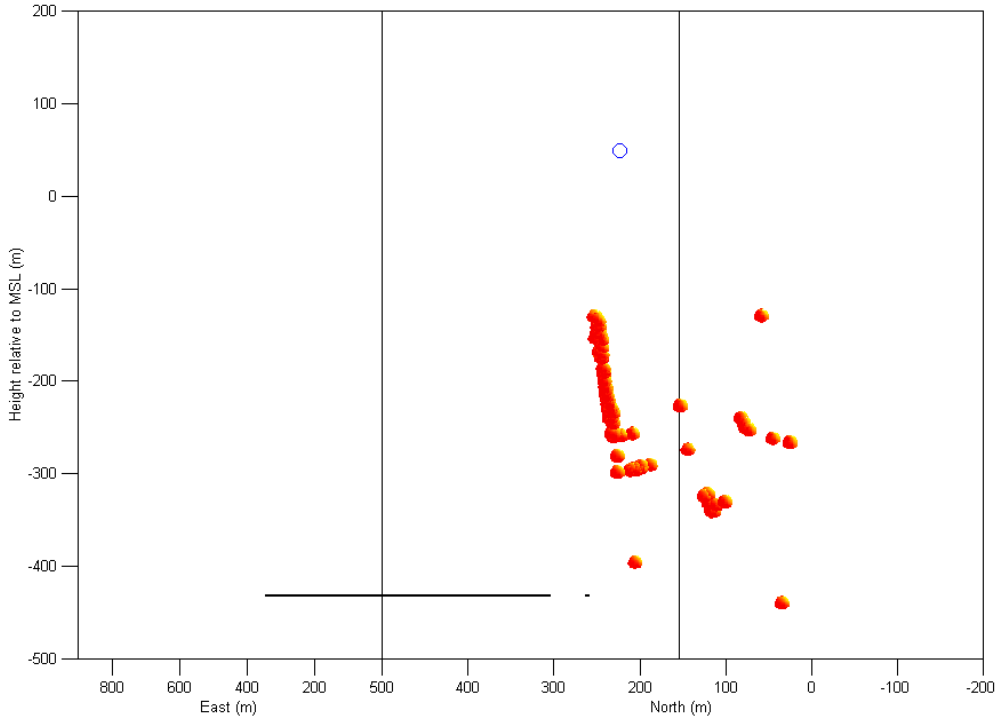

Figure 4.12 3-D view of the locations of microseismic events recorded by Cants Thorn 1 upper sonde after application of the collapsing method.

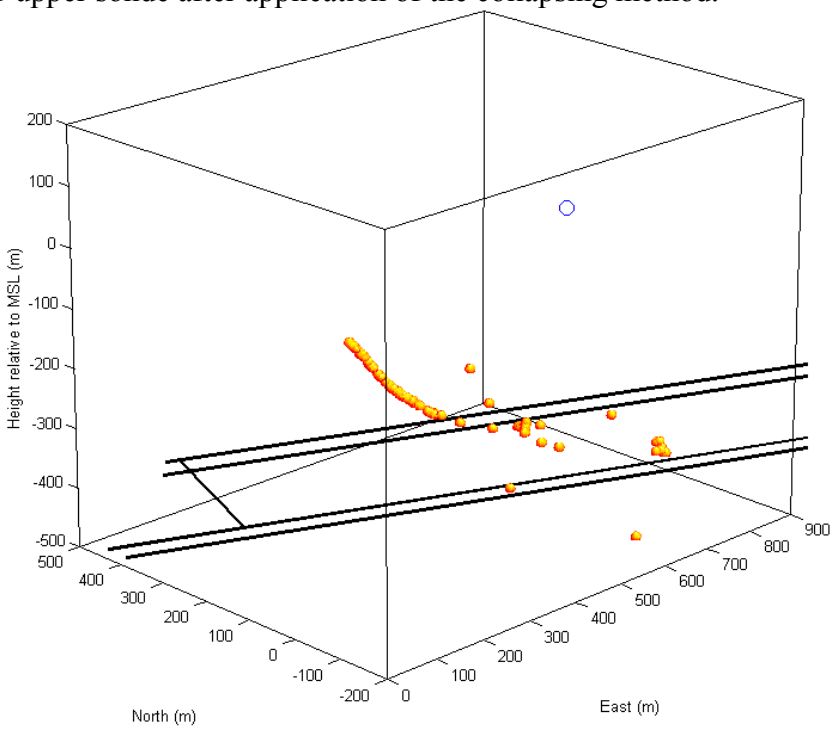

it is poorly defined by the collapsed mechanisms. The structure above the tail gate has been interpreted (section 3.3.1) as either a fracture propagating down through the roof or reactivation of a fault plane. If it was the latter, it may be expected that the collapsed locations would show a planar structure, although this is very dependent on the structure dimensions. It is not possible to distinguish between these two interpretations given the results of the collapsing method. The collapsed locations show that a linear region of fractured rocks extends down through the roof strata to the base of the aquifer. From there, a vertical region of fractured rock extends down to the seam. Thus there is a path for water in the aquifer to travel down to seam level and cause the flooding experienced at the face. This fracture geometry is the same as described by *Gale and Nemcik* [1998] for a numerical model of a longwall with strong roof conditions and periodic weightings, which are the conditions at Asfordby.

4.5 Application of the collapsing method to the Phase-Two hole 1 dataset

4.5.1 Original locations

The calculated locations of the 135 seismic events recorded by the Hole 1 sonde during the second phase of monitoring are shown as figures 3.17 to 3.20. There are two distinct clusters of events, one above the main gate and one below the sill but above the centre of the panel. Figures 3.21 to 3.24 show estimated error volumes for the locations. Apart from the events forming two clusters, there is no evidence of any structures that are controlling the locations of the seismic events. The events tend to form diffuse clouds of seismicity. However, the seismicity shows patterns similar to the fracture patterns observed from physical models of the Asfordby stratigraphy [*Sun et al.*, 1992a, 1992b]. If the seismic activity is showing the same fracture pattern as the physical models, then it would be expected that the seismic events are delineating discrete fractures.

Applying the collapsing method to the calculated locations should allow any possible structures that are not shown by the calculated locations to be identified. If the seismic activity is not being controlled by any structures and does indeed form diffuse clouds, then that will be shown by application of the collapsing method.

Figure 4.14 The distributions of location movements compared to the control distribution after application of the collapsing method to the two Hole 1 sonde datasets, each from a different three-component set of geophones. The top plot is from the first set, the bottom plot is from the second set.

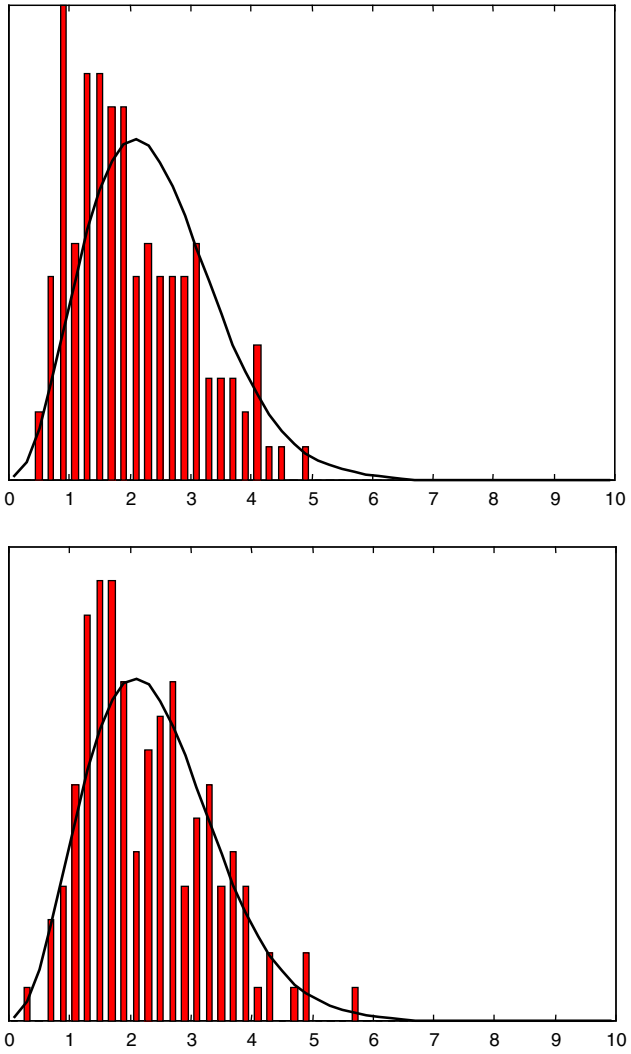

4.5.2 Collapsed locations

The collapsing method was applied independently to the two Hole 1 sonde event location datasets, one from each three-component set of geophones. The collapsing method terminated after 13 and 7 iterations for the first and second three-component set respectively. The distribution of movement of event locations is shown as figure 4.14. The respective values of the chi-square test applied to the final distribution of event location movement were 5.8 and 6.0 with 11 degrees of freedom. These relate to significance probabilities of 0.89 and 0.87. The significance probability calculated after applying the collapsing method to the Cants Thorn 1 upper sonde dataset was

0.70, so all three values are high. This is a further indication that the method used to estimate event location uncertainties is satisfactory. The higher significance probabilities for the Phase-Two dataset are probably due to the larger number of events, and the simpler velocity model.

The collapsed locations are shown as figure 4.15 to 4.18. They show the same views as 3.17 to 3.20, the top plots show the data for the first three-component set of geophones, and the bottom plots show the data for the second set. The collapsed locations for both sets show similar structures. The cluster of seismic events above the main gate has defined an approximately linear structure that dips shallowly in the direction of face advance. The linear structure is not as well defined as that seen in the Cants Thorn 1 upper sonde data. It appears to have a non-zero volume, so rather than being an actual geological structure, it is probably a heavily fractured volume of rock. The cluster has split into two distinct clusters. The cluster farther from the face starting position has a smaller number of events, and is closer to the edge of the face. It is only just higher than seam level at the lowest point, which is approximately at the point where the face becomes square. The larger cluster extends to a height of about 70m above the seam, and has a larger volume than the lower cluster. Thus it appears that above the main gate a heavily fractured zone has been formed, and that this zone narrows as it dips down to meet the edge of the panel being mined where the face becomes square.

The collapsed locations show a second structure that runs North-South below the sill. It is approximately horizontal, and is at a height of about 40m above the seam. It is much more defined than the structure above the main gate, and appears to have near-zero volume. The position of this structure is slightly different for each of the two datasets, but it is probably above the centre of the face, and extends over nearly the complete face width. It appears to join up with the structure above the main gate at the gap between the two clusters. Figure 4.17 shows that this structure and the main

Figure 4.15 Plan view of the locations of microseismic events recorded by Hole 1 sonde after application of the collapsing method. The top plot shows locations for data recorded on one of the three-component sets of geophones, the bottom plot shows locations for data recorded on the second set.

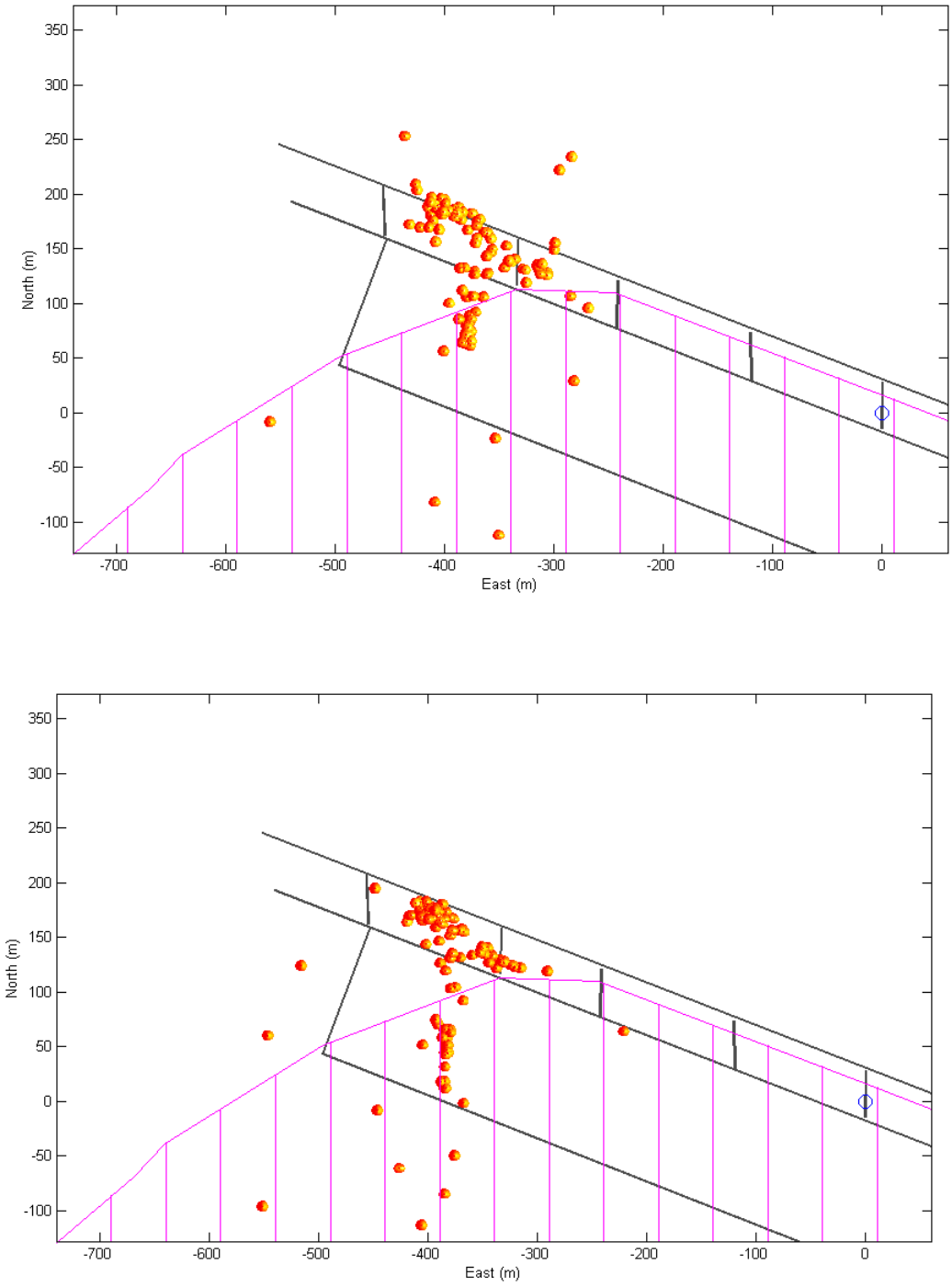

Figure 4.16 Sectional view of the locations of microseismic events recorded by Hole 1 sonde after application of the collapsing method, looking perpendicular to the direction of face advance. Face advance is left to right in this plot. The top plot shows locations for data recorded on one of the three-component sets of geophones, the bottom plot shows locations for data recored on the second set.

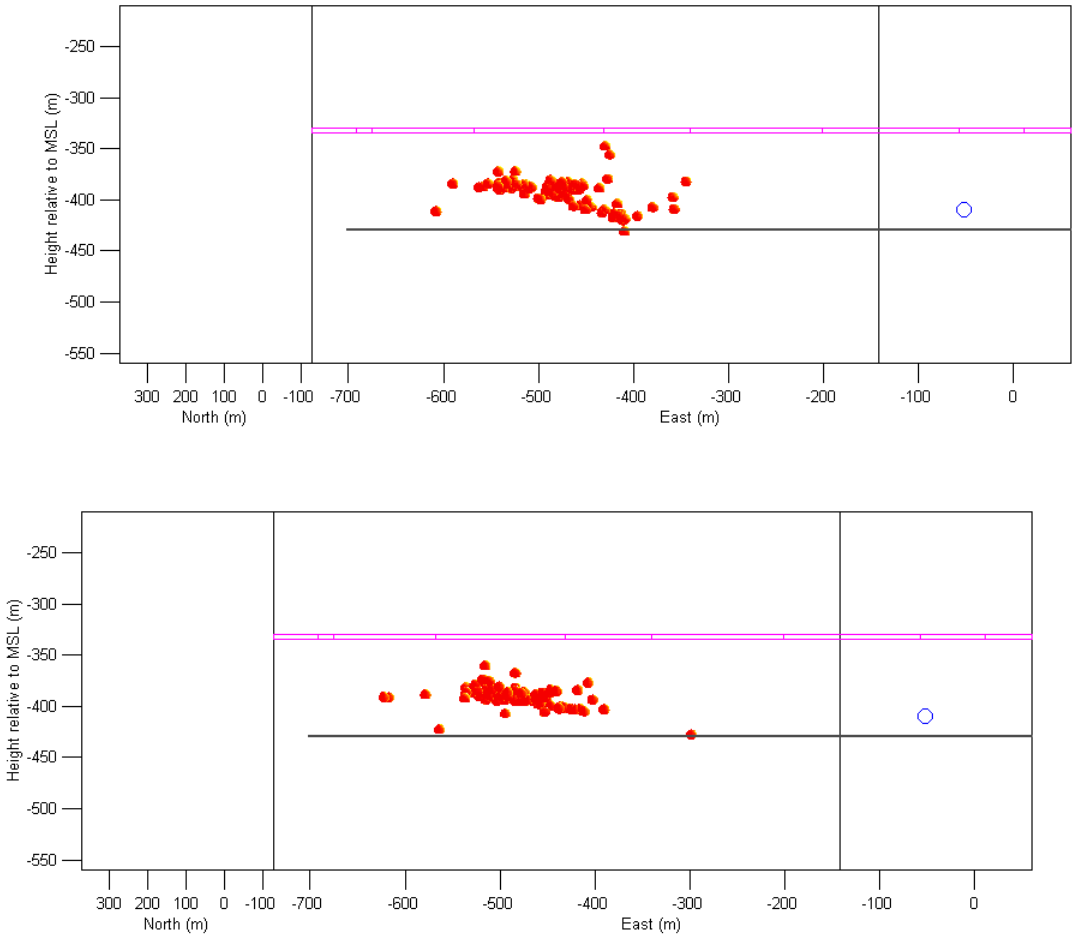

Figure 4.17 Sectional view of the locations of microseismic events recorded by Hole 1 sonde after application of the collapsing method, looking in the direction of face advance. Face advance is into the page in this plot. The top plot shows locations for data recorded on one of the three-component sets of geophones, the bottom plot shows locations for data recorded on the second set.

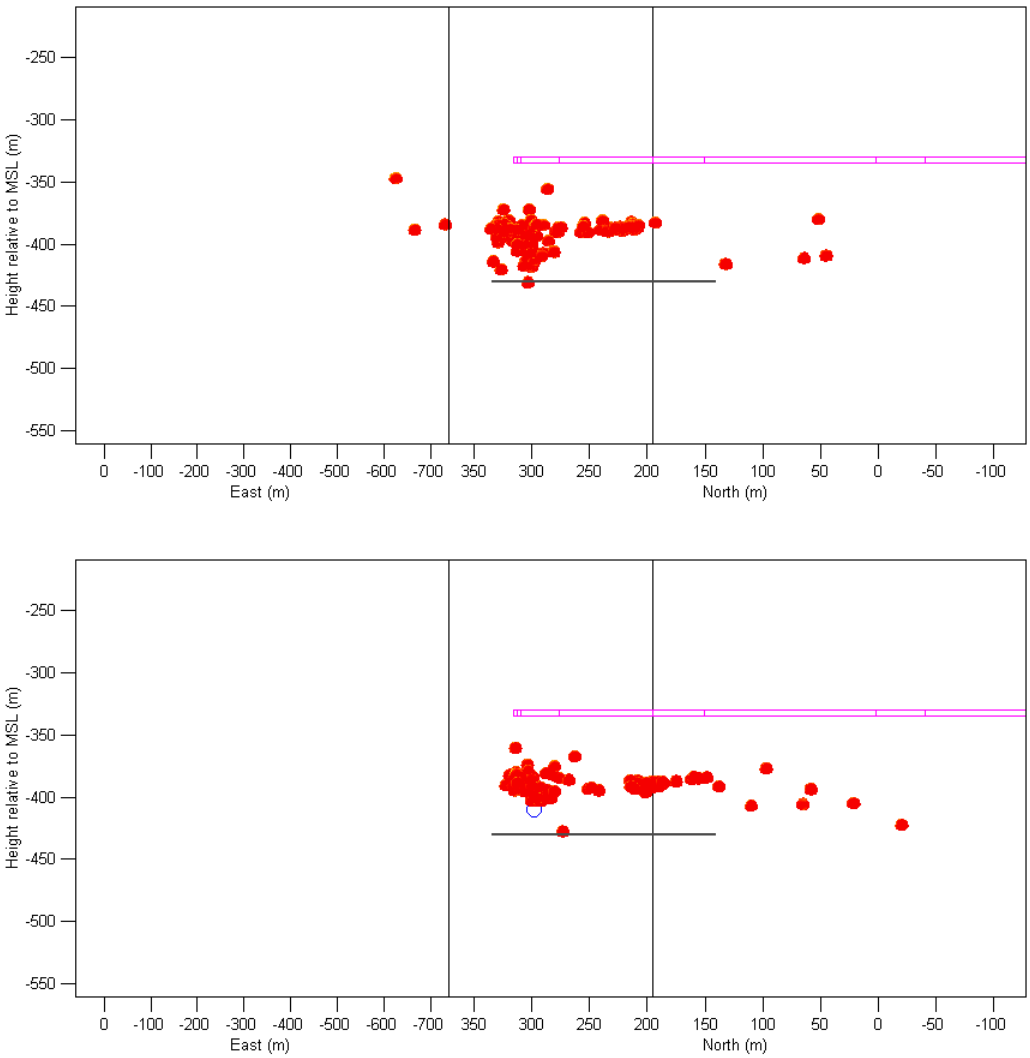

Figure 4.18 3-D view of the locations of microseismic events recorded by Hole 1 sonde after application of the collapsing method. The top plot shows locations for data recorded on one of the three-component sets of geophones, the bottom plot shows locations for data recored on the second set.

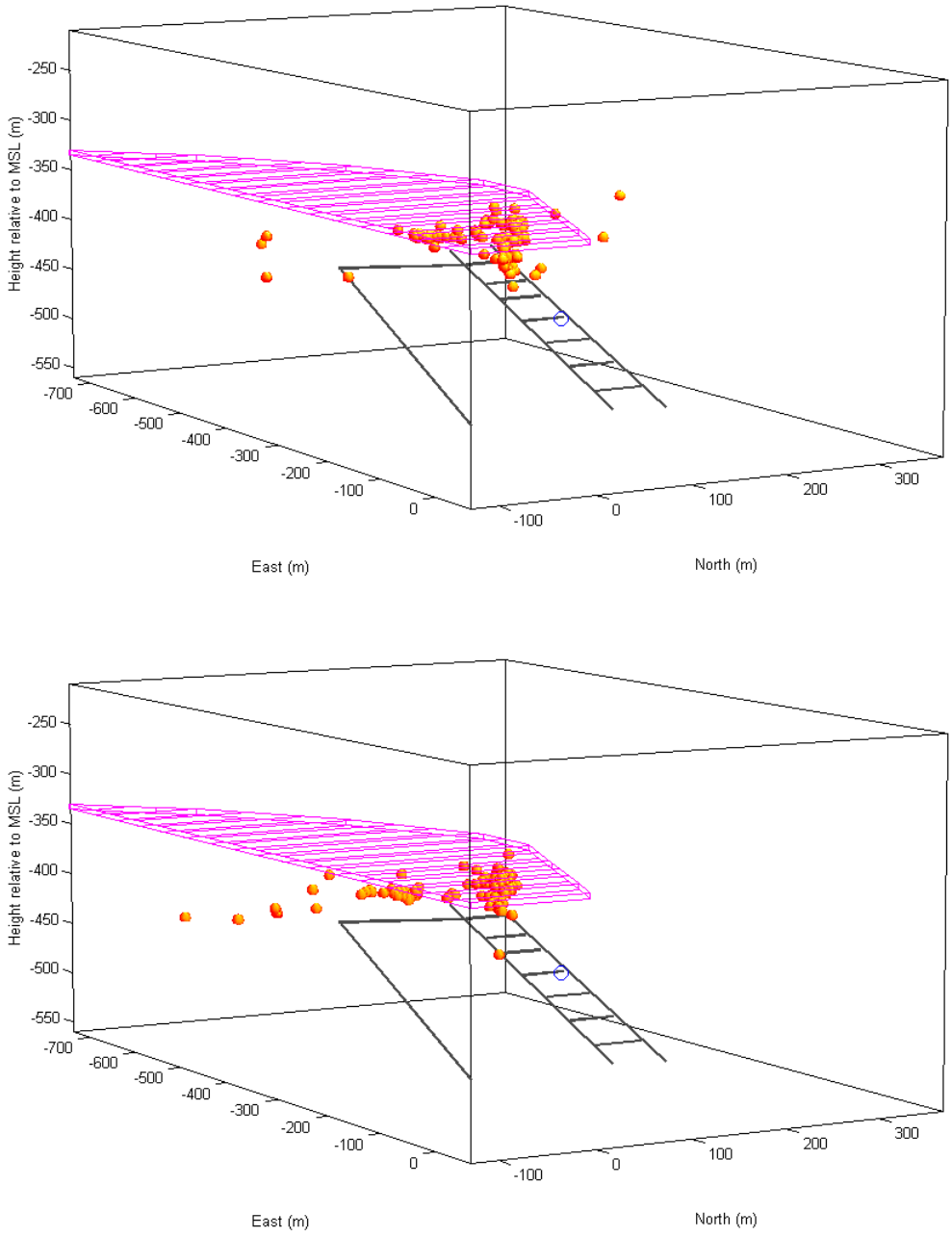

gate structure form an arch above the face. The arch is not obvious in figure 3.19, which shows the uncollapsed locations. The arch is particularly well seen in the top plot of figure 4.17, that for the first three-component set of geophones. The same arch structure is observed by *Hatherley et al.* [1995, 1997], and is shown in the figure reproduced here as figure 1.5. This arch type structure is also shown by the physical models of the Asfordby stratigraphy [*Sun et al.*, 1992a, 1992b]. This suggests that the seismicity observed during Phase-Two is the more expected seismicity for a longwall mine, typified by the observations of *Hatherley et al.* [1997], and implies that the roof collapse was more controlled.

Taking the more accurate location for each event from the two possible locations calculated using the two three-component sets of geophones can make a third dataset. The locations of the events in this dataset should better constrain any structures that are present. Applying the collapsing method to this better dataset gives the results shown as figure 4.19. The collapsing method terminated after 14 iterations to give a chi-square test value of 4.1, and a significance probability of 0.96. The structures described above can be clearly seen in the combined dataset. The linear structure in the roof above the face is seen to dip to the North, and the way that it joins the clusters above the main gate is better seen. Figure 4.19 (bottom plot) shows patterns of seismicity that are very similar to the physically modelled fracture patterns [*Sun et al.*, 1992b] that are shown as figure 2.3.

4.5.3 Effects of different error values

Applying the collapsing method using different error values for the Cants Thorn 1 upper sonde dataset shows that the method works most successfully using the errors estimated in chapter 3. The same test needs to be applied to this dataset, especially given the very high significance probability found after applying the collapsing method to the combined dataset. Such a high value could point to the data being suspect, and that there is less variation than might be expected [*Daly et al.*, 1995, p.358]. Applying the collapsing method with different error values should show whether or not this is the case here. The test is carried out in exactly the same way as before, and the combined dataset is used.

Figure 4.19 The collapsed locations of the dataset containg the most accurately located events recorded on the Hole 1 sonde. The top plot shows a plane view, the middle plot shows a sectional view looking from the South in the direction perpendicular to the face advance, and the bottom plot shows a sectional view looking from the West in the direction of face advance.

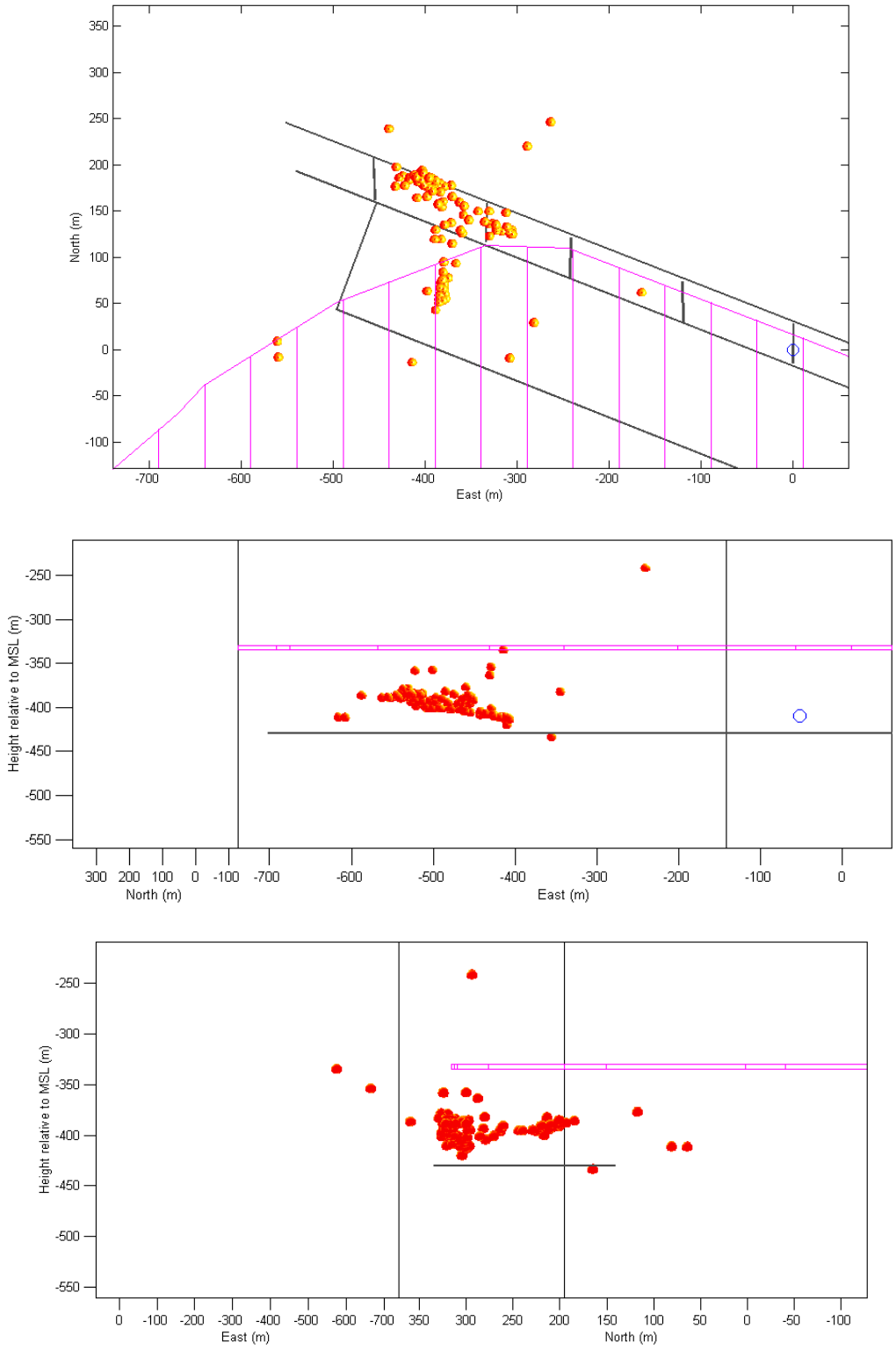

4.6 Conclusions

A method has been described that "collapses" clusters of seismic event locations within their error bounds until a solution is obtained that matches a theoretical location movement distribution. The error bounds of the event locations are defined in polar co-ordinates. Synthetic tests of the method showed that it works well in a variety of situations, but can introduce artefacts into the data. The method described is partly based on a method used in an earlier study by *Jones and Stewart* [1997]. It differs in a number of ways, and it is found that introduction of a weighting factor when calculating event location movements decreases some of the artefacts identified by the synthetic tests.

The Phase-One event location dataset from the Cants Thorn 1 upper sonde shows distinct structures controlling the seismic activity. When applied to this dataset, the collapsing method simplifies these structures, and supports the interpretation made of the raw event locations.

The Phase-Two event location dataset recorded at the Hole 1 sonde shows a more diffuse pattern of seismicity. There is the suggestion of geological structures controlling the seismic activity as distinct clusters are seen. Application of the collapsing method to this dataset identifies three approximately linear structures that join above the main gate. Identification of these structures simplifies the interpretation of the seismic activity, and allows a better understanding of the behaviour of the rock mass around the mine. In particular, the arch structure above the face suggests that the patterns of seismicity observed were indicating more controlled roof collapse, as predicted by the physical models of the Asfordby stratigraphy.

There is a possibility that the collapsing method over-simplifies structures. It is not entirely clear what geological structure would appear to be linear. A planar structure may be more expected. Tests with synthetic data show that event locations perturbed from a planar structure collapse back to a planar structure, although it reduces in size. This only works if the error volumes are smaller than the structure. If error volumes

were larger than the structure, the event locations would collapse to a simpler structure than a plane, for instance a line or a point.

The collapsing method is able to greatly simplify the observed patterns of seismic activity. This, in turn, allows simpler interpretations to be made. The identification of geological structures that are controlling the seismic activity allows a much better understanding of the interaction between the rock mass and the mining activity. This should make it possible to produce better models of the rock mass, and hence increase the safety and production of the mine.

5 MICROSEISMIC EVENT SOURCE MECHANISMS

5.1 Introduction

Seismic events are the sudden release of accumulated strain energy as it exceeds the strength of the rock and fracturing or faulting occurs. The energy is dissipated as heat, in the deformation of the rock, and in the generation of seismic waves. The form of the generated seismic waves is controlled by the dynamics of the fracturing event. With sufficient records of the seismic waveforms it is possible to determine the fracture dynamics, and these can then be used to infer many properties of the rock at the point of fracturing. This kind of analysis is known as seismic source mechanism inversion.

There are several different ways in which a seismic source mechanism can be described. The two most commonly used are the double-couple mechanism, and the moment tensor source. The double-couple mechanism is regarded as the best representation of a seismic event that occurs as slip on a fault plane. It describes a pure-shear failure with no change in volume. The moment tensor source is more general. It describes crack motions as nine equivalent forces, of which six are independent. The moment tensor source can describe volumetric changes. An extension of the moment tensor source is the time dependent moment tensor. This is an even more complete description of the seismic source mechanism, and can be used to determine and describe very complex fracture dynamics.

The more complex the source mechanism model that is used, the more problematic the analysis to determine the parameters defining that model becomes. To determine a moment tensor source mechanism for a seismic event, a number of records, recorded at locations which give a good coverage of the focal sphere for that event, are required. The moment tensor has six independent elements, so at least six pieces of data are required to perform a linear inversion. A double-couple mechanism is defined by only three parameters, which means less data is required. Only a fraction of seismic events have a considerable non-double-couple source mechanism part e.g. volcanic tremors [e.g. *Fehler*, 1983], ice quakes [e.g. *Dudko et al.*, 1998], hydrofracturing [e.g. *Ohtsu*,

1991]. Hence the double-couple mechanism is the most widely used description of the seismic source mechanism.

The three parameters that define a double-couple mechanism are the strike, rake and dip. These are shown on figure 5.1. The dip is simply the dip of the fault plane measured from the horizontal plane i.e. a vertical fault plane will have a dip of 90°. The strike is the strike direction of the fault plane i.e. the direction of zero-dip that is 90° anti-clockwise from the direction of maximum dip. The strike is measured clockwise from the North direction. The rake is the angle between the direction of slip on the fault plane and the strike direction. In this study, rakes are measured clockwise from the strike direction, hence normal faults have positive rakes, and reverse faults have negative rakes. A normal dip-slip double-couple mechanism will have a rake equal to 90°.

Figure 5.1 The definition of the strike, rake and dip that describe a double-couple mechanism in a geographical co-ordinate system. The x-axis points east, the y-axis points north and the z-axis points up. The strike, *s*, is measured clockwise from north. The dip, *d*, is measured from the horizontal (x-y) plane. The rake, *r*, is measured clockwise from the strike direction. The slip vector, b, and fault normal, n, are also shown.

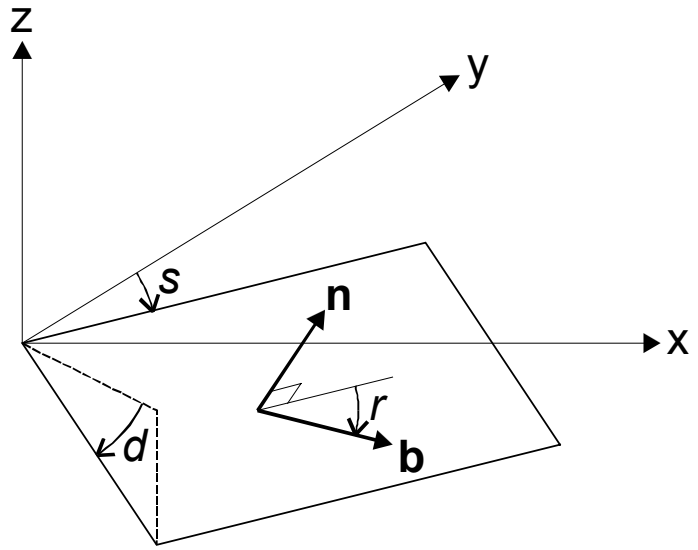

There are three fundamentally different methods used to determine double-couple source mechanisms for earthquakes. One method uses the polarities of first-motion observations to determine the focal mechanism. A criterion for accurate application of this method is many observations giving a good coverage of the focal sphere, and this is usually not satisfied for mine tremors. Another method is to determine the focal mechanism from inversion of waveforms. Several studies have used this technique successfully for local earthquakes recorded at only a few stations, and even at a single station [*Dreger and Helmberger*, 1993]. However, waveform inversions can be very sensitive to choice of velocity model [*Dreger and Helmberger*, 1993]. The third method is to invert the P and S amplitudes to determine the focal mechanism. This method has been successfully used for teleseismically [*Pearce*, 1987] and locally [*Rognvaldsson and Slunga*, 1993] recorded events. *Langston* [1982] showed that it was possible to distinguish between fault types (e.g. strike-slip versus dip-slip) using only the relative amplitude between P and SH waves recorded at a single station. One major advantage of amplitude methods is that data processing and analysis are relatively easy compared to waveform inversion methods, making it more practical for the study of the large numbers of induced events observed during mining or rock excavation.

A method which combined first motion polarities and amplitude ratios has been used to determine focal mechanisms for aftershocks of the 22 April 1991 Costa Rica and the 25 April 1992 Cape Mendocino, California, earthquakes [*Schwartz*, 1995]. This method uses a grid search over all possible values of strike, rake, and dip in 10° increments, and was successful for numerous events recorded at local distances (<100km) by sparse three-component networks.

Here a method is described that determines double-couple mechanisms that fit single three-component seismic data. The method measures amplitude ratios of P-waves and S-waves, then uses a grid search to find mechanisms that fit the measured amplitudes. The method is subject to a number of tests using synthetic seismograms that establish the value and the limitations of the method.

Integrated Microseismic Monitoring and Numerical Modelling for the Determination of Fracture Architecture Around Longwall Coal Mines for Geomechanical Validation.

5.2 An amplitude ratio inversion method using a single three-component seismogram

In terms of design, set-up, and costs, the simplest microseismic monitoring system is a single three-component seismometer. In chapter 3 it is shown how such a system can be used to determine the location of seismic activity giving a better understanding of the effects of mining strategy on the surrounding rock mass. To determine the seismic source mechanism from recorded seismograms it is usually necessary to have several records of the same seismic event. To record such data the monitoring system must be more sophisticated, and therefore more costly. It would be advantageous to be able to determine the source mechanism of a seismic event from a single three-component seismogram. High quality seismic data is recorded during most microseismic monitoring studies. Also the velocity structure of the rock mass surrounding the mine is usually simple. The method described below utilises these facts to determine a representative double-couple source mechanism for a seismic event from a single three-component seismogram. The method described also satisfies the criterion that the computer processing time per event is short, which is essential if it is to be applied to mining induced seismic events since these can occur at hundreds or thousands of events per hour. Finding a double-couple mechanism that fits the observed seismic data could be achieved using more time consuming methods e.g. minimisation, grid search. The method described here uses a grid search to find the double-couple mechanism that best fits the observed seismic data, but significantly reduces the computational time by assuming a homogeneous velocity model and using co-ordinate transforms to keep the source-receiver direction constant in a specified co-ordinate system. The ratios of seismic wave amplitudes are used, and since these ratios will only vary with source-receiver direction, the grid of amplitudes used will be the same for each event in the specified co-ordinate system.

5.2.1 Transforming data to a new co-ordinate system

The three-component seismic data are transformed to a new co-ordinate system. As described above, the new co-ordinate system is such that the location of the seismic event has a certain fixed azimuth and elevation in polar co-ordinates i.e. the source-

receiver direction is fixed. A 2-D example is shown as figure 5.2. The left-hand plot shows an event location with an azimuth of θ measured in the original co-ordinate system (the x-axis and y-axis). The receiver is at the origin of the co-ordinate system. A co-ordinate transform is applied so that the event location has an azimuth of θ′ measured in the new co-ordinate system (shown by the x′-axis and y′-axis). The azimuth θ′ is the fixed azimuth. The transformation consists of rotating the co-ordinate axes clockwise by the angle θ-θ′. The principal is the same in the 3-D case except the elevation of the event location in the new co-ordinate system is also fixed.

Figure 5.2 Two-dimensional example of a co-ordinate transform applied to an event location such that it has a fixed azimuth (θ′) in the new co-ordinate system (x′-y′).

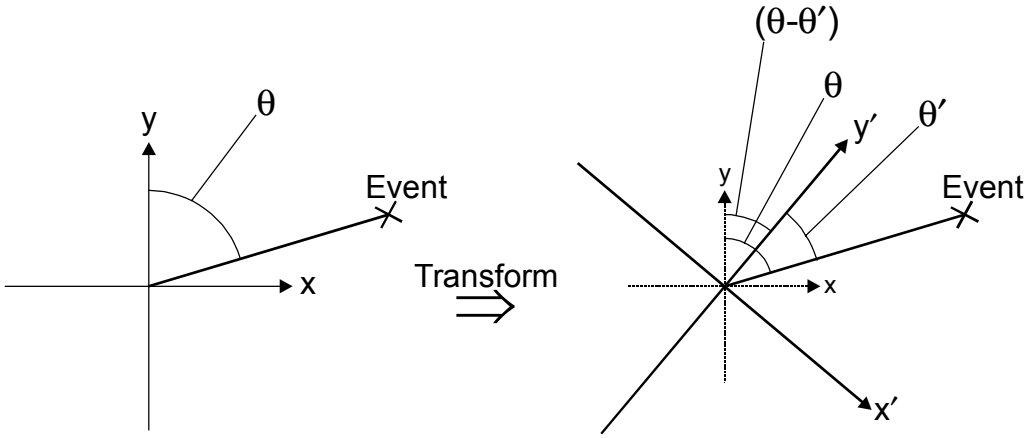

The three angles that define the transform matrix in the 3-D case are:

$$\begin{aligned} \chi &= az \\ \varphi &= el - el'_0 \\ \theta &= az'_0 \end{aligned} \qquad \ldots(5.1)$$

In equation 5.1, *az* is the azimuth of the event location in polar co-ordinates measured anti-clockwise from the x-axis (East). az'_0 is the fixed azimuth in the new co-ordinate system. *el* is the elevation of the event location in polar co-ordinates measured from the x-y plane, positive upwards. el'_0 is the fixed elevation in the new co-ordinate system. The dash, ′, is assigned to any variables measured in the new co-ordinate system.

It is quite simple to calculate the transform matrix by considering three separate rotations. Initially the co-ordinate system is rotated anti-clockwise around the vertical z-axis by the angle χ. The rotation matrix for this step is:

$$\mathbf{R}_1 = \begin{bmatrix} \cos\chi & -\sin\chi & 0 \\ \sin\chi & \cos\chi & 0 \\ 0 & 0 & 1 \end{bmatrix} \quad \ldots(5.2)$$

In this intermediate co-ordinate system the event location lies in the x-z plane. The intermediate co-ordinate system is then rotated around its y-axis by the angle φ. The rotation matrix for this step is:

$$\mathbf{R}_2 = \begin{bmatrix} \cos\varphi & 0 & -\sin\varphi \\ 0 & 1 & 0 \\ \sin\varphi & 0 & \cos\varphi \end{bmatrix} \quad \ldots(5.3)$$

The event location in this second intermediate co-ordinate system is in the x-z plane, and has the elevation el'_0. The second intermediate co-ordinate system is then rotated clockwise around its z-axis by the angle θ. The rotation matrix for this step is:

$$\mathbf{R}_3 = \begin{bmatrix} \cos\theta & \sin\theta & 0 \\ -\sin\theta & \cos\theta & 0 \\ 0 & 0 & 1 \end{bmatrix} \quad \ldots(5.4)$$

In this new co-ordinate system the event location has the azimuth az_0 and the elevation el_0.

A single transform matrix can be defined as the product of the three rotation matrices shown above:

$$\mathbf{R} = \mathbf{R}_1.\mathbf{R}_2.\mathbf{R}_3 \quad \ldots(5.5)$$

The seismic data is stored as an n-by-3 matrix, with the x-, y-, and z-components in columns 1, 2, and 3 respectively. To transform the data to the new co-ordinate system it is multiplied by the rotation matrix R:

$$\mathbf{XYZ'} = \mathbf{XYZ.R} \qquad \ldots(5.6)$$

XYZ is the seismic data in the original co-ordinate system, and XYZ′ is the same seismic data in the new co-ordinate system. The event location in the new co-ordinate system has a fixed azimuth and elevation. If the event location is calculated as described in section 3.2 using the XYZ′ data, the calculated location has the expected azimuth, az'_0, and elevation, el'_0.

5.2.2 Splitting seismic data into principal components

Once the data is in the required co-ordinate system the seismic wave amplitudes need to be measured and compared to those that have been calculated for the fixed source-receiver direction. The amplitude data that is required is the P-wave and S-wave first motion amplitudes for each of the three components. The S-wave first motion amplitudes are effected by shear wave splitting due to any shear wave anisotropy. To remove this effect it is necessary to split the data into three principal components, corresponding to a P-wave and two S-wave components, before measuring the first motion amplitudes. A singular value decomposition can be applied to the three-component P-wave data to calculate three eigenvectors that correspond to the three principal components. The three eigenvectors can be used to define a matrix that transforms the seismic data in the new co-ordinate system to principal component data. The transform matrix is given by:

$$\mathbf{V} = [\mathbf{P} \quad \mathbf{S}_1 \quad \mathbf{S}_2] \qquad \ldots(5.7)$$

where P is the column eigenvector with the largest associated eigenvalue, corresponding to the P-wave polarisation direction. S_1 and S_2 are the two column eigenvectors corresponding to the two S-wave components. The principal component

seismic data is then obtained by multiplying the three-component data, XYZ′, by the matrix V:

$$\mathbf{PSS} = \mathbf{XYZ'}.\mathbf{V} \qquad \ldots(5.8)$$

PSS is the seismic data split into principal components. The zero-peak first motion amplitudes of the three principal components are measured. The principal component first-motion amplitudes can be used to calculate the P-wave and S-wave first-motion amplitudes for the three components of the new co-ordinate system. This is done by multiplying a matrix containing the principal component amplitude data by the transpose of V:

$$\mathbf{A} = \begin{bmatrix} A_{\mathbf{P}} & 0 & 0 \\ 0 & A_{\mathbf{S}_1} & A_{\mathbf{S}_2} \end{bmatrix}.\mathbf{V}^{\mathrm{T}} \qquad \ldots(5.9)$$

The first row of the resultant matrix A will contain the P-wave first-motion amplitudes for the three components of the new co-ordinate system. The second row will contain the S-wave first-motion amplitudes for the three components of the new co-ordinate system. The amplitudes values in A are normalised by dividing them by the maximum absolute value in A.

5.2.3 Grid search to find possible mechanisms

In order to identify possible source mechanisms, the normalised P-wave and S-wave first-motion amplitudes are compared with similarly normalised P-wave and S-wave first-motion amplitudes calculated for a grid of double-couple mechanisms. First-motion amplitudes are calculated using the far-field Green's functions for a homogeneous full space, described in detail in appendix 5. The grid consists of mechanisms covering all strikes, rakes, and dips in 10° increments, plus 10,000 mechanisms with random strike, rake, and dip from a uniform distribution. This minimises the effect of grid spacing. Amplitudes are transformed to three principal components in order to save computer memory (i.e. three numbers take up less memory than six numbers). The P-wave and S-wave amplitudes for each component

are transformed to P, SV and SH amplitudes in the new co-ordinate system. The P amplitude is the amplitude of the seismic waves measured in the radial direction, the SV and SH are the amplitudes of the seismic waves measured in the transverse vertical and horizontal directions respectively. This transformation to principal components is carried out by multiplying the amplitude data by a certain transformation matrix. The three principal components can be transformed back to give the six required P-wave and S-wave first-motion amplitudes for comparison with observed data by multiplying by the transpose of the transform matrix in the same way as described in section 5.2.2.

Amplitude ratios, and hence normalised amplitudes, are only dependent on source-receiver direction. By transforming the seismic data and event location to a specific co-ordinate system, the source-receiver direction can be forced to be the same for each event, although the specific co-ordinate system will be different for each event. Since the source-receiver direction in the new co-ordinate system is the same for each event, the amplitudes calculated for the more than 20,000 different double-couple mechanisms making up the grid are the same for each event. Thus the amplitude grid only needs to be calculated once, and not for each event analysed. Calculating the amplitude grid typically takes a few hours on a mid-range PC such as a 200 MHz Pentium Pro with 64MB RAM. The method has to be fast enough that hundreds of events can be analysed per day, so if the amplitude grid must be calculated for each event analysed the method would fail this criterion. By using the co-ordinate transforms described, the amplitude grid is only calculated once as it is the same for each event analysed. This reduces the computational time significantly, so analysing an event typically takes less than a minute on a mid-range PC such as that defined above.

The misfit between picked and calculated amplitudes is a simple sum of squares. The misfit is a measure of how well the double-couple mechanisms fit the observed seismic data. The minimum misfit for all the double-couple mechanisms is established and a misfit threshold is defined that is 100 times greater than the minimum. Any double-couple mechanisms that give a misfit above that threshold are discarded. Of the more than 20,000 double-couple mechanisms that are first considered, about 100 will have a

misfit to the observed data below the threshold. These are the possible double-couple mechanisms for that event.

5.2.4 Transforming possible mechanisms to original co-ordinate system

The strikes, rakes, and dips that describe possible mechanisms are all measured in the new event-specific co-ordinate system. The parameters of the source mechanisms need to be defined in the original co-ordinate system. To transform back to the original co-ordinate system it is necessary to define the possible double-couple mechanisms using two unit vectors. The double-couple mechanism description of a seismic source gives two possible fault planes. One of the two planes must be chosen before the two vectors defining the double-couple mechanism can be calculated. The plane that is chosen is the nominal fault plane. One vector, n′, is the normal to the nominal fault plane, and the second vector, b′, is the direction of slip on that plane. These vectors are shown on figure 5.1. To express these vectors in terms of strike, rake, and dip a transform matrix can be derived that transforms the axes of a Cartesian co-ordinate system so that one of the axes is in the n′ direction and another of the axes is in the b′ direction. To calculate the transform matrix, the transformation needs to be considered in three steps. Firstly is a rotation clockwise around the z-axis by the strike angle minus 90°. The transform matrix for this step is:

$$\mathbf{T}_1 = \begin{bmatrix} \sin s' & \cos s' & 0 \\ -\cos s' & \sin s' & 0 \\ 0 & 0 & 1 \end{bmatrix} \qquad \ldots(5.10)$$

The new x-axis then lies in the strike direction. Next is a rotation anti-clockwise around the new x-axis by the dip angle. The transform matrix for this step is:

$$\mathbf{T}_2 = \begin{bmatrix} 1 & 0 & 0 \\ 0 & \cos d' & \sin d' \\ 0 & -\sin d' & \cos d' \end{bmatrix} \qquad \ldots(5.11)$$

The new z-axis lies in the n′ direction. Next is a rotation clockwise around the new z-axis by the rake angle. The transform matrix for this step is:

$$\mathbf{T}_3 = \begin{bmatrix} \cos r' & -\sin r' & 0 \\ \sin r' & \cos r' & 0 \\ 0 & 0 & 1 \end{bmatrix} \qquad \ldots(5.12)$$

The x-axis the lies in the b′ direction, and the z-axis still lies in the n′ direction. The product of these three matrices is:

$$\mathbf{T} = \mathbf{T}_3.\mathbf{T}_2.\mathbf{T}_1 = \begin{bmatrix} \cos r'.\sin s' + \sin r'.\cos d'.\cos s' & \cos r'.\cos s' - \sin r'.\cos d'.\sin s' & -\sin r'.\sin d' \\ \sin r'.\sin s' - \cos r'.\cos d'.\cos s' & \sin r'.\cos s' + \cos r'.\cos d'.\sin s' & \cos r'.\sin d' \\ \sin d'.\cos s' & -\sin d'.\sin s' & \cos d' \end{bmatrix} \qquad \ldots(5.13)$$

Thus:

$$\begin{aligned} \mathbf{b}' &= [1 \quad 0 \quad 0]\mathbf{T} = [\cos r'.\sin s' + \sin r'.\cos d'.\cos s' \quad \cos r'.\cos s' - \sin r'.\cos d'.\sin s' \quad -\sin r'.\sin d'] \\ \mathbf{n}' &= [0 \quad 0 \quad 1]\mathbf{T} = [\sin d'.\cos s' \quad -\sin d'.\sin s' \quad \cos d'] \end{aligned} \qquad \ldots(5.14)$$

In equations 5.10 to 5.14, s' is the strike in the new co-ordinate system, measured clockwise from North (y-axis). d' is the dip in the new co-ordinate system, measured from the x-y plane. r' is the rake in the new co-ordinate system, measured clockwise from the strike direction i.e. positive rakes for normal faults.

b′ and n′ are transformed to the original co-ordinate system by multiplying them by the transpose of the original co-ordinate system to new co-ordinate system transform matrix:

$$\begin{aligned} \mathbf{b} &= [b_1 \quad b_2 \quad b_3] = \mathbf{b}'.\mathbf{R}^{\mathrm{T}} \\ \mathbf{n} &= [n_1 \quad n_2 \quad n_3] = \mathbf{n}'.\mathbf{R}^{\mathrm{T}} \end{aligned} \qquad \ldots(5.15)$$

The strike, rake, and dip of the possible double-couple mechanisms can then be found from b and n using the following relationships:

$$s = \tan^{-1}\left(\frac{-n_2}{n_1}\right)$$
$$d = \cos^{-1} n_3 \qquad \ldots(5.16)$$
$$r = \tan^{-1}\left(\frac{\frac{-b_3}{\sin d}}{b_1.\sin s + b_2.\cos s}\right)$$

In equation 5.16, s is the strike in the original co-ordinate system, measured clockwise from North (y-axis). d is the dip in the original co-ordinate system, measured from the x-y plane. r is the rake in the original co-ordinate system, measured clockwise from the strike direction i.e. positive rakes for normal faults.

Either the mechanism with the minimum misfit can be taken as the final result, or the possible mechanisms can be displayed allowing the final mechanism to be chosen by the user.

5.2.5 Incorporating a layered velocity model

The method that has been described relies on the rock mass between the source and receiver being homogeneous, and hence the seismic ray-path is a straight line. The direction of propagation, and hence the source-receiver direction, at the receiver will be the same as the ray take-off direction at the source. For a more complex velocity model, the direction of propagation at the receiver will not necessarily be the same as ray take-off direction since the ray-path may not be straight. To calculate the source mechanism from the recorded seismogram in such a case it is necessary to first calculate the actual take-off direction and then use that as a base to calculate theoretical wave amplitudes.

The seismic wave velocity model used for the Asfordby study is a 1D laterally homogeneous layered velocity model. This is the simplest model that is a good approximation to the real velocity structure of the rock mass surrounding the mine, and it has been discussed in detail in section 3.2.3. Such a model has the effect of changing the elevation of the direction of propagation along the length of the ray-path, while the azimuth remains constant. Thus it is necessary to calculate the direction of propagation

at the source i.e. calculate the take-off direction. To achieve this, the concept of a virtual sonde is introduced.

For each event location that is calculated, a virtual sonde location is also calculated such that if the seismic waves propagated through a homogeneous velocity structure in the direction of propagation at the source, the P-S delay time would be the same as that measured. For most events the direction of propagation at the sonde will not be the same as at the source. The three-component seismic data recorded at the sonde can be transformed onto a new co-ordinate system such that the direction of propagation at the source, and measured from the transformed data at the virtual sonde location, will be the same. The relationship between these co-ordinate systems and the sonde and virtual sonde locations is shown as figure 5.3.

Figure 5.3 The relationship between the actual sonde and virtual sonde locations for a given event. The different co-ordinate systems are also shown.

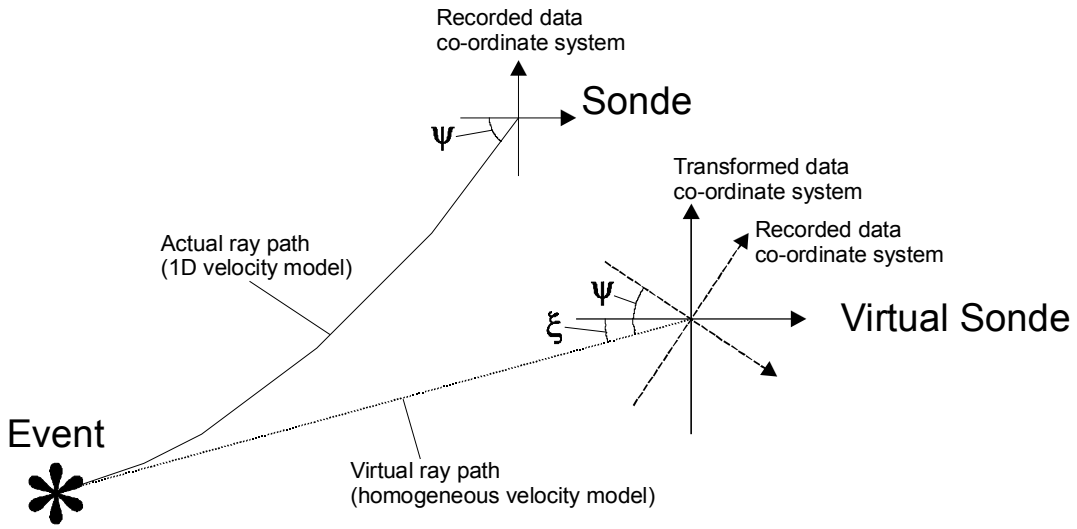

The co-ordinate transformation is simple when considered as a series of steps. Firstly the recorded seismic data are rotated anti-clockwise about the z-axis by the azimuth of the direction of propagation at the sonde, az_o. For azimuths measured clockwise from the x-axis, this will force the event to lie in the x-z plane with an elevation of ψ. The rotation matrix for this step is:

$$\mathbf{RM}_1 = \begin{bmatrix} \cos az_0 & -\sin az_0 & 0 \\ \sin az_0 & \cos az_0 & 0 \\ 0 & 0 & 1 \end{bmatrix} \quad \ldots(5.17)$$

Next is a rotation anti-clockwise about the new y-axis by ψ. The rotation matrix for this step is:

$$\mathbf{RM}_2 = \begin{bmatrix} \cos\psi & 0 & -\sin\psi \\ 0 & 1 & 0 \\ \sin\psi & 0 & \cos\psi \end{bmatrix} \quad \ldots(5.18)$$

This will force the event to lie along the positive x-axis. Next is a rotation clockwise about the new y-axis by ξ. The rotation matrix for this step is:

$$\mathbf{RM}_3 = \begin{bmatrix} \cos\xi & 0 & \sin\xi \\ 0 & 1 & 0 \\ -\sin\xi & 0 & \cos\xi \end{bmatrix} \quad \ldots(5.19)$$

This will force the event location to lie in the x-z plane, with an elevation of ξ. Finally, a rotation clockwise about the new z-axis by the azimuth of the direction of propagation at the event location is required. For a layered laterally homogeneous velocity structure this will be the same as the azimuth of the direction of propagation at the sonde, az_0. The rotation matrix for this step is:

$$\mathbf{RM}_4 = \begin{bmatrix} \cos az_0 & \sin az_0 & 0 \\ -\sin az_0 & \cos az_0 & 0 \\ 0 & 0 & 1 \end{bmatrix} \quad \ldots(5.20)$$

Multiplying the three-component seismic data recorded at the sonde by the product of these four rotation matrices, RM, given by:

$$\mathbf{RM} = \mathbf{RM}_1.\mathbf{RM}_2.\mathbf{RM}_3.\mathbf{RM}_4 \quad \ldots(5.21)$$

will transform the data onto a new co-ordinate system such that the direction of propagation measured from the transformed data will be the same as the actual direction of propagation at the source.

Thus the transformed three-component data will be the same as the geographical three-component seismic data that would be recorded at the virtual sonde if the ray path had travelled through a homogeneous velocity structure. The absolute amplitudes of the data will not be correct, but the relative amplitudes of the three components will be correct. Using the transformed data and the virtual sonde location it is possible to apply the method described above as the assumption of a homogeneous velocity model is satisfied.

5.2.6 Discussion of assumptions

The two assumptions that are made in this method are that the seismic events will have double-couple source mechanisms, and that a homogeneous full-space velocity model is a sufficiently accurate approximation to the actual velocity structure.

Ideally all seismic source mechanisms would be considered, but the limited data makes this impossible, and the assumption must be made that the event has a double-couple mechanism. Studies have shown that many mining induced earthquakes are +caused by shear failures on fault planes in a rockmass [*Spottiswoode and McGarr*, 1975; *Gay and Ortlepp*, 1979; *McGarr et al.*, 1979; *Hatherley et al.*, 1997], although this is not always the case [*Wong and McGarr*, 1990]. Seismic events that do not have a double-couple mechanism are also of importance to a mining induced seismicity study. The method could be easily adapted to only consider source mechanisms of another specific type e.g. tensile failure, and could then be applied to determine crack orientations if it was known that events would only have source mechanisms of the specified type.

A homogeneous full-space velocity model can only be used in a limited number of cases. For instance, in this study a 1-D laterally homogeneous velocity model is used when locating the events. It is demonstrated that a homogeneous velocity model is

applicable with the introduction of the concept of a virtual sonde. This concept allows the seismic data, that are subject to one co-ordinate transform, to be treated as if it is recorded at the virtual sonde location for an event where the ray-path travels through a region with a homogeneous velocity structure. For any microseismic study, either a full-space or a half-space velocity model can be used. Which is chosen depends upon the receiver depth. The receivers used in this study are at depths of 100m to about 550m below the ground surface. Source-receiver distances are typically in the same range. Thus it is unlikely that the ground surface has any effect on the recorded waveform, and the assumption of a full space is justified.

5.3 Synthetic tests

The inversion method described above can be tested extensively using synthetic seismic data. An attempt is made to test the method mimicking the patterns of seismicity that have been observed in mining environments.

5.3.1 Random locations and random double-couple mechanisms

Synthetic seismograms are generated using Green's functions for a homogeneous full space for 5000 events. The events have random locations, taken from a normal distribution, and random strike, rake and dip, taken from a uniform distribution. For each event, the double-couple mechanism that gives the best fit to the data is found and compared to the actual event mechanism. Double-couple mechanisms can be expressed as the orientation of the centres of the dilational and compressional quadrants. The so-called pressure axis (P-axis) is located in the centre of the dilational quadrant and the tension axis (T-axis) is located in the centre of the compressional quadrant [*Aki and Richards*, p110, 1980]. The fault plane for any double-couple mechanism makes an angle of 45° with both the P-axis and the T-axis. A correctly determined mechanism is defined as having pressure and tension axes which both make angles of less than 15° with those of the actual mechanism. This angle was chosen after comparing the 'beach-ball' representations of pairs of double-couple source mechanisms with P-axis and T-axis orientations varying by certain angles. There is little observable difference for angles P-axis and T-axis orientations of 15° or

less. An approximately determined mechanism is defined as having P-axis and T-axis orientations which both make angles of less than 45° with those of the actual mechanism. This angle was chosen in the same way as the 15° angle. A wrongly determined mechanism is defined as having either a P-axis or T-axis orientation that makes an angle of more than 45° with that of the actual mechanism. Examples of the differences between the 'beach-ball' representations of typical correct, approximate and wrong mechanisms are shown as figure 5.4.

Figure 5.4 Examples of what have been defined as (a) correct, (b) approximate, and (c) wrong determined mechanisms. The actual mechanism is shown on the left, and determined mechanisms are shown on the right.

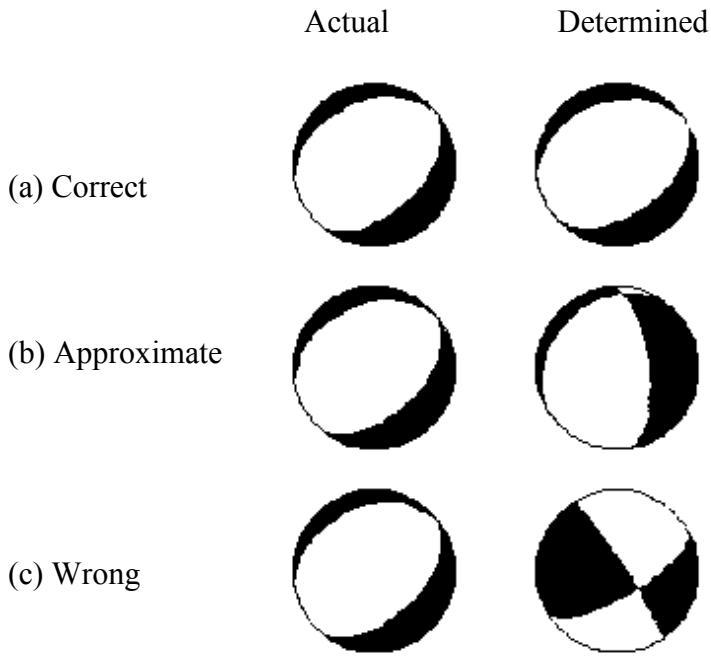

The percentages of correctly, approximately and wrongly determined mechanisms are shown as the first row in table 5.1. For each event there are generally only two distinct types (i.e. two of normal, reverse or strike-slip) of double-couple mechanism that fit the seismic data. This fact is reflected in the percentage of wrongly determined mechanisms being close to fifty. Another interesting outcome of this test is that there is no pattern in the locations of the events the method determines a wrong mechanism for i.e. correct results do not correspond to certain source-receiver directions.

Table 5.1 Percentages of correctly, approximately and wrongly determined mechanisms for synthetic seismograms with different levels of random noise.

No. of events	Noise Amplitude (standard deviation)	% correct	% approximate	% wrong
5000	0	17.54	34.54	47.92
5000	5% of signal	15.50	36.98	47.52
5000	10% of signal	11.84	37.68	50.48
5000	15% of signal	9.34	38.66	52.00
5000	20% of signal	7.32	36.16	56.52
5000	25% of signal	6.04	35.30	58.66
5000	No signal	0.58	13.10	86.32

The above test is carried out again, but this time the synthetic seismic wave amplitudes were replaced with random values i.e. background noise and no signal. The aim of this is to see what percentage of correct or approximate results can be attributed to chance. The results are shown as the last row in table 5.1. It is clear that the results of the real test (52% correctly or approximately determined) are a great deal better than chance (14% correctly or approximately determined).

Figure 5.5 is a histogram showing how the percentage of events varies with the angle between the determined T- axis and the actual T-axis. Figure 5.6 shows the histogram expressed as a cumulative sum. Figures 5.7 and 5.8 show the same information for the P- axis. The cumulative sum histograms for both axes are similar. They represent the level of confidence that either of the determined P-axis and T-axis orientations differ from the actual orientations by a certain angle. For example, it can be said with 70% confidence that one of the axis orientations makes an angle of less than 40° with the actual orientation of that axis.

5.3.2 The effects of noisy data

Synthetic seismograms are generated for 5000 events with the same locations and source mechanisms as those in the previous test. Random noise of various amplitudes is added to the seismograms. The noise has a normal distribution, and the standard deviation is expressed as a percentage of the maximum seismic wave amplitude. Examples of synthetic data with zero, 10%, and 20% noise added are shown as figure

5.9. For each event, the double-couple mechanism that gives the best fit to the data is found and compared to the actual event mechanism.

Figure 5.5 Histogram showing how the percentage of events varies with the angle separating the determined T-axis and the actual T-axis.

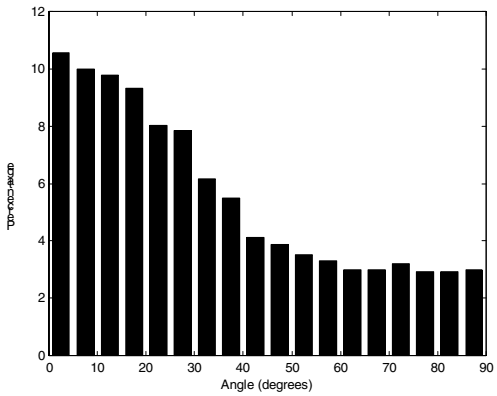

Figure 5.6 Histogram showing how the cumulative percentage of events varies with the angle separating the determined T-axis and the actual T-axis.

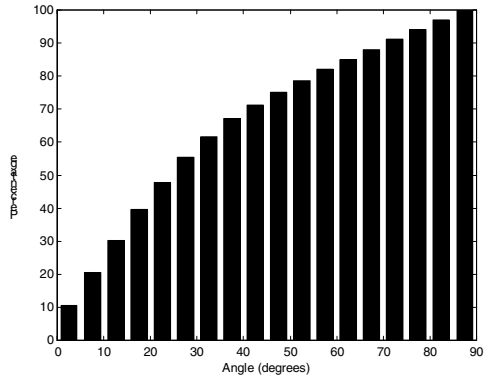

Figure 5.7 Histogram showing how the percentage of events varies with the angle separating the determined P-axis and the actual P-axis.

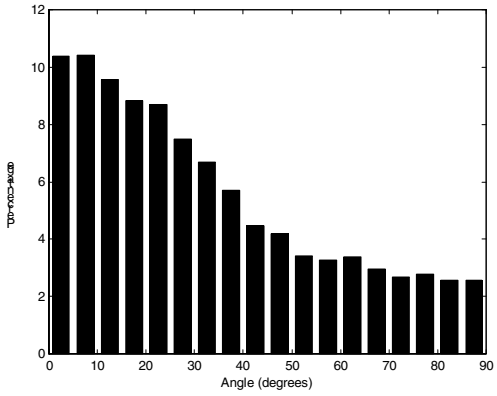

The percentages of correctly, approximately and wrongly determined mechanisms are shown in table 5.1. Noise below 15% causes only a small increase in the percentage of wrongly determined mechanisms. The percentage of correctly determined mechanisms decreases as the noise amplitude increases.

Figure 5.8 Histogram showing how the cumulative percentage of events varies with the angle separating the determined P-axis and the actual P-axis.

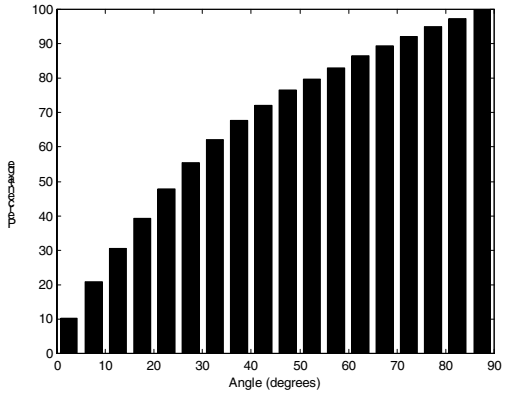

Figure 5.9 Examples of synthetic seismograms with (a) zero, (b) 10%, and (c) 20% random noise added.

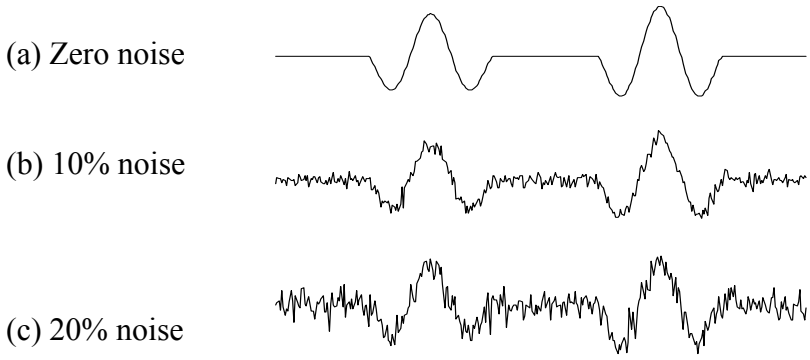

5.3.3 The effects of event mislocation errors

Synthetic seismograms are generated for 5000 events with the same locations and source mechanisms as those in the previous test. The locations are expressed in polar co-ordinates. Normally distributed random errors are added to the azimuth, elevation and displacement. The standard deviation of the errors is expressed as an angle in the

case of azimuth and elevation errors, and as a percentage of the displacement in the case of displacement errors.

The percentages of correctly, approximately and wrongly determined mechanisms are shown in table 5.2. Error in the displacement, i.e. the source-receiver distance, has no effect on the percentages of correctly, approximately and wrongly determined mechanisms. The fact that the relative amplitudes of the seismic waves are independent of displacement and only depend on the source-receiver direction is used by this method to reduce computing time. Thus it is expected that errors in the source-receiver distance do not effect the success of the method. For the rest of the tests, errors in displacement are ignored since they have no effect. Error in the azimuth and elevation of the event location, i.e. error in the source-receiver direction, does effect the success of the method. Errors up to 15° do not significantly increase the percentage of wrongly determined mechanisms. For errors above that the success rapidly approaches a level similar to that of chance.

Table 5.2 Percentages of correctly, approximately and wrongly determined mechanisms for synthetic seismograms calculated with event mislocation errors.

No. of events	Azimuth and elevation error	Displacement error	% correct	% approximate	% wrong
5000	0°	0%	17.54	34.54	47.92
5000	0°	10%	17.54	34.54	47.92
5000	5°	0%	16.36	34.76	48.88
5000	10°	0%	13.36	38.40	48.24
5000	15°	0%	8.80	40.98	50.22
5000	20°	0%	6.24	39.94	53.82
5000	30°	0%	3.84	33.90	62.26

5.3.4 Random locations and source mechanisms of a certain known type

Synthetic seismograms are generated for 5000 events with random locations taken from a normal distribution. The events have double-couple mechanisms with uniformly distributed random strikes, rakes and dips, with the constraint that the absolute values of the rakes all lie between 60° and 120°. Thus all the source

mechanisms are dip-slip type mechanisms. This test is designed to find out what effect having some information about the probable type of source mechanism will have on the success of the method. Dip-slip type mechanisms are chosen because it would be expected that seismicity induced by longwall mining would partly be controlled by near-vertical stresses, particularly in the region above and behind the face where the roof is collapsing. The P-axis and T-axis of a double-couple mechanism can be inferred to be the maximum (σ_{max}) and minimum (σ_{min}) compressive stress orientations [*Aki and Richards*, p110, 1980], although this is not necessarily the case [*McKenzie*, 1969]. If one of the two inferred stress orientations for a double-couple mechanism is near-vertical, then the other must be near-horizontal. Since the fault plane must make an angle of 45° with both inferred stress orientations, in such a case the double-couple mechanism must be of dip-slip type with a dip of approximately 45°. Such double-couple mechanisms have been observed by other studies [e.g. *Kaneko et al.*, 1990; *Hatherley et al*., 1997].

The method is applied to the synthetic seismograms. When applying the method, it is "known" that all the actual source mechanisms are of dip-slip type. After the possible mechanisms have been transformed from the event specific co-ordinate system to the original co-ordinate system (described in section 5.2.4), possible mechanisms that have absolute values of rake outside a certain range of values centred on 90° are ignored. The remaining possible mechanism that gives the best fit to the amplitude data is found and compared to the actual event mechanism.

The percentages of correctly, approximately and wrongly determined mechanisms are shown in table 5.3. Three different ranges of rake values are used to discriminate between dip-slip type and other types of double-couple mechanisms. The range of values that is the same as the range of actual rake values of the double-couple mechanisms, i.e. between 60° and 120°, give the highest success level, with a good representative mechanism being determined for more than 80% of the events. The percentage of events for which a correct double-couple mechanism is determined is over 40%, far higher than is found for random double-couple mechanisms. When a larger range of rake values is considered, i.e. between 45° and 135°, the success level

drops, but it is still quite high. Applying the test without any constraint on the values of rake considered gives a success level similar to that found for random double-couple mechanisms, as is expected.

Table 5.3 Percentages of correctly, approximately and wrongly determined mechanisms for synthetic seismograms calculated for dip-slip type double-couple mechanisms. The rake range is the range of absolute values of rake of possible double-couple mechanisms that were considered.

No. of events	Rake range	% correct	% approximate	% wrong
5000	60°-120°	40.68	40.68	18.64
5000	45°-135°	31.58	41.82	26.60
5000	0°-180°	19.24	35.30	45.46

5.3.5 Clustered locations with similar source mechanisms

Synthetic seismograms are generated for 5000 events located in 10 distinct clusters, each of 500 events. All the events in any one cluster have strikes and rakes in a 40° range centred on a random value for each cluster. Dips for one cluster of events are in a 20° range centred on a random value. This mimics the observation made in chapter 3, where spatial clusters of events are seen to have similar waveforms and hence similar source mechanisms.

The percentages of correctly, approximately and wrongly determined mechanisms are the same as those for random locations and random mechanisms. Since it is known that all the events in one cluster have a similar source mechanism, the determined mechanisms for all the events in one cluster may be used to find a mechanism that approximates the similar mechanisms of all the events. This is attempted by using a minimisation technique to find the mechanism closest to all the individual mechanisms in one cluster. Before a minimisation can be applied to the determined source mechanisms, an error function has to be defined. P-axes and T-axes are used to define the mechanisms rather than strike, rakes, and dips (see section 5.3.1). The error function is defined as the sum of the angles between the orthogonal P-axis and T-axis being considered and the determined P-axes and T-axes orientations of all the events in the cluster. A simplex minimisation is applied, using the error function described, to

find the orthogonal compressive and tensile stress directions that have a minimum value of the error function, and hence best represent the source mechanism solutions for one cluster.

The angles between the determined cluster representative P-axis and T-axis orientations and the actual P-axis and T-axis orientations of the double-couple mechanism for each cluster are given in table 5.4. The 'double-couple mechanism for each cluster' has been defined as the mechanism that has the strike, rake and dip which are at the centre of the ranges of strikes, rakes and dips of all the events in the cluster. The P-axis and T-axis orientations controlling the double-couple mechanisms for each cluster is well determined for most of the clusters. The method appears to determine the T-axis orientation more accurately than the P-axis orientation. This is probably the effect of the small sample size (only 10 clusters considered).

Table 5.4 The angle between the determined cluster representative T-axis and P-axis orientations and the actual T-axis and P-axis orientations used to calculate synthetic seismograms.

Cluster	Angle between determined and actual T-axis orientations	Angle between determined and actual P-axis orientations
1	4.7°	7.3°
2	12.5°	28.4°
3	13.1°	13.7°
4	7.9°	51.5°
5	15.4°	56.8°
6	6.5°	6.1°
7	5.2°	37.6°
8	15.9°	15.7°
9	5.1°	4.5°
10	1.8°	2.6°
Mean	**8.8°**	**22.4°**

5.3.6 Discussion of results of synthetic tests

The synthetic tests show that this method can determine a representative double-couple source mechanism with a slightly more than 50% confidence level from a single three-component seismic record for an event considered in isolation. For each recorded event there are usually two possible double-couple source mechanisms that fit the

available data. Thus it is possible to exclude certain types of mechanism with a high confidence i.e. only mechanisms that fit the data are possible.

The results of the test using events with a known type of source mechanism show that given some knowledge about the type of mechanism that would be expected, double-couple source mechanisms are determined with a high level of confidence, greater than 80%. This knowledge can be gained in a variety of ways e.g. examining structures controlling seismicity to give possible fault plane orientations; using rock mechanical models to exclude types of source mechanism; using analogous studies to predict what types of source mechanisms might be expected.

The test designed to mimic the spatial clustering of seismic events with approximately the same source mechanism, which is often observed in mining environments, also has encouraging results. It is demonstrated that the actual P-axis and T-axis orientations for a cluster can be quite accurately determined by considering the P-axis and T-axis orientations of each event in the cluster. Such clusters are regularly observed when monitoring mining induced seismicity, and in these cases this method would be useful.

5.4 Determining P-axis and T-axis orientations rather than double-couple mechanisms

5.4.1 Synthetic test

All the tests described in section 5.3 are concerned with finding the double-couple mechanism that best fits the seismic amplitude data, and comparing it with the actual mechanism. The actual and calculated mechanisms are compared by examining the angles between P-axis and T-axis orientations for the two mechanisms, and the determined mechanism is defined as being correct, approximate or wrong depending on these angles. This sections describes a slightly different approach, where rather than finding the strike, rake and dip of a double-couple mechanism which fits the data, the P-axis and T-axis of a double-couple mechanism are found. In section 5.3.1 it was stated that the P-axis and T-axis determined by the method described in section 5.2 have 70% confidence errors of about 40°. This suggests that the P-axis and T-axis are

perhaps better parameters to calculate from the seismic data, which the test described here is designed to investigate.

The top 100 double-couple mechanisms that best fit the seismic amplitude data are found using the method described above. P-axis and T-axis orientations are calculated for the 100 mechanisms. Using a minimisation identical to that described in section 5.3.5 orthogonal P-axis and T-axis orientations are then found that best fit the P-axes and T-axes orientations from the 100 possible double-couple mechanisms found for the event being analysed. In this way, representative P-axis and T-axis orientations are determined for the event by considering a large number of possible mechanisms, rather than finding the single double-couple mechanism that best fits the amplitude data.

This analysis is carried out for 10,000 synthetic events with random locations and random double-couple mechanisms. For each event the angles between the best fit P-axis and T-axis orientations and the P-axis and T-axis orientations of the actual double-couple mechanism are calculated. The standard deviations of each of the three components of the hundred P-axis and T-axis vectors are also calculated. If the P-axes and T-axes orientations of the 100 possible mechanisms are all similar these standard deviations will be low. If the P-axes and T-axes orientations of the 100 possible mechanisms are scattered these standard deviations will be high. The standard deviations of the three components of the 100 possible P-axes and T-axes vectors are summed for the P-axes and T-axes. This gives two numbers, one describing how similar the possible P-axes orientations are, and one describing how similar the possible T-axes orientations are.

Figure 5.10 shows the relationship between the angle separating best fit and actual P-axes and T-axes orientations and the sum of the three standard deviations. The top plot shows the relationship for the T-axis, the bottom plot shows the relationship for the P-axis. Lines relating to a range of confidence levels are also shown on each plot. These lines have been calculated by considering points within a number of windows of summed standard deviation. For each window, the angle value below which the specified percentage of points lies is found. Thus 95% of the data is below the 95%

line shown, and so on. By assuming that these lines then represent confidence levels, it would be possible to define a certain confidence level error for a best fit P-axis or T-axis orientation from the standard deviation of the 100 possible P-axes or T-axes vectors.

Figure 5.10 Scatter plots showing the relationship between the summed standard deviations of the three components of P-axis and T-axis vectors of possible double-couple mechanisms and the angle separating the best fit and actual axes orientations for 10,000 synthetic events. The top plot shows the relationship for the T-axis, the bottom plot shows the relationship for the P-axis. Lines relating to various confidence levels are also shown.

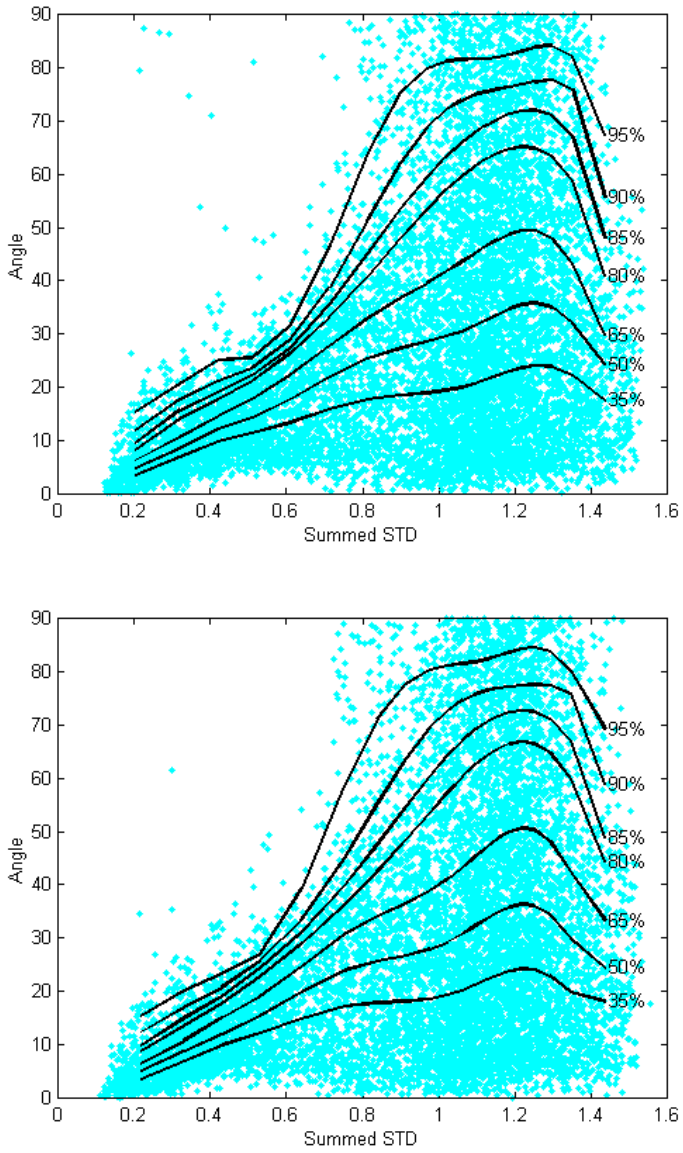

5.4.2 Discussion

A method has been described that differs from the method described in section 5.2 in that it finds P-axis and T-axis orientations, rather than the strike, rake and dip, of a double-couple mechanism that fits the amplitude data. Synthetic tests show that the method can make a reliable estimate of the error in the P-axis and T-axis orientations by considering the standard deviations of the three components of the possible P-axes and T-axes vectors. This is a considerable improvement on the previous method, which finds the double-couple mechanism that best fits the seismic amplitude data. Using the previous method the confidence level is the same for each analysed event, and this confidence level is low unless certain assumptions are made. This means the method is only useful for large numbers of events with similar characteristics, or for events where some constraint can be made on the type of mechanism. Using the axis-fitting method the confidence level will vary for each event, but the confidence level will be known.

This is an important result. It means that given three-component seismic data of sufficient quality, with a relatively simple velocity structure (e.g. layered), unambiguous information about P-axis and T-axis orientations can be obtained. This information could be used to infer the orientation of the maximum and minimum compressive stresses, or to make conclusions about possible fault plane orientations. The only assumption that must be made is that events have a double-couple mechanism. Furthermore, it may be possible to construct a composite source mechanism for a number of events using the P-axis and T-axis information from those events. For example, for a cluster of events with similar source mechanisms (see section 5.3.5) P-axes orientations may be determined with high confidence levels for some events and T-axes orientations for others. The P-axis and T-axes orientations could then be used to construct a double-couple mechanism for that cluster. If this is done, then that composite source mechanism could be used to exclude other possible types of source mechanism, and hence obtain the higher confidence levels described in section 5.3.4.

It should be noted that an approximation to either the P-axis or T-axis can be made by considering the source-receiver direction and the first-motion polarity of the P-wave. If the P-wave first motion is dilational, then the source-receiver direction must lie in the dilational quadrant. Thus the source-receiver direction is a first approximation of the P-axis orientation. A compressional P-wave first motion means that the source-receiver direction must lie in the compressional quadrant and hence is a first approximation of the T-axis orientation. However, high confidence error bounds for these approximate axis orientations would be too large for significant conclusions to be drawn from the orientations calculated.

5.5 Conclusions

A method has been described that determines double-couple mechanisms that are good fits to P-wave and S-wave amplitude data from a single three-component record. By assuming a homogeneous velocity model the method can use co-ordinate transforms to vastly reduce computing time. If a homogeneous velocity model can not be assumed, the concept of a virtual sonde can be used for relatively simple velocity models so that the method is still applicable. The reduced computing time makes the method suitable for use in a mining study where large numbers of events are typically recorded and need to be analysed within a short time limit. Synthetic testing of the method has shown that double-couple mechanisms can be determined with a confidence of slightly more than 50% for individual events. If some information is known about the type of possible double-couple mechanisms, this confidence level can be greatly increased to more than 80%.

An application of the method has been described that determines the P-axis and T-axis orientations of the source mechanism of the event. It is possible to assign errors for a certain confidence to these determined orientations using the results of synthetic testing of the method. This means unambiguous information about the P-axis and T-axis orientations, and therefore inferred maximum and minimum compressive stress orientations, for an individual event can be obtained from a single three-component seismogram, provided the assumptions made are valid.

The synthetic tests carried out using the method described demonstrate that while there are limitations to the method, in most cases it should be possible to derive meaningful information about the P-axis and T-axis orientations of the double-couple mechanism of an event. From the axis orientations, strike, rake and dip can be calculated to examine fault plane orientation, or the direction of σ_{max} and σ_{min} can be inferred. Thus it is possible to use just a single three-component seismometer to monitor a region of rock mass and still obtain unambiguous fault orientation or stress orientation data.

6 INFERRED STRESS ORIENTATIONS AND SOURCE MECHANISMS FOR ASFORDBY DATA

6.1 Introduction

In the previous chapter, a method is described that can be applied to a single three-component record of a seismic event to derive information about the source mechanism. Nearly all microseismic events recorded at Asfordby were recorded by a single three-component seismometer. In fact the method was developed with the specific aim of being able to find some meaningful information about the source mechanisms, in particular the orientation of the P-axis and T-axis, of the seismic events recorded at Asfordby. The limitations of the method were explored, and it was found that the method provides meaningful information if applied to the records of longwall mining induced seismic events. However, there were a few conditions that had to be satisfied: the source mechanisms had to be pure shear failures (double-couple mechanisms); the velocity structure had to be relatively simple (e.g. laterally homogeneous layers); the data had to be of high quality so reliable picks of the seismic wave first-motions could be made. The last two conditions are satisfied for the data recorded at Asfordby. The first condition, that recorded events have double-couple mechanisms, is not necessarily satisfied for the events recorded at Asfordby. However, as previously stated (section 5.2.6), analogous studies [e.g. *Hatherley et al.*, 1997] have shown that many mining induced earthquakes are caused by shear failures on fault planes. Thus it is assumed that the events recorded at Asfordby are similarly caused by shear failures.

Analysis of the location of the induced seismicity recorded during Asfordby Phase-One suggests that it is strongly controlled by geological structures, but it shows similarities to modelled seismicity for strong roof conditions with regular weightings [*Gale and Nemcik*, 1998]. This is an interesting result, as the Asfordby Phase-One face suffered from severe weightings. The seismicity recorded during Phase-Two shows the more expected patterns of longwall induced seismicity [e.g. *Hatherley et al.*, 1997]. Rock mechanical modelling also predicts stress directions and source mechanisms for

the induced seismicity [e.g. *Gale and Nemcik*, 1998]. By examining any source mechanism information it should be possible to make a more accurate comparison between the observed patterns of induced seismicity, and those predicted by modelling. If the observed and predicted seimicity show very different characteristics, then the extra source mechanism and stress direction information should lead to a better understanding of the processes causing the observed seismicity.

The seismicity recorded during the two phases of mining show very different patterns. The differences between the seismicity observed during the two phases of monitoring is attributed (see chapter 3) to the change in mining strategy (the narrower face during Phase-Two) and the change in geology (the presence of the sill above the face in Phase-Two). The seismicity recorded during Phase-Two can be split into two distinct clusters showing different characteristics. There are several strong layers in the roof above Panel 101 at Asforbdy, in particular the Sherwood Sandstone. Strong layers in the roof above a longwall are a possible cause of weightings [*Minney et al.*, 1997] such as those experienced during Phase-One of mining. Thus it is probable that the Sherwood Sandstone is having an effect on the location of seismicity. The seismicity recorded during Phase-Two can be split into two distinct clusters showing different characteristics. It is suggested in section 3.4.1 that the presence of the sill above the face in Phase-Two is responsible for the two distinct clusters of seismicity. An explanation is that the sill, also a strong layer, is controlling the effect of the Sherwood Sandstone aquifer. The sill is below the sandstone, and a strong layer in the roof closer to the seam may mean that the roof can collapse in a more controlled fashion, rather than in large blocks causing weightings. The results of analysis of source mechanisms of the two clusters of seismicity should determine whether this interpretation is supported by the seismic data.

The importance of even a small amount of information about the source mechanisms of recorded events is clear. For a mine to be as safe and as efficient as possible it is necessary to have a thorough understanding of the interactions between mining strategy and geological structures that control the behaviour of the surrounding rock mass. Any information about controlling stress directions will allow a much better

understanding of these interactions, which in turn should lead to a safer, more efficient, mine.

6.2 P-axis and T-axis orientations for Asfordby data

In section 5.4.1 a method is described that determines the P-axis and T-axis orientations and error bounds, of the double-couple mechanism of an event. It does this by firstly finding 100 possible double-couple mechanisms that fit the observed amplitude data, and calculating the P-axis and T-axis orientations for each of the 100 mechanisms. Using a simplex minimisation, orthogonal P-axis and T-axis orientations are found that best-fit the 100 possible pairs of axes orientations. These are taken to be representative of the actual P-axis and T-axis orientations for that event. Two parameters are also calculated that describe how similar the 100 pairs of P-axes and T-axes are. These parameters are the sum of the standard deviations of the three components of the 100 pairs of P-axis and T-axis vectors. In section 5.4.1 a clear relationship was shown between these two parameters and the accuracy of the determined axis orientations. Thus for any event it is possible to calculate P-axis and T-axis orientations, and using the two standard deviation parameters calculated, error bounds for a certain confidence level can also be found. The P-axis, or pressure axis, and the T-axis, or tension axis, are the principal stress axes if the event fault plane is a plane of maximum shear [*Aki and Richards*, p110, 1980]. However it should be noted that if the event fault plane is a reactivated existing fault plane then this is not necessarily the case [*McKenzie*, 1969]. Assuming that the fault planes of seismic events recorded at Asfordby are planes of maximum shear, the maximum and minimum compressive stress orientations can be inferred to be the P-axis and T-axis orientations.

6.2.1 Comparing P-axis and T-axis orientations calculated for the same event recorded at two sondes

In section 3.2.2 a number of events that were recorded at two sondes during Phase-Two of monitoring are analysed to prove that the event location method works within estimated errors. The same thing can be done to prove that the method of determining

P-axis and T-axis orientations works within estimated errors. For each three-component event record the P-axis and T-axis orientations are calculated. Error bounds for the 95% confidence level are also calculated for each axis. The calculated axis orientations from two three-component records of the same event recorded at two different sondes can then be compared. If the angle between the calculated axis orientations from the two different records is less than the sum of the error bounds then the method is successful. The analysis has only been applied to the seismograms that were of sufficiently high quality; i.e. first motion amplitudes could be clearly identified. Typical principal component first-motion waveforms for such high quality data are shown as figure 6.1.

Figure 6.1 Typical principal component waveforms. The vertical dotted line shows the approximate arrival time. The waveforms are very similar for the three principal components. The effect of shear-wave splitting can be seen in the two S-wave components.

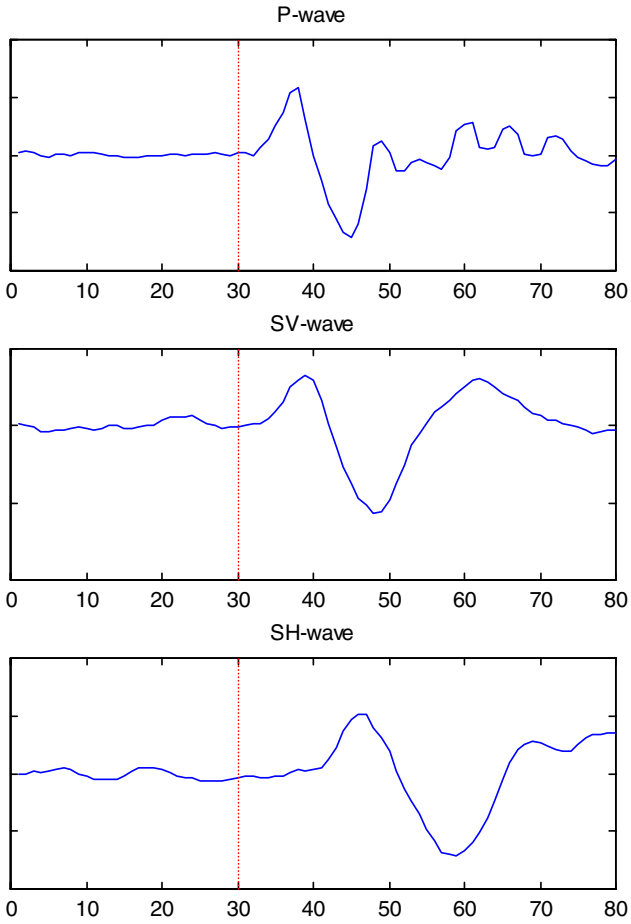

Table 6.1 The results of determining and comparing the maximum compressive stress orientations calculated for the same event recorded at two different sondes.

Event 1	Event 2	Angle between σ_{max} directions (°)	Event 1 σ_{max} error (°)	Event 2 σ_{max} error (°)
c2_03_002	d2_03_006	41	83	83
c2_03_003	d2_03_022	5	83	83
c2_03_004	d2_03_027	14	21	20
c2_03_005	d2_03_028	11	83	84
c2_03_006	d2_03_045	1	83	83
c2_03_007	d2_03_081	48	83	83
c2_03_008	d2_03_221	24	83	83
c2_04_001	d2_04_026	64	83	83
c2_04_002	d2_04_061	34	83	83
c2_04_003	d2_04_118	36	83	83
c2_06_005	d2_06_009	42	82	84
c2_06_189	d2_06_306	5	84	83
c2_06_303	d2_06_475	14	83	83
c2_07_013	d2_07_032	16	83	84
c2_07_016	d2_07_036	16	82	75
c1_06_005	d1_06_009	75	83	83
c1_06_142	d1_06_243	7	26	21
c1_06_189	d1_06_306	35	83	84
c1_06_303	d1_06_475	6	83	83
c1_07_013	d1_07_032	15	83	83
c1_07_016	d1_07_036	28	81	84
c1_07_022	d1_07_042	17	83	84
c2_06_005	d1_06_009	62	83	83
c2_06_189	d1_06_306	32	84	84
c2_06_303	d1_06_475	9	83	83
c2_07_013	d1_07_032	59	83	83
c2_07_016	d1_07_036	25	82	83
c1_06_005	d2_06_009	55	83	84
c1_06_142	d2_06_243	9	26	21
c1_06_189	d2_06_306	2	83	83
c1_06_246	d2_06_386	53	82	82
c1_06_303	d2_06_475	12	83	83
c1_07_013	d2_07_032	38	83	84
c1_07_016	d2_07_036	14	81	75
c1_07_022	d2_07_042	12	83	81

Table 6.2 The results of determining and comparing the minimum compressive stress orientations calculated for the same event recorded at two different sondes.

Event 1	Event 2	Angle between σ_{min} orientations (°)	Event 1 σ_{min} error (°)	Event 2 σ_{min} error(°)
c2_03_002	d2_03_006	10	25	53
c2_03_003	d2_03_022	4	22	23
c2_03_004	d2_03_027	16	82	82
c2_03_005	d2_03_028	5	16	50
c2_03_006	d2_03_045	7	12	17
c2_03_007	d2_03_081	28	16	12
c2_03_008	d2_03_221	19	18	10
c2_04_001	d2_04_026	29	22	14
c2_04_002	d2_04_061	15	10	15
c2_04_003	d2_04_118	38	16	23
c2_06_005	d2_06_009	35	19	16
c2_06_189	d2_06_306	4	20	22
c2_06_303	d2_06_475	10	22	21
c2_07_013	d2_07_032	18	22	25
c2_07_016	d2_07_036	15	23	29
c1_06_005	d1_06_009	26	22	17
c1_06_142	d1_06_243	12	80	82
c1_06_189	d1_06_306	17	20	19
c1_06_303	d1_06_475	2	23	22
c1_07_013	d1_07_032	16	17	22
c1_07_016	d1_07_036	17	23	26
c1_07_022	d1_07_042	22	22	23
c2_06_005	d1_06_009	29	19	17
c2_06_189	d1_06_306	20	20	19
c2_06_303	d1_06_475	1	23	22
c2_07_013	d1_07_032	48	22	22
c2_07_016	d1_07_036	19	23	26
c1_06_005	d2_06_009	33	21	15
c1_06_142	d2_06_243	41	80	82
c1_06_189	d2_06_306	2	20	22
c1_06_246	d2_06_386	9	22	23
c1_06_303	d2_06_475	12	23	21
c1_07_013	d2_07_032	51	17	25
c1_07_016	d2_07_036	11	23	29
c1_07_022	d2_07_042	17	22	23

The results of this analysis are summarised in table 6.1 for the calculated P-axis orientations and table 6.2 for the calculated T-axis orientations. Table 6.1 shows that for most of the P-axis orientations the error bounds are so large (>80°) that the results are almost meaningless (an error of 90° would mean that any orientation is possible). However, the angle between the two calculated P-axis orientations is typically far less than the high error estimates. This is because the errors given are for a 95% confidence level, and the various confidence levels plotted on figure 5.9 show that the errors for the 50% confidence level for instance are much lower than those for the 95% confidence level. So we would expect that the angle between the two calculated P-axis orientations would be less than the 50% confidence error for half of the events, and so on. There are three pairs of events that have low 95% confidence errors, typically about 20°-25°. The angles between the two calculated P-axis orientations for these three pairs of events are significantly less than the sum of the errors. Again this is due to the 95% confidence error being used, whereas a lower confidence error would be smaller. Table 6.2 shows that the pairs of events that have large error bounds for the P-axis orientations have small error bounds for the T-axis orientations, and vice-versa. Of all the pairs of events in table 6.2, only two have angles between their calculated T-axis orientations that are larger than the sum of the two error bounds. There are 35 pairs of events in total, so the percentage of pairs of events for which the angle between the calculated T-axis orientations is less than the sum of errors is 94%. This sort of percentage would be expected since the 95% confidence level errors are used.

This analysis shows that the method can determine P-axis and T-axis orientations from a single three-component seismogram and calculate accurate error bounds. This shows that the assumptions made by the method (section 5.2.6) are satisfied for the Asfordby microseismic data. The P-axis and T-axis orientations for an event with a double-couple mechanism are the same as the maximum and minimum compressive stress orientations if the fault plane of the event is a plane of maximum shear. Thus it should be possible to obtain some information about causative stress directions for most of the events recorded during both phases of monitoring at Asfordby.

6.2.2 P-axis and T-axis orientations calculated for events recorded during Phase-One

The seismicity recorded at the Cants Thorn 1 upper sonde during the first phase of monitoring shows some very interesting features. Of particular interest is a linear cluster of events above the tail gate. The locations of events in this cluster advanced at the same time and in the same direction as the face. Thus the cluster of events is interpreted as being a propagating fracture, beginning high in the roof and extending down to the Sherwood Sandstone aquifer. The propagation is shown in figures 3.14 and 3.15, which clearly demonstrate the association with face advance. The other possibility is that the seismic events are occurring as slip on a pre-existing fault plane, the part of the fault plane being reactivated controlled by face position. The source mechanisms of the events in that cluster should distinguish between these two possibilities. This is important since the first case would agree with the rock mechanical model of *Gale and Nemcik* [1998] for strong roof conditions. The second case, reactivation of a fault plane, would not necessarily agree with the model. The events in the main cluster all have similar recorded waveforms, which suggests that the events all have similar source mechanisms. This means that information from a number of events can be used to deduce a composite source mechanism.

P-axis and T-axis orientations and error bounds are calculated for 104 of the events recorded at the Cants Thorn 1 upper sonde. These events have records of a sufficiently high quality that accurate picks can be made of first-motion amplitudes. For most of the events the P-axis orientation is the more accurately determined of the two axis orientations i.e. it has smaller error bounds. The calculated P-axis orientations are shown as figures 6.2 to 6.4. Figure 6.2 shows a plan view. Figure 6.3 shows a sectional view looking perpendicular to the direction of face advance from the S (i.e. direction of face advance is left to right). Figure 6.4 shows a sectional view looking in the direction of face advance from the W (i.e. direction of face advance is into the page). The calculated T-axis orientations are shown as figures 6.5 to 6.7. Figures 6.5 to 6.7 show the same views as figures 6.2 to 6.4 respectively. On all of these six figures the axis orientations are shown by cones. The event location is at the apex of the cone. The calculated axis orientation is along the axis of the cone, and the width of the cone is

the error bound. Therefore it can be said with 95% confidence that the actual axis orientation lies within the cone. The probability that any orientation is the correct axis orientation is highest along the axis of the cone, and decreases towards the outside surface of the cone. For instance, in the case of the wide cones that correspond to large 95% confidence error bounds, the correct axis orientation is most likely to be along the axis of the cone. Cones are not plotted for errors larger than 45°. Similarly to the plot of event location error volumes, it is the smaller (i.e. sharper) cones that have the greatest importance as these have the smallest uncertainties. The P-axis or T-axis orientations that are calculated are all approximately parallel to the source-receiver direction. Thus it is the axis that has an orientation closest to the source-receiver direction that is the more accurately determined. In section 5.4.2 it was stated that the source-receiver direction is an approximation to either of the P-axis or T-axis orientations, depending on the first-motion polarity of the P-wave. It was noted in section 5.4.2 that such approximate orientations would have such large error bounds that they would be meaningless. However, this is the reason that the axis orientation closest to the source-receiver direction is the more accurately determined.

Figure 6.2 Plan view of calculated maximum compressive stress orientations for events recorded at the Cants Thorn 1 upper sonde during the first phase of mining. Cones represent the size of the 95% confidence errors.

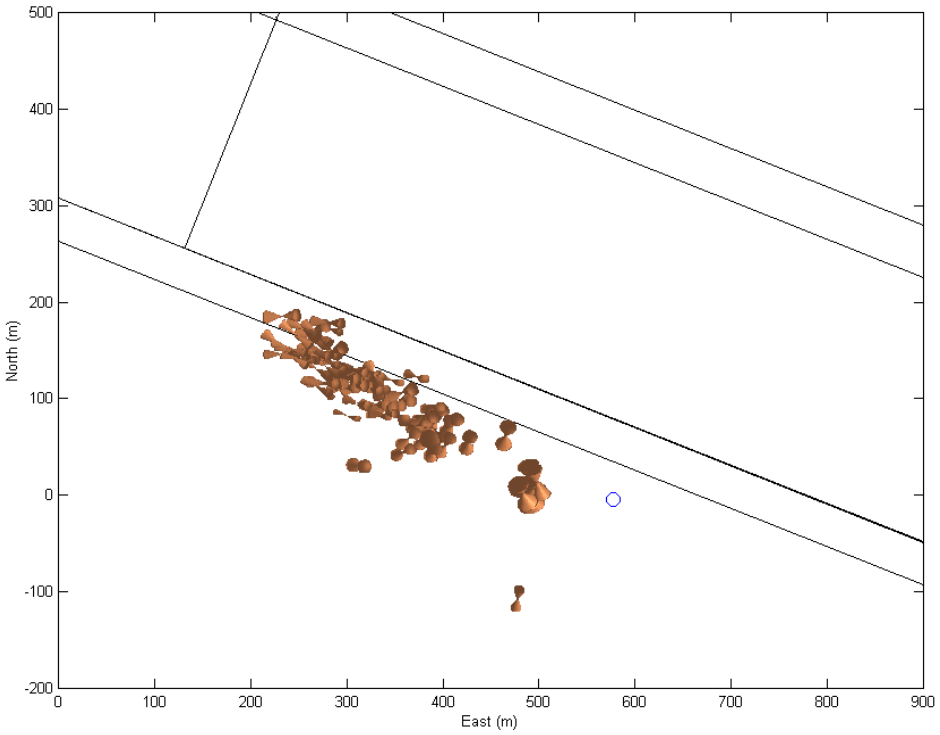

Figure 6.3 Sectional view of calculated maximum compressive stress orientations for events recorded at the Cants Thorn 1 upper sonde during the first phase of mining, looking perpendicular to the direction of face advance from the South. Cones represent the size of the 95% confidence errors.

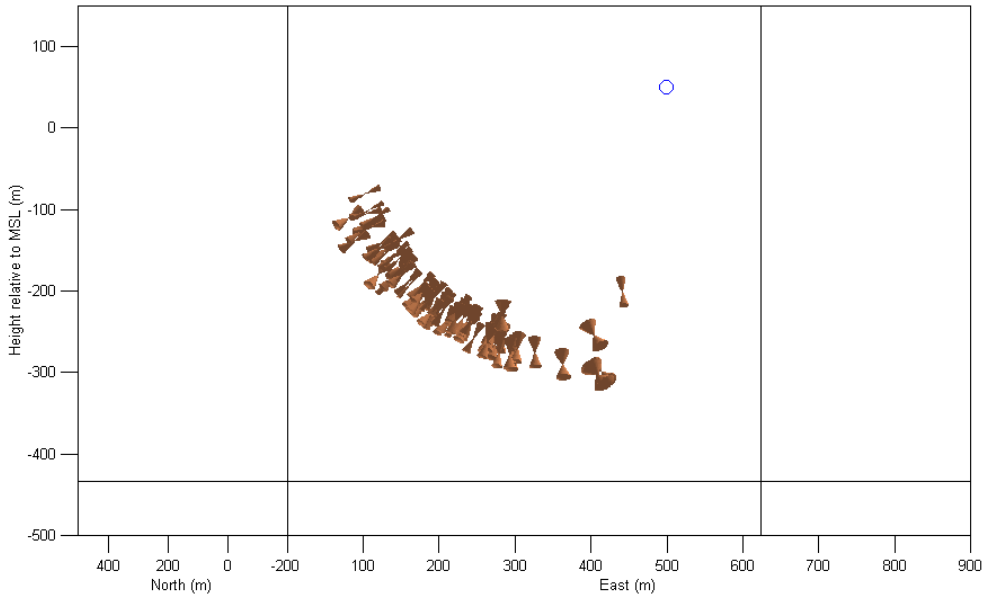

Figure 6.4 Sectional view of calculated maximum compressive stress orientations for events recorded at the Cants Thorn 1 upper sonde during the first phase of mining, looking along the direction of face advance from the West. Cones represent the size of the 95% confidence errors.

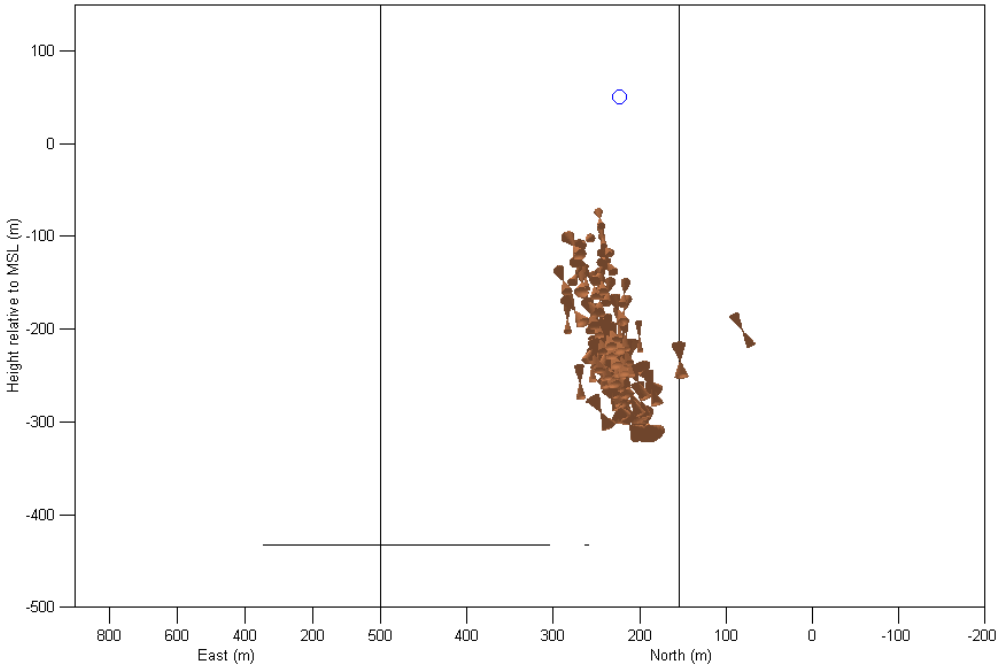

Figure 6.5 Plan view of calculated minimum compressive stress orientations for events recorded at the Cants Thorn 1 upper sonde during the first phase of mining. Cones represent the size of the 95% confidence errors.

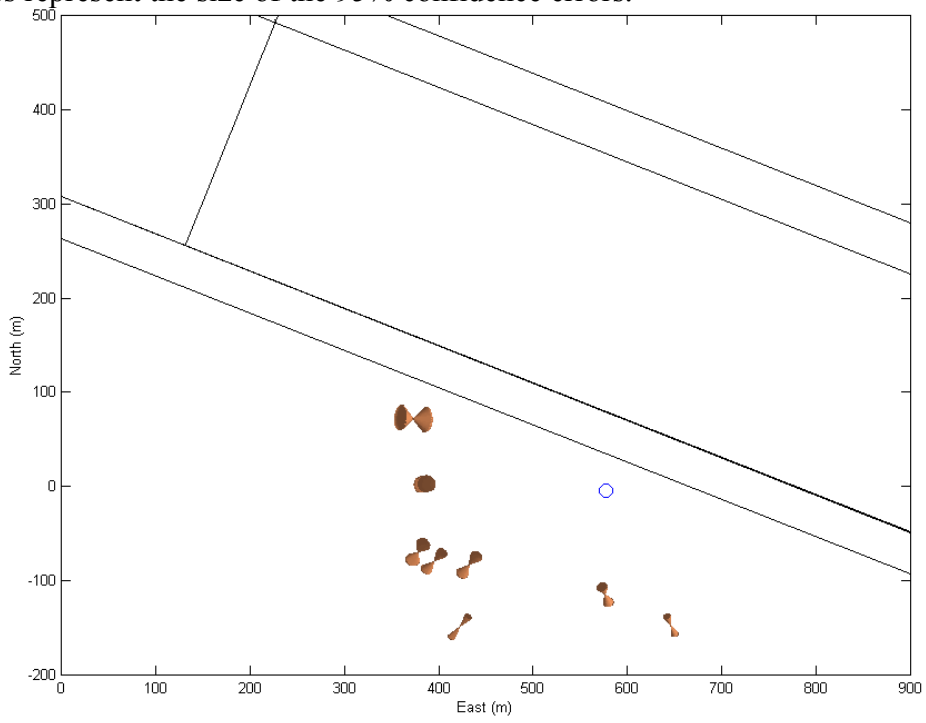

Figure 6.6 Sectional view of calculated minimum compressive stress orientations for events recorded at the Cants Thorn 1 upper sonde during the first phase of mining, looking perpendicular to the direction of face advance from the South. Cones represent the size of the 95% confidence errors.

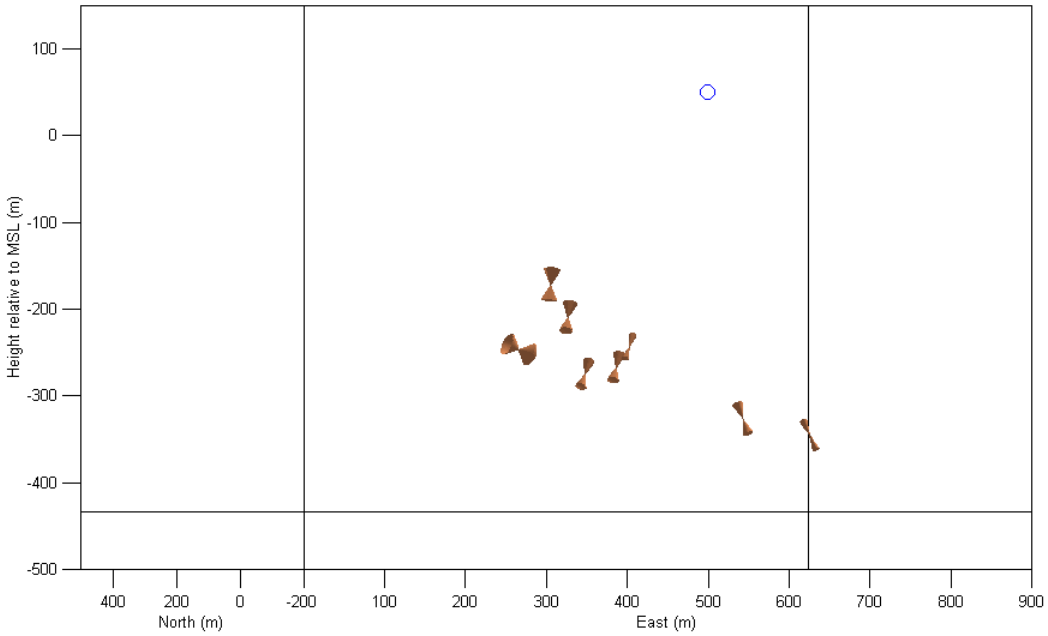

Figure 6.7 Sectional view of calculated minimum compressive stress orientations for events recorded at the Cants Thorn 1 upper sonde during the first phase of mining, looking along the direction of face advance from the West. Cones represent the size of the 95% confidence errors.

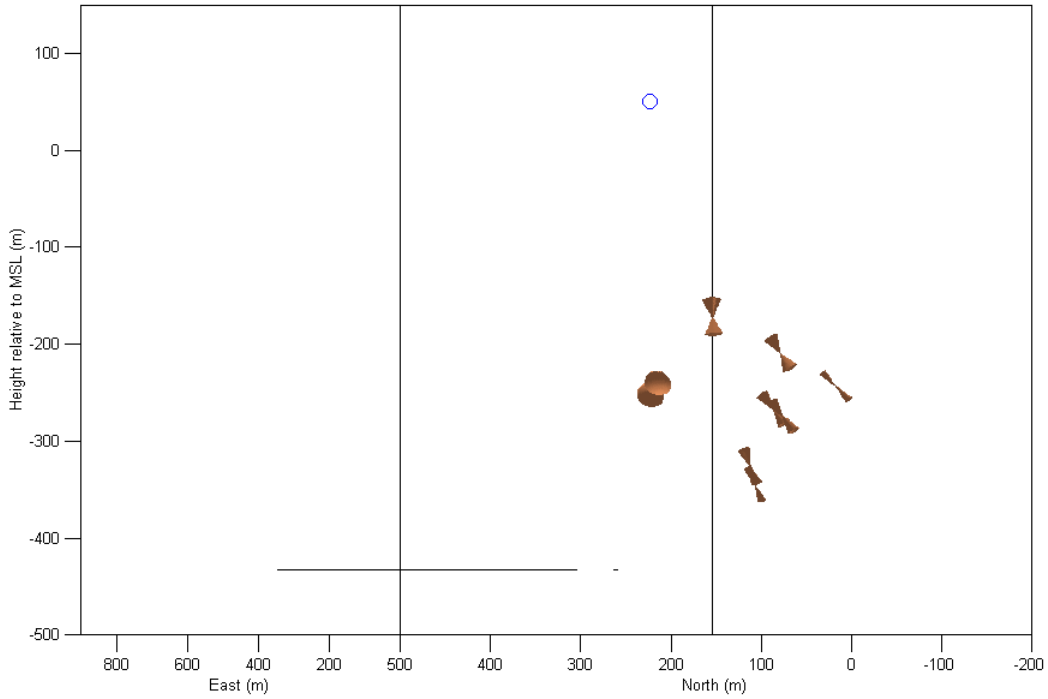

Typical 95% confidence error bounds for the calculated P-axis orientations are between 10° and 20°. Only a small number of calculated P-axis orientations have error bounds above 45°, and these are not shown on figures 6.2 to 6.4. There are clear relationships between the geometry of the main cluster of events (those above the tail gate) and the calculated P-axis orientations. Figure 6.2 shows that the azimuths of the calculated P-axis orientations are approximately the same as the azimuth of the linear cluster of events. Figure 6.3 shows clearly that the P-axis orientations are perpendicular to the linear cluster of events, and in figure 6.4 it can be seen that the calculated P-axis orientations all lie within the same plane as the cluster of events. The error bounds at the higher end of the main cluster tend to be smaller than at the lower end of the cluster. This reflects the fact that the highest quality data were recorded for events in the higher end of the cluster. The calculated P-axis orientations of the events at the lower end of the main cluster (i.e. at approximately 400m E and 50m N) are all nearly vertical. The P-axis and T-axis are orthogonal so the T-axis orientations for these events must be approximately horizontal. Since both axis orientations must make angles of 45° with both nodal planes, the double-couple mechanism for these events must be a normal dip-slip failure with a dip of approximately 45°. The small cluster of events at the lower tip (at approximately 500m E 0m N) of the main cluster has P-axis orientations that are not perpendicular to the linear direction of the cluster, but are at approximately 45° to it (i.e. they are oriented up-West/down-East). In section 3.3.1 this cluster of events was interpreted as the beginning of a vertical fracture connecting the face to the main cluster, so it might be expected that these events have a different source mechanism, and hence different P-axis orientations, from events in the main cluster. In fact, the P-axis orientation described (up-West/down-East) is consistent with a vertical shear failure.

Only a small number of calculated T-axis orientations have error bounds less than 45°. These are the events that have large P-axis orientation error bounds, and generally are not part of the main cluster. A T-axis orientation with an error of about 40° is determined for one event in the main cluster. The determined orientation is the same as the linear orientation of the cluster of events. The P-axis orientation is perpendicular to the cluster of events in an approximately vertical plane, and if the T-axis orientation is

along the the cluster of events, then the double-couple mechanism will be of dip-slip type, striking approximately NNE-SSW. In fact the range of possible T-axis orientations for that event is limited from all orientations within 40° of the calculated orientation to all orientations within 40° of the calculated orientation that are also perpendicular to the calculated P-axis orientations. This is because the events in the main cluster all have similar waveforms, and hence presumably have similar source mechanisms. Events to the south of the tail gate have steep T-axis orientations with azimuths perpendicular to the direction of face advance. These events are quite far from any mining activity, and it is not clear what is controlling the seismicity in that area.

The two possible interpretations of the main cluster of events are that it is either a new fracture propagating down through the roof, or that it is a pre-existing fault plane reactivated by the mining activity. The location of the panel being mined during Phase-One was chosen, based on seismic surveys, to be free of faults. However, if the latter interpretation is correct, all the events would lie on the pre-existing fault plane, and the fault planes of the individual events would be expected to all have the same orientation as the pre-existing fault plane [e.g. *Wiejacz and Ługowski*, 1997; *Seeber et al.*, 1998]. This gives two possible fault plane strikes, either striking approximately NNE-SSW (i.e. perpendicular to the linear orientation of the cluster) with a shallow dip, or striking approximately WNW-ESE (i.e. along the cluster) with a steep dip. The calculated P-axis orientations are perpendicular to the cluster of events. Event fault planes make an angle of 45° with the P-axis and T-axis orientations. If the event fault planes strike NNE-SSW then, based on the calculated P-axis orientations, the T-axis orientations will be along the cluster of events. The fault planes therefore will make an angle of 45° with the cluster of events. To be reactivation of a pre-existing fault plane the event fault planes would need to be parallel to the cluster of events. Thus from the calculated P-axis orientations it can be concluded that the event fault planes can not strike NNE-SSW if they are reactivation of a pre-existing fault plane. The one T-axis orientation calculated with an error bound below 45° for the main cluster of events is along the cluster, suggesting that the double-couple mechanism for events in the cluster would be a dip-slip failure on a NNE-SSW striking fault plane. If this is indeed

the case, then the events cannot be a reactivation of a pre-existing fault plane, they are the propagation of a new fracture.

6.2.3 P-axis and T-axis orientations calculated for events recorded during Phase-Two

The location of the seismicity recorded during the second phase of monitoring appears to be controlled by the mining activity and the geological conditions in the roof. The seismicity is split into two clear clusters, one that shows similar features to the seismicity recorded during Phase-One, and one cluster that shows the more expected characteristics of longwall mining induced seismicity i.e. similar to the activity observed by *Hatherley et al.* [1997]. The patterns of seismic activity showed some similarities to physically modelled fracture patterns [*Sun et al.*, 1992a, 1992b], which was more clearly seen in the collapsed seismic event locations (see section 4.5.2). The cluster of seismic events above the main gate could again be the propagation of a new fracture or events occurring as the reactivation of an existing fault plane. Analysis of the P-axis and T-axis orientations distinguished between these two possibilities for the seismicity recorded during Phase-One. The same analysis applied to the Phase-Two seismicity may also distinguish which of these two possible interpretations is correct. Alternatively, the seismicity may not be controlled by geological structures, and is showing the position of a fractured volume of rock above the main gate, as predicted by the physical model. Analysing the P-axis and T-axis orientations of the cluster of events that occur in the centre of the panel will hopefully give more information about the cause of these events. These events are interpreted as being more typical of longwall mining induced seismicity, and that this type of seismicity only occurs at that location because of the presence of the dolerite sill in the roof. The calculated P-axis and T-axis orientations can be inferred to be the same as the maximum and minimum compressive stress orientations, and these may show whether the events actually are the more typical induced seismicity.

Stress directions and error bounds are calculated for the 90 events with data of a sufficiently high quality recorded at the Hole 1 sonde. There were two three-component sets of data recorded at this sonde. The second three-component set is used,

as this is of better quality. A large fraction of the events in the main gate cluster have records of sufficient quality that the analysis can be applied, but only a small fraction of the events in the panel cluster have data of the same quality. T-axis orientations are the more accurately determined of the two axis orientations for the events in the main gate cluster. Most of the events in the panel cluster have more accurately determined P-axis orientations, but some have more accurately determined T-axis orientations. Some of the panel cluster events have similar waveforms to the main gate cluster events, and it is for these events that the T-axis orientation is more accurately determined. Since these events have dissimilar waveforms to the other panel cluster events, the T-axis and P-axis orientations in that area cannot be used to deduce a composite double-couple mechanism. The calculated P-axis orientations are shown as figures 6.8 to 6.10. Figure 6.8 shows a plan view. Figure 6.9 shows a sectional view looking perpendicular to the direction of face advance from the S (i.e. direction of face advance is left to right). Figure 6.10 shows a sectional view looking in the direction of face advance from the W (i.e. direction of face advance is into the page). The calculated T-axis orientations are shown as figures 6.11 to 6.13. Figures 6.11 to 6.13 show the same views as figures 6.8 to 6.10 respectively. The axis orientations are represented by cones in the same way as figures 6.2 to 6.7. The error bounds used are for a 95% confidence level. Cones are not plotted for errors larger than 45°. As noted in section 6.2.2, it is the axis orientation closest to the source-receiver direction that has been more accurately determined.

Figure 6.8 Plan view of calculated maximum compressive stress orientations for events recorded at Hole 1 sonde during the second phase of mining. Cones represent the size of the 95% confidence errors.

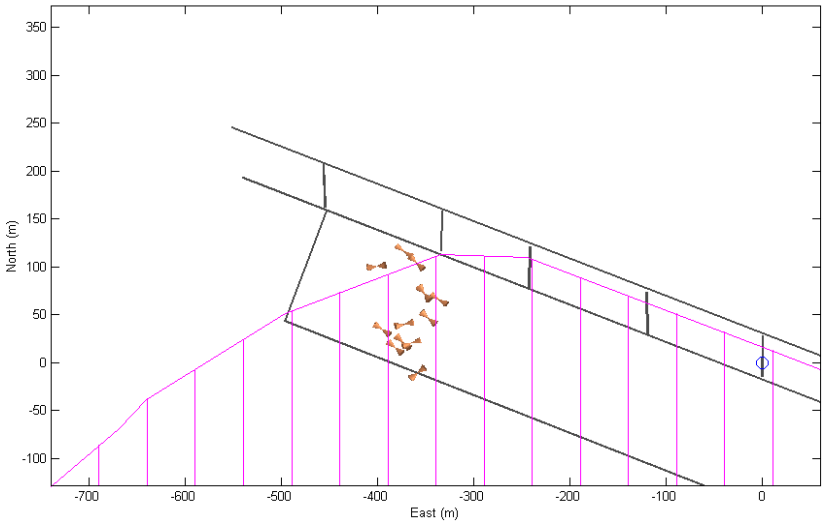

Figure 6.9 Sectional view of calculated maximum compressive stress orientations for events recorded at the Hole 1 sonde during the second phase of mining, looking perpendicular to the direction of face advance from the South. Cones represent the size of the 95% confidence errors.

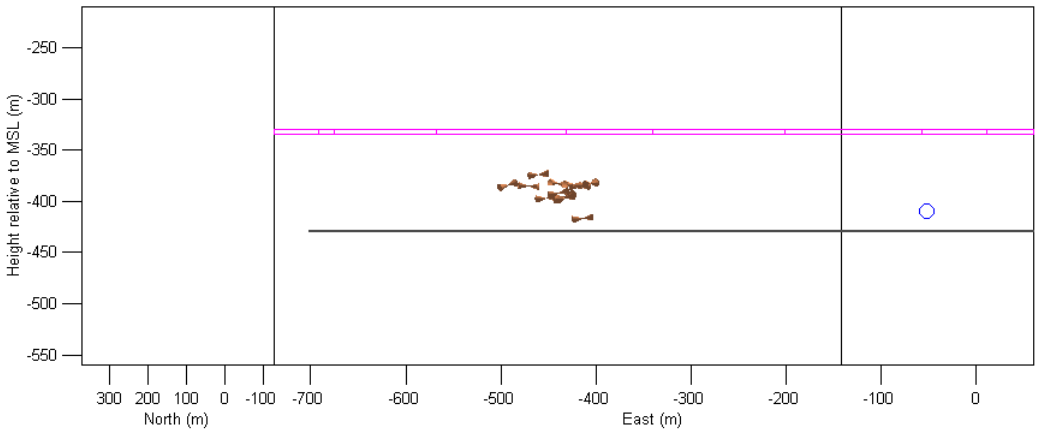

Figure 6.10 Sectional view of calculated maximum compressive stress orientations for events recorded at the Hole 1 sonde during the second phase of mining, looking along the direction of face advance from the West. Cones represent the size of the 95% confidence errors.

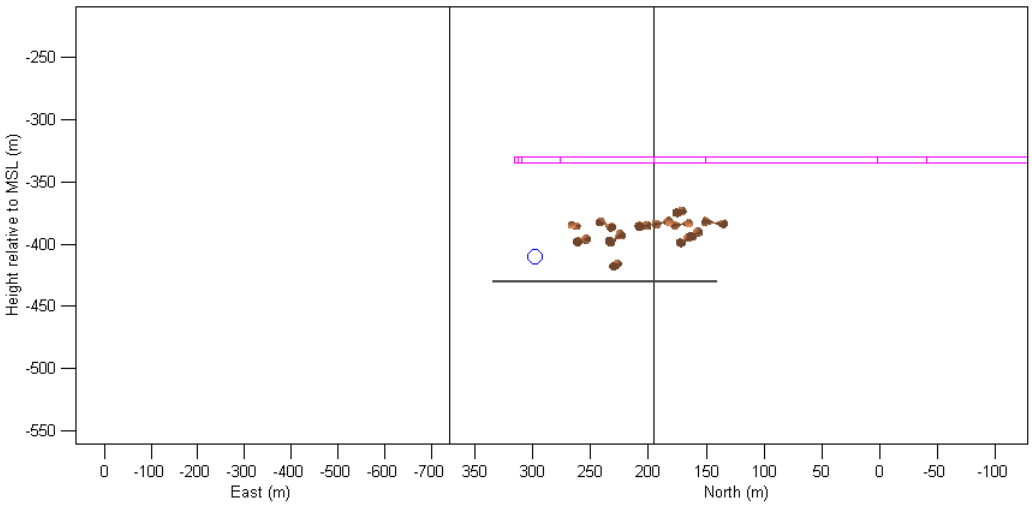

Figure 6.11 Plan view of calculated minimum compressive stress orientations for events recorded at Hole 1 sonde during the second phase of mining. Cones represent the size of the 95% confidence errors.

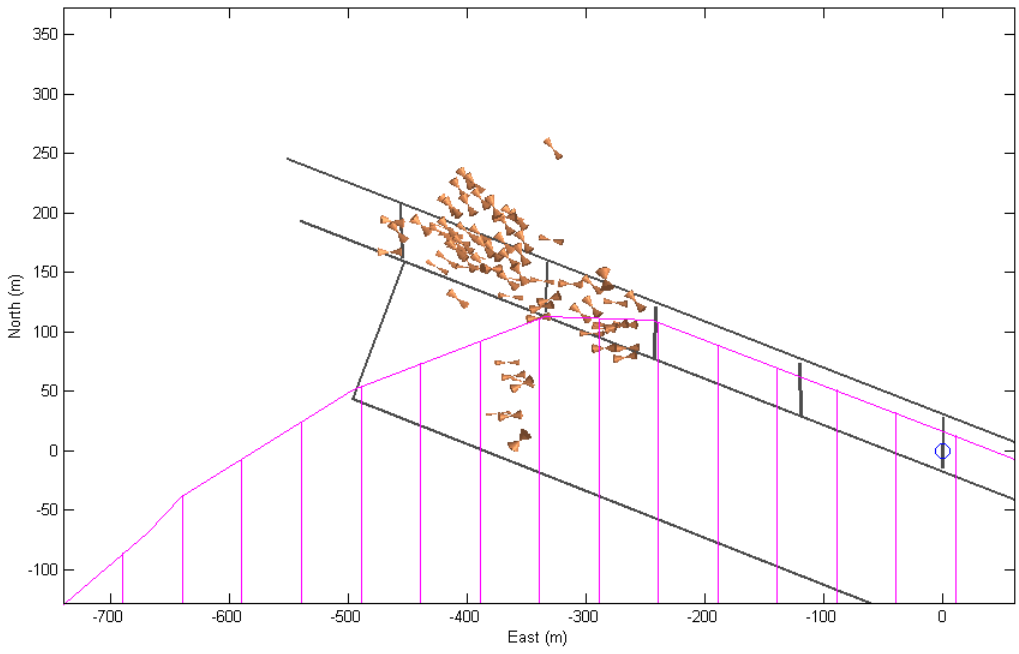

Figure 6.12 Sectional view of calculated minimum compressive stress orientations for events recorded at the Hole 1 sonde during the second phase of mining, looking perpendicular to the direction of face advance from the South. Cones represent the size of the 95% confidence errors.

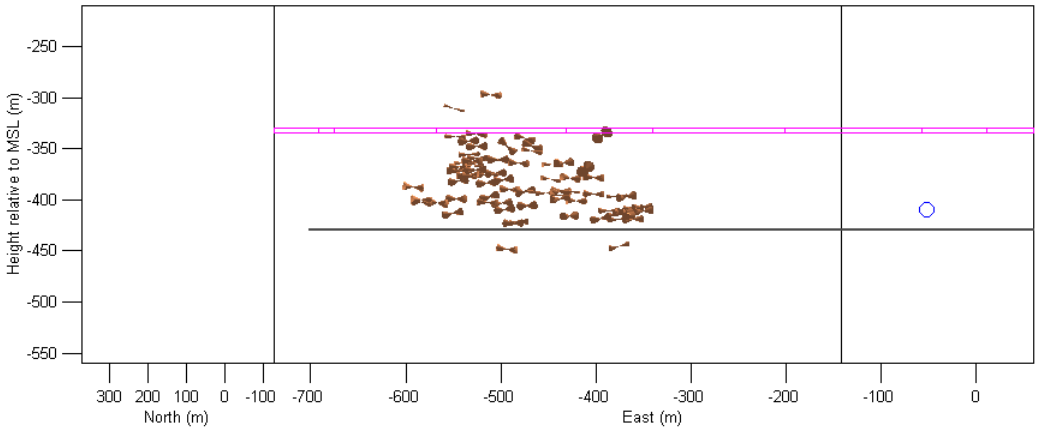

Figure 6.13 Sectional view of calculated minimum compressive stress orientations for events recorded at the Hole 1 sonde during the second phase of mining, looking along the direction of face advance from the West. Cones represent the size of the 95% confidence errors.

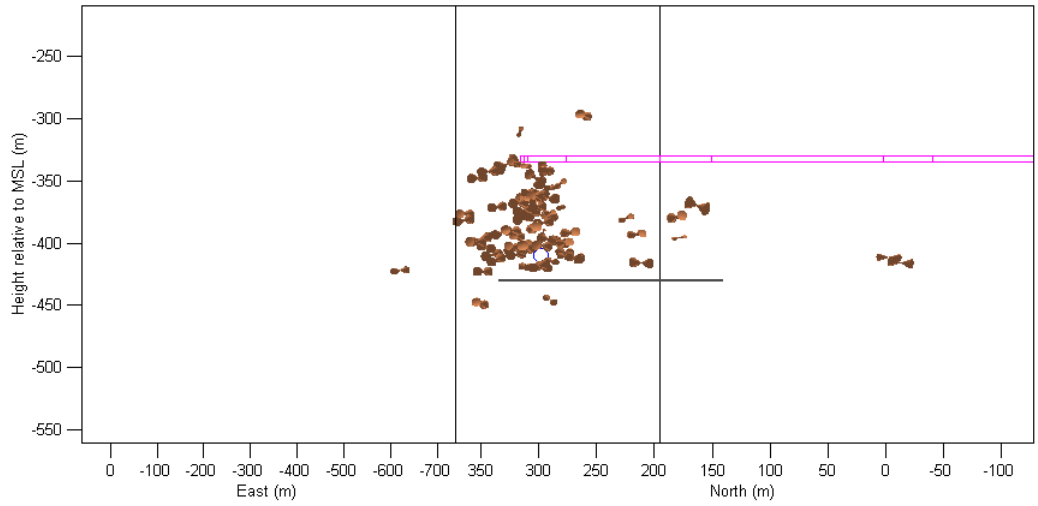

Typical 95% confidence level error bounds for the more accurately determined of the two axis orientations are in the range 10° to 20°. P-axis orientations are more accurately determined for only a small proportion of the total number of events. These events are below the sill and above the panel being mined. Figure 6.8 shows that most of the events have NW-SE oriented P-axes, which is the same as the regional maximum compressive stress orientation in the Asfordby area deduced from borehole breakout studies [*Altounyan and Bigby*, 1996]. Figure 6.9 shows that the determined P-axis orientations are near-horizontal. In section 6.2.2 it was stated that one of either the P-axis or T-axis being vertically oriented infers that the other must be horizontally oriented, and hence the double-couple mechanism must be dip-slip. The converse is not true, so the P-axis orientations calculated for the Phase-Two data cannot be used to identify a certain type of double-couple mechanism. The study by *Hatherley et al.* [1997], which observed typical patterns of induced seismicity around a longwall mine, found reverse faulting mechanisms above the panel being worked. The mechanisms they found had an approximately horizontally oriented P-axis for all the events analysed. For most of the events the P-axis orientation calculated was parallel to the regional maximum compressive stress orientation, the same situation that is found for the Phase-Two events in the panel cluster. Based on this, it can be said that the panel cluster of events shows some characteristics typical of expected longwall mining induced seismicity. Thus the interpretation of these events as being typical of the expected seismicity is still valid.

T-axis orientations are more accurately determined for most of the events recorded during Phase-Two. Figure 6.11 shows that the determined T-axis orientations generally have one of two azimuths: NW-SE or in the direction of face advance (approximately WNW-ESE). Those events that have NW-SE oriented T-axes are farther away from the panel being mined than those that have T-axis orientations parallel to the direction of face advance. The NW-SE orientation is the same as the regional maximum compressive stress orientation. Figure 6.12 shows that the calculated T-axis orientations are near-horizontal and again they cannot be used to identify a certain type of double-couple mechanism. It does mean that these events cannot have reverse faulting mechanisms similar to those found by *Hatherley et al.*

[1997], as that would require near-vertically oriented T-axes. Instead the events must have either normal or strike-slip faulting mechanisms.

6.3 Double-couple mechanisms for Asfordby data

The method that derives P-axis and T-axis orientations from a single three-component seismogram is a modification of a method that determines double-couple mechanisms that best fit the available data. The axis orientation method is more reliable as estimates of error bounds can be made for the calculated information. This is not possible for the double-couple mechanism method. In the previous chapter the double-couple mechanism method is extensively tested using synthetic seismograms generated for known double-couple mechanisms. This testing shows that although there are limitations to the method, in many situations meaningful source mechanism information can be obtained. At worst the method can determine double-couple mechanisms with a confidence of just over 50%, but if some constraint on the type of mechanism is made, this confidence is over 80%. The axis orientation analysis is able to give some information about the possible types of double-couple mechanisms, which means that applying the double-couple mechanism analysis to the Asfordby data may produce higher confidence results.

6.3.1 Comparing double-couple mechanisms calculated for the same event recorded at two sondes

In section 6.2.1 the axis orientation analysis is tested by calculating P-axis and T-axis orientations using two three-component seismograms of the same event recorded at different sondes. The calculated directions are then compared to see if they agree within the estimated error bounds. This test shows that the stress direction analysis works as expected for real data. The same analysis can be carried out to investigate how well the double-couple mechanism method works with real data. For each three-component event record the double-couple mechanism that gives the best fit to the observed P-wave and S-wave amplitudes is calculated. The double couple mechanisms are expressed as P-axis and T-axis orientations. The P-axis and T-axis orientations can then be compared for records of the same event from different sondes. In section 5.3.1

a correct agreement of two double-couple mechanisms agree is defined as both axis orientation pairs disagreeing by less than 15°. An approximate agreement is defined as both axis orientation pairs disagreeing by less than 45°. If either axis orientation pair disagrees by more than 45°, the mechanisms are defined as being different.

Table 6.3 The results of determining and comparing double-couple mechanisms calculated for the same event recorded at two different sondes.

Event 1	Event 2	Angle between σ_{max} orientations (°)	Angle between σ_{min} orientations (°)
c2_03_002	d2_03_006	16	10
c2_03_003	d2_03_022	26	8
c2_03_004	d2_03_027	12	17
c2_03_005	d2_03_028	24	7
c2_03_006	*d2_03_045*	*12*	*7*
c2_03_007	d2_03_081	33	27
c2_03_008	d2_03_221	83	15
c2_04_001	d2_04_026	11	34
c2_04_002	d2_04_061	22	23
c2_04_003	d2_04_118	10	33
c2_06_005	d2_06_009	18	29
c2_06_189	*d2_06_306*	*3*	*2*
c2_06_303	d2_06_475	45	21
c2_07_013	d2_07_032	13	56
c2_07_016	d2_07_036	31	75
c1_06_005	d1_06_009	70	28
c1_06_142	d1_06_243	22	25
c1_06_189	*d1_06_306*	*12*	*8*
c1_06_303	*d1_06_475*	*5*	*3*
c1_07_013	d1_07_032	23	16
c1_07_016	d1_07_036	22	83
c1_07_022	d1_07_042	73	41
c2_06_005	d1_06_009	35	9
c2_06_189	d1_06_306	16	4
c2_06_303	d1_06_475	26	5
c2_07_013	d1_07_032	75	48
c2_07_016	d1_07_036	18	73
c1_06_005	d2_06_009	59	30
c1_06_142	d2_06_243	27	25
c1_06_189	*d2_06_306*	*5*	*3*
c1_06_246	d2_06_386	41	13
c1_06_303	d2_06_475	42	24
c1_07_013	d2_07_032	48	19
c1_07_016	d2_07_036	36	85
c1_07_022	d2_07_042	19	20

The results of this test are summarised in table 6.3. For each pair of events the angle between the two P-axis orientations and the angle between the two T-axis orientations are given. Out of the 35 pairs of events analysed, only 11 have a pair of P-axis or T-

axis orientations that disagree by more than 45° (highlighted in bold text). This gives a success rate for the method of nearly 70%. This is a great deal higher than the success rate achieved in synthetic tests, and this is possibly due to the seismic events not having random locations and random double-couple mechanisms. A synthetic test is carried out for clusters of events with similar mechanisms in section 5.3.5, but again the similar source mechanisms have some mathematical distribution, and this may not be the case for real events. This would be especially true if events were occurring as the reactivation of a pre-existing fault plane. Or, this higher success could be due to the small sample size. The success rates stated in chapter 5 are calculated using 5000 events, where as only 35 events are used here. It is also possible that within the set of event pairs that have mechanisms that agree there are some for which the same wrong mechanism has been found for both events. This would lead to a higher apparent success rate, but since the two records are from different sondes, this could only occur by coincidence. Of the 35 pairs of events analysed, 5 have pair of axis orientations that agree to within 15° (highlighted in italics). In the synthetic tests, it was found that 18% of the events have correctly determined mechanisms i.e. P-axis and T-axis orientations determined to within 15°. This is similar to the 14% of pairs of double-couple mechanisms calculated here that have P-axis and T-axis orientations which agree to within 15°.

The analysis of two three-component seismograms of the same seismic event recorded at two different sondes suggests that the success of the method that determines double-couple mechanisms is as good as that calculated using synthetic data. In fact, the success appears to be better than that calculated using synthetic data, possibly due to the non-random nature of the real events. This implies that the events have double-couple mechanisms. If, for instance, the events were tensile failures, then the real radiation patterns of seismic waves would be very different from those calculated assuming a double-couple mechanism. In that case there would be little chance of similar double-couple mechanisms being calculated using two records of the same event from different sondes. Application of the method to all events recorded with sufficient quality during the two phases of monitoring should give more information

about the source mechanisms, and allow a fuller understanding of the recorded seismicity.

6.3.2 Double-couple mechanisms calculated for events recorded during Phase-One

The results of the axis orientation analysis applied to the seismicity recorded during the first phase of mining at Asfordby helped to answer several questions raised by previous interpretation. One particular question was whether the large cluster of seismicity observed above the main gate is caused by the propagation of a new fracture, or the reactivation of a pre-existing fault plane. The P-axis orientations calculated for events in the cluster suggest that it is not the latter. The P-axis orientations calculated for some events in that cluster are near-vertical. This is an important result as it means that these events are normal dip-slip failures, and as such a much higher confidence can be placed on their calculated double-couple mechanisms. The events in the main cluster have similar waveforms, implying they have similar source mechanisms. Thus if some events can have their source mechanisms determined with a good confidence, then these mechanisms can be taken to be indicative of the type of mechanisms expected for all events in that cluster. These facts mean that more information about the source mechanisms of events recorded during Phase-One should be obtainable.

Double-couple mechanisms are calculated for 104 of the events recorded at the Cants Thorn 1 upper sonde during the first phase of mining. These are the same events for which the axis orientation analysis is carried out. The calculated double-couple mechanisms are represented as ‘beach-balls’ in figure 6.14, which shows a plan view of the upper half of the focal spheres. In section 6.2.2 the P-axis orientations that are calculated for the events at approximately 400m E and 50m N are all near-vertical. This means that the mechanisms for these events must be normal dip-slip failures. This fact is taken into account when these events are analysed, and only possible dip-slip mechanisms are considered. In section 5.3.4 it is shown that in such a situation the success of the method used to calculate double-couple mechanisms is above 80%. Thus an 80% confidence can be placed on the double-couple mechanisms calculated for those events that have near-vertical calculated P-axis orientations.

Figure 6.14 Plan view showing double-couple mechanisms of events recorded at the Cants Thorn 1 upper sonde during the first phase of mining.

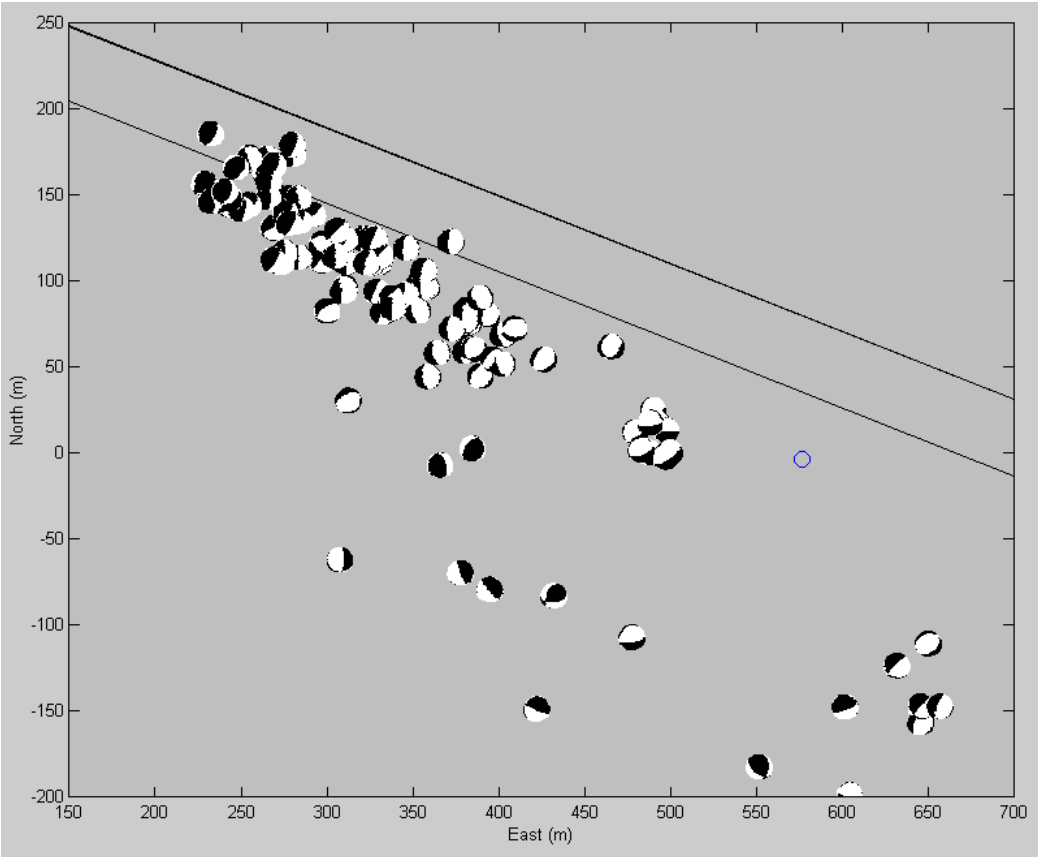

Figure 6.14 shows that these events are indeed normal dip-slip failures with dips of approximately 45°. It is the calculated strike directions that are most interesting though. The calculated double-couple mechanisms for nearly all of these events have strikes that range from N-S to NE-SW. Seismograms of events in the main cluster all show similar waveforms, and this implies that the source mechanisms of the events in the cluster are all similar. Thus it would be expected that the events in the cluster would all have similar mechanisms to those found with the 80% confidence level for the events that had near-vertical calculated P-axis orientations. This is indeed the case, as for most of the events in the cluster normal dip-slip double-couple mechanisms have been calculated, with strikes that range from N-S to NE-SW, i.e. strikes are approximately perpendicular to the orientation of the cluster. It was stated in section 6.2.2 that given the calculated P-axis orientations of the events in the cluster, double-

couple mechanisms with strikes perpendicular to the orientation of the cluster would imply that the event fault planes would make an angle of 45° with the orientation of the cluster. Thus the events are not occurring as slip on a pre-existing fault plane, since the cluster of events would have to be in the events fault planes not at an angle to them. There is a steady change in the mechanisms of events with their location in the cluster. At the lower end dips are approximately 45°. Higher up the cluster the calculated double-couple mechanisms are such that the event fault planes are either horizontal or vertical. At the top end of the cluster there are a few reverse-faulting mechanisms. This is highlighting changes in event fault plane orientation along the length of the cluster, and hence changes in P-axis and T-axis orientation. It was stated in section 6.2 that the P-axis and T-axis orientation can be inferred to be the maximum and minimum compressive stress orientations.

Figures 6.15 and 6.16 show the inferred maximum compressive stress orientations for the double-couple mechanisms shown in figure 6.14. Figure 6.15 shows a plan view, and figure 6.16 shows a sectional view looking perpendicular to the direction of face advance from the S. The maximum compressive stress orientations shown in these figures are virtually identical to the P-axis orientations shown in figures 6.2 and 6.3. The relationship between the cluster of events and the inferred maximum compressive stress orientation is clear. Figure 6.17 and 6.18 show the inferred minimum compressive stress orientations for the double-couple mechanisms shown in figure 6.14. Figure 6.17 shows a plan view, and figure 6.18 shows a sectional view looking perpendicular to the direction of face advance from the S. Figure 6.17 shows that most of the inferred minimum compressive stress orientations have azimuths approximately the same as the orientation of the cluster of events. Figure 6.18 shows that most of the inferred minimum compressive stress orientations have elevations that depend on the position of the event in the cluster i.e. they are oriented with the dip of the cluster. The inferred minimum compressive stress orientations for the events in the cluster are essentially parallel to the cluster.

Figure 6.15 Plan view of maximum compressive stress orientations inferred from the double-couple mechanisms of events recorded at the Cants Thorn 1 upper sonde during the first phase of mining.

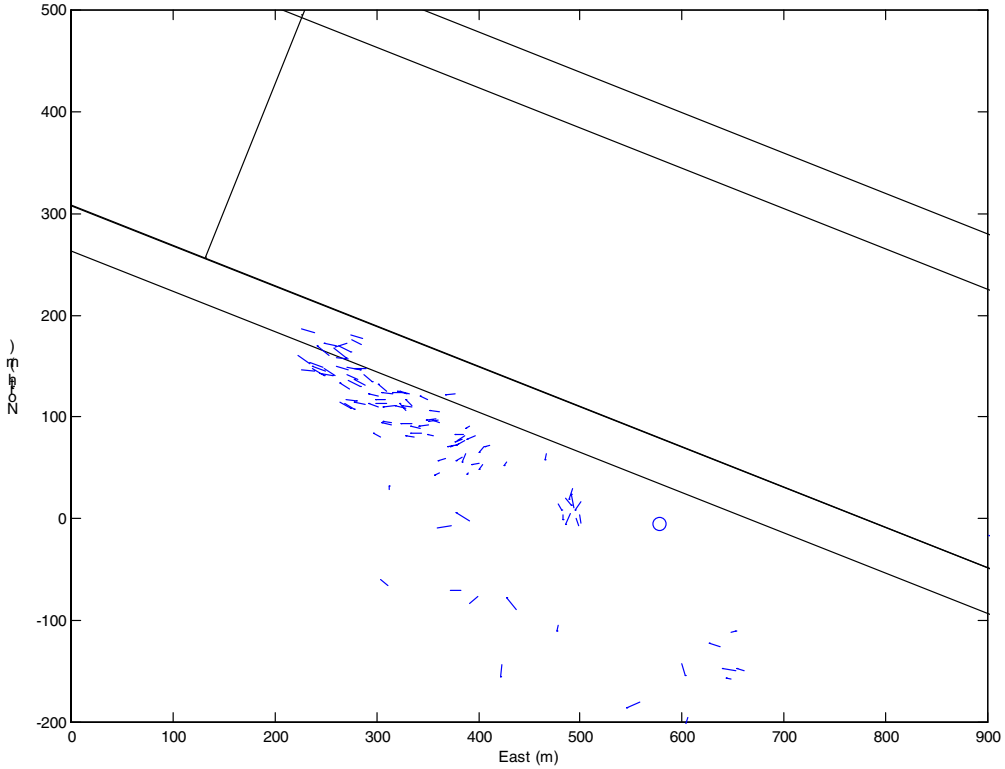

Figure 6.16 Sectional view looking perpendicular to the direction of face advance from the South of maximum compressive stress orientations inferred from the double-couple mechanisms of events recorded at the Cants Thorn 1 upper sonde during the first phase of mining.

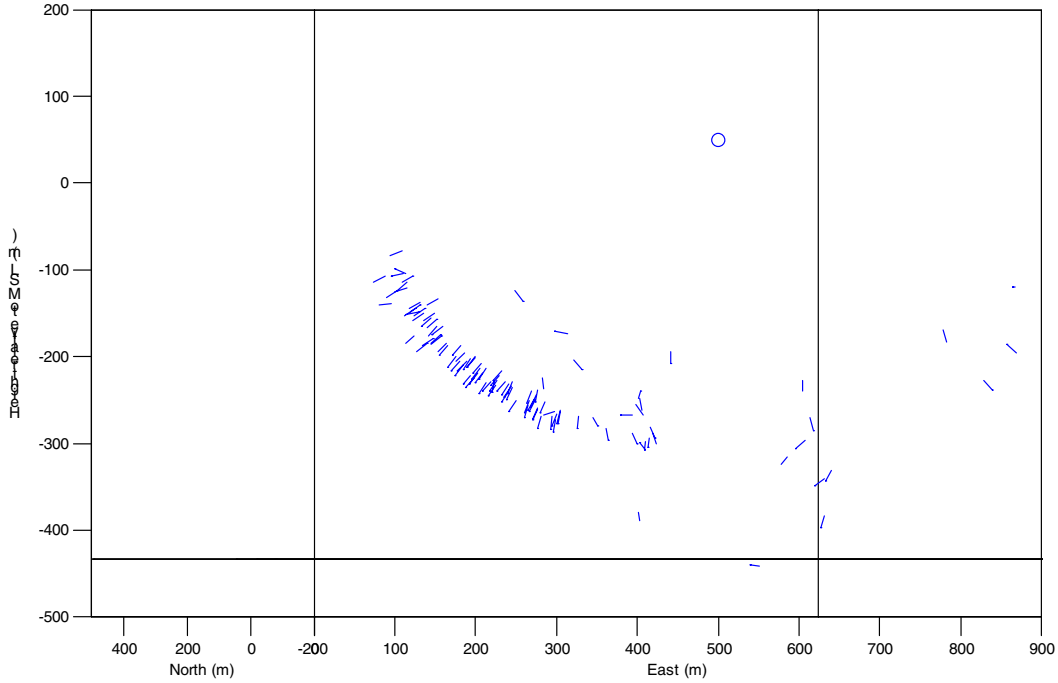

Figure 6.17 Plan view of minimum compressive stress orientations inferred from the double-couple mechanisms of events recorded at the Cants Thorn 1 upper sonde during the first phase of mining.

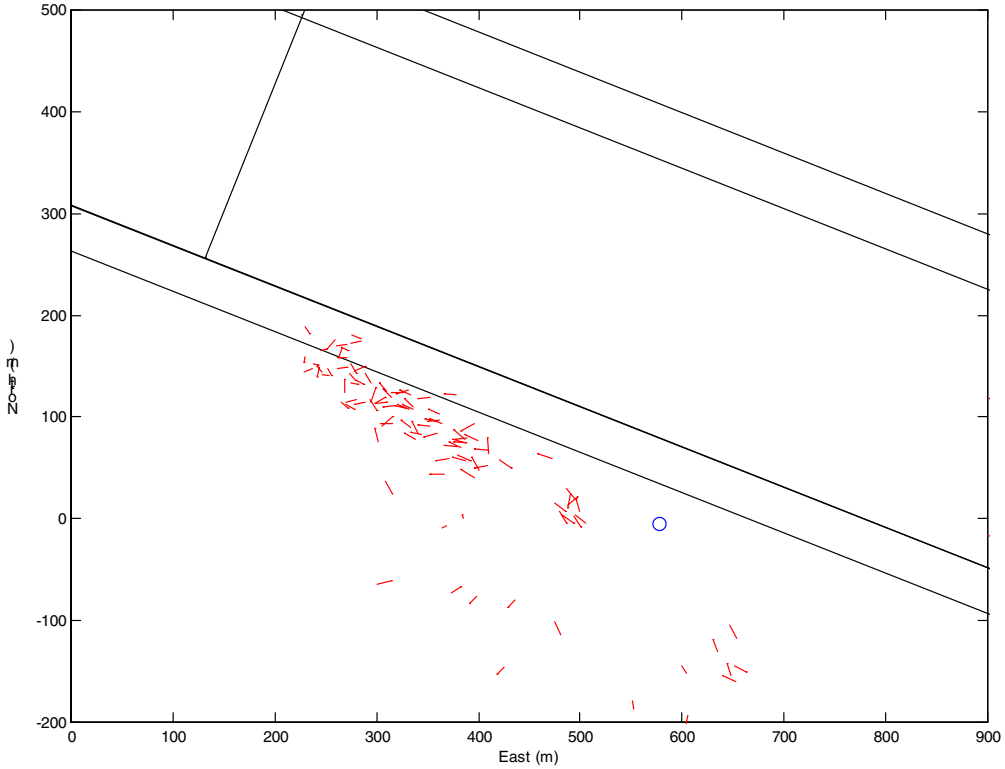

Figure 6.18 Sectional view looking perpendicular to the direction of face advance from the South of minimum compressive stress orientations inferred from the double-couple mechanisms of events recorded at the Cants Thorn 1 upper sonde during the first phase of mining.

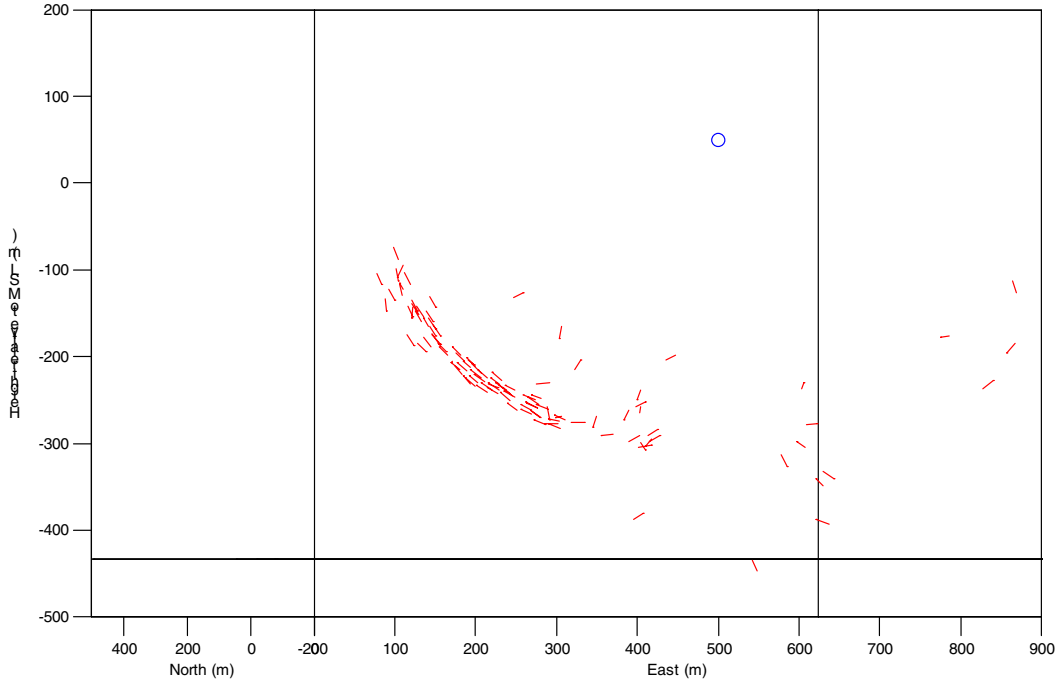

Figures 6.16 and 6.18 show clear relationships between the geometry of the cluster of events above the main gate and the inferred maximum and minimum compressive stress orientations. The maximum compressive stresses are perpendicular to, and the minimum compressive stresses are parallel to, the orientation of the cluster of events. The stress orientations are inferred from the P-axis and T-axis orientations. Thus the fault plane of a double-couple mechanism makes angles of 45° with the inferred maximum and minimum compressive stress orientations. Thus the fault planes of the events in the main cluster must make an angle of 45° with the linearity of the cluster. In figures 3.14 and 3.15 it can be clearly seen that the linear cluster of events begin at shallower depths of about 100m below sea-level, and then propagate downwards to depths of about 300m. The propagation is controlled by the face position. One possible interpretation of this was that the cluster of events is the propagation of a new fracture. Another possible interpretation is that the events are occurring as reactivation of a pre-existing fault plane. In section 6.2.2 P-axis orientations are calculated for the events in the cluster, and they do not support the latter interpretation. The double-couple mechanisms calculated for the events in the main cluster show that the latter interpretation, slip on a pre-existing fault plane, is not possible. Thus it appears that the cluster of events above the main gate are caused by the propagation of a new fracture high in the roof. The relationships between the directions of inferred maximum and minimum compressive stress orientations, event fault plane orientations, and fracture propagation are shown schematically as figure 6.19.

Figure 6.19 Diagram showing the relationships between the directions of maximum and minimum compressive stress orientations, event fault plane orientations, and fracture propagation for the main group of events recorded at Cants Thorn 1 upper sonde during the first phase of mining.

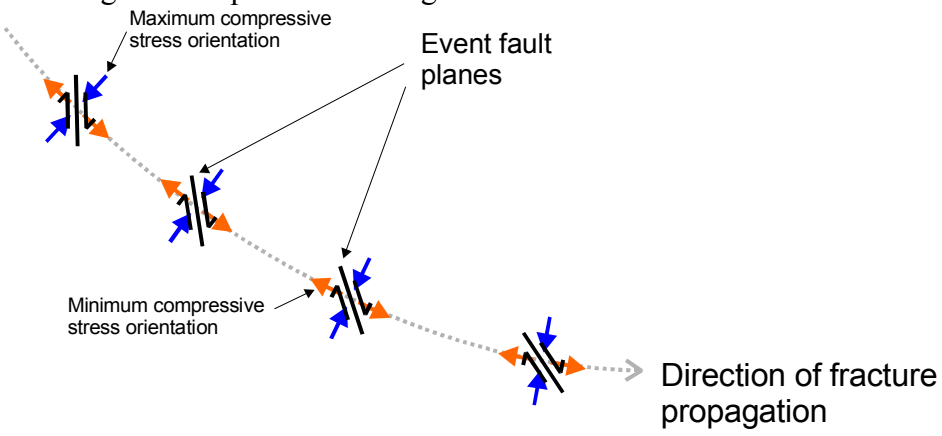

6.3.3 Double-couple mechanisms calculated for events recorded during Phase-Two

The results of the axis orientation analysis applied to the seismic events recorded during the second phase of mining at Asfordby eliminated certain types of double-couple mechanisms for some of the clusters of events. Analysis of the seismicity above the main gate produces well-constrained T-axis orientations. The T-axis orientations calculated are all near-horizontal, and this is particularly well shown by figure 6.12. Reverse faulting double-couple mechanisms, such as those observed by *Hatherley et al.* [1997], require the T-axis orientation to be near-vertical. Hence reverse faulting mechanisms are not possible for the events above the main gate. P-axis orientations are better constrained for the events towards the centre of the panel. These are also all near-horizontal, and most are parallel to the regional maximum compressive stress orientation as deduced from borehole breakout studies. Near-horizontal P-axis orientations parallel to the regional maximum compressive stress orientation were observed by *Hatherley et al.* [1997] for events located above the panel being mined. Thus the events recorded above the panel during the second phase of mining at Asfordby show similar characteristics to what might be expected. Calculating double-couple mechanisms for the events recorded during Phase-Two should allow the controlling factors of these events to be better understood. The elimination of certain types of mechanism is not enough to give the 80% confidence levels previously discussed. However, the test of the method using two records of the same event from different sondes (see section 6.3.1) was carried out using Phase-Two data. This test suggested a confidence level of 70% could be applied.

Figure 6.20 Plan view showing double-couple mechanisms of events recorded at the Hole 1 sonde during the second phase of mining.

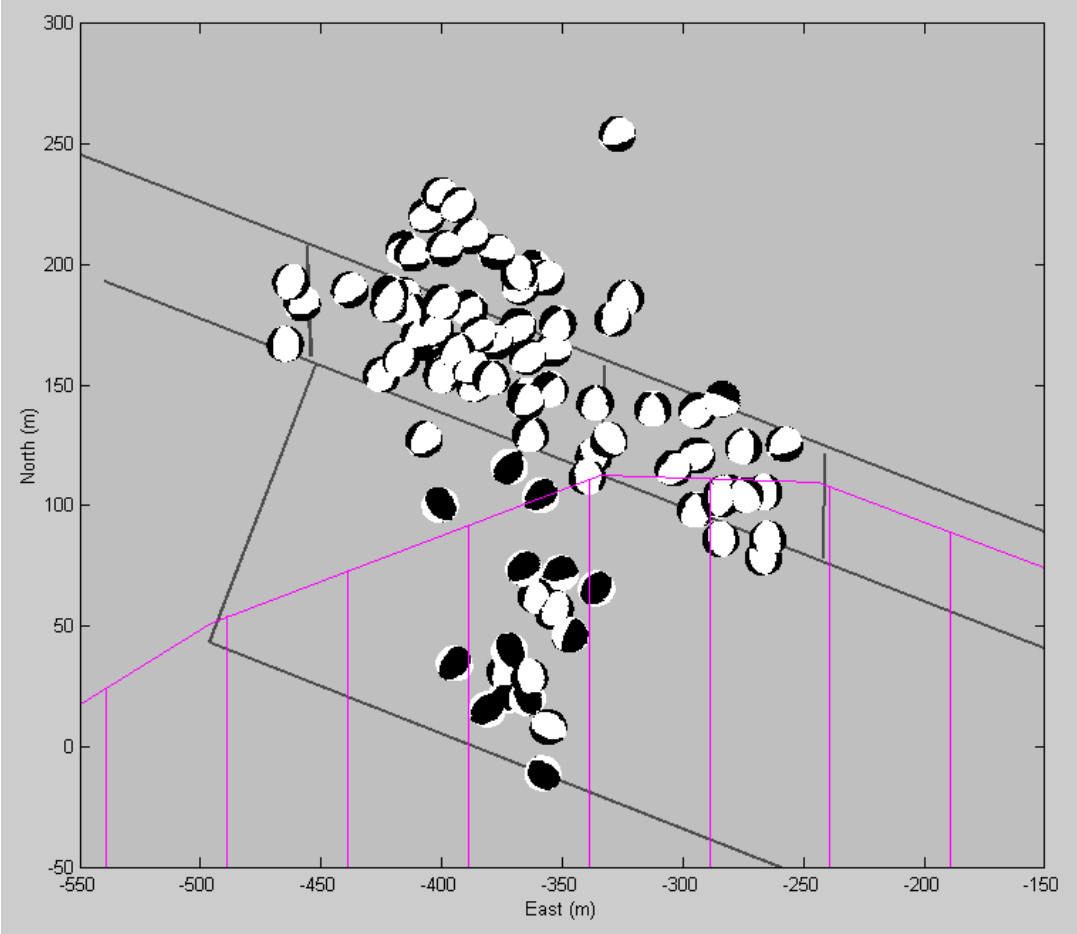

Double-couple mechanisms are calculated for 90 of the events recorded at the Hole1 sonde during the second phase of mining. These are the same events for which the axis orientation analysis is carried out in section 6.2.3. The calculated double-couple mechanisms are represented as 'beach-balls' in figure 6.20, which shows a plan view of the upper half of the focal sphere. The sonde location is off this plot to the right, at the origin. The events located above the main gate nearly all have normal dip-slip double-couple mechanisms, with strike directions in the range N-S to NE-SW. The mechanisms calculated are consistent with the T-axis orientations that are calculated for these events. There are a few mechanisms that are different from the typical mechanisms of these events e.g. striking E-W, or a strike-slip mechanism. This is expected given a confidence level of 70%. Lines of identical mechanisms can be seen, for instance at -400m E 170m N, where the mechanisms have strike directions along the line. These are possibly showing failure occurring on linear fractures, although this

could also be an artefact produced by errors in event locations. It is not clear from the 'beach-ball' representations of the double couple mechanisms whether or not the events could be slip on a pre-existing fault plane. The events above the centre of the panel and below the sill mainly have reverse faulting double-couple mechanisms. This is consistent with the horizontal P-axis orientations that were calculated for these events. Above and behind the face, where these events are located, is the region were caving of the roof occurs to form the goaf. It would be expected in such a situation that one of the compressive stress orientations would have a large vertical component. The events have a horizontal P-axis orientation, and hence a horizontal inferred maximum compressive stress orientation. Therefore the minimum compressive stress orientation must have a large vertical component. This is exactly the relationship between the two inferred stresses for a reverse faulting double-couple mechanism, and has been observed by *Hatherley et al.* [1997], and now in this study. There are a few events above the panel that have normal faulting mechanisms. The seismic data for these events show the opposite P-wave first-motion polarity to those events for which reverse faulting mechanisms were found. Thus it would seem that these few events do have a different type of double-couple mechanism from the majority of events in that area.

In section 6.3.2 the P-axis and T-axis orientations are inferred to be the maximum and minimum compressive stress orientations. The same can be done for the double-couple mechanisms found for the Phase-Two events. The inferred maximum compressive stress orientations are shown as figure 6.21. The top plot shows a plane view, the centre plot shows a sectional view looking perpendicular to the direction of face advance from the S, and the bottom plot shows a sectional view looking in the direction of face advance from the W. The plan view shows the same orientations as the calculated P-axes shown as figure 6.8 for the events in the centre of the panel. The two sectional plots show that the events above the main gate have near-vertical maximum compressive stress orientations. The inferred minimum compressive stress

Figure 6.21 Plan view (top) and two sectional views, looking perpendicular to (middle) and along (bottom) the direction of face advance, of maximum compressive stress orientations inferred from the double-couple mechanisms of events recorded at the Hole 1 sonde during the second phase of mining.

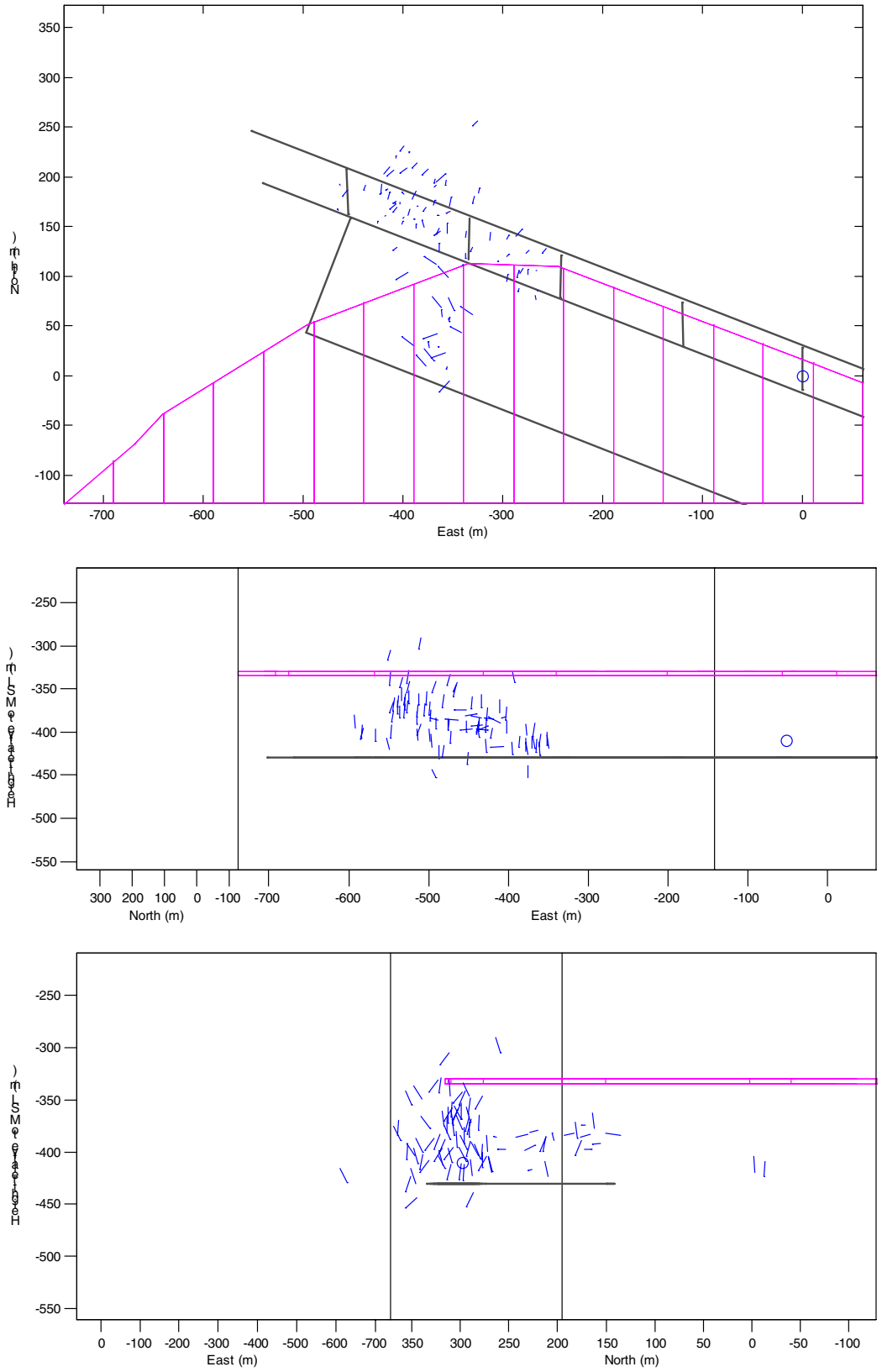

Figure 6.22 Plan view (top) and two sectional views, looking perpendicular to (middle) and along (bottom) the direction of face advance, of minimum compressive stress orientations inferred from the double-couple mechanisms of events recorded at the Hole 1 sonde during the second phase of mining.

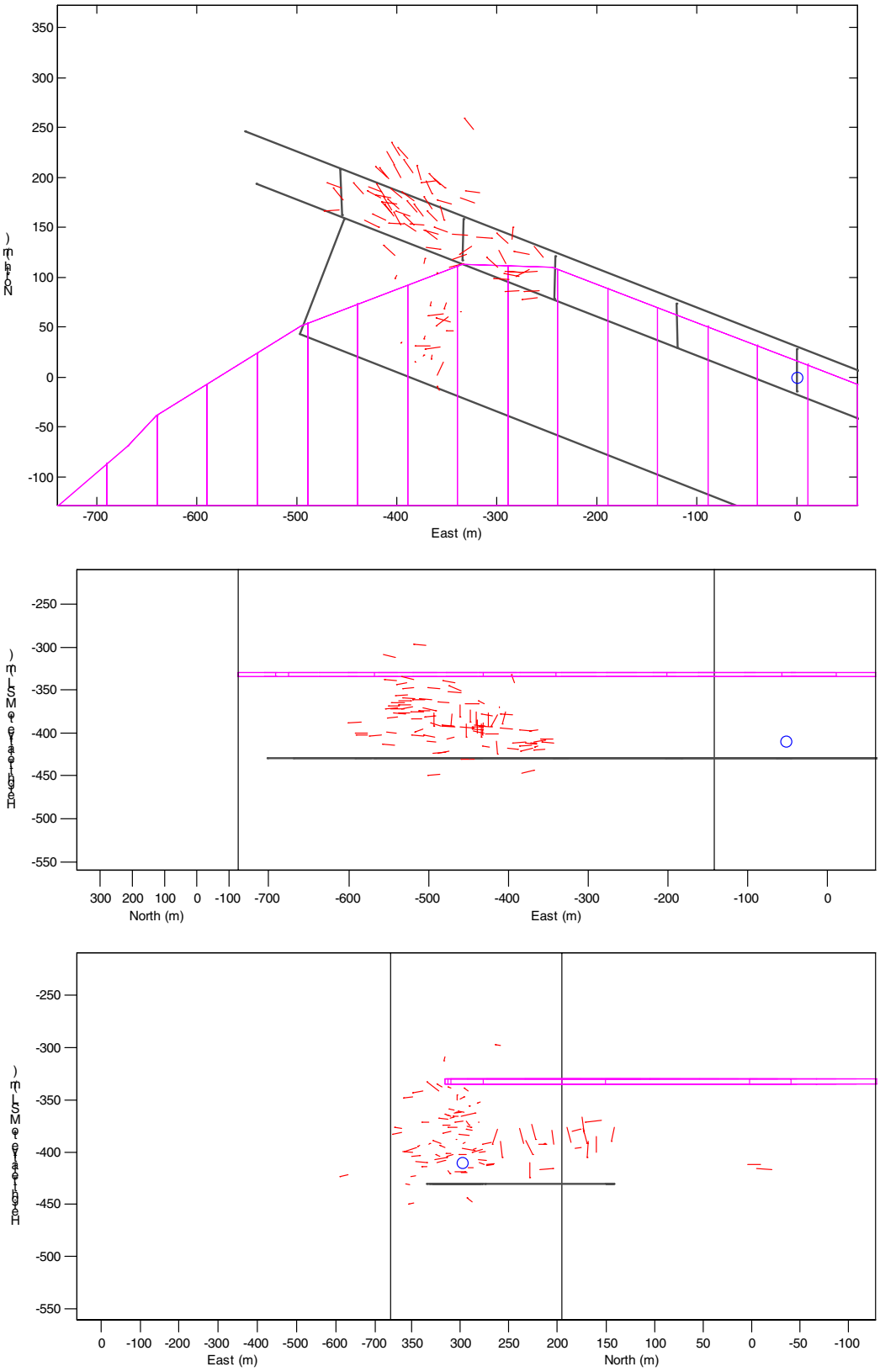

orientations are shown as figure 6.22. The three plots shown have the same viewpoints as those shown as figure 6.21. These plots show the same orientations as the calculated T-axes shown as figures 6.11 to 6.13.

The events in the cluster above the main gate are characterised by near-vertical maximum compressive stress and horizontal minimum compressive stress orientations. The near-vertical maximum compressive stress could be showing the effect of the overburden pressure. The alignment of the stresses infers fault planes with dips of approximately 45°, as shown by the 'beach-ball' representations of the double-couple mechanisms in figure 6.20. The NW end of the cluster of events defines a plane that dips at approximately 45°, and this can be well seen in the middle plots of figure 6.21 and 6.22, and the collapsed locations shown as figure 4.19. The SE end of the cluster similarly defines a plane that dips at a slightly lower angle, about 35° to 40°. The strike of these planes is approximately NE-SW, i.e. parallel to the typical strike directions of the double-couple mechanisms calculated for the events. Thus it seems likely that the events above the main gate are occurring on some pre-existing fault planes, with the relationship between the pre-existing fault plane, the event fault planes, and the inferred stress orientations shown as figure 6.23. The near-vertical maximum compressive stress above the edge of the panel is similar to results of numerical modelling described by *North and Jeffrey* [1991]. However, the modelling found that the minimum compressive stress would be horizontal, and parallel to the face, whereas the minimum compressive stress direction shown by the microseismicity is parallel to the direction of face advance. This suggests that the source mechanisms are being effected by regional stress directions, pre-existing zones of weakness, or some combination of the two. These factors are not taken into account by the 2-D numerical model.

Figure 6.23 Diagram showing the relationships between the pre-existing fault plane, the event fault planes, and the inferred stress orientations for the main gate group of events recorded at Hole 1 sonde during the second phase of mining.

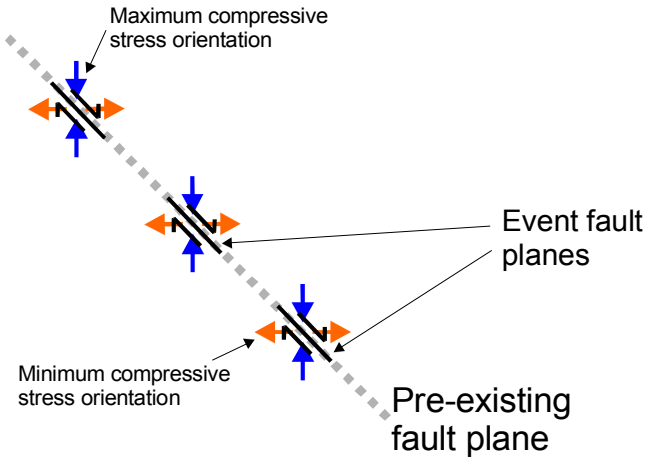

The events in the cluster above the centre of the panel and below the sill are characterised by near-vertical minimum compressive stress and horizontal maximum compressive stress orientations. The double-couple mechanisms of these events are the same as those observed above the panel in the study by *Hatherley et al.* [1997]. Their observations were supported by numerical modelling of longwall roof collapse. Vertical minimum compressive stress above the centre of the panel was predicted by the numerical modelling described by *North and Jeffrey* [1991]. Thus the collapsing roof probably causes the reverse faulting events, and this would explain the near-vertical minimum compressive stress orientation. In section 6.1 it was hypothesised that a strong layer in the roof closer to the seam than the Sherwood Sandstone may allow the roof to collapse in a more controlled manner. It certainly appears that this may be the case, as the microseismic activity observed below the sill show the same characteristics as that observed by *Hatherley et al.* [1997], which was associated with controlled roof collapse. The bottom plot of figure 6.21 shows a definite correlation between the edge of the sill and the region of vertical maximum compressive stress. This suggests that the weight of the overburden is the major controlling factor on the seimicity not below the sill, hence the vertical maximum compressive stress orientations, although numerical modelling does suggest vertical maximum compressive stress orientations beyond the edge of the extracted panel. Below the sill

the weight of the overburden is not the controlling factor, instead it is the roof collapse. The strong sill is removing the effect of the weight of the overburden. This explains why some normal faulting events are observed above the panel. The sill may be removing the effect of the overburden, but not entirely, so that there are still some events characterised by vertical inferred maximum compressive stress orientations.

6.4 Conclusions

The location of seismicity recorded during both phases of monitoring at Asfordby was in general very different from seismicity observed by an analogous study [*Hatherley et al*., 1997] where roof collapse was controlled and no problems were experienced. The location of seismicity recorded during Phase-Two shows similarities to the seisimicity observed by the analogous study. Serious problems were experienced during the first phase of mining that led to the face being abandoned. During Phase-Two poor working conditions were experienced, though not as bad as during Phase-One. However the decision was made after several weeks of mining to abandon the face and the mine. Causes of the problems experienced and the differences between the two phases were identified from analysis of the location of seismicity recorded. Applying the methods described in chapter 5 to the seismic data allows information about fracture orientations and causative stresses to be obtained, and this information improves the interpretations made from event locations.

The methods described in chapter 5 were tested using real data recorded at two sondes. The tests show that the methods are successful, and are applicable to real single receiver three-component seismic data if the assumptions made by the methods are satisfied.

The seismic activity observed during Phase-One was dominated by the propagation of a fracture down through the roof strata to the base of the aquifer above the seam. From there a vertical fracture extends down to the seam. This situation is very similar to a model of a longwall mine with strong roof conditions and periodic weightings [*Gale and Nemcik*, 1998]. This network of fractures also explains the flooding experienced at the face. The event source mechanism data allowed the fracture propagation to be

examined in detail, showing how the orientation of individual fractures and the direction of propagation of the main fracture related.

The seismic activity observed during Phase-Two is different from that observed during Phase-One. Based on the event source mechanisms, two types of event are identified, one associated with controlled roof collapse, and the other associated with possible reactivation of pre-existing fault planes. The source mechanism results for the Phase-Two events show complex interactions between mining strategy and geological conditions, which were controlling the observed seismicity. Identifying and understanding these interactions is essential if rock mechanical models are to be tested or improved. Some similarities between the stress orientation predicted by numerical models of the Asfordby stratigraphy and those calculated from the seismic activity were observed. However there were also dissimilarities that showed the limitations of the numerical model.

7 CONCLUSIONS

7.1 Introduction

This study has produced new and improved techniques for the analysis and interpretation of mining induced seismic data. These techniques have been applied to seismic data recorded during two phases of mining at Asfordby to understand how the rock mass responds to the mining activity. The results of the seismic data analysis demonstrate that there are two very different responses of the rock mass. One shows similarities to the typical rock mass response to longwall coal mining observed by other seismic monitoring studies and predicted by numerical and physical models. The other shows a rock mass response unlike that observed by other studies, and only predicted by numerical models that also predict serious problems at the face. Analysis of the seismic data shows that the differences between the response of the rock mass to the two phases of mining can be attributed to both changes in the roof strata and changes in mining strategy.

7.2 New and improved analysis techniques

The method used to locate seismic events using a single three-component seismogram (section 3.2.1) is a development of that used by previous studies [e.g. *Toon and Styles*, 1993] carried out by the Microseismology Research Group at the University of Liverpool. The introduction of ray tracing and a 1-D velocity model is an important improvement (section 3.2.3), as is a technique to estimate location errors (section 3.2.2) which allows a better interpretation to be made of the observed seismic event locations. Estimates of event location errors allowed the development of a method that moves event locations within error bounds into clusters that identify possible structures that are controlling seismic activity (section 4.2).

A method that determines a double-couple source mechanism from a single three-component seismogram has been developed and tested using synthetic seismograms (chapter 5). The results of synthetic tests show that although there are limitations to the

method (section 5.3.6) it is possible to calculate certain information about the source mechanism of a seismic event from a single three-component seismogram provided particular assumptions can be made.

In many cases, either because of site limitations (e.g. deep boreholes) or cost, only a single three-component seismometer is available. A single seismometer is the simplest, and cheapest, seismic array that can be installed. This thesis has shown that using a single three-component seismogram it is possible to calculate locations and source mechanism information for recorded seismic events. Source parameters (e.g. moment, stress release) can also be estimated using a single three-component seismogram. Thus a single three-component seismometer is able to yield a great deal of information about induced seismic events, allowing a better understanding of the response of the rock mass to excavation to be obtained from a limited dataset.

7.3 A typical response of the rock mass to mining activity as shown by the analysis of induced seismicity

During Phase-Two of mining at Asfordby generally poor roof and face conditions were experienced. The face, and mine, were abandoned after about 160m of face advance. The observed seismicity was initially located above the main gate, but as the face advanced below a sill in the roof seismic events began to occur above the face (section 3.4.1). The locations of seismic events recorded during Phase-Two have been "collapsed" to delineate possible discrete structures (section 4.5). The collapsed locations show a dense region of seismic activity above the main gate and a discrete horizontal structure 40m above the panel, a very similar fracture pattern to that obtained from physical models of the Asfordby stratigraphy [*Sun et al.*, 1992a, 1992b]. Double-couple source mechanisms have been calculated for many of the recorded seismic events (sections 6.2.3 and 6.3.3), which show that the events above the main gate are normal shear-failures and the events above the panel are predominantly reverse shear-failures. Reverse shear-failure above the panel was observed by an analogous study [*Hatherley et al*., 1997] at Gordonstone Mine, Australia, where no roof control problems were experienced. The maximum compressive stress orientation

inferred from the source mechanisms of the events above the panel is the same as the orientation of the regional stress field. The minimum compressive stress orientation inferred from the same events is approximately vertical suggesting the removal of coal is the major controlling factor for these events. The maximum compressive stress orientation inferred from the source mechanisms of events above the main gate is approximately vertical suggesting the weight of the overburden is a controlling factor for these events. The extent of the dolerite sill between the face and the Sherwood Sandstone delineates the boundary between the vertical maximum compressive stress and vertical minimum compressive stress orientations. This suggests that the presence of the dolerite sill is allowing the roof to collapse in a more controlled manner, and is inhibiting the weighting events experienced during Phase-One.

7.4 An atypical response of the rock mass to mining activity as shown by the analysis of induced seismicity

During Phase-One of mining at Asfordby, weightings, water inflow, and poor roof conditions were experienced, which led to the abandonment of the face after 555m of face advance. The frequency of occurrence of seismic events recorded during Phase-One of mining at Asfordby showed a strong correlation with the timing of the principal mining events (section 2.6), in particular the problems experienced at the face. The seismic event locations are very different to those observed by studies of longwall faces that experienced few problems e.g. Coventry Colliery [*Toon and Styles*, 1993], Gordonstone Mine [*Hatherley et al.*, 1997]. These other studies found that most seismic events were located in the roof immediately in front of or behind the advancing face. In this study the observed seismicity concentrated above the tail gate, in the Sherwood Sandstone and the shallower mudstones (section 3.3). Event locations in sectional view, looking perpendicular to the direction of face advance, resemble modelled seismicity for strong roof conditions and periodic weightings [*Gale and Nemcik*, 1998] (section 3.3.1). Event locations vary with time, and show that the seismicity above the tail gate defines a fracture that propagates down through the mudstone to the base of the Sherwood Sandstone (figures 3.14 and 3.15). From there a vertical fracture forms from the base of the Sandstone to seam level. The first, and

largest, weighting occurred shortly after formation of the vertical fracture. Double-couple source mechanisms have been calculated for many of the seismic events recorded during Phase-One (sections 6.2.2 and 6.3.2). The source mechanisms support the interpretation of the seismicity as a propagating fracture, and show a definite relationship between the direction of propagation and the orientation of individual event fault planes. The weighting would be associated with a reverse shear failure along the developed fracture, which occurred over a period of hours as the hydraulic roof supports slowly collapsed. Thus the weighting event is aseismic and no associated large seismic events with reverse double-couple mechanisms are observed. The fracture in the mudstone began to form over 10 weeks before the first weighting event (figure 3.14 and 3.15), which given real-time microseismic monitoring could have been predicted and remedial action taken.

7.5 Implications of this work and suggestions for future work

Numerical and physical models relevant to the Asfordby mining activity, and the induced seismicity show some similarities. However, there are many differences, demonstrating that improved models are required. In particular, the seismic activity recorded during Phase-One shows that the rock mass around the excavation was not responding as predicted by numerical and physical models of the Asfordby stratigraphy. This would have been shown by a real-time monitoring system long before the first weighting, and the weighting and other problems might have been avoided by remedial work or a change in mining strategy.

At present numerical modelling of the response of the rock mass to excavation is carried out before the mining strategy is planned; a better modelling approach would be to use the results of real-time microseismic monitoring to actively improve numerical models. This would mean that the numerical model used to plan mining strategy would better represent the response of the rock mass as the development of the mine proceeded. After the problems experienced during Phase-One of mining at Asfordby, extraction was carried out during Phase-Two with a narrower face width. This changed the induced seismicity, but the planned change in face width was not

based on modelling results. A new model that incorporated the results of the Phase-One seismic monitoring might have suggested a different mining strategy allowing the Asfordby mine to be successful. A real-time monitoring system needs to be used if the monitoring results are to effect decisions on mining strategy (this was not the case for the Asfordby project) or be used to update numerical models.

During Phase-One of mining a propagating fracture was identified. The fault planes of individual seismic events along the fracture make an angle of 45° to the direction of propagation of the fracture. A similar relationship between microcracks and throughgoing fractures has been observed in laboratory acoustic emission experiments [*Reches and Lockner*, 1994]. This highlights the significance of mining induced seismicity studies to the fields of rock physics and fracture dynamics. A mine can be used to study in detail the response of rock to a change in stress at a meso-scale between laboratory experiments and earthquake-scale investigations. The advantages of such a study are that the change in stress can be calculated and it is the macroscopic in-situ behaviour of rock that is observed. Thus the study of mining induced seismicity serves as an intermediate step that allows the scaling relationships of laboratory and earthquake observations to be determined.

Integrated Microseismic Monitoring and Numerical Modelling for the Determination of Fracture Architecture Around Longwall Coal Mines for Geomechanical Validation.

REFERENCES

Aki, K., and P. G. Richards. *Quantitative Seismology - Theory and Methods*, W. H. Freeman and Company, New York, 1980.

Altounyan, P. F. R., and D. N. Bigby (1996). Investigations into recent water inflows and weightings on 101's longwall panel, Deep Main Seam, Asfordby Mine, *Rock Mechanics Technology (RMT) report*.

Baria, R., K. Hearn and A. S. Batchelor (1989). The monitoring of the induced seismicity during the hydraulic fracturing of the potential hot dry rock geothermal reservoir, in *Proceedings of the Fourth Conference Acoustic Emission / Microseismic Activity in Geological Structures and Materials* (Hardy ed.), Trans Tech Publications, 327-352.

Bataille, K. and J. M. Chiu (1991). Polarization analysis of high-frequency, three-component seismic data, *Bull. Seism. Soc. Am. 81*, 622-642.

Bieniawski, Z. T. 1978. Determination of rock mass deformability: Experience from case histories. *International Journal of Rock Mechanics, Mining Sciences and Geomechanical Abstracts.* 15, pp 237-247.

Bieniawski, Z. T. (1987). *Strata control in mineral engineering*, AA Balkema, Rotterdam

Bishop, I., P. Styles and M. Allen (1993). Mining-induced seismicity in the Nottinghamshire Coalfield, *Quarterly Journal of Engineering Geology*, *26*, 253-279.

Browitt, C. W. A. (1979). Seismograph Networks of the Institute of Geological Sciences, U.K., *Physics of the Earth and Planetary Interiors*, *18*, 127-134.

Brown, K. M. and P. McDonald, P. (1984). A microseismic study of an outburst-prone coal seam, in *Proceedings of the Third Conference Acoustic Emission / Microseismic Activity in Geological Structures and Materials* (Hardy and Leighton eds.), Trans Tech Publications, 479-497.

Choi, D. S., and D. L. McCain (1982). Design of longwall systems, *Trans. SME-AIME*, *268*.

Cook, N. G. W. (1963). The seismic location of rockbursts, in *Rock Mechanics: Proceedings of the Fifth Symposium on Rock Mechanics* (C. Fairhurst ed.), Pergammon Press, New York, 493-516.

Daly, F., D.J. Hand, M.C. Jones, A.D. Lunn and K.J. McConway, *Elements of Statistics*, Addison-Wesley Publishing Company, Wokingham, England, 1995.

Davison, C. (1905). Earthquakes in mining districts, *Geological Magazine*, *2*, 219-223.

Davison, C. (1919). The Stafford earthquakes of January 1914-15, 1916, and the relationship between twin earthquakes of the Midland counties, *Geological Magazine*, *6*, 302-312.

Dennison, P. J. G. and van Aswegen, G. 1993. Stress modelling and seismicity on the Tanton fault: A case study in a South African Gold Mine. In: Young, R. P. (ed.) *Rockbursts and Seismicity in Mines, Proceedings of the 3rd International Symposium on Rockbursts and Seismicity in Mines, Kingston, Ontario, Canada, 16-18 August 1993.* Balkema, Rotterdam.

Dollar, A. T. J. (1951). Catalogue of Scottish earthquakes, 1916-1949, *Transactions of the Geological Society of Glasgow*, *21*, (2), 283-361.

Dreger, D. S. and D. V. Helmberger (1993). Determination of source parameters at regional distances with three-component sparse network data, *J. Geophys. Res. 98*, 8107-8125.

Dudko, Y. V., H. Schmidt, K. vonderHeyt and E. K. Scheer (1998). Edge wave observation using remote seismoacoustic sensing of ice events in the Arctic, *J. Geophys. Res. 103*, 21775-21781.

Fehler, M. (1983). Observations of volcanic tremor at Mount St. Helens volcano, *J. Geophys. Res. 88*, 3476-3484.

Fehler, M., L. House and H. Kaieda (1987). Determining planes along which earthquakes occur: Method and application to earthquakes accompanying hydraulic fracturing, *J. Geophys. Res. 92*, 9407-9414.

Feignier, B. and R. P. Young (1993). Failure mechanisms of microseismic events generated by breakout development around an underground opening, in *Rockbursts and Seismicity in Mines* (R. P. Young ed.), A. A. Balkema, Rotterdam, 181-186.

Follington, I. L. (1988) Geotechnical influences upon Longwall Mining, *Ph.D. Thesis*, University of Wales.

Gale, W. J., and J. A. Nemcik (1998). Prediction of strata caving characteristics and its impact on longwall operation, *COAL98*, Wollongong, New South Wales.

Gay, N. C. and W. D. Ortlepp (1979). Anatomy of a mining-induced fault zone, *Bull. Geol. Soc. Am. 90*, 47-58.

Gibowicz, S. J. (1984). The mechanism of large mining tremors in Poland, in *Rockbursts and Seismicity in Mines* (N. C. Gay and E. H. Wainwirght ed.), SAIMM, Johannesburg, 17-28.

Gibowicz, S. J. (1993). Keynote address: seismic moment tensor and the mechanism of seismic events in mines, in *Rockbursts and Seismicity in Mines* (R. P. Young ed.), A. A. Balkema, Rotterdam, 149-155.

Gibowicz, S. J., and A. Kijko. *An Introduction to Mining Seismology*, Academic Press, San Diego, California, 1994.

Hardy, H. R. (1977). Emergence of acoustic emission/microseismic activity as a tool in geomechanics, in *Proceedings of the First Conference on Acoustic Emission / Microseismic Activity in Geological Structures and Materials* (Hardy and Leighton eds.), Trans Tech Publications, 13-31

Hatherly, P., X. Luo, R. Dixon, B. McKavanagh, M. Barry, Z. Jecny, and C. Bugden (1995). Roof and goaf monitoring for strata control in longwall mining. *CSIRO Report no: 189F*.

Hatherley, P., X. Luo, R. Dixon, and B. McKavanagh (1997). Seismic monitoring of ground caving processes associated with longwall mining of coal, in *Rockbursts and Seismicity in Mines* (Gibowicz and Lasocki eds.), A. A. Balkema, Rotterdam, 121-124.

Holla, L. 1997. Ground Movement Due to Longwall Mining in High Relief Areas in New South Wales, Australia. *International Journal of Rock Mechanics and Mining Sciences* 34(5) pp. 775-787.

Hughes, J. E. T. (1973). Outbursts of coal and gas of the anthracite area of S. Wales, *MSc thesis (unpublished)*, University of Wales, Cardiff.

Isaacs, A.K., and I. L. Follington (1988). Geotechnical influences upon longwall mining, in *Engineering Geology of Underground Movements*, *Geol. Soc. Engineering Geology Special Publication*, *5*, 234-242.

Integrated Microseismic Monitoring and Numerical Modelling for the Determination of Fracture Architecture Around Longwall Coal Mines for Geomechanical Validation.

Ishida, T., Kanagawa, T., Uchita, Y., Urayama, M. 1993. Fault-plane solutions of microseismicity induced by progressive excavations of a large underground chamber. In: Young, R. P. (ed.) *Rockbursts and Seismicity in Mines, Proceedings of the 3rd International Symposium on Rockbursts and Seismicity in Mines, Kingston, Ontario, Canada, 16-18 August 1993.* Balkema, Rotterdam.

Itasca Consulting Group, 1996. UDEC Universal Distinct Element Code: Version 3.0. User's Manual.

Kelly, M., Gale, W., Hatherley, P., Balusu, R. and Luo, X. 1996. New understanding of longwall caving processes: results of microseismic monitoring and initial computational modelling at Gordonstone Mine. In: McNally, G. H. and Ward, C. R. (eds.), *Geology in Longwall Mining: Proceedings of a Symposium held at the University of New South Wales, 12-13 November 1996.* Conference Publications, NSW.

Lightfoot, N. 1993. The use of numerical modelling in rockburst control. In: Young, R. P. (ed.) *Rockbursts and Seismicity in Mines, Proceedings of the 3rd International Symposium on Rockbursts and Seismicity in Mines, Kingston, Ontario, Canada, 16-18 August 1993.* Balkema, Rotterdam.

Lloyd, P. W., Mohammad, N. and Reddish, D. J. 1997. Surface Subsidence Prediction Techniques for UK Coalfields – An Innovative Numerical

Jones, R.H., and R.C. Stewart (1997). A method for determining significant structures in a cloud of earthquakes, *J. Geophys. Res.*, *102*, 8245-8254.

Kaneko, K., K. Sugawara and Y. Obara (1990). Rock stress and microseismicity in a coal burst district, in *Rockbursts and Seismicity in Mines* (C. Fairhurst ed.), A. A. Balkema, Rotterdam, 183-188.

Kelly, M., W. Gale, P. J. Hatherley, R. Balusu and X. Luo (1996). New understanding of longwall caving processes - Results of microseismic monitoring and initial computational modelling at Gordonstone Mine, in *Symposium on Geology in Longwall Mining* (G. H. McNally and C. R. Ward eds.), Coalfield Geology Council of NSW, 12-13 November 1996, 153-161.

Kusznir, N. J., I. W. Farmer, D. P. Ashwin, L. G. Bradley and N. H. Al-Saigh (1980). Observations and mechanics of seismicity associated with coal mining in North Staffordshire, England, in: *Proceedings of 2lst U.S. Symp. on rock mechanics, University of Rolla, Missouri, 27 May 1980*, 632-640.

Kusznir, N. J., N. H. Al-Saigh and D. P. Ashwin (1984). Induced seismicity generated by long-wall mining in the North Staffordshire coal-field, U.K, in *Rockbursts and Seismicity in Mines* (N. C. Gay and E. H. Wainwirght ed.), SAIMM, Johannesburg, 153-160.

Langston, C. A. (1982). Single-station fault plane solutions, *Bull. Seism. Soc. Am. 72*, 729-744.

Leighton, F. (1984). Microseismic monitoring and warning of rockbursts, in *Rockbursts and Seismicity in Mines* (N. C. Gay and E. H. Wainwirght ed.), SAIMM, Johannesburg, 287-295.

Lienert, B. R., E. Berg and L. N. Frazer (1986). Hypocenter - An earthquake location method using centred, scaled, and adaptively damped least-squares, *Bull. Seism. Soc. Am. 76*, 771-783.

Lloyd, P. W., Mohammad, N. and Reddish, D. J. 1997. Surface Subsidence Prediction Techniques for UK Coalfields – An Innovative Numerical Modelling Approach.

Integrated Microseismic Monitoring and Numerical Modelling for the Determination of Fracture Architecture Around Longwall Coal Mines for Geomechanical Validation.

Proceedings of the 15th Mining Conference of Turkey, Ankara, May 6-9. pp 111-124.

McGarr, A., S. M. Spottiswoode, N. C. Gay and W. D. Ortlepp (1979). Observations relevant to seismic driving stress, stress drop, and efficiency, *J. Geophys. Res. 84*, 2251-2261.

McKavanagh, B. M. and J. R. Enever (1980). Developing a microseismic outburst warning system, in *Proceedings of the Second Conference Acoustic Emission / Microseismic Activity in Geological Structures and Materials,* (Hardy and Leighton eds.), Trans Tech Publications, 359-373

McKenzie, D. P. (1969). The relation between fault plane solutions for earthquakes and the directions of principal stresses, *Bull. Seism. Soc. Am. 54*, 295-346.

Martin, C. D. and R. P. Young (1993). The effect of excavation-induced seismicity on the strength of Lac du Bonnet granite, in *Rockbursts and Seismicity in Mines* (R. P. Young ed.), A. A. Balkema, Rotterdam, 367-371.

Maxwell, S. C. and R. P. Young (1997). Assessing induced fracturing around underground excavations using velocity imaging and induced seismicity, in *Rockbursts and Seismicity in Mines* (Gibowicz and Lasocki eds.), A. A. Balkema, Rotterdam, 179-183.

McNally, G. H. 1996. Estimation of the geomechanical properties of coal measures rock for numerical modelling. In: McNally, G. H. and Ward, C. R. (eds.), *Geology in Longwall Mining: Proceedings of a Symposium held at the University of New South Wales, 12-13 November 1996.* Conference Publications, NSW.

McNally, G. H., Willey, P. L. and Creech, M. 1996. Geological factors influencing longwall-induced subsidence. In: McNally, G. H. and Ward, C. R. (eds.), *Geology in Longwall Mining: Proceedings of a Symposium held at the University of New South Wales, 12-13 November 1996.* Conference Publications, NSW.

Mendecki, A. J. (1993). Keynote address: Real time quantitative seismology in mines, in *Rockbursts and Seismicity in Mines* (R. P. Young ed.), A. A. Balkema, Rotterdam, 287-295.

Mendecki, A. J. (1997a). *Seismic monitoring in mines*, Chapman & Hall, London, 1997.

Mendecki, A. J. (1997b). Keynote address: Principles of monitoring seismic rockmass response to mining, in *Rockbursts and Seismicity in Mines* (Gibowicz and Lasocki eds.), A. A. Balkema, Rotterdam, 69-80.

Minney, D., G. Kotze and G. van Aswegen (1997). Seismic monitoring of the caving process above a retreating longwall at New Denmark Colliery, South Africa, in *Rockbursts and Seismicity in Mines* (Gibowicz and Lasocki eds.), A. A. Balkema, Rotterdam, 125-129.

Mohammad, N., Reddish, D. J. and Stace, L. R. 1997a. The relationship between in situ and laboratory rock properties used in numerical modelling. *International Journal of Rock Mechanics, Mining Sciences and Geomechanical Abstracts.* 34(2) pp 289-297.

Mohammad, N., Reddish, D. J. and Lloyd, P. W. 1997b. Longwall Surface Subsidence Prediction through Numerical Modelling. *Proceedings of the 16th International Conference on Ground Control in Mining,* West Virginia, USA, August 4-6. pp 34-42.

Montalbetti, J. F. and E. R. Kanasewich (1970). Enhancement of teleseismic body waves with a polarization filter, *Geophys. J. R. Astr. Soc. 21*, 119-129

Neilson, G., R. M. W. Musson. and P.W. Burton (1984). Macroseismic reports on the historical British earthquakes, V., Midlands, *Global Seismology Report No. 228(b)*, British Geological Survey, Edinburgh.

Nicholson, G. A. and Bieniawski, Z. T. 1990. A nonlinear deformation modulus based on rock mass classification. *International Journal of Mining and Geological Engineering.* 8 pp. 181-202.

North, M. D., and R. I. Jeffrey (1991). Prediction of water inflow into coal mines from aquifers, *Commission of the European Communities*, ECSC Agreement 7220-AF/826.

Ohtsu, M. (1991). Simplified moment tensor analysis and unified decomposition of acoustic emission source - application to in situ hydrofracturing test, *J. Geophys. Res. 96*, 6211-6221.

Ohtsu, M. (1995). Acoustic emission theory for moment tensor analysis, *Res. Nondestr. Eval. 6*, 169-184.

Park, J., F. L. Vernon and C. R. Lindenberg (1987). Frequency-dependent polarization analysis of high-frequency seismograms, *J. Geophys. Res*. *92*, 12664-12674.

Pearce, R. G. (1987). The relative amplitude method applied to 19 March 1984 Uzbekistan earthquake and its aftershocks, *Phys. Earth Planet. Inter. 47*, 137-149.

Peng, S. S. and Chiang, H. S. 1984. *Longwall Mining.* John Wiley and Sons, New York.

Phillips, W. S., T. D. Fairbanks, J. T. Rutledge and D. W. Anderson (1998). Induced microearthquake patterns and oil-producing fracture systems in the Austin chalk, *Tectonophysics*, *289*, 153-169.

Potgieter, G. J. and Roering C. 1982. The Influence of Geology on the Mechanisms of Mining-associated Seismicity in the Klerksdorp Gold-field. In: Gay, N. C and Wainwright, E. H. (eds.) *Proceedings of the 1st International Congress on Rockbursts and Seismicity in Mines, Johannesburg, 1982.* SAIMM. Johannesburg. 1984

Press, W.H., B.P. Flannery, S.A. Teukolsky and W.T. Vetterling, *Numerical Recipes: The Art of Scientific Computing*, Cambridge Univ. Press, New York, 1986.

Reches, Z., and D. A. Lockner (1994). Nucleation and growth of faults in brittle rocks, *J. Geophys. Res. 99*, 18159-18173.

Reddish, D. J., Mohammad, N. and Lloyd, P. W. 1998. The Numerical Modelling of International Trends in Subsidence Models. (*Paper accepted for presentation at International Conference on Geomechanics / Ground Control in Mining and Underground Construction – GGM'98, to be held on 14-17 July 1998* at Wollongong, NSW, Australia)

Redmayne, D. W. (1988). Mining induced seismicity in UK Coalfields identified on the BGS National Seismograph Network, in *Engineering Geology of Underground Movements*, *Engineering Geology Special Publication*, *5*, Geological Society, London, 405-413.

Redmayne, D. W., J. A. Richards and P. W. Wild (1996). Seismic monitoring of mining-induced earthquakes during the closing stages of production at Bilston Glen Colliery, Midlothian, 1987-1990, *Technical Report WL/96/14*. British Geological Survey, Edinburgh.

Revolar, R., J. P. Josien, J. Ch. Besson and A. Magron (1990). Seismic and seismo-acoustic experiments applied to the prediction of rockbursts in French coal mines,

in *Rockbursts and Seismicity in Mines* (C. Fairhurst ed.), A. A. Balkema, Rotterdam, 301-306.
Riefenberg, J. S. (1989). A simplex-method-based algorithm for determining the source location of microseismic events, *U. S. Bureau of Mines*, RI 9287, 12.
Rigby, N. and J. Wardle (1984). Microseismic monitoring and outburst prediction, in *Proceedings 15th Ann. Inst. Coal Mine Health, Safety and Research, Blacksburg, Virginia*.
Rigby, N. and P. B. Bolt (1989). Development and application of an underground microseismic monitoring system for outburst prone coalmines, *The Mining Engineer*, *November 1989*, 197-203.
Rognvaldsson, S. and R. Slunga (1993). Routine fault plane solutions for local networks: a test with synthetic data, *Bull. Seism. Soc. Am. 83*, 1232-1247.
Rutledge, J. T., W. S. Phillips and B. K. Schuessler (1998). Reservoir characterization using oil-production induced microseismicity, Clinton County, Kentucky, *Tectonophysics*, *289*, 129-152.
Samson, J. C. (1973). Descriptions of the polarisation states of vector processes: Applications to ULF magnetic fields, *Geophys. J. R. Astr. Soc. 34*, 403-419.
Sato, K., Y. Fujii, Y. Ishijima, and S. Kinoshita (1989). Microseismic activity induced by longwall coal mining, in *Proceedings of the Fourth Conference Acoustic Emission / Microseismic Activity in Geological Structures and Materials* (Hardy ed.), Trans Tech Publications, 249-263.
Schwartz, S. Y. (1995). Source parameters of aftershocks of the 1991 Costa Rica and 1992 Cape Mendocino, California, earthquakes from inversion of local amplitude ratios and broadband waveforms, *Bull. Seism. Soc. Am. 85*, 1560-1575.
Seeber, L., J. G. Armbruster, W.-Y. Kim, N. Barstow and C. Scharnberger (1998). The 1994 Cacoosing Valley earthquakes near Reading, Pennsylvania: A shallow rupture triggered by quarry unloading, *J. Geophys. Res.*, *103*, 24505-24521.
Seedsman, R. and Stewart, A. 1996. A design method to assess massive strata for longwall face and subsidence behaviour. In: McNally, G. H. and Ward, C. R. (eds.), *Geology in Longwall Mining: Proceedings of a Symposium held at the University of New South Wales, 12-13 November 1996.* Conference Publications, NSW.
Spottiswoode, S. M. and A. McGarr (1975). Source parameters of tremors in a deep-level gold mine, *Bull. Seism. Soc. Am. 65*, 93-112.
Spottiswoode, S. M. (1984). Source mechanisms of mine tremors at Blyvooruitzicht Gold Mine, in *Rockbursts and Seismicity in Mines* (N. C. Gay and E. H. Wainwirght ed.), SAIMM, Johannesburg, 29-37.
Spottiswoode, S. M., and A. M. Milev (1998). The use of waveform similarity to define planes of mining-induced seismic events, *Tectonophysics*, *289*, 51-60
Styles, P. and S. J. Emsley (1987a). Integrated microseismic monitoring and early warning system for outbursts of coal and firedamp, *NCB/ECSC Research Contract YCE 28/17619: Final Report*.
Styles, P., T. Jowitt and E. Browning (1987b). Surface microseismic monitoring for the prediction of outbursts, *22 Int. Conference Safety in Mine Research, Bejing, China* (Dai Guoquang ed.), 767-780.
Styles, P., S. J. Emsley and E. A. McInairnie (1991). Microseismic prediction and control of coal outbursts in Cynheidre Colliery. In *Proceedings of the Fifth Conference Acoustic Emission / Microseismic Activity in Geological Structures and Materials* (Hardy ed.), Trans Tech Publications, 265-274.

Integrated Microseismic Monitoring and Numerical Modelling for the Determination of Fracture Architecture Around Longwall Coal Mines for Geomechanical Validation.

Styles, P. (1993). Implications of harmonic-tremor precursory events for the mechanism of coal and gas outbursts, in *Rockbursts and Seismicity in Mines* (R. P. Young ed.), A. A. Balkema, Rotterdam, 415-421.

Styles, P. , Toon. S., and Bryan-Jones. A., (1996). Microseismic Monitoring Work in the vicinity of Asfordby Colliery including the seismic Mapping of the Location of mechanical Failures in the Overburden: Research Contract 2069/3 (International Mining Consultants.). 116 p.

Sun, G. X., D. J. Reddish and B. N. Whittaker (1992a). Subsurface fracture development due to longwall mining and its interpretation using image processing techniques, *11th International Conference on Ground Control in Mining*, The University of Wollongong, New South Wales.

Sun, G. X., D. J. Reddish and B. N. Whittaker (1992b). Image analysis technique for rock fracture pattern studies around longwall excavations, *Trans. Instn. Min. Metall. (Sect. A: Min. industry) 101*, A159-A165.

Toon, S. M. (1990). The location of faults in coal seams using microseismic activity. *B.Sc. Dissertation (unpublished)*, University of Liverpool.

Toon, S. M., P. Styles and P. Jackson (1992). Microseismic imaging of fractures around longwall coal faces using downhole three component geophones. *XVIIth General Assembly, European Geophysical Society, Edinburgh, 6-10 April 1992*. Abstract.

Toon, S. M. and P. Styles (1993). Microseismic event location around longwall coal faces using borehole in-seam seismology. In *Rockbursts and Seismicity in Mines* (R. P. Young ed.), A. A. Balkema, Rotterdam, 441-444.

Urbancic, T. I., C-I. Trifu and P. Young (1993). Microseismicity derived fault-planes and their relationship to focal mechanism, stress inversion and geologic data, *Geophys. Res. Lett.*, *20*, 2475-2478

Vidale, J. E. (1986). Complex polarization analysis of particle motion, *Bull. Seism. Soc. Am. 76*, 1393-1405.

Walker, A. B., and D. D. Galloway (1997). Musselburgh earth tremors, *UKGA-21, Southampton, 2-4 April 1997*. Abstract.

Westbrook, G. K., N. J. Kusznir, C. W. A. Browitt and B. K. Holdsworth (1980). Seismicity induced by coal mining in Stoke-on-Trent (UK), *Engineering Geology*, *16*, 225-241.

Whitworth, K., M. D. North and K. R. Onions (1994). Investigation into the effects of lithology on the magnitude and ratio of in-situ stress in Coal Measures, *Commission of the European Communities*, Agreement number 7220-A-F/854, DG XVII-D2.

Wiejacz, P. and A. Ługowski (1997). Effects of geological and mining structures upon mechanism of seismic events at Wujek coal mine, Katowice, Poland, in *Rockbursts and Seismicity in Mines* (Gibowicz and Lasocki eds.), A. A. Balkema, Rotterdam, 27-30.

Wong, I. G. and A. McGarr (1990). Implosional failure in mining-induced seismicity: a critical review, in *Rockbursts and Seismicity in Mines* (C. Fairhurst ed.), A. A. Balkema, Rotterdam, 45-51.

Wong, I. G. (1993). Tectonic stresses in mine seismicity: are they significant?, in *Rockbursts and Seismicity in Mines* (R. P. Young ed.), A. A. Balkema, Rotterdam, 273-278.

Integrated Microseismic Monitoring and Numerical Modelling for the Determination of Fracture Architecture Around Longwall Coal Mines for Geomechanical Validation.